

# Design Synthesis Exercise

## Final Report - Group 24 Next- Generation Close Air Support Combat Aircraft

Technische Universiteit Delft



# Design Synthesis Exercise

## Draft Final Report

by

Group 24

Next-Generation Close Air Support Combat Aircraft

Authors:	Piet Bastiaanssen	4373413
	Charlie Bogaerts	4380770
	Yair Brouwer	4488989
	Josh Coglan	4429893
	Thom Dotman	4351843
	Alain Faddegon	4485718
	Dave Koch	4331141
	Joris Koopman	4306430
	Andrej Nikolajevic	4445953
	Tjomme Posthuma de Boer	4460227
Group Tutor:	Dr. Ir. Wim Verhagen	TU Delft (ATO)
Group Coaches:	Ir. Reynard de Vries	TU Delft (FPP)
	Ir. Yasir Zahoor	TU Delft (ASCM)
Supporting member of staff:	Maj. Jeff Newcamp, MSc.	TU Delft (ATO)
With our sincere gratitude:	Mr. Andy Deacon	

## Preface

Our DSE group consists of ten prospective aerospace engineers, currently in the final stages of obtaining their Bachelor of Science in Aerospace Engineering from the Delft University of Technology. To conclude this final assignment (DSE) of the aforementioned bachelor, our tutor gave us the assignment to deliver a successful and innovative close air support combat aircraft design.

The DSE is our first encounter with the designing of a complete aircraft in a high level of detail, and is intended to enhance our engineering and teamwork skills. Moreover, it allows the team to apply all knowledge obtained in the bachelor's degree to a realistic problem.

The team would like to express its gratitude to its tutor dr. ir. Wim Verhagen and both coaches ir. Reynard de Vries and ir. Yasir Zahoor. In addition, we would like to thank Maj. Jeff Newcamp for his efforts to help us whenever needed.

Group 24  
Delft, June 2018

# Changelog

Whole report - Formulation and writing errors fixed.

Executive Overview - Added loiter performance to [Table 1](#).

[chapter 20](#) - Added to centralise recommendations.

[chapter 20](#) - Added weapons system recommendations.

[Figure 13.3](#) - Added figure axis units.

[section 13.4](#) - Edited figure axis units.

[section 17.2](#) - Edited introduction.

[section 19.2](#) - Edited manufacturer & assembly location.

[chapter](#) - Changed nominal payload weight.

[chapter 5](#) - Changed nominal payload weight.

[section 6.2](#) - Changed nominal payload weight.

[section 8.2](#) - Added references to related chapters.

[section 13.3](#) - Changed title of [Figure 9.2](#).

[chapter 10](#) - Updated sentences.

[section 13.3](#) - Corrected units in the axis labels of [Figure 13.6b](#) through [Figure 13.7b](#) and [Figure 13.9b](#) through [Figure 13.10b](#).

[section 13.4](#) - Added discussion on why lift was not included for the tail analysis.

[section 11.1](#) - Free body diagram added.

[section 11.5](#) - Restructured and split into [section 11.5](#) and [section 11.6](#) and improved content.

[chapter 1](#) - Added missing chapter references.

## Executive Overview

Up to this point in time the Fairchild Republic A-10 Thunderbolt II has been the forerunner in Close Air Support (CAS) missions since its introduction into service in 1977. It has had a long service life which is now reaching its end, having been extended multiple times. This means there is a need for a replacement which has equivalent or improved functionality for the current CAS needs. This mostly concerns battlefield availability, which translates into the loiter time the aircraft should be capable of. Currently UAVs are the benchmark in loitering time with up to 42 hours of flying, which is far more than the 2.5 hours which is common among current CAS aircraft. There is now a demand for dedicated CAS aircraft that have an increased loiter time but still carry the same amount of firepower as previous generation aircraft, which leads to the project objective statement for this exercise:

*“Deliver a successful and innovative close air support combat aircraft design which outperforms the A-10 in the current environment of asymmetric warfare.”*

This report marks the final instalment in the series of reports covering the work performed in the DSE. The previous reports are the project plan, baseline report and midterm report which dealt with the organisation of the project, conceptual design of multiple concepts that were then analysed when a trade-off was performed between four concepts. One of these concepts was chosen from this trade-off and then smaller subsystem trade-offs were performed in order to come up with the final concept that has been taken forward into this report and analysed and designed further.

Initially user requirements were given that had to be adhered to in order to have what is considered a successful design. An initial market analysis was also performed to come up with functionalities that would allow the aircraft to outperform current CAS aircraft. Using these, a functional analysis was done to generate additional requirements the aircraft has in order to fulfil these functionalities. Around fifteen concepts were created using design option trees for the options arising from varying wings, empennages and engines used in different aircraft. From these fifteen concepts, four were taken forward to the trade-off through the use of a qualitative analysis and are summarised in [Table 2.1](#).

The trade-off contained six criteria with one extra added when a sensitivity analysis was performed to make sure there was not any conflict as to which concept would be chosen to be taken forward in the design process. Each criterion had its own weight depending on how important that particular criteria was determined to be. The criteria were as follows: loiter performance, structural weight, austere airfield capability, rate of climb, hardpoint availability, and damage tolerance. The criterion added during the sensitivity analysis was the turning performance. During the sensitivity analysis each criterion had its weight raised and lowered. The results of the trade-off saw concept one as the best. During the sensitivity analysis, none of the remaining three concepts came within a reasonable margin to concept one and so this was taken forward to the next design phase.

In order to perform the analysis required on the aircraft, a mission profile needs to be defined so that a functional breakdown structure, FBS, can be found and the driving requirements can be identified. The mission profile is stated in [section 3.1](#) and is set to be the most stringent mission profile available with a period of loiter for 6 hours, combat for 20 minutes and a cruise segment each way of 500 km. The mission profile is then used to create the FBS which is split into 5 sections: pre-flight operations, flight operations, post-flight operations, maintenance and abnormal operations. The identification of the driving requirements is aided by the mission profile and the FBS and are as follows:

- The internal weapon system shall be able to disable ground targets at a range of at least 800 m.
- The system shall have a nominal range of 2000 km.
- The system shall have a loitering capability of 6 hours at 10000 feet in racetrack pattern at maximum endurance airspeed.
- The system shall have a ferry range of 4150 km.
- The system shall be able to take off at non-paved airfields.

- The system shall have a minimum landing distance of less than 6000 ft at 10 000 ft altitude.
- The MTOW shall be less than 23 000 kg.
- The maximum payload weight of the system shall be at least 4000 kg including 1 crew member, armament and external fuel.
- The unit cost of the system shall be less than \$15 million.

The outcome of the design process is presented in [Table 1](#) which contains the main characteristics of the design. A render of the aircraft can be found on the title page.

Table 1: Main characteristics of the final design.

Description	Value	Reference
Maximum take-off weight	21 880 kg	<a href="#">section 8.1</a>
Maximum landing weight	18 592 kg	<a href="#">section 4.3</a>
Maximum fuel weight	6747 kg	<a href="#">section 11.3</a>
Nominal payload weight	4527 kg	<a href="#">section 4.3</a>
Wing surface area	52.9 m <sup>2</sup>	<a href="#">section 13.3</a>
Wing span	20.6 m	<a href="#">section 13.3</a>
Nominal range	5244 km	<a href="#">section 11.4</a>
Ferry Range	6798 km	<a href="#">section 11.4</a>
Minimum take-off distance	599.4 m	<a href="#">section 11.2</a>
Minimum landing distance	325.7 m	<a href="#">section 11.2</a>
Nominal loiter time	6 h	<a href="#">section 11.4</a>

After choosing one concept to take forward, the design process was set up with two distinct phases, phase one and phase two. A N2-chart was used to keep an overview of the two phases of the design which can be found in [Figure 4.1](#). Phase one concerned the use of Class I and II estimations and the preliminary sizing of components of the aircraft such as the high lift devices and the empennage. Once the maximum takeoff weight, MTOW, had converged to within 0.1%, phase one was considered finished and the sizing and characteristics of the aircraft are considered to be accurate such that the detailed design of the aircraft can be performed. Mass budgets and contingencies were setup at a value of 5% lower than the required value to account for any growth throughout the design.

Verification and Validation is an important part of the design process. Code verification was done through the use of code specifications which includes the description of code by the writer so that it can be independently verified. Another form of verification that has been performed is unit testing. This is made up of continuity and consistency tests. In the former an input is changed, usually to zero, and the output is checked for changes. In a consistency test, an input value is changed by a specific amount and then the output value is checked to make sure the change is of an expected amount or order of magnitude. Validation was performed by obtaining real flight data or data about aircraft and then inputting it into the codes to see if the outputs are within a certain amount of the actual data for the aircraft that is being looked at.

One of the main characteristics of the designed aircraft, is the weapons configuration. The weapons consist of a gun system, and external weapons mounted to hardpoints. The gun system is chosen to be the THL-20 turret as made by Nexter. The turret has a total of 60 deg of freedom in elevation and 120 deg in azimuth to fire the weapon. The gun is attached underneath the fuselage, in a so-called canoe (aerodynamic fairing). The gun is fed by 20 mm cartridges which weigh 273 g. The total gun ammunition weight will be 273 kg.

The aircraft has a total of 9 hardpoints, of which 3 are placed on the fuselage and 3 are placed on each wing. The placement was determined based on the maximum payload weight of 5361 kg and aircraft stability reasons. The ordnance which can be placed on the hardpoints can be found in [Table 6.3](#).

Also with respect to the hardpoint accessibility, the wing positioning is of huge importance. In [chapter 7](#) it is determined that the aircraft has a low wing. This is for maintainability, accessibility, and propeller diameter reasons. Since the propeller diameter is 3.81 m, a quick engine change-out will become complicated with a mid or high wing configuration.

With a low wing configuration, and a big propeller the engine position is up for discussion. With the landing gear extended, the propeller has a ground clearance of 0.945 m and a fuselage clearance of 0.2 m. The

engines are placed as close as possible to the fuselage, to reduce the yaw moment produced by asymmetric thrust in case one engine becomes inoperative.

In order to come up with the first weight estimations for the aircraft, Class I and Class II weight estimations are performed. For the Class I estimation a list of reference aircraft and their weights, [Table 8.1](#), was setup. From this data a relation between OEW and MTOW was calculated. Furthermore, weight fractions for the mission profile were selected and a relation for the MTOW was setup. The Class II weight estimation focused on the structural weight, powerplant weight, and fixed equipment weight. Using the equations from Airplane Design Part V: Component Weight Estimation [1], the respective weights were determined to be 5121.3 kg, 3491.9 kg, and 2922.9 kg.

Furthermore the centre of gravity range was determined at this stage in the analysis. The range in centre of gravity of the wing and fuselage were considered separately in order to help with the longitudinal placement of the wing. For the fuselage, systems which have a volume were reduced to point masses which got their mass from the Class II weight estimation. When looking at the wing, a similar method was used and the maximum and minimum wing weight was considered as this greatly affects the placement of the wing longitudinally.

Since the concept was based on a turboprop aircraft, several turboprop engines were analysed. It became clear that the turboprop engines could easily make the range and endurance requirements. However, the T/W requirement posed a challenge. It was assumed that the T/W was most critical at ingress velocity. Based on this flight condition, two Rolls Royce AE2100A engines with Dowty Aerospace R381 six blade propellers were selected.

Following the engine selection, the analysis of the takeoff and landing performance was done. For the exact calculation method, one is referred to [section 11.2](#). The results are summarised in [Table 2](#) and [Table 3](#).

Table 2: Minimum take-off and landing distances for specified conditions.

Condition	Altitude	Take-off Distance [m]	Landing Distance [m]
Dry Asphalt	Sea Level	599.4	325.7
Dry Asphalt	10 000 ft	811.8	433.4
Wet Grass	Sea Level	649.0	444.8
Wet Grass	10 000 ft	878.6	598.5

Table 3: Critical landing conditions and their respective landing distances.

Condition	Dry Asphalt, Only Brakes	Wet Grass, Only Brakes	Any Surface, Only $T_{rev}$
Landing Distance [m]	631.0	1120	908.8

Furthermore, the performance of the aircraft was analysed into detail. The fuel burn is estimated in [section 11.3](#) and serves as input for the payload-range and mission profile analysis. In [Table 4](#) the payload-range values are specified. The nominal range of the aircraft is 3783 km, and the ferry range is 6798 km.

Table 4: Payload-range diagram point specifications.

Point	Range [km]	TOW [kg]	OEW [kg]	Reserve fuel [kg]	Fuel [kg]	Payload [kg]
0	0	17063	11447	255	0	7000
1	2433	21880	11447	255	3178	7000
2	3783	21880	11447	255	4817	5361
3	5244	16544	11447	255	4817	0
4	5556	21880	11447	255	6702	3446
5	6798	16716	11447	255	6702	172

After the performance analysis is finished the wing can be designed, which is discussed in [chapter 9](#). Here it is concluded that the root airfoil is going to be the NACA 65(3)-618, and the tip airfoil is going to be the NACA 6412. Between the root and the tip the airfoil is linearly interpolated over the wing span.

To obtain the most efficient lift distribution over the wing, which is elliptical, a taper ratio,  $\lambda$ , of 0.4 was obtained. The quarter chord sweep-angle of the wings will be 0 deg since the Mach number during cruise is 0.5. Since the sweep angle is 0 deg, a dihedral angle of 3 deg is desired to obtain roll stability. Furthermore, to ensure the wing root stalls before the tip does, a twist angle of  $-3$  deg is used. To make sure the fuselage is at a reasonable angle of attack during the loitering phase the incidence angle of the wing is set at 6.3 deg. To achieve a higher  $C_{L_{max}}$  during take-off and landing, slotted flaps are designed to complement the wing. The hinge line of the flaps is at 70% of the chord line which is 10% of the chord behind the wingbox aft spar, and the flapped area is determined to be 24.96 m<sup>2</sup>.

Since the wing is designed, the aerodynamic analysis can be started. At first a drag breakdown was made. In this breakdown the wing, fuselage, empennage, engine nacelle, flap, canopy, store, canoe and gun drag were considered. Drag polars were setup for the aircraft in various conditions, to calculate the combined drag polars. To supplement the drag polars, the lift characteristics are setup for the same flight conditions. Finally, the aerodynamic moment characteristics are calculated, which are input for the stability analysis of the aircraft.

In [chapter 12](#), the split-X tail is sized. It is determined that the x-areas (diagonal parts) of the tail are set at an angle of 60 deg, and that the tail dimensions are as can be seen in [Figure 1](#). Furthermore the horizontal stabiliser aspect ratio  $AR_{H_{eff}}$  is 4.5, and the diagonal aspect ratio  $AR_{V_{eff}}$  is 0.8734.

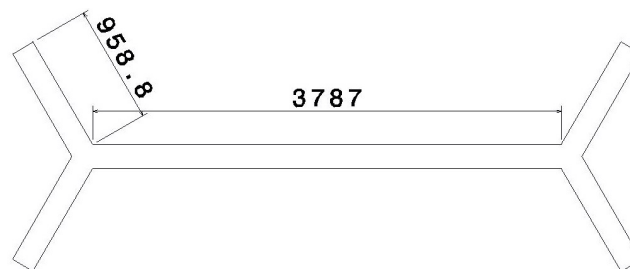


Figure 1: Split-x tail front view, all values given in mm.

The analysis of the structure of the aircraft was started by identifying the load cases the aircraft should be able to cope with during operation. To start with a manoeuvring load diagram was made taking into the user requirement of the ability to do manoeuvres with load factors of +6 and -3 followed by a gust load diagram as well. The gust load factors were found to not be dominant in any condition due to the load factors that must be designed for as per the user requirements, so the manoeuvre loads were taken forward as the loads to design for with a safety factor of 1.5. These load factors now become +9 and -4.5.

Landing on austere airfields was seen to be a loading case that should be considered, especially as it was specified in the user requirements for the project guide [2]. Taking the maximum vertical landing speed with a safety factor of 1.5, 15 ft/s, and the maximum landing weight of 182 390 N the main landing gear should be able to cope with a force equal to 96 909 N. Following this the wing, fuselage and empennage were looked at to find the resultant forces and moment acting on them so that they are able to be designed for.

Firstly looking at the wing, the forces acting on the wing were analysed during both cruise condition and during the maximum load factor of +9. After making free body diagrams to show where the forces are acting on the wing, the resultant forces and moments acting on the wing were found by marching through the wing from tip to root. Visualisations of this are found, for the cruise load case, in [Figure 13.5a](#) through [Figure 13.7b](#) and for the +9 load factor case, in [Figure 13.8a](#) through [Figure 13.10b](#).

As the wing is a crucial part of the design of the aircraft, more detail was explored into the design of the wing box and the loads and stresses acting on it. After assumptions were made about the shape of the wingbox, the taper ratio in chordwise and thickness directions were found. In order to start the analysis it was decided to use structural idealisation to start with and then calculate the skin and stringers that are needed to be able to cope with the loads on the wing. Booms were made around the cross section and shear and torsion were designed for using the boom method. Once the shear flow was found, the shear stress around the cross section found and a required thickness was obtained for this specific case from assuming a boom area and the fractions of the boom area that should be taken up by the stringers and skin. Bending was investigated next followed by buckling of the skin and spar and again a required thickness was found for each part of the wingbox via the aforementioned method. The next step in designing the wingbox is the component design of

stringers, spars and ribs. The flange sections of the Z-stringer are both 0.03 m with a height of 0.05 m and a thickness of 0.0026 m. The spar height ranges from 0.1586 m to 0.5949 m between the tip and root chord with a flange length of 0.1082 m and thickness of 0.0055 m. Having found dimensions for each part of the wingbox, the stress distributions can be plotted for the different load cases and are visualised in [Figure 13.18a](#) through [Figure 13.21](#) for most extreme load factors of +9 and -4.5. Finally the wing deflection was calculated throughout the wingbox using the superposition of standard solutions and is visualised in [Figure 13.24](#). The tip deflection at cruise can be seen to be 0.368 m.

The forces acting on the tail, weight and drag, were analysed during cruise in the same way as the wing. First the upper part of the split X tail was walked through, then the lower part and finally the horizontal part of the tail. Visualisations of the forces and moments acting throughout the wing are presented in [Figure 13.26a](#) through [Figure 13.28b](#). The resultant forces and moments from the wing and the tail were then fed into the analysis performed on the fuselage which consisted of the same analysis as with the tail.

Various materials that might have been used for the structure were investigated and aluminium, titanium and steel alloys were found. However, the aluminium found, AL2090-T86, was seen to be the most optimal and was decided to be used throughout the design. Having performed this analysis there are some recommendations that come out for further analysis into the fuselage and tail for example. The cross sectional design of the fuselage and the tail should be performed as well as analysis on how the inertial forces between the wing, hardpoints and landing gear act on the wing among others.

For the landing gear, the retractable tricycle configuration was selected. The retractable configuration was chosen due to loiter and performance considerations, while the tricycle offers good visibility and steering characteristics. For stability reasons the nose and main landing gear are placed at respectively 1.5 m and 7.57 m measured from the nose. In addition, the shock absorbers are designed to have a maximum stroke of 0.333 m.

The fuel system consists of two wing and two fuselage located fuel tanks. All fuel tanks hold the same amount of fuel, which is equal to 1360 kg of fuel per tank. The wing tanks are self-sealing, and the fuselage tanks are placed in the top of the fuselage to protect them from damage due to enemy fire. The aircraft is also capable of performing aerial refuelling missions, and can distribute fuel by opening and closing crossfeed valves.

Furthermore in [section 14.3](#) the computer breakdown of the aircraft is setup. It is determined that the aircraft uses a full 'triplex monitored' FBW control system, since it saves weight and can be programmed to respect the aircraft's flight envelope. The actuators used for the FBW control system are Power By Wire and are called "fixed displacement electro-hydrostatic actuators". To power all actuators and on-board control systems, the aircraft relies on five different power sources which are dependent on the phase of flight. These power sources are: the engines, APU, ram air turbine, battery, and ground power unit.

To investigate the cost of all the subsystems a market and cost analysis was performed. The market analysis from the Baseline Report is presented with a more in-depth look at the various costs associated with the production and selling of the aircraft as well as the return on investment that is expected to be made throughout the aircraft life. A SWOT analysis was made to see where in the market the aircraft should be positioned in order to maximise its appeal and where threats to the appeal of the aircraft will come from, for example the push toward unmanned platforms would be detrimental to the production and sale of this aircraft as a manned platform is being produced. A market share was estimated to be around 600 aircraft as a maximum value to be sold and produced throughout the aircraft's life. A unit price is estimated using aircraft that perform similar roles on the battlefield, the F-35 Joint Strike Fighter and the MQ-9 Reaper, of \$45.57 million. Unit cost of the aircraft is also evaluated and it is seen that the greater the number of aircraft that can be sold, the cheaper the aircraft can become. Using a DAPCA IV cost model modified by Raymer an exponential model was obtained that described the relationship between the number of aircraft sold with the unit cost of each aircraft. In order to comply with the user requirement of a unit cost of \$15 million it can be seen that around 650 aircraft need to be sold. If, however, only 100 aircraft are sold, it can be seen that the unit cost will be around \$32 million. As the DAPCA IV cost model is unreliable with low production numbers due to the exponential nature of the trend, it is assumed that \$32 million is the maximum unit cost of the aircraft.

Operational costs are a big part of the lifetime cost of an aircraft and is investigated next. It was found that newer aircraft benefit from reduced operating costs compared to older aircraft of the same type. An operational cost of between \$2500 and \$3500 is found for the aircraft which excludes the cost of the fuel and ammunition. For the fuel the costs are estimated to be around \$3700 for full fuel tanks however the ammunition costs will vary depending on the loadout chosen for each mission. The operational costs for the

mounted gun are estimated to be around \$350 per 100 rounds of ammunition used. A calculation for the return on investment was performed and found that, depending on the unit cost, a range of 42.4% to 203.8% return on investment can be made. To account for all the costs that are expected to be encountered a cost breakdown was made and can be found in [Figure 15.3](#).

Following the current trends in aviation it is important to pay attention to a sustainable development strategy. Especially, the engine choice was influenced by the sustainable philosophy. The engine chosen for the aircraft is the Rolls Royce AE2100. Furthermore the armaments are checked for sustainability, and therefore the armaments selected do not contain depleted uranium, as is used by comparable aircraft. In addition, the operational cost of the aircraft implies greater economical sustainability than its competitors. Lastly, the primary structural material of the aircraft will be made of aluminium, which is easy to recycle.

The reliability of the aircraft is an important aspect of how well it can perform. The reliability of the engine was looked at first, the Rolls-Royce AE 2100A engine was selected and was seen to have a dispatch reliability of 99.85% which should be increased upon as this figure is from 1999. Three separate fly-by-wire systems are used with three flight control computers meaning two fly-by-wire systems can fail and the aircraft will still be able to fly, making the aircraft more reliable. To increase reliability fault detection methods can be implemented and are recommended to look into further in the future. Other methods to improve reliability have been looked into and will be presented within the risk assessment and mitigation.

The availability of a CAS fleet is one of the most important operational characteristics it possesses. Availability is achieved by a simple and sturdy design, implementing proven engines and weapons systems. Maintenance procedures have been established, leading to an optimal availability. The proper planning of preventive maintenance can help increase the availability. This is very applicable to CAS aircraft due to the nature of their mission. Maintenance data on military aircraft is not readily available and so availability figures for the AE 2100A engine have been looked into. It can be seen that the mean time between repairs is 3500 hours and per hour of flight time, half an hour will need to be used for maintenance.

Maintenance is an important part of keeping the plane available but also part of the reliability of the aircraft. In terms of the engine, it has been placed on top of the wing, the required change out time will be smaller due to this as a single crane will be sufficient to remove the engine. Easy access panels are going to be placed around the aircraft increasing the maintainability of the aircraft as it will then be easier to access systems that would take a longer time to get to earlier.

The nature of CAS mission means that safety is another important aspect of keeping the aircraft flying as well as the pilot safe and implies earlier failure rates than with other types of aircraft. Measures have been taken, for example active damage suppression, to reduce the vulnerability of the aircraft and will also be dealt with in the section on the risk assessment and mitigation of the entire system. For the fuel system, two of the four fuel tanks have been placed in the upper half of the fuselage so that the risk of them getting punctured is minimised and the two fuel tanks in the wing will be self sealing along with the use of redundant fuel pumps. These will also be filled with a fire retardant foam to minimise the risk of fire. There is also redundancy designed into the control surfaces of the split X tail. The control surfaces inherently have redundancy due to the nature of the split X tail, with redundancy in pitch and roll control and will be split into two sections to reduce the impact of one section failing during flight. Other than redundancy there is also active and passive countermeasures included such as flare and chaff pods and the possibility of including jamming systems as well. A titanium bathtub to protect the pilot is also included to increase the safety of the pilot and the plane.

A detailed look at the risks posed to both the pilot and the aircraft's safety is followed with mitigation strategies presented such that any risks can be minimised to a reasonable level depending on the severity of the consequence. As can be seen in the risk map in [Figure 17.1](#) there are no risks in the upper right section meaning that all risks that have a high probability of occurring have negligible consequences and vice versa.

The operational procedures of the aircraft are split up into combat mission operations and gun operations. For combat operations a flow chart is setup in [section 18.2](#). In this flow chart the operating procedures for a normal combat mission are placed into chronological order. In [section 18.3](#) the operational procedures for the gun use are discussed. Either the pilot can control the gun movement or a ground operator can do it via a complex communication system, this is subject to further investigation in future design phases.

After the completion of the DSE the preliminary technical design of the aircraft can be seen as completed. However, more technical analysis is required in the detailed design phase before entering the pre-production

stage. The detailed design phase consists of Class III and Class IV analysis. Class III analysis is considered to be done after the recommendations from respectively the aerodynamics, control & stability, performance, structural, and weight analysis are executed. Class IV analysis covers the most intricate design of the aircraft and will consist of FEM, generating detailed CAD drawings, performing detailed component weight and MOI estimations, and finally creating a detailed operations manual. After Class IV is done, the aircraft prototype can be built and tested.

Subsequently, the production plan of the aircraft can be started. Initially, a breakdown of the aircraft components is made. Here the aircraft is split up into fifteen components which will be combined into sub-assemblies. Those sub-assemblies then will be input for the final production line.

The sub-assemblies are the fuselage, wings, tail, cockpit, landing gear, weapon system, and engines. The production line will be in their respective order. To ensure smooth production procedures all components are labelled and a warehouse is located at the beginning of the production line. Based on the locations at which each component will be made, the production line will be setup in Amsterdam for logistic reasons.

In order to see how well aircraft is designed, the project objective statement should be looked at. The aircraft can be seen to outperform the A-10 Thunderbolt II as the requirements on performance have been met with a minimum unit cost of \$15 million. This, however, means that the unit price of the aircraft will be around \$45 million which might be seen as a steep asking price. This can be countered with the low operating costs that are expected with this aircraft. The requirement for the loiter period was met through the use of highly efficient engines, the Rolls-Royce AE 2100A, which were combined with an endurance optimised wing. This combination also allowed the aircraft to exceed the range requirements. A variety of mission profiles have also been thought about, with an increase in payload up to 7000 kg available or an increase of loiter time up to over 10 hours through the use of an external fuel tank or in-flight refuelling. Another feature of the aircraft that is specifically for CAS missions and is an innovative solution to an overworked pilot is to have the turret-mounted gun able to be controlled either by the pilot or a ground-operator and have a wide field of view. Concluding on this, the aircraft being designed outperforms the A-10 in contemporary CAS situations and will successfully replace it.

# Contents

<b>Preface</b>	<b>i</b>
<b>Executive Overview</b>	<b>iii</b>
<b>1 Introduction</b>	<b>1</b>
<b>2 Initial Conceptual Design</b>	<b>2</b>
2.1 Conceptual Design	2
2.2 Trade-off Between The Four Concepts	2
2.3 Preliminary Design	4
<b>3 Mission Objectives &amp; System Requirements</b>	<b>5</b>
3.1 Mission Profile	5
3.2 Functional Breakdown Structure	6
3.3 Driving Requirements	7
<b>4 Overview of the Complete Design Process</b>	<b>8</b>
4.1 Set-up of the Iterative Design Phase	8
4.2 Mass Budgets & Contingencies	9
4.3 Progression Of The Main Mass Group Computations	10
4.4 Aircraft Design Summary	12
4.5 Verification & Validation Procedures	12
<b>5 Presentation of Final Design</b>	<b>14</b>
<b>6 Weapons Configuration</b>	<b>16</b>
6.1 Gun System	16
6.2 Hardpoint analysis	18
<b>7 Wing Position, Engine Position and Fuselage Layout</b>	<b>19</b>
7.1 Vertical Wing Position	19
7.2 Engine Position	19
7.3 Fuselage Layout	20
<b>8 Class I &amp; Class II Weight Estimations</b>	<b>21</b>
8.1 Class I Weight Estimation	21
8.2 Class II Weight Estimation	24
8.3 Center of Gravity Range	25
<b>9 Wing Design</b>	<b>26</b>
9.1 Airfoil Design	26
9.2 Wing Design	27
9.3 Drag Polar Estimations	31
9.4 Verification & Validation	32
<b>10 Aerodynamic Characteristics</b>	<b>33</b>
10.1 Lift Characteristics	33
10.2 Drag Breakdown	40
10.3 Moment characteristics	44
<b>11 Flight Performance</b>	<b>50</b>
11.1 Engine Selection & Turboprop Characteristics	50
11.2 Take-off & Landing Performance	51
11.3 Fuel Burn Estimation	52
11.4 Payload-Range & Mission Profile Analysis	53
11.5 Improved Aircraft Performance Computations	54
11.6 Aircraft Performance Diagram	56
11.7 Verification & Validation	56
<b>12 Empennage Design and Stability Analysis</b>	<b>58</b>
12.1 Adaptations of Conventional Tail Sizing Methods	58
12.2 Preliminary Horizontal Tail Sizing	58
12.3 Vertical Tail Sizing	59
12.4 Detailed Horizontal Tail Sizing and Longitudinal Wing Positioning	60
12.5 Empennage Planform Design	60
12.6 Conclusion of the Empennage Design	61
12.7 Static Stability Analysis	61

12.8	Dynamic Stability Analysis . . . . .	61
12.9	Recommendations . . . . .	64
<b>13</b>	<b>Structural Analysis</b>	<b>65</b>
13.1	Coordinate System . . . . .	65
13.2	Maximum Load Cases . . . . .	65
13.3	Wing Structural Design . . . . .	67
13.4	Tail Design. . . . .	84
13.5	Fuselage Design . . . . .	85
13.6	Materials. . . . .	86
13.7	Verification & Validation . . . . .	88
<b>14</b>	<b>Subsystem Design</b>	<b>90</b>
14.1	Landing Gear Design. . . . .	90
14.2	Fuel System Description . . . . .	92
14.3	Electrical System . . . . .	93
<b>15</b>	<b>Market &amp; Cost Analysis</b>	<b>99</b>
15.1	Preliminary Market Analysis . . . . .	99
15.2	Market Volume and Available Share . . . . .	100
15.3	Unit Price . . . . .	101
15.4	Unit Cost. . . . .	101
15.5	Operational Cost . . . . .	102
15.6	Return on Investment . . . . .	103
15.7	Cost Breakdown Structure . . . . .	103
<b>16</b>	<b>Sustainable Development Strategy</b>	<b>105</b>
<b>17</b>	<b>Reliability, Availability, Maintainability and Safety</b>	<b>107</b>
17.1	Reliability . . . . .	107
17.2	Availability. . . . .	107
17.3	Maintainability . . . . .	108
17.4	Safety. . . . .	109
17.5	Risk Assessment . . . . .	109
<b>18</b>	<b>Operations and Logistics</b>	<b>113</b>
18.1	JTAC . . . . .	113
18.2	Combat Mission . . . . .	113
18.3	Gun Operation . . . . .	113
<b>19</b>	<b>Post-DSE Development</b>	<b>115</b>
19.1	Further Technical Design . . . . .	115
19.2	Production Plan. . . . .	115
19.3	Operational life . . . . .	118
19.4	Post-DSE Gantt Chart . . . . .	119
<b>20</b>	<b>Recommendations</b>	<b>120</b>
<b>21</b>	<b>Conclusion</b>	<b>123</b>
	<b>Bibliography</b>	<b>124</b>
<b>A</b>	<b>Class II Weight Estimation</b>	<b>127</b>
A.1	Structural Weight . . . . .	127
A.2	Powerplant Weight . . . . .	127
A.3	Fixed Equipment Weight . . . . .	128
<b>B</b>	<b>Functional Breakdown Structure</b>	<b>130</b>
<b>C</b>	<b>Requirements &amp; Compliance Matrix</b>	<b>132</b>
C.1	Requirement indicator definitions . . . . .	132
C.2	Requirement List . . . . .	132

## List of Symbols

Symbol	Description	Unit
$\alpha$	Angle of attack	[rad]
$\alpha_{0L}$	Zero-lift angle of attack	[rad]
$\alpha_{C_{Lmax}}$	Angle of attack at maximum lift coefficient	[rad]
$\alpha_{stall}$	Stall angle of attack	[rad]
$\alpha_{trim}$	Trim angle of attack	[rad]
$\alpha^*$	Last angle of attack of the linear region	[deg]
$\beta$	Compressibility factor	[-]
$\delta$	Deflection angle	[deg]
$\eta$	Efficiency factor	[-]
$\epsilon$	Twist angle	[-]
$\lambda$	Taper ratio	[-]
$\lambda_c$	Eigenvalue of state space matrix	[-]
$\Lambda$	Wing sweep	[rad]
$\mu$	Friction coefficient	[-]
$\mu_b$	Relative density, asymmetric motion	[-]
$\mu_c$	Relative density, symmetric motion	[-]
$\omega$	Distributed load	[N/m]
$\sigma$	Normal stress	[MPa]
$\rho$	Density	[kg/m <sup>3</sup> ]
$\tau$	Shear stress	[MPa]
$a$	Acceleration	[m/s <sup>2</sup> ]
$AR$	Aspect ratio	[-]
$b$	Wing span	[m]
$C_{buckle}$	Buckling mode	[]
$C_d$	Airfoil drag coefficient	[-]
$C_{D_w}$	Wing drag coefficient	[-]
$C_D$	Aircraft drag coefficient	[-]
$C_{D_0}$	Zero-lift drag coefficient	[-]
$C_{D_{misc}}$	Miscellaneous drag coefficient	[-]
$C_f$	Flat plate friction coefficient	[-]
$C_{w_f}$	Skin friction coefficient of the wing	[-]
$c_p$	Specific fuel consumption	[N/w]
$C_l$	Airfoil lift coefficient	[-]
$C_{L_w}$	Wing lift coefficient	[-]
$C_L$	Aircraft lift coefficient	[-]
$C_L^*$	Last lift coefficient of the linear region	[-]
$C_{L\alpha}$	Lift curve slope	[rad <sup>-1</sup> ]
$C_{L_{design}}$	Design lift coefficient	[-]
$C_{L_{max}}$	Maximum lift coefficient	[-]
$C_{l_p}$	Stability derivative of roll damping due to rolling	[-]
$\frac{c_l}{c_d}$	Lift over drag ratio	[-]
$c_m$	Airfoil moment coefficient	[-]
$C_{m_w}$	Wing moment coefficient	[-]
$C_m$	Aircraft moment coefficient	[-]
$C_{m_0}$	Zero-lift moment coefficient	[-]
$C_p$	Pressure coefficient	[-]
$C_r$	Root chord	[m]
$C_t$	Tip chord	[m]
$\frac{c'}{c}$	Increment of chord length due to flaps	[-]
c.g.	Center of gravity	[-]
$D$	Drag	[N]

$D_{\text{prop}}$	Propeller diameter	[m]
$\frac{d\epsilon}{d\alpha}$	Downwash gradient	[rad <sup>-1</sup> ]
$E_{\text{kin}}$	Kinetic energy	[J]
$f$	Fineness ratio	[-]
$FF$	Form factor	[-]
$F_{\text{landing}}$	Force on airframe during landing	[N]
$g$	Gravitational acceleration	[m/s <sup>2</sup> ]
$h$	Altitude	[m]
$i_w$	Incidence angle of wing	[deg]
$i_h$	Incidence angle of tail	[deg]
$IF$	Interference factor	[-]
$I_{xx}$	Moment of Inertia	[m <sup>4</sup> ]
$K_\lambda$	Factor for downwash gradient that takes taper ratio into account	[-]
$K_\Lambda$	Factor for wing planform geometry	
$K_A$	Factor for downwash gradient that takes aspect ratio into account	[-]
$K_W$	Factor for downwash gradient that takes the vertical position of the horizontal tail	[-]
$K_W$	Factor for variable or swept wing	
$K_{wf}$	Interference factor of wing-fuselage combination	[-]
$k_{1,2,3}$	Factor for $C_{l_{\text{max}}}$ that takes flap geometry into account	[-]
$K_X^2$	Dimensionless radius of gyration squared along roll axis	[-]
$K_Y^2$	Dimensionless radius of gyration squared along pitch axis	[-]
$K_Z^2$	Dimensionless radius of gyration squared along yaw axis	[-]
$l$	Moment around roll axis	[Nm]
$l_h$	Tail arm	[m]
$l_{fs}$	Fuselage length	[m]
$M$	Moment	[Nm]
$M_{\text{condition}}$	Mach number for a condition	[-]
$M_{\text{mass}}$	Mass	[kg]
$M_\infty$	Freestream Mach number	[-]
$m$	Moment around pitch axis	[Nm]
$MAC, \bar{c}$	Mean Aerodynamic Chord	[m]
MTOW	Maximum Take-Off Weight	[kg]
$n$	Load factor	[-]
$n$	Yaw rate	[Rad/s]
$N$	Number	[-]
$OEW$	Operating Empty Weight	[kg]
$P$	Power	[W]
$p$	Roll angular velocity	[Rad/s]
$q$	Pitch angular velocity	[Rad/s]
$q_s$	Shear flow	N/m
$Re$	Reynold's number	[-]
$R_{wf}$	Wing-fuselage interference factor	[-]
$R_{LS}$	Lift surface correction factor	[-]
$r$	Yaw angular velocity	[Rad/s]
$s$	Displacement	[m]
$S$	Surface area	[m <sup>2</sup> ]
$S_H$	Surface area of horizontal part of tail	[m <sup>2</sup> ]
$S_S$	Surface area of the stabiliser of tail	[m <sup>2</sup> ]
$S_X$	Surface area of angles part of tail	[m <sup>2</sup> ]
$S_V$	Surface area of vertical part of tail	[m <sup>2</sup> ]
$S_{\text{ref}}$	Reference wing surface area	[m <sup>2</sup> ]
$S_r$	Rudder area	[m <sup>2</sup> ]
$S_{\text{wet}}$	Wetted area	[m <sup>2</sup> ]

$Swf$	Wetted flapped area	[m <sup>2</sup> ]
$t$	Thickness	[m]
$\frac{t}{c}$	Thickness-to-chord ratio	[-]
$T$	Thrust	[N]
$u$	Velocity deviation from equilibrium	[m/s]
$v$	Deflection	[m]
$V$	Shear force	[N]
$V_{\text{condition}}$	Velocity	[m/s]
$V_H$	Tail volume	[-]
$V_{\text{vertical,max}}$	Maximum vertical speed during landing	[m/s]
$W$	Work	[J]
$W$	Weight	[N]
$w_s$	Sink speed	[m/s]
$WF$	Fuel Weight	[kg]
$W_{L_{\text{max}}}$	Maximum landing weight	[kg]
$\frac{x}{c}$	Position on chord	[-]
$x_{ac}$	Longitudinal position of the aerodynamic center	[-]
$\bar{x}_{ac}$	Position of the aerodynamic center as fraction of the MAC	[-]
$x_{\text{LEMAC}}$	Longitudinal position of the leading edge of the MAC	[m]
$X$	Longitudinal force on aircraft	[N]
$Y$	Lateral force on aircraft	[N]
$Z$	Vertical force on aircraft	[N]
<b>Abbreviation</b>	<b>Description</b>	
APU	Auxiliary Power Unit	
CAS	Close-Air Support	
CBS	Cost Breakdown Structure	
DC	Direct Current	
DOT	Design Option Tree	
EOL	End-Of-Life	
FBS	Functional Breakdown Structure	
FFD	Functional Flow Diagram	
FBW	Fly By Wire	
FCC	Flight Control Computer	
ISR	Intelligence, Surveillance and Reconnaissance	
MEA	More Electric Aircraft	
MTBR	Mean Time Between Repairs	
RAMS	Reliability, Availability, Maintainability, Safety	
RoI	Return on Investment	
SFC	Specific Fuel Consumption	
SWOT	Strengths, Weaknesses, Opportunities and Threats	
UAV	Unmanned Aerial Vehicle	
UCAV	Unmanned Combat Aerial Vehicle	
USD	U.S. Dollars	

# 1

## Introduction

As the role of Close Air Support (CAS) aircraft continues to evolve, the USAF A-10 Thunderbolt II is starting to show its age and is in need of a replacement. Current world conflicts are often fought under asymmetric warfare conditions, leading to greater demand of dedicated CAS aircraft on the battlefield. CAS warfare involves engagement of enemy ground forces in close proximity to friendly forces. Because of this, CAS aircraft must be ready to engage enemy forces for large amounts of time, leading to high loiter time requirements. The current-generation CAS aircraft have great firepower, but lack loitering performance. This is where the need for a next-generation CAS combat aircraft originates, requiring loitering performance comparative to current Unmanned Aerial Vehicles (UAVs) and the ability to neutralise non-stationary ground targets while still taking the safety of the aircraft and pilot into account. This leads to the mission statement as used for this DSE:

*“Deliver a successful and innovative close air support combat aircraft design, which outperforms the A-10 in the current environment of asymmetric warfare.”*

This report is the final in the series of reports covering this DSE. The predecessors of this report are the project plan, the baseline report, and the midterm report. In these reports the first conceptual designs were setup and a final concept was chosen after an extensive trade-off. Furthermore, preliminary analyses were executed on this concept and were used as input for this report.

In this final report the final concept is investigated further. The report is divided into five general parts, of which there is no formal division in the report. The first part consists of a recap of the earlier design phases, the design method that is followed during the last phase of this project ([Chapter 4](#)) and decisions which had to be made before the start iteration phase, including the weapon system ([Chapter 6](#)). The final design is also presented in this part ([Chapter 5](#)). In the second part the technical design has started the wing position, engine position, and fuselage layout are presented in [Chapter 7](#). Furthermore an iteration is performed on the Class I and II weight estimations ([Chapter 8](#)), performance analysis and aerodynamics analysis. Thereafter the wing design is completed ([Chapter 9](#)). The results of the iteration are used for more detailed calculations and analyses which can be used in a future design phase, which is beyond the scope of this project. The aerodynamic characteristics ([Chapter 10](#)), performance characteristics ([Chapter 11](#)), stability & control characteristics ([Chapter 12](#)) and structural characteristics ([Chapter 13](#)) are designed into detail. Next to the technical design, the most important (sub-)systems are designed in detail as well, which was done in the third part. This involves the landing gear system ([Section 14.1](#)), fuel system ([Section 14.2](#)) and the electrical system ([Section 14.3](#)).

In the fourth part the non-technical analyses are discussed. In the market and cost analyses, the return on investment and unit cost per aircraft are estimated ([Chapter 15](#)). Thereafter, the approach with respect to sustainability can be found ([Chapter 16](#)). RAMS-characteristics and risks ([Chapter 17](#)) are examined to gain an overview of the qualities and deficiencies of the designed aircraft. Finally, the operations and logistic side of the spectrum is treated ([Chapter 18](#)) and the production plan for the aircraft is established ([Chapter 19](#)). The final part contains the formal chapters, which also includes the conclusions and recommendations ([Chapter 21](#)) and the compliance matrix ([Appendix C](#)).

# 2

## Initial Conceptual Design

In this chapter the initial conceptual design is discussed. In [section 2.1](#) the contents of the baseline report are recapped [3]. In [section 2.2](#) the executed tradeoff between the four final concepts is discussed. Lastly, in [section 2.3](#) the design results from the midterm report are summarized.

### 2.1. Conceptual Design

The project started with user requirements that were given in the project guide [2]. Following this a market analysis was performed in order to see what functionalities the aircraft should have in order to be competitive. Along with this market analysis a functional analysis was done to see what functions the aircraft should have which gave rise to additional requirements on the aircraft. Around fifteen concepts were generated according to design option trees which were made for the wing, empennage and engine type. Following a preliminary qualitative analysis on these concepts, four concepts were chosen to be taken forward to the trade-off which is detailed below. The main parameters of each of the four concepts are detailed in [Table 2.1](#).

Table 2.1: Main parameters of the four concepts taken forward into the trade-off.

Concept	Wing position	Aspect ratio	Empennage	Engine type	Engine configuration
1	Mid	10	Conventional	AE2100A	2 underslung wing mounted turboprops
2	High	6	H-tail	TF34-GE-100	2 fuselage mounted turbofans underneath the wing
3	Low	8	Canard and one vertical tail	TF34-GE-100	2 fuselage mounted turbofans near the rear
4	High	10	Twin tail	GE F118	1 turbojet embedded into the fuselage

### 2.2. Trade-off Between The Four Concepts

After arriving at the four concepts, a trade-off method was set up to select the concept that had the best characteristics to meet all requirements. Additionally, insights from the analyses, performed for the trade-off, were used to optimise the chosen concept. The trade-off method was created before the analyses were done to ensure that the trade-off was free of any bias towards one of the concepts.

The first step in setting up the trade-off was to select the trade-off criteria. Since having a lot of trade-off criteria averages out the final score and produces unclear results, a total of six criteria, with an additional one for the "sensitivity analysis", were selected. This selection was made based on the driving requirements, and on how well the analysis to be performed would be able produce distinguishing results between the concepts. After the selection of the criteria themselves, weights were assigned to the criteria based on how critical they were for achieving the mission goals. The resulting criteria and corresponding weights are given in [Table 2.2](#).

The earlier mentioned sensitivity analysis refers to the method that was implemented to identify and counteract the effect of any wrong judgement in the trade-off method, the selection of the criteria or the determination of the weights. It consisted of varying the trade-off criteria weights one by one, and including the "Turning Performance" criterion to the trade-off scoring.

With the criteria known, a scoring system was created in which all team members individually scored the concepts and all results were averaged. The scoring categories (with corresponding grades) were set up with two goals in mind: the final score had to be a good representation of the quality of a concept, and all criteria had to be scored on one scale. The first goal, combined with the design philosophy that a bad aircraft

Table 2.2: Trade-off parameters and respective weights.

Parameter	Used for	Weight
Loitering Performance	Trade-off	5
Structural Weight	Trade-off	4
Austere Airfield Capability	Trade-off	3
Rate of Climb	Trade-off	3
Hardpoint Availability	Trade-off	3
Damage Tolerance	Trade-off	2
Turning Performance	Sensitivity an.	2

characteristic costs more to correct than a good characteristic provides in benefit, resulted in a more negative grade for the lowest scoring categories. This can be seen in [Table 2.3](#) below.

Table 2.3: Qualitative scoring categories.

Category	Score
Great	2
Good	1
Moderate	0
Marginal	-1
Meagre	-2
Poor	-4

The second goal was important because two different types of analyses were performed for the trade-off criteria: the Austere Airfield Capability, Hardpoint Availability, Damage Tolerance and Turning Performance were analysed in a qualitative manner and the other three criteria were analysed quantitatively. For the qualitative analyses, all concepts were simply assigned to scoring categories. For the quantitatively analysed criteria, only the best and worst concept were assigned to scoring categories. The two "average" concepts were then scored by interpolating between the two extremes.

The reason that qualitative analysis methods were used, was the insufficient level of detail needed for actual calculations. The qualitative analyses consisted of identifying for each criteria what aircraft characteristics affected it and how. This was then applied to the concepts to provide insight in their performance. The characteristics that were used to determine the scores for the qualitative criteria are listed below.

- **Austere Airfield Capability:** distance between the engine air intake and the ground.
- **Hardpoint Availability:** usable space for internal & external hardpoints.
- **Damage Tolerance:** control and stability redundancy, engine vulnerability due to placement.
- **Turning Performance:** roll damping caused by aspect ratio.

For the quantitative analyses, Class I and partial Class II Weight Estimation methods from Roskam [4] [1] were used to determine the main weight characteristics. This also resulted in the data used for the Structural Weight criterion. A preliminary engine selection was performed for each concept and this was combined with the weight data to calculate the Loitering Performance and the Rate of Climb. The methods used for these calculations were taken from the TU Delft Flight Mechanics course [5]. The results are presented in [Table 2.4](#).

Table 2.4: Quantitative analysis results used in the trade-off.

Criteria	Concept 1	Concept 2	Concept 3	Concept 4
Loitering Performance [hrs]	10,0	5,0	6,3	2,5
Structural Weight [kg]	6705	5404	6673	7241
Rate of Climb [m/s]	38	31	39	46

Using the data from all the analyses, the final scoring was performed. Concept 1 was found to be the winner as can be seen in the trade-off matrix, [Table 2.5](#), below. The sensitivity analysis was also performed but none of the alterations to the scoring methods resulted in another winner: Concept 1 was the best in all cases.

A discussion on the gained insights and the resulting optimisation of concept 1 will be presented in the next section.

Table 2.5: Results of the trade-off for the concept, where concept 1 is the clear winner. Where red resembles poor, yellow meagre, and green good characteristics.

Criteria	Weight	Concept 1	Concept 2	Concept 3	Concept 4
Loiter performance	5	2.00	-2.00	-0.96	-4.00
Structural weight	4	0.64	1.40	0.60	-1.20
Austere airfield cap.	3	0.40	-1.50	1.30	-1.90
Rate of climb	3	0.58	-0.40	0.72	1.70
Hardpoint availability	3	-0.40	-0.10	1.00	-0.40
Damage tolerance	2	-0.30	0.40	-0.70	-0.40
Turning performance	0	-1.70	1.70	0.20	-1.60
<b>Final</b>	20	13.7	-9.6	5.2	-27.4

## 2.3. Preliminary Design

From the results present above, it was concluded that a substantial amount of design space was left in terms of maximum take-off weight. Compared to the user requirement, 5000 kg of total aircraft weight could still be added. Approximately half of this weight increase would consist of added operational empty weight, but the other half could be used to increase the aircraft capabilities. Four main options for the use of the design space were identified:

1. Keep the lower MTOW, thus minimising the unit and operational costs.
2. Add engine power to increase flight performance.
3. Add fuel to increase the range, and loiter performance.
4. Increase the payload capabilities, to increase combat effectiveness and versatility.

Based on the performance analysis from the concept trade-off, the current conceptual design will already possess great flight and loitering performance, as well as very good maximum ranges. Therefore, options 2 and 3 were eliminated.

The decision between options 1 and 4 was harder to make, primarily because no cost estimations were performed at this point. The importance of cost reductions could therefore only be estimated by comparing the design to other aircraft and from that comparison, the cost reductions were not found to be extremely critical. The results from the sensitivity analysis in [Equation 8.1](#) indicated that increasing the payload weight induced the biggest change in the MTOW. Despite this result, the decision was made to focus on maximising the payload capabilities. The deciding factor was that the requirement for the payload weight was initially set at 7500 kg, but was then lowered to 4000 kg based on a preliminary feasibility analysis. Now that design space is available to increase the payload weight again, it was decided that the goal would be to come as close to the initial user requirement as possible.

## Mission Objectives & System Requirements

In this chapter the main mission profile the aircraft will adhere to is described first. From this profile, a list of functions will be generated, which the aircraft must fulfil to successfully complete the mission profile. This list of functions will be represented in a functional breakdown structure. Then, from this breakdown structure, a list of requirements will originate from this breakdown structure. The requirements that drive the design the most are listed here while the full list of requirements can be found in [Appendix C](#).

### 3.1. Mission Profile

The main mission objective of the aircraft is to deliver close air support to friendly ground troops. It should be able to loiter for six hours, and thereafter fly to the battlefield to engage the enemy and finally return to base. This should all happen while the safety of the aircraft and pilot is respected. The mission profile is visualised in [Figure 3.1](#).

In the mission profile the following phases are distinguished, in chronological order:

1. Engine start and warm-up.
2. Taxi.
3. Take-off.
4. Climb to 30,000 ft. altitude.
5. Cruise for 500 km at 30,000 ft.
6. Descend to 10,000 ft. altitude.
7. Loiter at 10,000 ft. for six hours.
8. Perform combat phase for 20 minutes.
9. Climb to 30,000 ft. altitude.
10. Cruise to home base at 30,000 ft.
11. Descend to airfield altitude.
12. Land, taxi and engine shut-off.

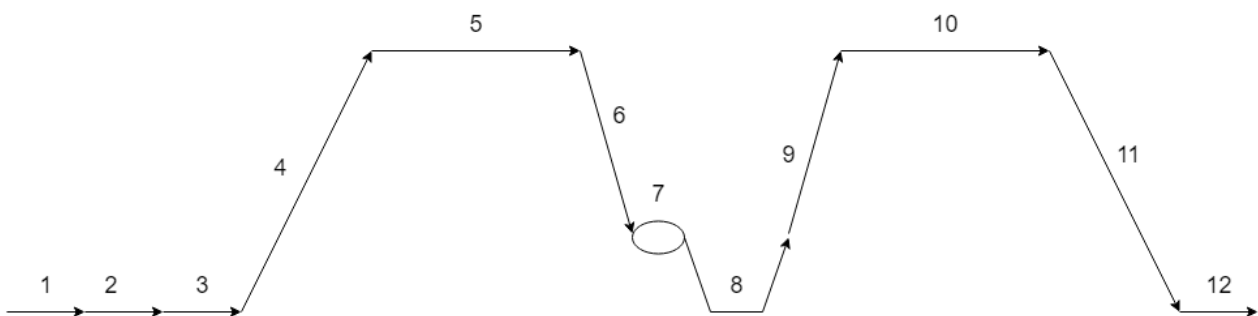


Figure 3.1: Mission profile of the aircraft portraying all the phases.

### 3.2. Functional Breakdown Structure

Based on the mission profile in [section 3.1](#), the Functional Breakdown Structure (FBS) is constructed. A FBS provides an overview of every function the aircraft should be able to perform in the form of an AND tree. The aircraft functions are divided into different top level functions: pre-flight operations, flight operations, post-flight operations, abnormal operations and the maintenance. By further dividing every function in more detail, a clear overview of all the required functions to successfully accomplish the mission of the aircraft is established. This helps to identify constraints that will lead to the requirements, and in the end, these requirements will lead to the final design. A shortened version of the FBS can be found in [Figure 3.2](#), while the full FBS can be found in [Appendix B](#).

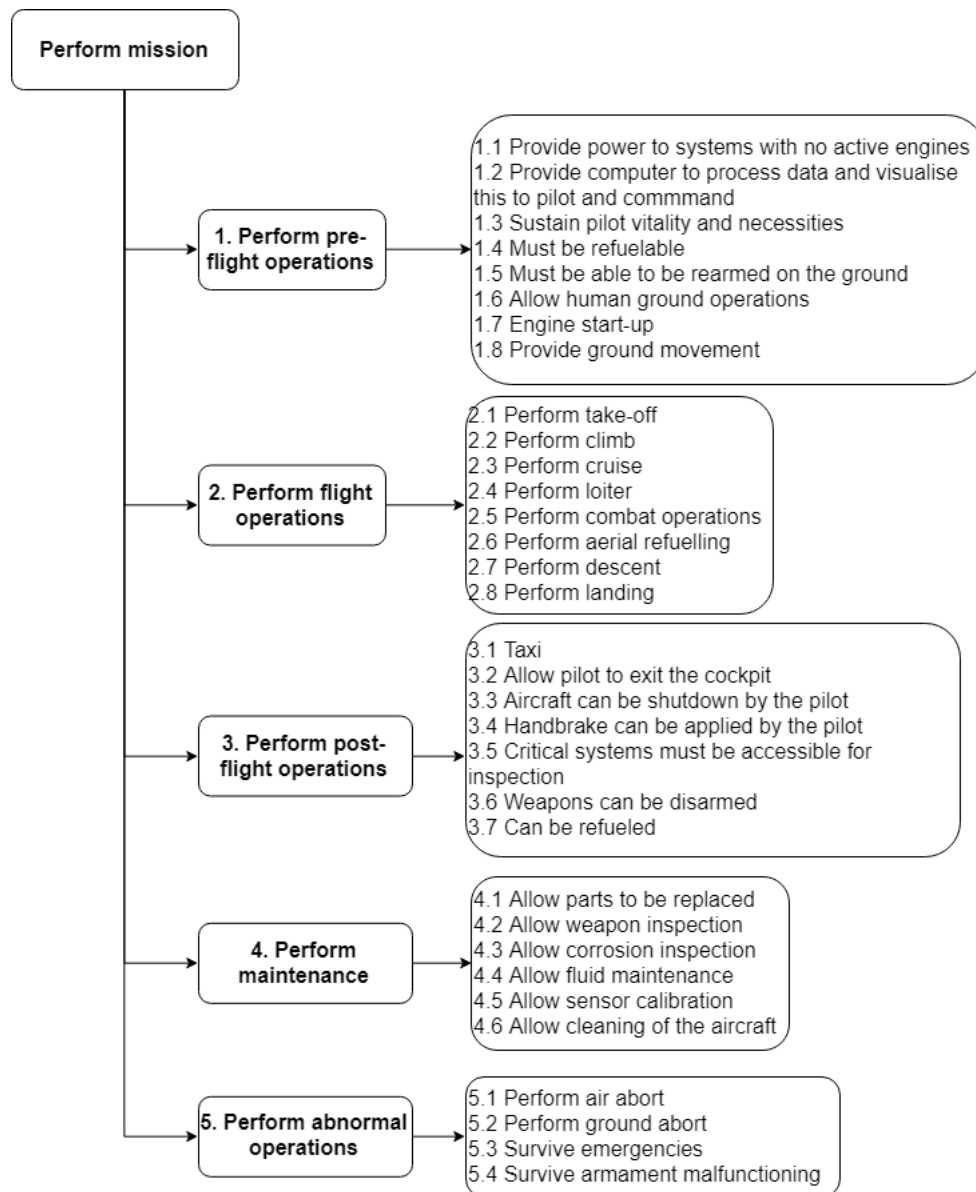


Figure 3.2: Functional Breakdown Structure of the aircraft.

### 3.3. Driving Requirements

Based on the mission profile and the FBS, a list of requirements was generated. The full list of requirements can be found in [Appendix C](#). From these requirements, the following were identified to be the driving requirements for the aircraft:

- The internal weapon system shall be able to disable ground targets at a range of at least 800 meters.
- The system shall have a nominal range of 2000 km.
- The system shall have a loitering capability of 6 hours at 10 000 ft in racetrack pattern at maximum endurance airspeed.
- The system shall have a ferry range of 4150 km.
- The system shall be able to take off at non-paved airfields.
- The system shall have a minimum landing distance of less than 6000 ft at MLW at 10 000 ft altitude.
- The MTOW shall be less than 23 000 kg.
- The Maximum Payload Weight of the system shall be at least 4000 kg including 1 crew member, armament and external fuel.

# 4

## Overview of the Complete Design Process

In this chapter the complete design approach is discussed. Starting off with the set-up that was used for the iteration and the mass budgets and contingencies that were taken into account. Following from that, the iteration results are discussed by first looking at the progression of the mass groups during the iteration and than by listing the most important results over both iteration phases. Finally the verification and validation approach is explained.

### 4.1. Set-up of the Iterative Design Phase

In order to design the aircraft such that it is capable of fulfilling all requirements, an iterative design method is required. The method for this process was set up in detail before the start of the iterations with the goal of structuring all necessary calculations. It is now presented to the reader to provide insight in the system engineering approach that was implemented, and to place the technical content in the report in a more global framework. The used iteration method is an extension of the method presented in the Systems Engineering and Aerospace Design course at the TU Delft [6].

In the global context, two main design phases have been distinguished. The goal of the first phase is to size all main aircraft elements such that the requirements can be met. The goal of the second phase is to design the aircraft to a subsystem level by using the sizing and characteristics obtained from the first phase. During phase 2, more elaborate analyses of the aircraft characteristics are also performed. The two design phases will be discussed in more detail in the next subsections. First, an overview of the complete design process is presented in Figure 4.1 in the form of the Design Structure Matrix. The Design Structure Matrix is an N2-chart: the performed computations are on the diagonal, the corresponding outputs are placed in the same row as the computation block, and the computation inputs are placed in the corresponding columns. From here on, one completion of all steps in a design phase will be referred to as a "cycle" and any sub-iterations will be called "loops".

		<-- Outputs -->					
		Phase I			Phase II		
	<b>1.) Class I Weight Estimation</b>	- MTOW - OEW <sub>1</sub> / OEW <sub>1</sub> * - MFW	- MTOW - MFW	- MTOW - MFW - PLW	- Change in MTOW - MFW - PLW	- MTOW - MFW - PLW	
	<b>2.) Conceptual Design</b>	- 2.1) Performance analysis - 2.2) Wing planform - 2.3) Longitudinal wing position * - 2.4) Tail planform ** - 2.5) Aerodynamic analysis *	- Initial 3-D aircraft definition - Ultimate loadfactor - Extreme flight conditions			- Extreme flight conditions - Structural requirements - Engine specifications	
	- OEW <sub>2</sub>		<b>3.) Class II weight estimation</b>	- Mass range of wing and fuselage group - Cg range of wing and fuselage group - OEW <sub>2</sub>	- OEW <sub>2</sub>	- OEW <sub>2</sub> - C.g. range - Preliminary mass budgets	
	- LID	- Tail size & position - Wing size & position - Landing gear position	- Tail size & position - Wing size & position - Landing gear position	<b>4.) Conceptual Design</b>	- 3-D aircraft definition - C.g. range - Aerodynamic characteristics - Performance characteristics	- 3-D aircraft definition - Landing gear position - Aerodynamic requirements - Performance requirements	
				<b>5.) System Feasibility Checks</b>			
						<b>Preliminary Design</b>	- Subsystem designs - Structural design
							- Subsystem characteristics
						<b>Weight Calculations</b>	- Actual subsystem weights - Actual structural weights - OEW - C.g. range
						- Subsystem mass budgets - Subsystem requirement updates	<b>Iteration Result Analysis</b>
							<b>Final Technical Design</b>
							<b>Post-Design Analyses</b>

Figure 4.1: Design Structure Matrix of the final design stage of the project. The diagonal represents the performed computations, where the in- and outputs are placed in the corresponding columns.

### Design Phase 1

As can be seen in [Figure 4.1](#), design phase 1 mainly concerns the iteration of Class I and II weight estimations. The weight estimation methods will be discussed in more technical detail in [chapter 8](#). As stated in [section 2.3](#), the design choice was made to maximise the payload weight and increase the MTOW with respect to the initial conceptual design. In order to maximise for the payload weight, this value will be continuously adjusted to converge the MTOW to the specification value.

Due to the MTOW change, the preliminary conceptual results are no longer valid and a large part of the initial aircraft sizing had to be re-done during the first iteration cycle. These initial computations are marked with an asterisk, and are replaced with their more accurate counterparts from block 4 after the first iteration. These will be performed with  $OEW_2$ , which is the operational empty weight as calculated by the Class II estimation in the previous cycle.

The normal iteration cycle starts with a loop between block 1 and the performance analysis from block 2. This performance analysis consists of analysing the fuel burn. When the outputs from this loop converged, the results were used to compute the rest of computation block 2 and perform the Class II weight estimations (block 3). With the outputs from the Class II weight estimations, more detailed analysis and sizing is performed, listed in block 4. Blocks 3 and 4 also form an iteration loop. This loop is required because the tail sizing is based on the c.g. estimation, but a change in tail size in turn affects the c.g. location. After this loop converges, the full cycle is completed by performing the System Feasibility Check. Aside from checking convergence, this block is incorporated as a sanity check to ensure that no bad characteristics, not calculated in phase 1, are overlooked. It therefore consisted mostly of preliminary qualitative analyses.

### Design Phase 2

After design phase 1 has been concluded, the sizing and characteristics are assumed to be accurate enough to start actual design of the aircraft. The technical content of this phase is described in part 2 and 3 of the report. One of the most important inputs for this design phase are the subsystem weight estimations, these are translated into weight budgets as described later in this chapter, in [section 4.2](#). Since the results from phase 1 are deemed accurate enough such that no large changes to the design are necessary, design phase 2 has much less of an iterative nature. In professional aircraft design, there are still a lot of iterations performed at this stage, but that is beyond the scope of this design. As can be seen in [Figure 4.1](#), the second phase follows the same general flow as the first phase: first the (more detailed) design is done, then the weight is estimated and finally, adjustments are made to correct for deviations from the previous estimates. When the results from all aircraft (sub-)systems are deemed satisfactory, the second design phase will be concluded.

### Supporting Matlab Architecture

When observing the goals and methods of the design phases, it was quickly concluded that the integration of all the separate computations into one complete system had to be structured very concisely. Roughly for each separate computation in phase 1 of the Design Structure Matrix, one Matlab program was written. All these programs had to be able to use the outputs from the most recent, preceding steps in their computations. As mentioned previously, the convergence of the iterations is also of great importance. To track this convergence, the history of the important design parameters had to be kept.

These two main requirements on the Matlab architecture were met by using a database system. To use the database, all programs had to be converted to contain exactly equal nomenclature for all parameters. Then a few lines of code were added to beginning and end of all programs. The first code activated a function that searches in the database folder for the most recent data file and loads it into the workspace. The loaded data is then used to run through the computations in the program and, when completed, the new data set is saved into a new file. This method enabled the tracking of all data, and was also very versatile in its application. Another advantage was that this method was very "secure", meaning that accidental deletion or unintended change of data was very unlikely and easy to correct.

## 4.2. Mass Budgets & Contingencies

As stated in [section 2.3](#), the MTOW will be increased. The MTOW value for which the aircraft will be designed is called the specification value. This specification value was obtained by taking the user requirement "CASCA-MASS-1) The MTOW shall be less than 23 000 kg", and applying a contingency factor to that value. The applied contingency factor was chosen such that a maximum increase of 5% with respect to the specification value is accounted for. This value is based on the average post-design weight increase, obtained from [7]. This results in a MTOW specification value of 21 905 kg.

For the current and future design phases, additional contingencies will be applied to account for the typical weight growth during the increasingly detailed design process. The initial mass budgets are generated by taking an additional 5% contingency on the Class II weight estimations. After the completion of the first design phase 2 cycle, the mass budgets will be re-distributed but are also allowed to increase such that in total, 4% contingency on the specification value for the MTOW remains. During the rest of the second design phase, this value can converge to 3%. The remaining contingency is planned to be used during the detailed design and flight test phases. These values were obtained from Dr.ir. W.J.C. Verhagen (personal communication, 4-6-2018). The resulting mass budgets are presented in [Table 4.1](#).

### 4.3. Progression Of The Main Mass Group Computations

During the first iteration phase, the progression of a large number of aircraft parameters was saved and monitored. The most important and intensively tracked parameters were the aircraft's main mass groups. These consisted of the maximum take-off weight, operational empty weight, maximum fuel weight and maximum payload weight. The progression of these mass groups over the course of the iterations can be seen in [Figure 4.2](#).

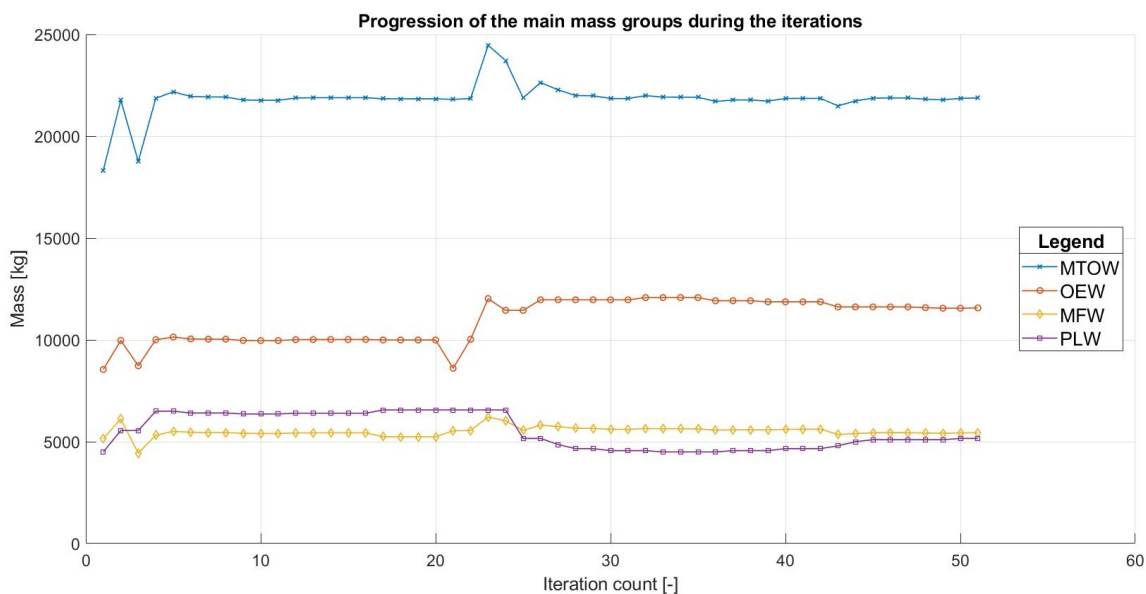


Figure 4.2: Progression of main aircraft masses during design phase 1.

When observing the progression of the mass groups, two large fluctuations stand out. Namely the fluctuation at the beginning, and the fluctuation around iteration number 23. The first fluctuation is caused by the change in the specification value for the MTOW. The characteristics of the initial conceptual design were still used for the first Class I estimation before adjusting the payload to increase the MTOW to the new specification value. This was done for completeness. Therefore large adjustments to the payload weight were made during the first iterations and the MTOW attained its specification value within those first few iterations. The second large fluctuation is caused by the an error in the Class II weight estimation program. This error was caused due to the integration process of all programs. By tracking the data, it was spotted and immediately corrected. The fluctuations in the graph visible because multiple "troubleshooting" computations were performed, and the data from these computations got saved to the database. Up to and including the moment the troubleshooting was completed, the iterations were all performed with the data file from just before the introduction of the errors, ensuring no wrong data was used in the determination of the final values.

Aside from the large fluctuations, a small but noticeable change can be seen around iteration 43. This was due to the implementation of an updated and more advanced tail planform computation. After this small fluctuation, the masses converge again and assumed their final phase 1 values. An overview of the converged Class II mass estimations can be found in [Table 4.1](#).

Table 4.1: Class II mass estimation results and design budgets.

Mass group	Part of mass group	Class II Results [kg]	Initial design budget [kg]
Maximum ramp weight	-	22324	21747
Maximum take-off weight	-	21880	21302
Operational empty weight	-	12130	11553
Aircraft structure	Operational empty weight	5118	4875
Engine & fuel system	Operational empty weight	3492	3326
Fixed equipment	Operational empty weight	3520	3353
Flight control system	Fixed equipment	2062	1964
Pilot amenities	Fixed equipment	242	230
Armament	Fixed equipment	960	914
Auxiliary gear & systems	Fixed equipment	191	182
Engine system	Fixed equipment	3112	2964
Fuel System	Fixed equipment	379	361
Max payload weight	Maximum take-off weight	4873	4873
Mission fuel weight	Maximum take-off weight	4993	4993
Crew weight	Maximum take-off weight	91	91
Trapped fuel & oil	Maximum take-off weight	66	66
Maximum fuel weight	Maximum take-off weight	5438	5438
<b>Mass subgroups</b>			
Paint	Fixed equipment	66	62
Fuel dumping system	Fuel system	13	12
Fuel system	Fuel system	347	331
In-flight re-fueling system	Fuel system	19	18
Gun control system, armour & countermeasures	Armament	399	380
Gun turret	Armament	288	274
Auxiliary power unit	Auxiliary gear & systems	136	129
Auxiliary flight gear	Auxiliary gear & systems	55	52
Air-conditioning, pressurisation & de-icing	Pilot amenities	162	154
Furnishings	Pilot amenities	73	69
Oxygen system	Pilot amenities	8	7
Both gearboxes	Engine system	421	401
Both air induction systems	Engine system	84	80
Engine control system	Engine system	39	37
Both engines (dry )	Engine system	1432	1364
Engine starting system	Engine system	29	28
Both engine nacelles	Engine system	254	242
Propeller control systems	Engine system	73	69
Both propellers	Engine system	781	743
Electrical systems	Flight control system	322	307
Flight control systems	Flight control system	595	566
Hydraulics/pneumatic system	Flight control system	216	206
Instrumentation, avionics & electronics	Flight control system	890	848
C.g. control system	Flight control system	38	36
Empennage structure	Structural	727	692
Fuselage structure	Structural	1672	1592
Landing gear	Structural	732	697
Main wing	Structural	1988	1893

## 4.4. Aircraft Design Summary

In Table 4.2 the most important iteration results of the iteration of both phase I and phase II are presented. These are only a small part of the total list of iteration results, but these were considered to be useful for a quick overview of the iteration outcome. These iteration results were subsequently taken forward into the next design phase.

Table 4.2: Iteration results.

Property	Unit	Result of iteration
AR	-	8
b	m	20.56
$C_{L\alpha}$	rad <sup>-1</sup>	5.30
$C_{L_{max, clean}}$	-	1.62
$C_{L_{max, land}}$	-	2.00
$C_{L_{max, to}}$	-	1.80
$C_r$	m	3.67
$C_t$	m	1.47
$l_{fs}$	m	13.5
$h_{cruise}$	m	9144
$h_{loiter}$	m	3048
MAC	m	2.73
$M_{fuel}$	kg	5237
$M_{mto}$	kg	21886
$M_{oe}$	kg	11569
$M_{pl}$	kg	4873
$M_{cruise}$	-	0.557
S	m <sup>2</sup>	52.86
$V_{cruise}$	m/s	158.0
$V_{loiter}$	m/s	81.59
taper	-	0.4

## 4.5. Verification & Validation Procedures

During the preliminary and detailed design phase, physical and mathematical models representing real-world conditions will be used extensively in determining the final design of the concept. Thus, it is required that these models — and their implementations in code — will be verified and validated. Otherwise, it could result in the design being based on inaccurate representations of real-world conditions which could have disastrous consequences for the effectiveness of the design. This chapter first details the procedures put in place to ensure any code written is properly verified. Secondly, it lists the procedures installed to ensure verification of the underlying physical and mathematical models used. Finally, the validation procedures are disclosed.

### Code Verification

During the verification stage, the software is tested to see whether it behaves as expected. This section covers that by first going over the procedure for detailing the code specifications, which will be used to check that the functionality of the code is as intended. Finally, the procedures for unit tests are described.

### Code Specifications

In order to ensure the code is properly functioning as intended, there needs to be a benchmark that accurately describes the intended function of said code. Especially since this is also required for independent code verification to be performed [8]. Thus, it has been determined that code specifications will be required for all software that is created by the team, as the code will, for a large part, consist of implementations of well-established formulas within the discipline of aerospace engineering. Therefore, the code specifications in this case can consist of a description of the use of established formulas since that is clarifying enough for independent code review to be performed.

### Unit Test Procedures

The two main unit tests used throughout development were continuity and consistency tests. In a continuity test, any model input is changed (usually to zero), after which the output is checked for change. This ensures

that the output of the software is dependent on the input, and enables discovery of redundant software variables/aspects. In a consistency test, a single input variable is changed, after which the output is checked for change. The change of the output should be within the expected order of magnitude (with respect to the change of the input variable), which verifies that the software written is behaving as expected. A final unit test involved comparing software outputs for a given set of inputs to hand calculations. These have been applied for all software developed for the detailed design.

### Validation

Given that the code has been verified to function as intended, it still needs to be validated that the intended function is an accurate representation of real life conditions. In light of the relatively early stages of the design currently taking place, as well as the limited amount of resources available, performing wind tunnel or flight tests is unfeasible. Therefore, when available, the code output will be compared to real flight data obtained from manufacturers or government agencies to ensure that the results obtained with it are within a good confidence interval. Any discrepancies from the expected/listed manufacturer data will be detailed per section in the report.

# 5

## Presentation of Final Design

The final product of Group 24's Design Synthesis Exercise is presented in [Figure 5.1](#). The aircraft uses two high-performance Rolls Royce AE 2100A turboprop engines, a fully rotatable 20mm turret-mounted gun located under the fuselage and 9 hardpoints located below the wing and fuselage. The engine is mounted on top of the low-wing configuration, and an unconventional split-X tail is present. The rotatable turret is the first of its specific kind on an attack aircraft, and it is stored within a 'canoe' fairing when not in use due to drag considerations. Because of the aerodynamic design, the aircraft is able to loiter for 6 hours after reaching a combat zone up to 500 km away from base, after which it can do a combat run and return to base. The hardpoints are compatible with numerous air-to-surface and air-to-air missile capabilities, as well as various unpropelled bombs. This makes the aircraft a versatile option that can adapt to numerous mission profiles.

Main characteristics of the aircraft can be found in [Table 5.1](#), a render of the aircraft is shown in [Figure 5.1](#) and technical drawings of the aircraft can be seen in [Figure 5.2](#).

Table 5.1: Aircraft main characteristics.

Description	Value	Reference
Maximum take-off weight	21 880 kg	<a href="#">section 8.1</a>
Maximum landing weight	18 592 kg	<a href="#">section 4.3</a>
Maximum fuel weight	6747 kg	<a href="#">section 11.3</a>
Nominal payload weight	4873 kg	<a href="#">section 4.3</a>
Wing surface area	52.9 m <sup>2</sup>	<a href="#">section 9.2</a>
Wing aspect ratio	8	<a href="#">section 9.2</a>
Wing span	20.6 m	<a href="#">section 13.3</a>
Nominal range	5244 km	<a href="#">section 11.4</a>
Ferry Range	6798 km	<a href="#">section 11.4</a>
Minimum take-off distance	600 m	<a href="#">section 11.2</a>
Minimum landing distance	326 m	<a href="#">section 11.2</a>



Figure 5.1: A render of the final design of the aircraft.

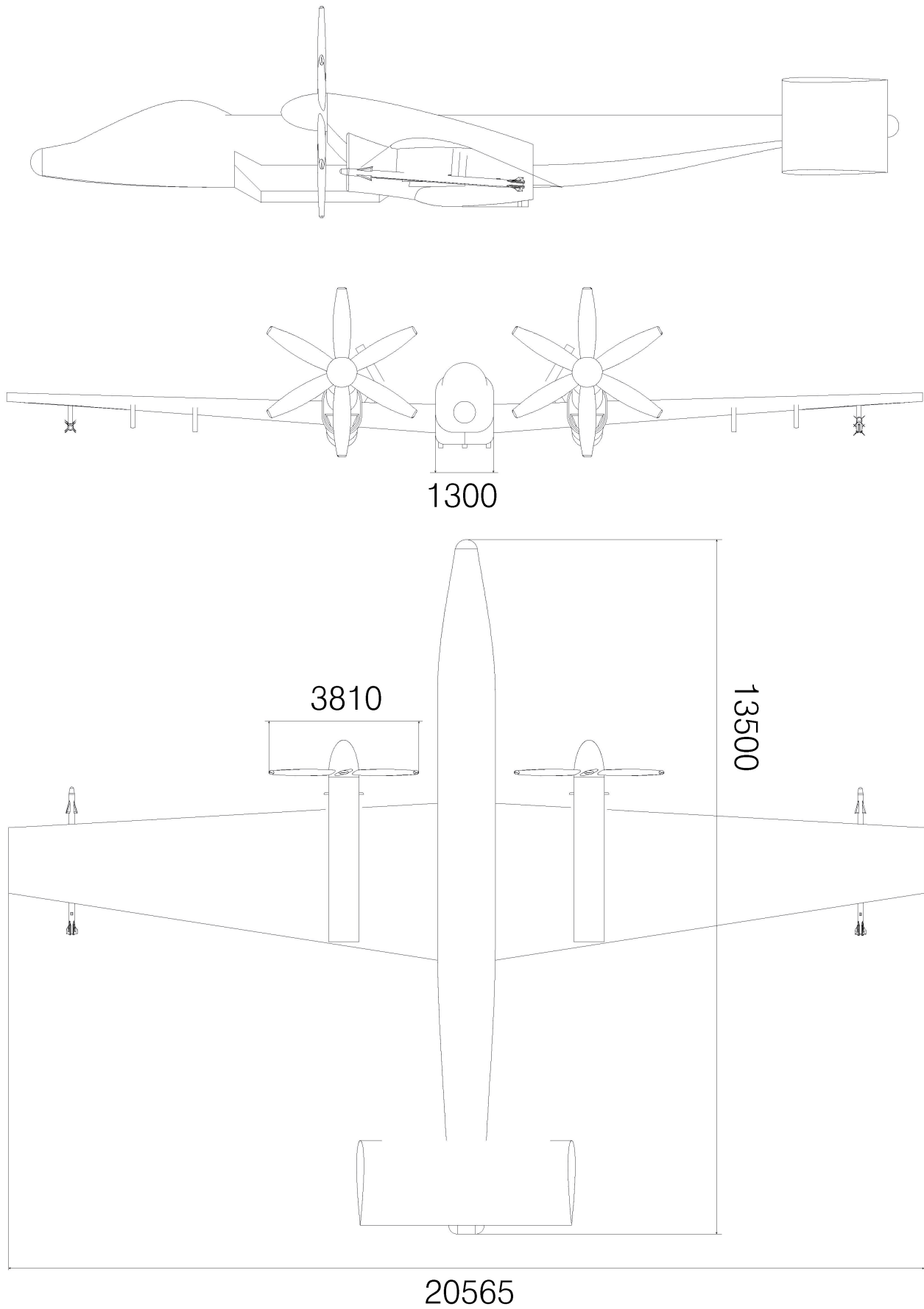


Figure 5.2: Side, front and top view of the final design. All dimensions are in mm.

# 6

## Weapons Configuration

In this chapter the weapon configuration of the aircraft is discussed. It was opted to use a mounted gun in the design, which will be further explained in [section 6.1](#). Furthermore the amount of hardpoints was determined and possible hardware-attached ordnance is evaluated in [section 6.2](#).

### 6.1. Gun System

In recent history the use of autocannons, such as the A-10's GAU-8 Avenger, has shown its effectiveness on the battlefield. After the functional analysis was performed, it became clear that an internal autocannon should be implemented into the design of the next generation CAS aircraft as well. This section will present the internal weapons system design, as well as its effects on the rest of the aircraft.

Since the user requirements determine that the autocannon capability does not need to be as significant and design-driving as the A-10 GAU-8 Avenger, a forward-facing, fixed gun was not the only option. Inspired by the Boeing AH-64 Apache's M230 Chain gun setup, and the Lockheed AC-130's sideward facing weaponry, more options were considered. The team opted for a hinged gun system, which makes use of a turret and a targeting system, to have increased attacking capabilities during a combat phase. This system will allow for the gun to aim at targets not only when flying straight at them, like a fixed-gun would, but also when flying over targets in a different manner. Considering the substantial amount of parasitic drag that such a gun system would create, as well as the ground clearance required, if it was attached outside of the aircraft, the weapon system will be incorporated into the fuselage. An aerodynamically efficient shaped fairing will be designed under the fuselage to cover the weapon system during non-combat mission phases. Then, during a combat phase, the fairing will fold open and the gun will be ready to engage.

After the gun system was selected, a gun type also had to be chosen. The autocannon market yields many viable options. However, a relatively new gatling gun, developed by General Dynamics, stood out. This weapon is the XM301 20mm Lightweight triple barrel rotary cannon. It was originally developed for the RAH-66 Comanche Stealth helicopter from 1992 onwards. However, the project was discontinued and the XM301 is not in active service. While the Comanche was never completed, the XM301 is still ready for use. The modern technology implemented into the weapon system ensures it performs better than its competitors in fields such as weight, recoil and accuracy. The specific characteristics of the XM301 can be found in [Table 6.1](#). The weight presented excludes feeding system and ammunitions mass.

Table 6.1: XM301 specifications [9].

Parameter	Unit	XM301
Mass	kg	36.5
Length	m	1.826
Width	m	0.250
Height	m	0.250
Muzzle velocity	m/s	1030
Firing rate	RPM	1500
Caliber	mm	20
Cartridge mass	g	272.5
Projectile mass	g	100.0
Recoil force	N	3500
Dispersion	mrad	2.2

The maximum effective range of the gun is classified, but the ammunition used has a maximum effective range of 2000 m. Moving target engagement lowers this range to a more conservative range of approxi-

mately 1500 m. Also, tracer burnout occurs at approximately 1500 m, which limits the practicality of tracers to this range if used<sup>1</sup>.

Subsequently, the weight and volume of the entire gun system was estimated. This includes the gun itself, the feeder system, ammunition storage and turret. For the feeder system and ammunition storage, the values of the 20 mm gatling gun system of the F-22A were used [10]. These were the only values of a similar gun system that were not classified and could be used as reference value for this report. Although the two guns have some differences, they are similar enough to be deemed comparable. The ammunition storage houses 1000 rounds. If this turns out to be an insufficient amount and more design space is available, the storage will be expanded.

For the turret, the THL-20 turret made by Nexter was selected<sup>2</sup>. This turret was originally designed for the RAH-66. The volume of this turret is not exactly known but it is expected that the turret will fit into the gun system properly. In the set-up of the RAH-66, the turret has a total of 60° of freedom in elevation and 120° in azimuth to fire the weapon<sup>3</sup>. The ability to hover eliminates the need for greater freedom in both directions for a helicopter. However, the turret is designed in such a manner that a full 360° coverage in azimuth can be achieved, as well as an elevation angle of 90° to allow for full freedom in the downward facing hemisphere. Since it is unclear what the exact effect of this coverage change is on the weight and size of the feeder system and feeder tube length, a contingency factor of 10% is taken into account for the mass and volume of the feeder system, based on technical drawing analysis. This yields the values of the mass, dimensions and volume of the different parts of the gun system that can be seen in Table 6.2. Also a sketch of the full gun system can be seen in Figure 6.1.

Table 6.2: Gun system specifications.

Parameter	Unit	XM301	Feeder System	Ammo Storage	Turret	Total
Mass	kg	36.5	88.0	272.5	164.0	561.0
Volume	m <sup>3</sup>	0.119	0.143	0.278	-	0.540

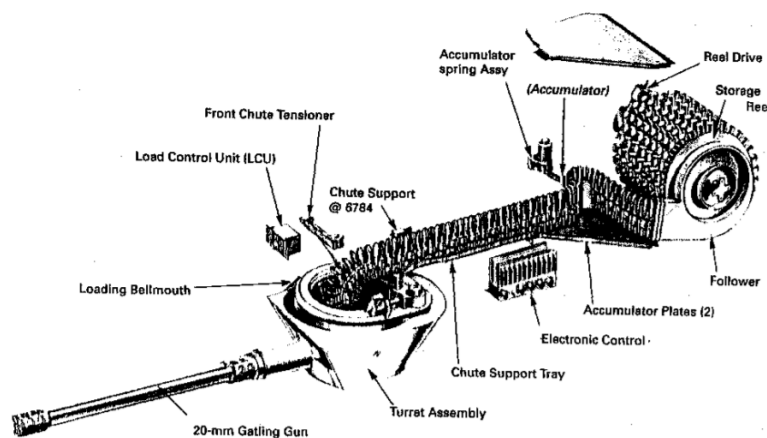


Figure 6.1: Full XM301 weapon system [11].

The gun will be attached underneath the fuselage inside a fairing. The fairing will open along the axis of symmetry of the aircraft, towards the sides of the fuselage, having equal freedom of movement in both directions. The fairing must ensure favourable aerodynamic properties, as well as being able to be retracted as far as possible for optimal gun movement freedom. The fairing used for the Comanche is not used since this design had low velocity and stealth properties as primary design objectives. The CAS aircraft is not designed for these characteristics and thus the fairing will be redesigned.

The origin of rotation will have to be below the fuselage for optimum freedom of movement. The rest of the turret will remain within the fuselage. The fairing which houses the full turret has the typical aerodynamic

<sup>1</sup>20-Millimeter, <http://www.aircav.com/cobra/ammo20.html> [Accessed: 07-06-2018]

<sup>2</sup>Nexter THL-20 Product <http://preprod.nexter-group.fr/en/products/item/351-th120> [Accessed: 08-06-2018]

<sup>3</sup>XM301 20mm cannon, <https://fas.org/man/dod-101/sys/ac/equip/m301.htm> [Accessed: 08-06-2018]

'canoe' shape to minimise drag. The canoe opens up along its plane of symmetry using hinges. The halves fold to the fuselage, effectively opening up the turret for nearly hemispherical motion. Both the pilot and a ground operator will be able to operate the gun, with the pilot mainly using it when it is pointed forward. In the unlikely case a ground operator is unavailable, the pilot can make full use of the rotating gun by allowing the aircraft's autopilot to take over. The turret and canoe design can be found in [Figure 6.2](#). In order to operate the turret, a camera will be placed behind it to allow for 360° views of the environment. The gun however, will not be free to point anywhere along the hemisphere. It is essential that there is clearance between payload and bullet trajectory. The longitudinal freedom must be limited to account for the fuselage mounted ordnance, while the lateral freedom must be limited to account for wing mounted ordnance. Therefore, the weapon will be preliminarily limited to operate in the following region. Longitudinally, the aircraft can fire from 0° in elevation to -135°. Laterally, the gun will be able to move between approximately -20° to -160°. This is a preliminary estimation, more detailed analysis has to be performed, taking into account wing deflection and possible ordnance size, to establish a clearance requirements. The three-dimensional freedom of movement can be established by fulfilling these requirements.

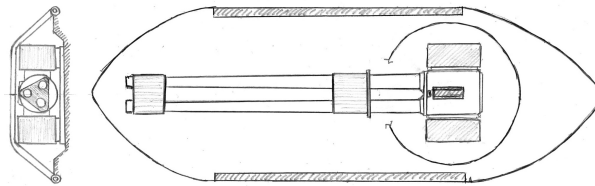


Figure 6.2: Full turret within fairing with front view (left) and bottom view cutout (right).

## 6.2. Hardpoint analysis

Next to the rotary cannon, external weapons will be mounted to the aircraft. These will be mounted to hardpoints, universal attachments which ensures ordnance is held on and released when it has to be. Hardpoints also allow ordnance loads to be properly introduced into the structure. The amount and positioning of the hardpoints will be analysed by examining the desired ordnance and aircraft geometry.

The payload weight will be 4873 kg for a nominal mission profile. The payload weight includes hardpoint mounted weapons or containers and ammunition for the internal weapon. Since the 20 mm cartridges weigh 272.5 g, the ammunition weight is 272.5 kg. The rest of the payload will be attached to hardpoints. Current hardpoint mounted systems in CAS are listed in [Table 6.3](#). Note that the fuel tank weight includes the weight of the dry tank.

Table 6.3: Typical CAS ordnance in use by USAF.

Name	Type	Weight [kg]
AGM-65 Maverick	Air-to-surface guided missile	211-306
Hydra 70	Air-to-surface unguided rocket	3.9 - 7.7
AGM-114 Hellfire	Air-to-surface guided missile	45 - 50
GBU-39 SMB	Precision-guided glide bomb	110
GBU-53/B SMB	Precision-guided glide bomb	113
AIM-9 Sidewinder	Air-to-air guided missile	85.3
Mark 81-84 bomb	Unguided general purpose bomb	113-907
GBU-24 Paveway III	Laser-guided bomb	1050
Mark 77	Unguided incendiary bomb	230
Lockheed Sniper	Targeting pod	202
AN/ALQ-131	Jammer pod	299
Drop tank 600 gal	Jettisonable fuel tank	2057

Payload and space analysis determined nine hardpoints to sufficiently incorporate the necessary armaments. Ground attack capabilities include expensive, guided ammunition and cheap, unguided ordnance. Due to stability, space and propeller clearance concerns, three hardpoints are located on the fuselage, while three hardpoints are located on each wing.

# 7

## Wing Position, Engine Position and Fuselage Layout

In this chapter the position of the engines and the vertical position of the wings will be discussed and fixed. Also the fuselage layout will be designed. The wing and engine position should be fixed before the iteration starts. During the iteration the landing gear height is checked whether it is feasible, as it depends on the vertical wing position. The longitudinal position of the wing will be iterated, since it is an important parameter for the sizing of the tail and will be done in [chapter 12](#). Finally, the fuselage layout is done before doing the iteration, and in the end checked whether the determined c.g. range from the iteration is still as expected with the layout with the assumed longitudinal position of the wing.

### 7.1. Vertical Wing Position

In a preliminary analysis of the wing, it was decided that a high wing configuration was not an option due to maintainability and hardpoint accessibility. The engine cannot be placed below the wing due to the large propeller diameter of 3.81 m, eliminating the advantage of a quick engine change-out when the whole nacelle can simply be lowered off the wing. To increase the accessibility and decrease the landing gear height a low wing configuration with the engines on top of the wing is chosen. Dihedral must be added to account for the lack of roll stability and will be determined in the wing design.

### 7.2. Engine Position

With the low wing configuration, the ground clearance of the wing should be considered. According to the regulations of the U.S. Government [12], a 0.18 m clearance should be present when the landing gear is statically deflected. Furthermore, the blades are not allowed to hit the ground when having a flat tire and the strut completely bottomed. With a nose landing gear length of 1.5 m and the propeller axis 1 m above the wing, a ground clearance of 0.945 m is obtained, which is clearly enough.

The lateral position of the engine will be as close as possible to the fuselage. There is a rule of thumb to estimate the lateral position by accounting for the noise produced by the engine. Based on the power available this can be determined. However, as it is a military aircraft, this rule is not valid. The fuselage clearance used is 0.2 m, which reduces the asymmetric thrust when one engine is inoperative.

A drawing of the front view of the aircraft is given in [Figure 7.1](#), to visualise the position of the wing and engine and its clearances.

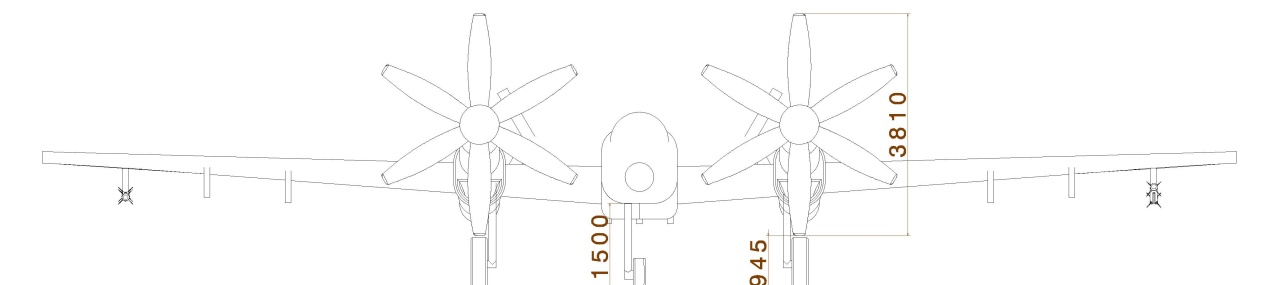


Figure 7.1: Drawing of the front view. The dimensions are in mm.

### 7.3. Fuselage Layout

The internal fuselage layout has a large effect on the total performance of the aircraft. Therefore, this section discusses how the internal layout of the fuselage was designed, which was based on two considerations.

First of all, due to drag considerations, it is preferable to use all space in the fuselage as efficiently as possible. In theory, every piece of unused space is an unnecessary increase in fuselage length, and therefore drag. However, one should also take into account a certain tail arm that should be met to avoid needing very large tail surfaces. So, in the ideal situation, the fuselage is completely filled with systems, and the systems are placed in such a way that the position of the cg results in a proper deal arm.

Secondly, to keep the size of the tail within bounds, the cg range should be small. Practically, this means that all components that change significantly in weight during flight should be as close to the average cg possible. These components are for example the fuel tanks and the ammunition container.

To elaborate on this, in reality it is very difficult to get a cg range close to zero. However, the shift in cg during flight can be used as an advantage. The loads on the tail change with velocity and flap settings. From preliminary analysis it is shown that during landing, a very negative (downward) tail force is required. This necessary tail force can be reduced by placing the cg more backward. This would thus reduce the necessary tail area. So, the cg should be positioned more backward towards the end of the flight. This can be achieved by placing the systems that change in weight, such as the fuel tanks and the ammunition container in front of the average cg.

To summarise, preferably, the fuselage should be filled as much as possible without disrespecting the necessary tail arm. Furthermore, systems that change in weight should be positioned slightly in front of the average cg, while avoiding an excessive cg range. Now, with the described design considerations, the fuselage layout can be designed. Running from front to back, first a nose cone with a length of 1.5 m was assumed. The nose cone is used to store the nose gear wheel, and could potentially be used to store noncritical systems. Due to visibility requirements, the cockpit, which has an estimated length of 2.5 m, is placed directly behind the nose cone. Under the cockpit the nose gear hinge is positioned. The only systems that have some significant weight that are left are the fuel tanks, the gun system, the APU and the tail planes. Both the gun system and the fuel tanks should be placed roughly in the middle to keep them close to the cg, which leaves APU and tail planes to counter the weight of the cockpit and nose gear. This layout is presented in [Figure 7.2](#).

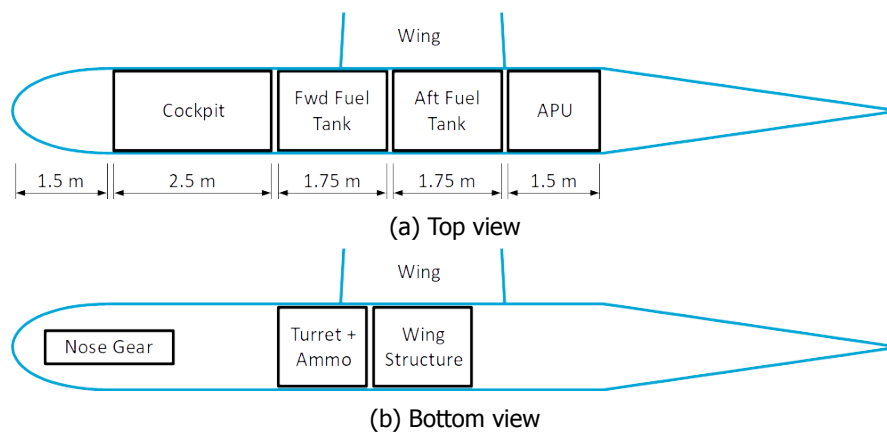


Figure 7.2: Schematic top view and bottom view of the preliminary fuselage layout.

As can be seen, the fuselage tanks combined have a length of 3.5 m. They are positioned slightly in front of the cg, so that if they empty throughout the flight, the cg shifts rearwards. The gun is also attached halfway along the fuselage. This allows for the recoil force of the gun to lie as close as possible to the cg. There is quite some fuselage space unused near the tail section. To get rid of this 'extra' fuselage length, the only option would be to literally get rid of it by shortening the tail section. To keep the same tail arm, one would have to shift the cg forward with respect to the fuselage. This however seems not possible by shifting around the different systems in the fuselage. The only valid option would be moving the engines more forward with respect to the wing. When looking at reference aircraft such as the Beechcraft King Air, one can see that this might indeed be a common solution to get rid of excess space in the tail section. In this case however, this would not be possible since the engines need to be above the wing for enemy ground fire protection. Therefore, the unused space in the tail section is accepted.

## Class I & Class II Weight Estimations

This chapter deals with the Class I and II weight estimations which were used in Phase I of the iteration process. First the Class I is detailed, finding the fuel fractions, range and endurance of the aircraft. Class II deals with the estimation of the operating empty weight made with different components from Airplane Design Part V. [1] Finally the position of the centre of gravity is estimated using the weights obtained from the Class II weight estimation.

### 8.1. Class I Weight Estimation

When any quantitative analysis is performed for an aircraft, at least the basic weight values (OEW, MTOW and fuel weight) are required. Therefore a Class I weight estimation is necessary before any other analysis can be performed. The main inputs for the Class I estimation are the correlation between the OEW and the MTOW of reference aircraft, the specific fuel consumption and the mission profile. These three inputs are discussed in respective order in the first three subsections, with the result being in the fourth and final subsection.

#### Reference Aircraft Relation

To begin with, the reference aircraft and their OEWs and MTOWs are displayed in Table 8.1<sup>1</sup>. Plotting these MTOW's against their corresponding OEW's and using a linear regression, the relation between the OEW and the MTOW is found to be:  $OEW = 0.4125 \cdot MTOW + 988$ . The  $R^2$  for this relation is equal to 0.97. This relation will be used as a basis for the determination of the concept weights.

Table 8.1: Reference aircraft for operating empty weight and maximum take-off weight.

Reference aircraft	OEW [kg]	MTOW [kg]
MQ-9 Reaper	2223	4760
F-15 Eagle	12700	30854
F-16 Fighting Falcon	8570	19200
F/A-18 Hornet	10433	23541
F-35 Lightning II	13154	31800
A-10 Thunderbolt II	11321	23000
Sukhoi Su-25	9800	19300
Textron AirLand Scorpion	5761	9979
M-346 Master	4610	9500
A-37 Dragonfly	2817	6350
FMA IA 58 Pucar	4020	6800
Rockwell OV-10 Bronco	3161	6553
EMB 314 Super Tucano	3200	5400
F-4 Phantom II	13757	28030
Nanchang Q-5	6375	11830

#### Fuel Weight

Using the specific fuel consumption of the AE2100a turboprop engine, it is possible to estimate the aircraft fuel weight, MF. In order to do so, the mission profile of the aircraft has to be used. The mission profile was described in section 3.1.

Each segment in the mission profile has an associated fuel fraction, which is defined as the total weight of the aircraft at the end of the phase over the total weight of the aircraft at the beginning of the phase. The fuel

<sup>1</sup>The reference aircraft were found from Jane's All The World's Aircraft, online database: <https://jan.es.ihs.com> Accessed on 24-05-2018.

fractions that have been taken from historical data are those for the engine start- and warm-up and the taxi phase [4]. Methods to calculate the fuel fractions for the climb, descent and combat phases are described in section 11.3.

For the cruise and loiter phases of the mission, the fuel fractions can be calculated using Breguet's range and endurance equations [4]. The range fuel fraction can be calculated for propeller aircraft using Equation 8.1. The endurance fuel fraction can be calculated with Equation 8.2.  $V_{\text{cruise}}$  and  $V_{\text{loiter}}$  are obtained from the phase 1 iterations.  $c_p$  is the propeller specific fuel consumption and  $\eta_p$  is the propeller efficiency. The  $L/D$  is taken at the point at which  $C_L/C_D$  is maximised for cruise flight and the point that  $C_L^3/C_D^2$  is maximised for endurance.

$$\left(\frac{W_5}{W_4}\right)_{\text{prop}} = e^{-\left(R\left(\frac{gc_j}{\eta_j}\right)_{\text{cruise}} \frac{1}{(L/D)_{\text{cruise}}}\right)} \quad (8.1)$$

$$\left(\frac{W_9}{W_8}\right)_{\text{prop}} = e^{-\left(E\left(\frac{Vgc_j}{\eta_j}\right)_{\text{loiter}} \frac{1}{(L/D)_{\text{loiter}}}\right)} \quad (8.2)$$

Using the specified mission profile and the corresponding equations for each of the concepts results in the concept specific fuel fractions. With the fuel fractions of all mission elements known, the total mass of the required fuel can be calculated using Equation 8.3. Note that it is assumed that the aircraft will bring 5% of the nominal fuel weight extra as reserve fuel. This fraction is called  $M_{\text{res}}$ .

$$\text{WF} = \left(1 - \frac{W_1}{W_{t0}} \prod_{i=1}^{i=n} \frac{W_{i+1}}{W_i}\right) \text{MTOW} + M_{\text{res}} \cdot \text{WF} \quad (8.3)$$

Noting that 0.3% of the maximum takeoff weight consists of fuel and hydraulic fluids that is trapped in pipes according to historical data, for which the mass fraction is denoted as  $M_{\text{tfo}}$ , and that the payload and crew weight are included in the MTOW, the MTOW can be calculated using Equation 8.4.

$$\text{MTOW} = \text{WF} + M_{\text{crew}} + \text{WPL} + \text{OEW} + M_{\text{tfo}} \quad (8.4)$$

### Sensitivity Analysis

A sensitivity analysis has been performed for the Class I weight estimation. The sensitivity analysis has been visualised in Figure 8.1. Eight parameters have been analysed for the effect on the MTOW of an increment of +1% and -1% of these parameters. The blue line indicates the MTOW in normal conditions, an upwards pointing arrow indicates a 1% increase of the associated parameter and a downwards pointing arrow indicates a 1% decrease.

It can be seen that the maximum increase and decrease in MTOW is 0.27% for a change of 1% of the payload weight. This result is deemed to prove that the Class I weight estimation is not sensitive. From this result, it is determined that the payload weight can be adjusted to vary during the phase I iterations. Furthermore, the engine selection can be done according to the requirements, without being concerned about the specific fuel consumption. Lastly, external hardpoints and ordnance can be added without a big increase in MTOW from an increase of parasitic drag.

### Verification and Validation

In order to be able to implement the Class I weight estimation program in the phase 1 iteration scheme, code specifications have been added as described in section 4.5. Furthermore, unit tests have been performed by changing parameters to zero and either increasing or decreasing parameters and observing the outcome. Whenever this outputted expected values, the program was deemed verified.

For the validation of the program, input values were acquired for the IA 58 Pucará, which is a reference propeller aircraft. Values were found for the mission profile, the planform, the payload and the turboprop engine. The outputs of the Class I program are tabulated in Table 8.2. It can be seen that the outputs for the MTOW and the OEW are close to the real-life values. The fuel weight deviates a 14.4% from the actual value, but as the final output of the program, the MTOW, is a mere 2.5% over the real value, the program is deemed validated.

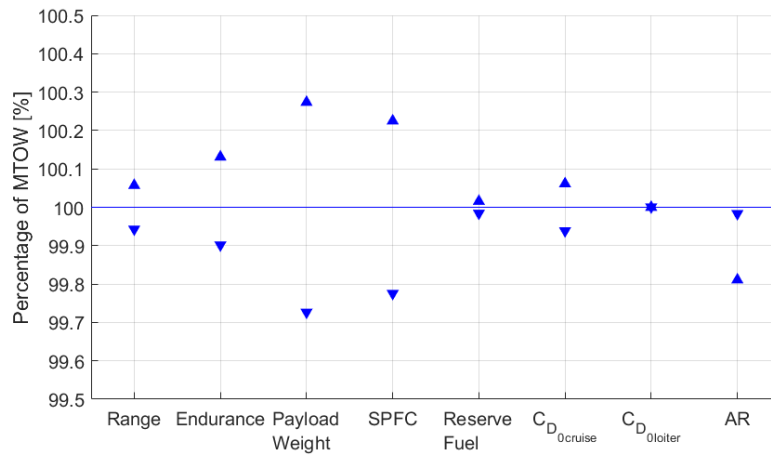


Figure 8.1: Sensitivity analysis of the Class I weight estimation. The eight parameters on the x-axis are analysed to see the effect of increasing or decreasing the MTOW with 1%.

Table 8.2: Validation of the Class I Weight Estimation.

Parameter	IA 58 Pucará
MTOW from Class I	6,971 kg
MTOW real	6,800 kg
Deviation	2.5 %
OEW from Class I	3,864 kg
OEW real	4,020 kg
Deviation	4.0%
WF from Class I	1,496 kg
WF real	1,280 kg
Deviation	14.4 %

## 8.2. Class II Weight Estimation

The Class II weight estimation is taken from Airplane Design Part V: Component Weight Estimation and gives a value of the operating empty weight of the aircraft based on statistics from previous aircraft. [1] There are various methods that are detailed in this book however one method should be adhered to when doing the full class II weight estimation as the mixing of methods may give an inaccurate estimation of the component weights and eventually the operating empty weight. The method for fighter and attack aircraft was used and whenever there was a split between the United States Air Force, USAF, planes and United States Navy, USN, planes, the USAF method was used. The formulas presented below use the imperial system of units and these were used to calculate each component weight, however the metric weight of each component will be presented converted into kg. The equations can be found in [Appendix A](#).

The structural weight estimation includes estimations for the wing,  $W_w$ , horizontal tail,  $W_h$ , vertical tail,  $W_v$ , fuselage,  $W_f$ , and landing gear,  $W_g$ . The equations for this part of the weight estimation are [Equation A.1](#) through [Equation A.5](#). The powerplant weight estimation includes estimations for the engines,  $W_e$ , nacelles,  $W_n$ , air induction system,  $W_{ai}$ , propeller,  $W_p$ , fuel system,  $W_{fs}$ , in-flight refueling,  $W_{inflref}$ , fuel dumping,  $W_{fd}$ , engine controls,  $W_{ec}$ , engine starting system,  $W_{ess}$ , and propeller controls,  $W_{pc}$ . The equations used for this are [Equation A.6](#) through [Equation A.15](#). The fixed equipment weight estimations includes estimations for the flight control system,  $W_{fc}$ , movable centre of gravity system,  $W_{fcg}$ , hydraulic and pneumatic system,  $W_{hps}$ , instrumentation, avionics and electronics,  $W_{iae}$ , electrical system,  $W_{els}$ , air-con, pressurisation, anti- and de-icing system,  $W_{api}$ , oxygen system,  $W_{ox}$ , auxiliary power unit,  $W_{apu}$ , furnishings,  $W_{fur}$ , paint,  $W_{pt}$ , armament,  $W_{arm}$ , and auxiliary gear,  $W_{aux}$ . The relevant equations are [Equation A.16](#) through [Equation A.27](#).

### Class II Weight Summary

The weights detailed in the appendix can be summed so that they fall under three categories, structural weight, powerplant weight and fixed equipment weight. The components that are in each category are presented below in [Equation 8.5](#) through [Equation 8.7](#) and the results of the sum for each section is presented in [Table 8.3](#). Finally the operating empty weight can be calculated as shown in [Equation 8.8](#) and is also shown in [Table 8.3](#).

The Class II weight results are used for further analyses in [chapter 11](#), and [chapter 13](#).

$$W_{\text{struc}} = W_w + W_h + W_v + W_f + W_g = 5121.3 \text{ kg} \quad (8.5)$$

$$W_{\text{pwr}} = W_e + W_n + W_{ai} + W_p + W_{fs} + W_{inflref} + W_{fd} + W_{ec} + W_{ess} + W_{pc} = 3491.9 \text{ kg} \quad (8.6)$$

$$\begin{aligned} W_{\text{fixequip}} &= W_{fc} + W_{fcg} + W_{hps} + W_{iae} + W_{els} + W_{api} + W_{ox} + W_{apu} + W_{fur} + W_{pt} + W_{arm} + W_{aux} \\ &= 2922.9 \text{ kg} \end{aligned} \quad (8.7)$$

$$W_{\text{OEW}} = W_{\text{struc}} + W_{\text{pwr}} + W_{\text{fixequip}} = 11575.1 \text{ kg} \quad (8.8)$$

Table 8.3: Summary of the weight of the class II weight estimation.

Weight component	Weight
Structural	5121.3 kg
Powerplant	3491.9 kg
Fixed equipment	2922.9 kg
Operating Empty Weight	11 575.1 kg

### Verification and Validation

In order to verify the code used to calculate the Class II weight estimations unit tests were performed on each of the formulae used. In the formulae parameters were changed to zero or another value and the output was observed. If the output was expected then the formula was considered verified, however if the expected

output was not obtained then the formula was looked into to see what was wrong with it and the process would start again with the new formula that was obtained. When these verification tests were performed, the formulae behaved as was expected and so they were considered to be verified. To validate the Class II weight estimations the Boeing 737 was used to make sure that the values obtained when using its data were around the actual values of the aircraft. The Boeing 737 was used as this had the greatest amount of data available and therefore offered the most complete validation. As the data obtained from the Class II weight estimations were within 10% of the data for the 737 this was considered an appropriate amount of accuracy and so the Class II weight estimations were considered validated.

### 8.3. Center of Gravity Range

In this section the more detailed cg range estimation that was performed is described. To make the resulting cg ranges useful for the longitudinal wing position determination in [section 12.4](#), the CG range for the wing and fuselage were considered separately.

First of all, the cg position determination of the fuselage was largely based on the fuselage layout presented in [section 7.3](#). As can be seen in [Figure 7.2](#), the fuselage is divided into rough volumes which each reserve space for systems. To find positions of the cg, the volumes were reduced to point masses. The masses of those points were assumed to be equal to the sum of all masses of systems assigned to that volume. The Class II weight estimation, which is discussed in [section 8.2](#), was used to determine the masses of all those systems. A certain position of the cg was found by summing the products of the position and mass of the point masses, and then dividing the resulting number by the total mass, as is presented in [Equation 8.9](#).

$$x_{cg} = \frac{\sum_{i=1}^n x_i M_i}{\sum_{i=1}^n M_i} \quad (8.9)$$

Different cg positions could be found by considering different mass distributions. Different mass distributions resulted from assuming different combinations of fuel tanks and ammunition containers to be full or empty. The cg range was determined by running through all possible weight distributions and determining the minimum and maximum positions of the cg. The corresponding total weights were also listed, which were necessary for proper positioning of the wing with respect to the fuselage.

A similar but more simplistic method was used for the cg estimation of the wing group. Because the fuel that is stored in the wing lays very close the average cg position of the wing group, the cg range of the wing group was assumed to be equal to zero. In other words, a single cg position was assumed. However, the minimum and maximum weight of the wing group were taken into account, since as mentioned before, this has influence on the longitudinal wing placement.

Verification was done by checking the contribution of every individual weight point. In other words, the masses of every component were set to zero, except for particular components. If the position of the cg was calculated this way, it should be the same as the know position of the component considered. This way, the contribution of every component was checked.

With the obtained wing area from the iteration, a base is formed to come up with a wing design. The criteria for the wing are part of the iteration cycle. The airfoil selection is based on the results of the iteration and is therefore not included in the iteration. The wing design includes the wing geometry and the sizing of high lift devices and the wing control surfaces. Finally, initial aerodynamic characteristics are estimated, which are used in the iteration phase.

### 9.1. Airfoil Design

The criteria listed below are considered for the airfoil selection trade-off. As both cruise and loiter are important for mission of the aircraft, the optimal lift-over-drag is analysed in both situations. For cruise  $C_l/C_d$  should be maximised, while for loiter this is  $C_l^{1.5}/C_d$ . Furthermore,  $C_d$  and  $C_m$  will be analysed at the angle of attack of the design lift coefficient  $C_{l_{\text{design}}}$ . This value will be determined later in this section. At this point the  $C_m$  characteristics are considered to be equal for every airfoil, to decrease the time spent on selecting airfoils and put more effort in the analysis of the lift, drag and moment characteristics.

- $C_{l_{\text{max}}}$  should be as high as possible.
- $C_{d_{\text{min}}}$  should be as low as possible.
- $\left(\frac{C_l}{C_d}\right)_{\text{max}}$  should be as high as possible.
- $\left(\frac{C_l^{1.5}}{C_d}\right)_{\text{max}}$  should be as high as possible.
- $C_d$  at  $C_{l_{\text{design}}}$  should be as low as possible.

In order to streamline the process of selecting suitable airfoils, the thickness-to-chord ratio  $t/c$  is fixed and the properties at the design lift coefficient  $C_{l_{\text{design}}}$  are determined.  $t/c$  is an important parameter for the wing performance. A thicker airfoil leads to a larger wing box, which in turns leads to reduced weight. But the lift over drag ratio also decreases with increasing thickness-to-chord ratio. Therefore,  $t/c$  should be chosen carefully. Since a part of the fuel will be stored in the wing, which will be further discussed in [section 14.2](#), a large thickness is desired to increase the wing volume. However, fuel will not be stored in the outboard section of the wing, which means that a smaller  $t/c$  is possible. Therefore, this increases the lift-over-drag of that part of the wing. This also means that the lift distribution shifts inboard, reducing the bending stresses at the root.

Having two different airfoils at the root and tip is the best choice for the wing design. However, these airfoils have to be combined into one complete wing. There are three ways to do this. The first option is to have one airfoil until a span wise location, where there is an immediate transition from one to the other. The second option is to have a smooth transition between these airfoils with a certain transition width. After a short analysis of how to do these kind of transitions, it became clear that this adds significant structural complexity to the wingbox and are therefore not deemed feasible. Then the final option was left, which have a linear interpolation between the root and tip airfoil. This is easy to manufacture, to analyse and still gives the advantage of having different thickness-to-chord ratios over the wing. Based on fuel volume, and structural weight considerations, it is decided to have a  $t/c$  of 0.18 at the root, while having a  $t/c$  of 0.12 at the tip.

The design lift coefficient is determined for the most fuel intensive phase of the mission, which is the loiter phase and is calculated using [Equation 9.1](#), where the loiter altitude is at 10 000 ft, with an average velocity of 81 m/s, and a begin and end weight of 20 777 kg and 18 600 kg. This yields a  $C_{l_{\text{design}}}$  of 1.15, which has to be converted to  $C_{l_{\text{design}}}$ . Since the wing has a finite wingspan, a non constant chord length and dihedral,

the airfoil does not experiences the same air as a wing, so this value will be larger. Assumed is that the wing lift coefficient is the same as the aircraft lift coefficient. Then according to Sadraey [13],  $C_{L_{\text{design}}}$  should be divided by 0.9 for the conversion from wing to airfoil lift coefficient, to finally obtain a  $C_{L_{\text{design}}}$  of 1.278.

$$C_{L_{\text{design}}} = \frac{1}{\frac{1}{2}\rho V^2 S} \frac{1}{2} (W_{\text{begin}_{\text{loiter}}} + W_{\text{end}_{\text{loiter}}}) \quad (9.1)$$

The airfoils chosen for the trade-off are selected from the online database of Airfoil Tools<sup>1</sup>. The criteria for selecting airfoils is the  $t/c$  for the root and tip. The airfoils and the trade-off matrix are shown in Table 9.1 for the root and in Table 9.2 for the tip. The values displayed in the trade-off matrix are obtained using XFLR5. Input for this software tool is the Reynold's number of  $1.59 \times 10^7$  for the root chord and  $6.37 \times 10^6$  for the tip chord and a loiter Mach number of 0.25. The colour of the cell indicates how good the airfoil is for that specific criteria.

Table 9.1: Trade-off of the airfoil in the inboard section of the wing. All airfoils have a  $t/c$  of 0.18. The score of the analysis is divided into four categories, where the result is indicated using colours. From a good to bad result, these colours are green, yellow, orange, red.  $C_{L_{\text{design}}}$  for loiter is 1.278.

Airfoil	$C_{l_{\text{max}}}$	$C_{d_{\text{min}}}$	$(C_l/C_d)_{\text{max}}$	$(C_l^{1.5}/C_d)_{\text{max}}$	$C_d$ at $C_{l_{\text{design}}}$
NACA 63(3)-018	1.695	0.0048	128.0	145.7	0.010
NACA 63(3)-218	1.822	0.0055	130.0	152.3	0.010
NACA 63(3)-418	1.927	0.0042	143.0	162.0	0.009
NACA 63(3)-618	1.982	0.0043	176.7	171.5	0.009
NACA 64(3)-218	1.841	0.0039	125.9	144.2	0.010
NACA 64(3)-418	1.913	0.0040	140.0	153.2	0.010
NACA 64(3)-618	1.978	0.0041	182.7	168.1	0.009
NACA 65(3)-218	1.849	0.0035	120.1	132.3	0.011
NACA 65(3)-618	1.970	0.0037	195.5	177.1	0.010
NACA 66(3)-218	1.778	0.0029	99.7	99.2	0.015
NACA 66(3)-418	1.852	0.0030	146.3	103.8	0.015
NACA 66-018	1.711	0.0029	96.6	96.8	0.016
NACA 16-018	1.532	0.0051	86.0	86.1	0.017
NACA 23-018	1.934	0.0056	149.9	178.0	0.009
NACA 2418	1.971	0.0055	141.9	164.9	0.009
NACA 4418	2.000	0.0056	153.2	175.0	0.008
NACA 0018	1.910	0.0056	133.4	158.9	0.010
NACA 6718	2.126	0.0043	106.7	135.8	0.013
Clark YM-18	1.851	0.0061	160.3	175.7	0.008
GOE 504	1.7223	0.0060	163.3	117.8	0.009
USA 34	1.935	0.0057	137.9	139.2	0.014
AS5049	1.847	0.0042	141.1	159.0	0.009

From the trade-off matrix it can be concluded that the NACA 63(3)-618, 64(3)-618 and 65(3)-618 all have comparable scores. The NACA 65(3)-318 scores a little bit lower at the maximum lift coefficient and a little bit higher at the minimum drag coefficient compared to the other two, but is substantially higher at the lift over drag ratios. Therefore, the NACA 65(3)-618 is chosen as the root airfoil.

For the tip the NACA 6412 airfoil is chosen. The NACA 4412 has the same colour indication of the scores, but it is outperformed especially on the lift over drag ratios. The two chosen airfoils are shown in Figure 9.1.

## 9.2. Wing Design

In this section the overall layout of the wing will be established. This includes the the planform, dihedral, twist and incidence. Also high lift devices and control surfaces will be discussed.

### Planform Design

In the preliminary phase of the design an initial wing planform was already determined. The planform will define the sweep angle and taper ratio. From the iteration procedure, it was concluded that the wing will

<sup>1</sup>Airfoil Tools <http://airfoiltools.com/search/index> [Accessed on 11-06-2018]

Table 9.2: Trade-off of the airfoil at the wing tip. All airfoils have a  $t/c$  of 0.12. The score of the analysis is divided into 4 categories, where the result is indicated using colours. From a good to bad result these colours are green, yellow, orange, red.  $C_{l_{design}}$  for loiter is 1.278.

Airfoil	$C_{l_{max}}$	$C_{d_{min}}$	$(C_l/C_d)_{max}$	$(C_l^{1.5}/C_d)_{max}$	$C_d$ at $C_{l_{design}}$
NACA 63(1)-212	1.706	0.0040	112.3	124.4	0.012
NACA 63(1)-412	1.801	0.0041	130.4	135.3	0.011
NACA 65(1)-212	1.631	0.0036	170.1	114.5	0.013
NACA 65(1)-412	1.740	0.0037	130.3	126.2	0.011
NACA 66(1)-212	1.576	0.0031	103.0	108.4	0.014
NACA 23-112	1.754	0.0052	139.9	147.8	0.010
NACA 24-112	1.725	0.0048	142.8	143.1	0.010
NACA 25-112	1.705	0.0045	141.7	139.2	0.010
NACA 1412	1.761	0.0052	121.0	139.4	0.011
NACA 2412	1.804	0.0053	126.4	146.3	0.010
NACA 4412	1.886	0.0056	165.4	164.4	0.009
NACA 6412	1.939	0.0059	179.2	185.2	0.008
E201	1.647	0.0046	153.0	140.5	0.011
Eppler 361	1.672	0.0041	128.2	141.1	0.010
Eppler 636	1.522	0.0042	157.1	156.3	0.011
EH 2.0/12	1.577	0.0045	142.8	131.2	0.012
GOE 593	1.770	0.0057	165.1	179.2	0.009
GOE 796	1.807	0.0062	138.8	143.8	0.010
HQ 2.5/12	1.640	0.0044	131.4	130.7	0.011

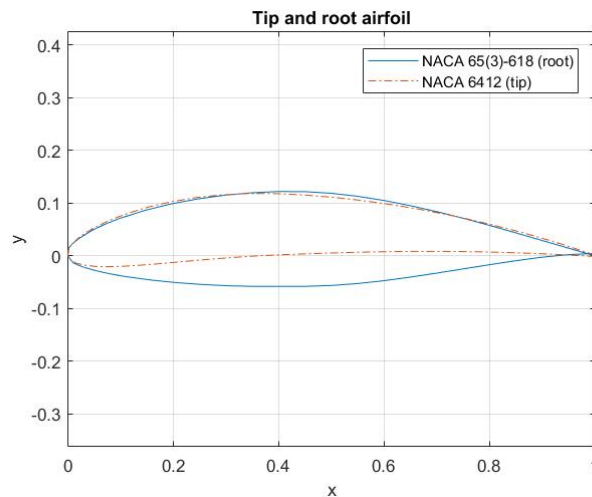


Figure 9.1: The two airfoils for the root and tip. The airfoils will be linearly interpolated to obtain the characteristics of the airfoil at every span wise location. The difference in  $t/c$  is clearly visible.

have an aspect ratio of 8, a surface area of 52.90 m<sup>2</sup> and thus a wingspan of 20.56 m.

Since the Mach number during cruise is 0.50, the wings do not need to be swept back, as the flow does not reach Mach 1 anywhere on the wing, which allows for a quarter-chord sweep angle of zero, which in turn allows for less structural reinforcement.

In order to get the most efficient lift distribution over the wing, an elliptical distribution is desired. For zero quarter-chord sweep angle, the lift distribution for wings with a taper ratio  $\lambda$  of 0.4 can be approximated to be elliptical. This taper ratio is thus taken for the wing planform [14]. Further analysis on how to obtain an elliptical lift distribution is performed in Equation 9.2.

The size of the root chord is given by Equation 9.2. This results in a root chord of 3.67 m. The tip chord is calculated by multiplying the root chord by the taper ratio, which results in a tip chord of 1.47.

$$c_r = \frac{2S}{(1 + \lambda)b} \quad (9.2)$$

### Wing configuration

The wing geometry consists of the dihedral, twist and incidence angle and are determined in this subsection. Also the lift distribution along the wingspan is established.

#### Dihedral

Dihedral and wing sweep influences the roll stability of the aircraft. Since the aircraft has no sweep, dihedral is desired to obtain this roll stability. With a low wing configuration, this means that an angle of 3 deg is needed. From reference aircraft this seems also as reasonable angle. Furthermore this will increase the ground clearance of the propeller blades by a small amount as well.

#### Twist angle

For safety concerns, it is desired that the inboard section of the wing stalls before the outboard section does. This is because the ailerons, which are located at the outboard section of the wing, cannot be used for roll control when having tip stall and therefore, cannot recover. There are two ways to tackle this problem: applying geometric or aerodynamic twist. Geometric twist is changing the incidence angle of the tip compared to the root, so called washout, when having the same airfoil through the wing. This ensures that the angle of attack at which the outboard section is always lower than the inboard section, meaning it will always stall later. Aerodynamic twist is used when the wing consists of different airfoils. As different airfoils have different characteristics, the stall characteristics are not the same. Therefore, it should be carefully considered whether the outboard airfoil stalls later and if not, apply geometric twist as well.

Geometric twist influences the lift distribution along the wing as well. Since it is desired to have an elliptical lift distribution, an analysis is done to obtain this distribution. This is done using the Lifting Line Theory [13]. The distribution is shown in Figure 9.2. As can be seen, twist is needed to obtain a more elliptical distribution and therefore the wing will have both aerodynamic and geometric twist. This ensures that both tip stall will not occur and an elliptical lift distribution is obtained. A twist angle of  $-3$  deg is chosen, which also seems an appropriate angle when looking at reference aircraft.

#### Incidence angle

An incidence angle is used to place the wing in an optimal angle compared to the fuselage during cruise and loitering. This angle has to be chosen such that the desired lift is produced, while having a minimal drag. As there is no requirement for the fuselage angle of attack, the optimal angle should be considered, which is zero. The incidence angle chosen for the wing is 6.3 deg. This is a high angle, which is caused by the high lift coefficient required for loitering. Even though the optimal angle is higher for loiter, cruise has to be taken into account as well, which is at a lower angle. Therefore, the fuselage angle of attack during loiter will be 1 deg, while for cruise this will be  $-6$  deg. With calculations the drag caused by the fuselage during cruise and loiter is determined and this happens to be the most optimal angle when considering both situations.

### High Lift Devices

During take-off and landing a higher  $C_{L_{\max}}$  is required than is achieved with just the regular wing. For this reason, high lift devices (HLD's) are used. The required  $\Delta C_{L_{\max}}$  follows from the iteration and is 0.5 for landing. To provide a margin against stall, a safety factor of 10% is assumed and thus a  $\Delta C_{L_{\max}}$  of 0.55 is used in the

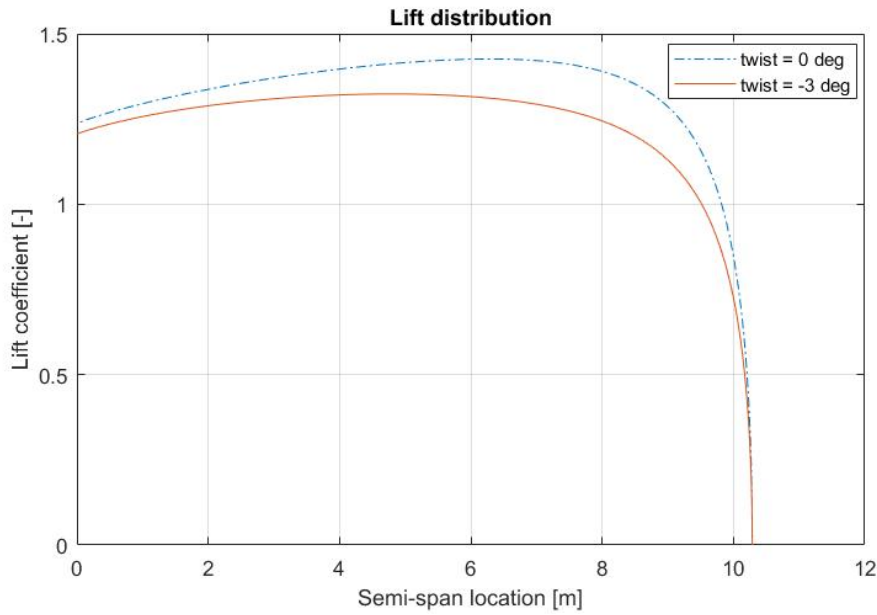


Figure 9.2: Spanwise lift distribution at different twist angles. As can be seen, a negative twist angle will decrease the lift further away from the root. An incidence angle of 6.3 deg is used.

designing of the flaps.

It was decided that the aircraft will have single slotted flaps as a trailing edge high lift device and that the aircraft will have no leading edge high lift devices. This configuration was chosen for the following reasons. Firstly, the slotted flaps were chosen since they are able to generate sufficient  $\Delta C_{L_{max}}$  while still leaving enough space on the wings for efficiently working ailerons. For slotted flaps deflection angles of 20° and 40° are assumed for take-off and landing respectively [15]. Other trailing edge HLD's were considered, like the Fowler flap and double slotted flaps. Although these HLD's are more efficient than the single slotted flap, they are also more complex. Since, this complexity brings more weight to the aircraft and decreases the ease of maintenance, these flap types were discarded.

Leading edge high lift devices were discarded for mostly the same reasons. Leading edge HLD's are used mainly to provide a margin against stall [15]. Since adding leading edge HLD's add to the weight and complexity of the aircraft, it was decided that this margin could also be taken into account in sizing the trailing edge HLD's. This is the reason the safety factor of 10% was used. Furthermore, a part of the trailing edge HLD's will be in the wake of the propeller. This will make the HLD's more efficient and provide an even bigger  $\Delta C_{L_{max}}$ . In case of engine failure, this will of course not be the case anymore so the added  $\Delta C_{L_{max}}$  because of the wake is not designed for, but can be seen as an extra margin.

Since the lift coefficient has to be higher in landing than in take-off, initial sizing of the HLD's was done using the landing lift coefficient. To calculate the wing flapped surface, Equation 9.3 was used [15].

$$\Delta C_{L_{max}} = 0.9 \Delta C_{l_{max}} \frac{S_{wf}}{S} \cos(\Lambda_{\text{hingeline}}) \quad (9.3)$$

Where  $\Delta C_{L_{max}}$  is the required increase of the lift coefficient,  $\Delta C_{l_{max}}$  is the increased lift coefficient of an airfoil with the HLD fully deployed and was determined to be 1.3 for slotted flaps [15]. Furthermore,  $\frac{S_{wf}}{S}$  is the ratio of the wing flapped surface over the total wing area and  $\Lambda_{\text{hingeline}}$  is the sweep angle at the hinge line of the HLD. The hinge line was determined to be at 70% of the chord line which is 10% of the chord behind the wing box aft spar, of which its placement is further elaborated upon in section 13.3. This distance was taken to have space in the wing for control system elements and mechanisms. The sweep angle at that point was determined geometrically.

From these calculations, the wing flapped surface area for single slotted flaps was found to be 24.96 m<sup>2</sup>. When taking the fuselage and the engine nacelle into account, which prevent the presence of flaps along the wing span there, the wing span covered by flaps is 10.14 m, which is about half of the total wing span. Resulting aerodynamic characteristics for the flaps down configuration can be found in section 10.1.

### Ailerons

Since there was no requirement driving the aileron design, it was decided that the ailerons should be as large as possible to maximise roll manoeuvrability. Taking a small clearance distance between the ailerons and the flaps and between the ailerons and the wing tip into account, this resulted in ailerons with a span-wise width of 4.91 m on each wing. The hinge-line of the aileron was taken to be at  $0.7c$  for the same reason as the placement of the hinge-line of the flaps in Figure 9.2.

To estimate the aileron control derivative  $C_{l_{\delta A}}$ , Equation 9.4 was used [13].

$$C_{l_{\delta A}} = \frac{2C_{L_{\alpha W}}\tau}{Sb} \int_{y_0}^{y_i} c_y dy \quad (9.4)$$

Where  $C_{L_{\alpha W}}$  is the lift curve slope of a finite wing, which is elaborated upon in section 10.1.  $\tau$  is the aileron effectiveness parameter and for an aileron chord of  $0.3c$  it is known to be 0.52 [13]. The resulting value for  $C_{l_{\delta A}}$  is equal to  $8.772 \times 10^{-4}$ .

Subsequently, the roll rate that can be achieved as a function of velocity is calculated using Equation 9.5 [16].

$$p = -\frac{C_{l_{\delta A}}\delta_A 2V}{C_{l_p} b} \quad (9.5)$$

Where  $\delta_A$  is the maximum deflection angle of the aileron. It has been chosen that this angle will be  $25^\circ$  upwards as well as downwards for this aircraft.  $C_{l_p}$  is the stability derivative that measures the roll damping and its value is determined in Equation 12.8. The roll rate that can be achieved can be seen in Figure 9.3.

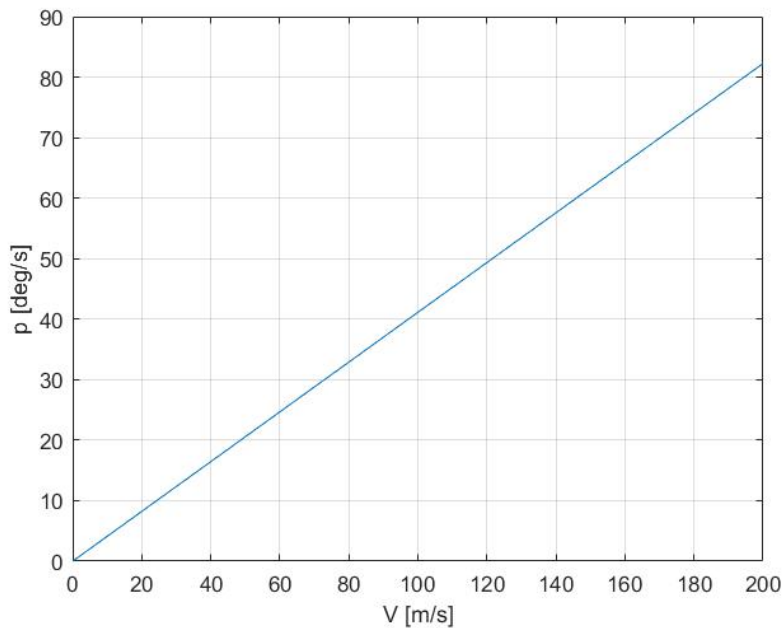


Figure 9.3: Roll rate as a function of velocity.

As can be seen, the roll rate varies linearly with the velocity. Since there is no requirement driving the roll manoeuvrability, it is yet to be determined whether these roll characteristics are sufficient for the aircraft mission profile. In case they are not, there are several ways to increase the roll rate. First off, more efficient flaps could be considered which will leave more space on the wing to be taken in by the aileron. Secondly, a combination of flaps and ailerons, flaperons, should be considered further in the design as a means to use the wing surface more effectively.

### 9.3. Drag Polar Estimations

For the Class I weight estimation the drag polar is needed and is determined in this section.

### Zero-Lift Drag Estimation

In order to construct the drag polar, from which the  $L/D$ -ratio can be acquired, a preliminary drag build-up is performed. The  $C_{D_0}$  is given by Equation 9.6, where  $C_f$  is the flat plate friction coefficient, which is used here to estimate the skin friction coefficients of the individual aircraft components,  $FF$  is the form factor, which estimates the pressure drag due to viscous flow separation and  $IF$  is the interference factor, which estimates the effect of the drag of components on other components. Please note that all equations used are taken from TU Delft course Aerospace Design & System Engineering Elements II [17].

$$C_{D_0} = \frac{1}{S_{\text{ref}}} \sum_c C_{f_c} \cdot FF_c \cdot IF_c \cdot S_{\text{wet}_c} + C_{D_{\text{misc}}} \quad (9.6)$$

$C_f$  can be calculated using Equation 9.7, for which a different Reynold's number is used for each component.  $FF$  can be calculated for the wing and tail using Equation 9.8, using Equation 9.9 for the fuselage and the canopy and Equation 9.10 for the nacelles and external stores. In Equation 9.8  $(x/c)_m$  is the location of the maximum thickness-to-chord ratio on the airfoil and  $\Lambda_m$  is the sweep at this location. Equation 9.9 and Equation 9.10 are functions of  $f$ , which is the fineness ratio of the components, defined as  $d/l$ , where  $d$  is the diameter of the component and  $l$  is the length of the component.

$$C_f = \frac{0.455}{(\log \text{Re})^{2.58} (1 + 0.144 M_\infty^2)^{0.65}} \quad (9.7)$$

$$FF_{\text{wing}} = \left[ 1 + \frac{0.6}{(x/c)_m} \left( \frac{t}{c} \right) + 100 \left( \frac{t}{c} \right)^4 \right] [1.34 \cdot M_\infty^{0.18} (\cos \Lambda_m)^{0.28}] \quad (9.8)$$

$$FF_{\text{fuselage}} = 1 + \frac{60}{f^3} + \frac{f}{400} \quad (9.9)$$

$$FF_{\text{nacelle}} = 1 + \frac{0.35}{f} \quad (9.10)$$

The input parameters for Equation 9.6 are tabulated in Table 9.3. The resulting zero-lift drag coefficients are equal to 0.023 for the loiter phase and 0.028 for the cruise phase. Using Equation 9.11 an Oswald's efficiency factor of 0.81 has been found. These values will be used as an input for the drag polar, which will be used to perform the Class I weight estimation.

$$e_{\text{clean}} = 1.78(1 - 0.045A^{0.68}) - 0.64; \quad (9.11)$$

Table 9.3: Input parameters for the parasitic drag calculation of the aircraft components.

Component	$C_f$ [-]	$FF$ [-]	$IF$ [-]	$S_{\text{wet}}$ [m <sup>2</sup> ]
Wing	0.0030	1.73	1	92.88
Horizontal tail	0.0031	1.73	1.08	15.51
Vertical tail	0.0031	1.73	1.08	16.82
Fuselage	0.0023	1.08	1	42.92
Engine nacelle	0.0029	1.09	1	5.73
Armament	0.0032	1.06	1	1.58
Canopy	0.0029	1.08	1	6.88

## 9.4. Verification & Validation

For the airfoil analysis XFLR5 was used. Verifying this software tool is beyond the scope of this project and therefore is assumed to be accurate. As already showed in the plot of the lift distribution, the twist angle is plotted for two values, which gives a check whether the program gives results as expected. For the high lift devices and aileron section the equations are also calculated by hand to verify the program, where giving zero  $\Delta C_{L_{\text{max}}}$  gives the expected result. Also this program is validated, using existing values from reference aircraft to see if roughly the same size surfaces would yield.

# 10

## Aerodynamic Characteristics

In this chapter the aerodynamic characteristics of the airfoil, wing and aircraft are estimated. This consists of the lift, drag and moment characteristics and will be analysed in different conditions, namely loiter, cruise, combat and landing and take-off at sea level and 10,000 ft. Also the effect of deploying flaps during landing and take-off on the characteristics will be determined. These characteristics then can be used for the analysis of the performance and stability of the aircraft. The values used flow from the iteration results. The results are not iterated and are only used to check the characteristics after the iteration. Another iteration should be performed in the next design phase, which is beyond the scope of this project to obtain better results. Note that the aerodynamic characteristics are assumed to be calculable in the mean aerodynamic chord.

### 10.1. Lift Characteristics

This section presents the lift characteristics for different configurations. The characteristics of the interpolated airfoil in the MAC will be used to construct the lift curves for flaps up and flaps down for the airfoil, the wing and the total aircraft. Methods from Airplane Design Part IV are used throughout this section [18].

#### Airfoil Flaps Up Lift Curve

From the interpolated airfoil at the mean aerodynamic chord, the lift curve characteristics can be acquired using XFLR5. The resulting lift curve is plotted in Figure 10.1 and the main characteristics have been tabulated in Table 10.1. It can be seen that the airfoil characteristics are similar for all situations, varying small amounts with changing Reynold's number. The characteristics for the cruise condition differ more, due to the higher Mach number, which demonstrates compressibility effects. The takeoff and landing characteristics of the airfoil are not complete, as the additional lift in flaps down configuration has to be included.

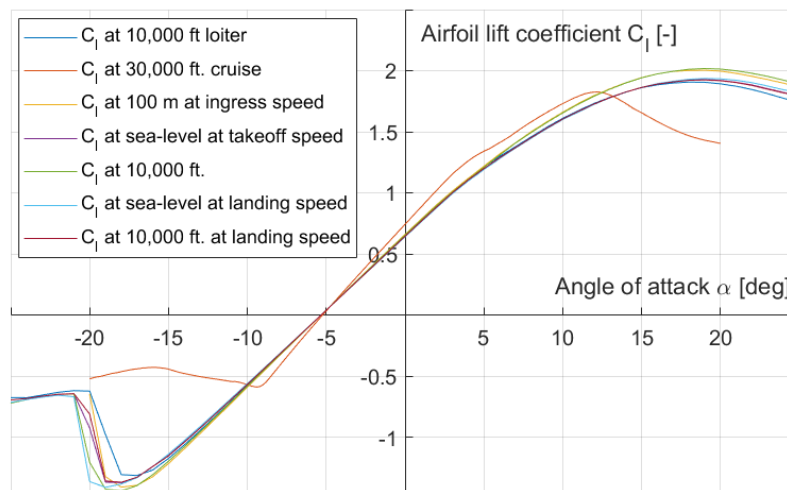


Figure 10.1: Airfoil lift coefficient vs. angle of attack curves.

#### Airfoil Flaps Down Lift Curve

The increment in the airfoil lift coefficient for the linear range, as a result of deflection of single-slotted flaps is given by Equation 10.1. In this relation  $\alpha_\delta$  is the flap effectiveness, which is dependent on the deflection angle and the flap-chord-to-chord ratio and can be taken from Roskam's Aircraft Design Part VI [18],  $(c'/c)$  is

Table 10.1: Flight parameters at several flight conditions.

Flight condition	Re [-]	Mach	$\alpha_{0l}$	$C_{l\alpha}$ [rad <sup>-1</sup> ]	$\alpha^*$ [deg]	$\alpha_{C_{l_{max}}}$ [deg]	$C_{l_{max}}$ [-]
Loiter	$1.18 \times 10^7$	0.25	-5.3	6.88	-16 – 3	18	1.91
Cruise	$1.27 \times 10^7$	0.50	-5.2	8.25	-9 – 3	12	1.83
Combat	$1.72 \times 10^7$	0.27	-5.3	6.92	-14 – 6	18	2.00
Sea-level takeoff	$1.31 \times 10^7$	0.21	-5.3	6.67	-15 – 4	19	1.93
10k ft takeoff	$1.20 \times 10^7$	0.25	-5.3	6.82	-16 – 3	19	2.02
Sea-level landing	$1.16 \times 10^7$	0.18	-5.3	6.74	-16 – 3	19	1.94
10k ft landing	$1.10 \times 10^7$	0.22	-5.3	6.86	-15 – 3	19	1.92

the ratio of the total chord length with flaps extended over the nominal chord length and  $\delta_f$  is the deflection angle of the flaps. The values for these deflection angles and the flap geometry can be found in Figure 9.2.

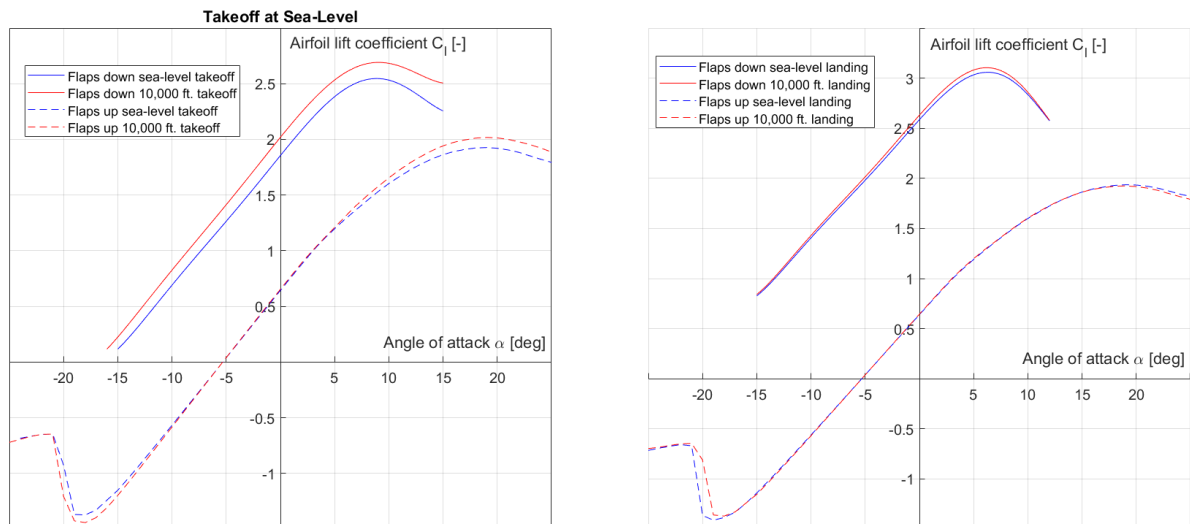
$$\Delta C_l = C_{l\alpha} \alpha_\delta (c'/c) \delta_f \quad (10.1)$$

The lift curve slope does not change as long as the chord of the airfoil does not change. However, as discussed before, the airfoil with flaps down is a factor of  $(c'/c)$  bigger than the flaps up airfoil for single-slotted flaps. The flaps down lift curve slope,  $(C_{l\alpha})_\delta$  is then calculable by multiplying  $C_{l\alpha}$  by  $(c'/c)$ .

The increment in  $C_{l_{max}}$  from single-slotted flaps is given by Equation 10.2, where  $k_1$ ,  $k_2$  and  $k_3$  are all factors that are dependent on the flap geometry and deflection and that correct the base increment in  $C_{l_{max}}$ ,  $(\Delta C_{l_{max}})_{base}$ .

$$\Delta C_{l_{max}} = k_1 k_2 k_3 (\Delta C_{l_{max}})_{base} \quad (10.2)$$

Using these first few parameters, the flaps down airfoil lift curves can be plotted, which are shown in Figure 10.2. The effects of the flaps can clearly be seen from the plots. An increase in  $C_{l_{max}}$  and  $C_{l_0}$  can be seen, as well as a decrease in  $\alpha_{C_{l_{max}}}$ . As the increase in chord length is not large for single-slotted flaps, the effect of the flaps on the lift curve slope is barely noticeable. When comparing Figure 10.2a and Figure 10.2b the difference in lift characteristics for a flap deflection of 20° and 40° can be seen. The landing flap deflection provides a bigger increase in  $C_{l_{max}}$  and  $C_{l_0}$ , which is desired as landing is performed at lower speeds.



(a) Flaps down sea-level and 10,000 ft takeoff airfoil lift curves.

(b) Flaps down sea-level and 10,000 ft landing airfoil lift curves.

Figure 10.2: Lift curves of the flaps down sea-level and 10,000 ft takeoff and landing situations.

### Wing Flaps Up Lift Curve

In order to construct the flaps up lift curves of the aircraft wing, the characteristics of the airfoil have to be converted to a finite wing. To begin with, the wing zero-lift angle of attack can be determined using Equation 10.3, where  $\epsilon_t$  is the wing twist,  $\Delta\alpha_0/\epsilon_t$  is the change in zero lift angle of attack per degree wing twist and  $(\alpha_{0_l})_{at M}/(\alpha_{0_l})_{at M=0.3}$  is a factor that corrects for compressibility effects.

$$\alpha_{0_{L_w}} = [\alpha_{0_l} + (\Delta\alpha_0/\epsilon_t)\epsilon_t] \cdot [(\alpha_{0_l})_{at M}/(\alpha_{0_l})_{at M=0.3}] \quad (10.3)$$

The lift curve slope of a finite wing,  $C_{L\alpha_w}$  is given by Equation 10.4. Here  $k$  is equal to  $C_{l\alpha}/2\pi$  and  $\beta$  is the compressibility factor, which is given by Equation 10.5.

$$C_{L\alpha_w} = \frac{2\pi A}{2 + \left( \frac{A^2 \beta^2}{k^2(1 + \tan \Lambda_{c/2}) + 4} \right)^{1/2}} \quad (10.4)$$

$$\beta = \sqrt{1 - M^2} \quad (10.5)$$

The last point on the lift curve that is needed in order for it to be constructed is the point at which the maximum lift coefficient occurs. This point can be identified by calculating the magnitude of the maximum lift coefficient and the angle of attack at which it is achieved.

The maximum lift coefficient of the finite wing,  $C_{L_{max_w}}$ , can be calculated from the section lift coefficient at which the wing angle of attack is equal to  $(\alpha_{C_{L_{max}}})_w$ . This angle is found by matching the spanwise distribution of the section lift coefficient with the lift distribution from Equation 9.2 by varying the angle of attack. At the point at which the two curves are tangential, the angle of attack is equal to  $(\alpha_{C_{L_{max}}})_w$  and the section lift coefficient is denoted as  $C_{l_{w_{stall}}}$ . From this,  $C_{L_{max_w}}$  can be calculated using Equation 10.6, where  $\eta$  is the spanwise location on the wing as a fraction of the total span.

$$C_{L_{max_w}} = \frac{1}{S} \int_0^{1.0} bc C_{l_{w_{stall}}} d\eta \quad (10.6)$$

For this stage of the analysis it is assumed that the linear range of the wing lift curve is the same as that of the airfoil, i.e.  $\alpha_w^* = \alpha^*$ . The wing lift curves have been plotted in Figure 10.3. It can be seen from Figure 10.3a that the  $C_{L\alpha_w}$  for the cruise phase is higher than for the loiter and combat phase. Again, this is due to the higher Mach number during cruise. The flaps up takeoff and landing curves are similar for both the sea-level and the 10,000 ft situation. This can be explained by the fact that the Mach and Reynold's numbers are similar for all situations.

### Flaps Down Wing Lift Curve

For the takeoff and landing situations, the changing lift characteristics as a result of the flap deflection have to be added for a finite wing as well. Similar procedures as for the flaps down airfoil characteristics can be performed. To begin with, the increment in lift coefficient for the linear region of the lift curve of the finite wing can be determined using Equation 10.7. In this relation  $K_b$  is a factor that is dependent on the fraction of the flap span over the total wing span. Furthermore,  $(\alpha_{\delta_{c_L}}/\alpha_{\delta_{c_l}})$  is the ratio of the two-dimensional flap effectiveness over the three-dimensional flap effectiveness.

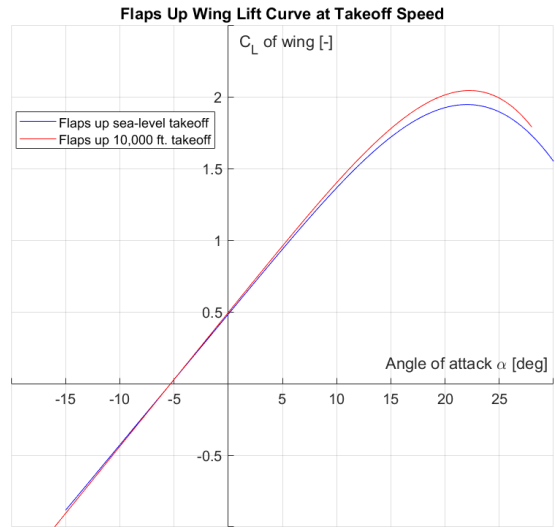
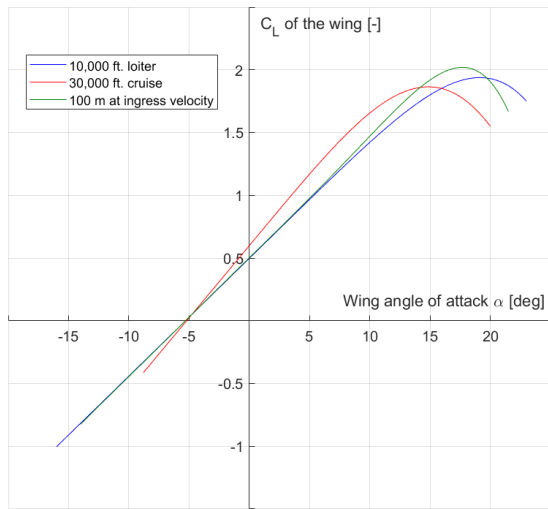
$$\Delta C_{L_w} = K_b \Delta C_{l_w} \frac{C_{L\alpha_w}}{C_{l\alpha}} (\alpha_{\delta_{c_L}}/\alpha_{\delta_{c_l}}) \quad (10.7)$$

As the single-slotted flap translates aft when it is deflected, the lift curve slope for the flaps down wing can not be approximated using the airfoil method with substitution of the finite wing characteristics. Rather, Equation 10.8 has to be used. The only parameter to be introduced here is the flapped wing area,  $S_{w_f}$ , which is defined as the wing area of the flap span.

$$(C_{L\alpha_w})_{\delta} = C_{L\alpha_w} \left[ 1 + (c'/c - 1) \frac{S_{w_f}}{S} \right] \quad (10.8)$$

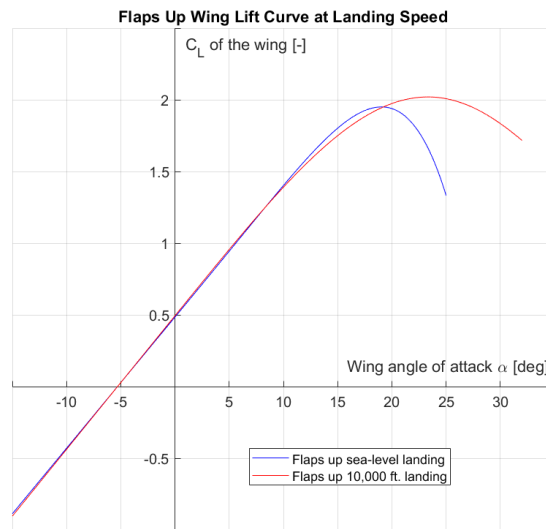
Lastly, the maximum lift coefficient of the wing has to be analysed. This can be done readily using Equation 10.9, in which  $K_{\Lambda}$  is a correction factor that accounts for the geometry of the wing planform.

$$\Delta C_{L_{max_w}} = \Delta C_{l_{max}} \frac{S_{w_f}}{S} K_{\Lambda} \quad (10.9)$$



(a) Flaps up wing lift curves for loiter, cruise and combat.

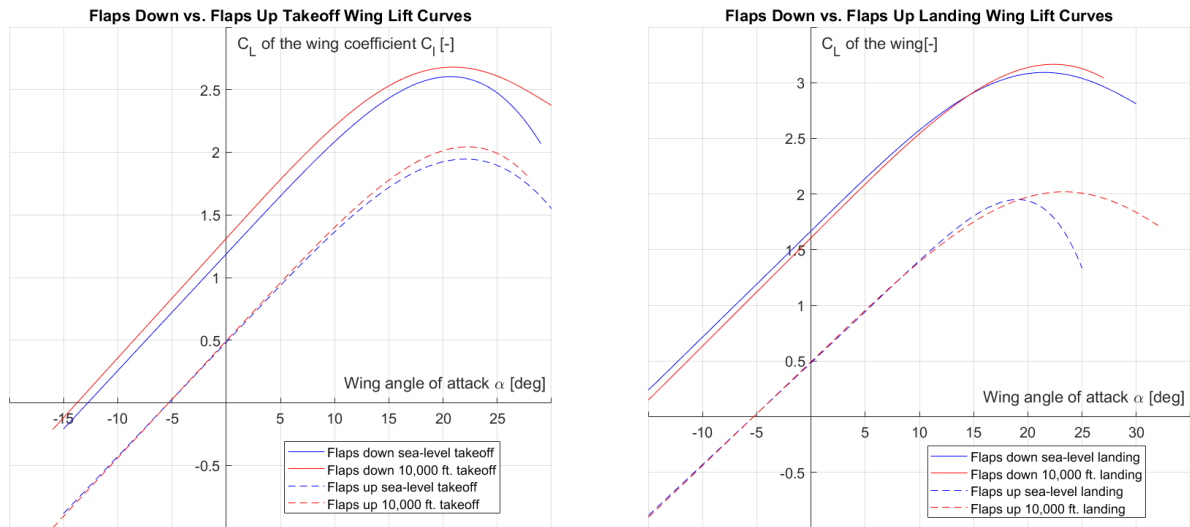
(b) Flaps up wing lift curves for sea-level and 10,000 ft takeoff.



(c) Flaps up wing lift curves for sea-level and 10,000 ft landing.

Figure 10.3: Flaps up wing lift curves for all seven flight situations.

The flaps down wing lift curves have been plotted in [Figure 10.4](#). Again, an increase in  $C_{L_{0w}}$  and  $C_{L_{\max w}}$  is clearly visible, with the landing situation having the bigger increase.



(a) Effect of the flaps on the wing lift for sea-level and 10,000 ft. takeoff.

(b) Effect of the flaps on the wing lift for sea-level and 10,000 ft. landing

Figure 10.4: Flaps up vs. flaps down for takeoff and landing situations.

### Flaps Up Aircraft Lift Curve

To finalise the lift characteristics the lift curve for the entire aircraft has to be constructed. In order to do this, the aircraft is considered to be built up from two parts only: a wing interacting with the fuselage it is mounted on and an empennage.

As before, the flaps up characteristics will be determined first. The zero-lift angle of attack of the total aircraft can be determined using [Equation 10.10](#). Here  $C_{L_0}$  is the lift coefficient at zero angle of attack and  $C_{L_\alpha}$  is the lift curve slope of the entire airplane. These two quantities have to be analysed first.

$$\alpha_{0L} = \frac{-C_{L_0}}{C_{L_\alpha}} \quad (10.10)$$

$C_{L_0}$  can be calculated using [Equation 10.11](#), also introducing new unknowns, namely the lift coefficient at zero angle of attack of the the wing-fuselage assembly,  $C_{L_{0wf}}$ , the lift curve slope of the horizontal tail,  $C_{L_{\alpha h}}$  and the dynamic pressure ratio of that of the horizontal tail over that of the wing,  $\eta_h$ . The knowns in this equation are the horizontal tail area  $S_h$ , the horizontal tail incidence angle  $i_h$ , which can both be retrieved from [section 13.4](#) and the tail downwash angle at zero angle of attack  $\epsilon_{0h}$ , which can be approximated to be equal to zero for flaps up configuration at this stage of the design.

$$C_{L_0} = C_{L_{0wf}} + C_{L_{\alpha h}} \eta_h \frac{S_h}{S} (i_h - \epsilon_{0h}) \quad (10.11)$$

Now,  $C_{L_{0wf}}$  is given by [Equation 10.12](#). In this relation  $C_{L_{\alpha wf}}$  is the wing-fuselage lift curve slope, which is calculable by multiplying the wing lift curve slope by the wing-fuselage interference factor  $K_{wf}$ . In turn, this factor is a function of the geometry of both the wing and the fuselage.  $C_{L_{\alpha h}}$  can be calculated using [Equation 10.4](#), using the correct substitutions for the tail geometry from [section 13.4](#).

$$C_{L_{0wf}} = (i_w - \alpha_{0Lw}) C_{L_{\alpha wf}} \quad (10.12)$$

The last parameter to be analysed in order to calculate the  $C_{L_0}$  is the dynamic pressure ratio. [Equation 10.13](#) presents an approximation which is valid for propeller aircraft. With the three parameters quantified,  $C_{L_0}$  can be calculated.

$$\eta_h = 1 + \frac{(S_h)_{\text{slip}}}{S_h} \frac{2200P_{\text{av}}}{qV_{\infty}^2 \pi D_{\text{prop}}^2} \quad (10.13)$$

Using the newly determined  $C_{L_{\alpha_{wf}}}$ ,  $C_{L_{\alpha_h}}$  and  $\eta_h$ , the lift curve slope of the total airplane can be calculated as well, as can be seen in Equation 10.14. One new parameter can be seen here, being the downwash gradient of the horizontal tail  $d\epsilon/d\alpha$ , which in turn can be calculated using Equation 10.15. In this equation  $K_A$  is a factor that depends on the aspect ratio,  $K_\lambda$  depends on the taper ratio and  $K_h$  depends on the height that the horizontal is installed at.

$$C_{L_\alpha} = C_{L_{\alpha_{wf}}} + C_{L_{\alpha_h}} \eta_h \frac{S_h}{S} \left( 1 - \frac{d\epsilon}{d\alpha} \right) \quad (10.14)$$

$$\frac{d\epsilon}{d\alpha} = 4.44 [K_A K_\lambda K_h (\cos \Lambda_{c/4})^{1/2}]^{1.19} \frac{(C_{L_{\alpha_h}})_{\text{at M}}}{(C_{L_{\alpha_h}})_{\text{at M=0}}} \quad (10.15)$$

The last parameter to be determined for the construction of the flaps up aircraft lift curve is the maximum lift coefficient. Equation 10.16 is given for  $C_{L_{\text{max}}}$ . It can be seen that all parameters have previously been determined. Thus, noting that the linear range of the aircraft lift coefficient is given by  $\alpha_{\text{aircraft}}^* = \alpha^* - i_w$ , the flaps up lift curve can be constructed.

$$C_{L_{\text{max}}} = C_{L_{\text{max}_w}} + C_{L_{\alpha_h}} \frac{S_h}{S} \left[ \alpha_{C_{L_{\text{max}}}} \left( 1 - \frac{d\epsilon}{d\alpha} - \epsilon_{0h} \right) + i_h \right] \quad (10.16)$$

The final aircraft lift curves can be constructed using all the acquired parameters. They are depicted in Figure 10.5 The observations on the wing lift curves apply for the total aircraft as well.

### Flaps Down Aircraft Lift Curve

The last lift curve construction to be done, is that of the aircraft with flaps deployed. As before,  $\Delta C_L$ ,  $(C_{L_\alpha})_\delta$  and  $\Delta C_{L_{\text{max}}}$  are analysed.

Equation 10.17 is given for the increment in lift coefficient for the linear part. In this equation  $k_{cw}$  is the canard-wing interference factor, which is equal to 1 for aircraft without canards, and  $\Delta\epsilon_f$  is the increment in tail downwash due to wing flap deflection, which is dependent on the flap deflection angle.

$$\Delta C_L = k_{cw} \Delta C_{L_w} + k_{wh} \frac{S_h}{S} \Delta C_{L_h} - C_{L_{\alpha_h}} \eta_h \frac{S_h}{S} \Delta\epsilon_f \quad (10.17)$$

The lift curve slope of the aircraft with flaps deployed is given by Equation 10.18, where  $\left(\frac{d\epsilon}{d\alpha}\right)_\delta$  is the downwash gradient of the horizontal tail, which is calculated in a manner analog to Equation 10.15.

$$(C_{L_\alpha})_\delta = K_{wf} (C_{L_{\alpha_w}})_\delta + C_{L_{\alpha_h}} \eta_h \frac{S_h}{S} \left[ 1 - \left(\frac{d\epsilon}{d\alpha}\right)_\delta \right] \quad (10.18)$$

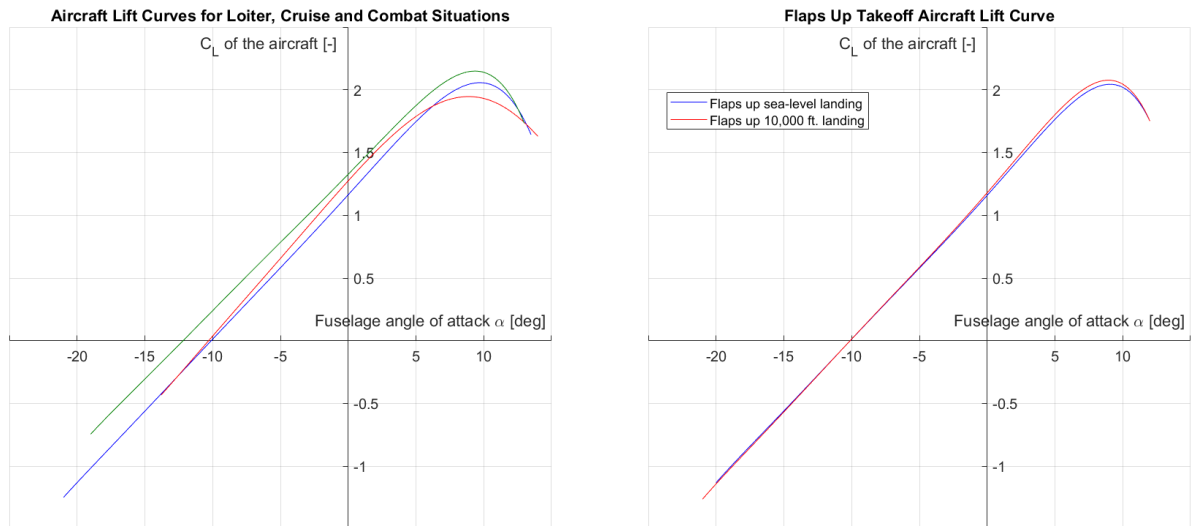
To conclude the lift characteristics, the increment in maximum lift coefficient for the aircraft with flaps down is calculable using Equation 10.19. Now all the parameters needed to construct the flaps down aircraft lift curve have been acquired

$$\Delta C_{L_{\text{max}}} = k_{cw} \Delta C_{L_{\text{max}_w}} + \frac{S_h}{S} C_{L_{\alpha_h}} \left[ \left( 1 - \frac{d\epsilon}{d\alpha} \right) + i_h - \Delta\epsilon_f \right] \quad (10.19)$$

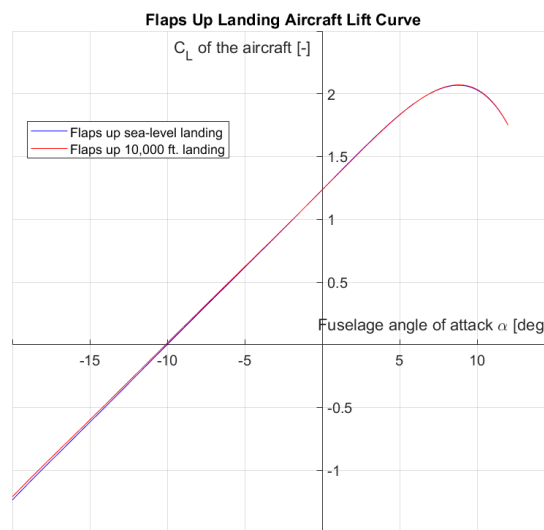
### Verification & Validation

In order to verify the lift characteristics calculations, the unit tests as described in section 4.5 have been applied. Inputting zeros and increasing or decreasing certain parameters gave expected results.

For the validation, an analysis on the airfoil lift curve with a flap deflection of 20° at sea-level, the wing lift curve at loiter conditions and the wing lift curve with a flap deflection of 20° at sea-level has been done. Unfortunately, the hardware that the project has been provided with, does not allow for a full aircraft analysis, which will therefore not be shown in this section.

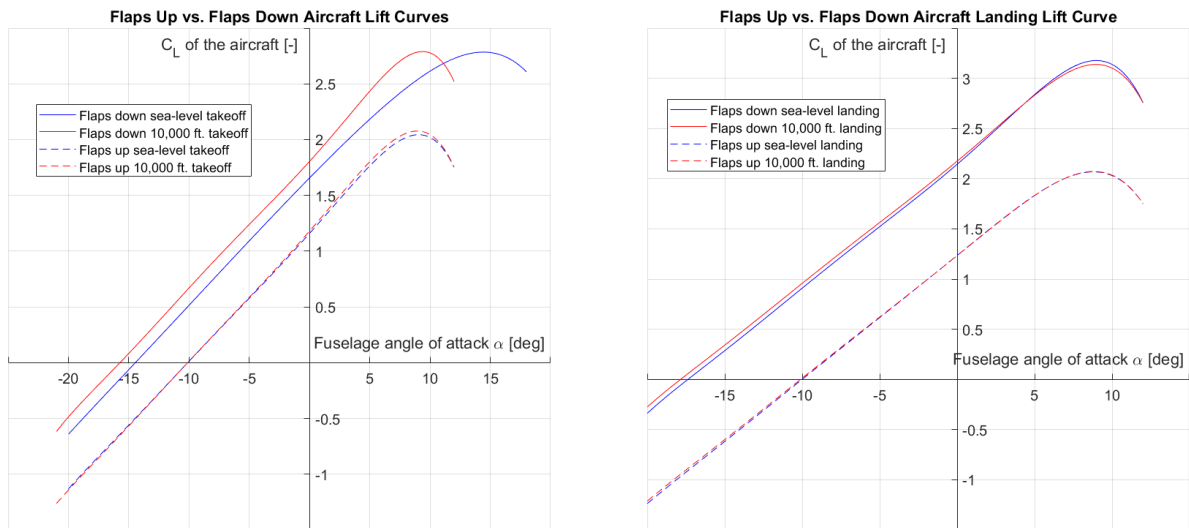


(a) Flaps up aircraft lift curves for loiter, cruise and combat. (b) Flaps up aircraft lift curves for sea-level and 10,000 ft takeoff.



(c) Flaps up aircraft lift curves for sea-level and 10,000 ft landing.

Figure 10.5: Flaps up aircraft lift curves for all seven flight situations.



(a) Effect of the flaps on the aircraft lift for sea-level and 10,000 ft. takeoff.

(b) Effect of the flaps on the aircraft lift for sea-level and 10,000 ft. takeoff.

In [Figure 10.7a](#) it can be seen that the model shows similar behaviour to the data outputted by XFLR5. The slope of the linear part of the curve is almost identical and the  $C_{L_{max}}$  is 16% off. It should be noted that the model uses the fact that the A-24 Barracuda will have single-slotted flaps, while XFLR5 is only able to analyse plain flaps. This also explains the dent in the XFLR5 data curve, as for plain flaps at certain angles of attacks stagnation points occur, which causes a sudden decrease in lift. This has also been verified by inspecting a visual representation of the airflow.

The model data in [Figure 10.7b](#) is almost identical to the validation data. The lift curve slope is approximately the same and the maximum lift coefficient of the model is a mere 2.7% bigger than that of the validation data.

Lastly, the model curve in [Figure 10.7c](#) has the same  $C_{L_{0w}}$  and similar  $C_{L_{maxw}}$  when compared to the XFLR5 data. Even though the  $C_{L_{\alpha w}}$  is different for the XFLR5 and model data, the results of this validation are deemed positive and in turn the model is deemed validated.

## 10.2. Drag Breakdown

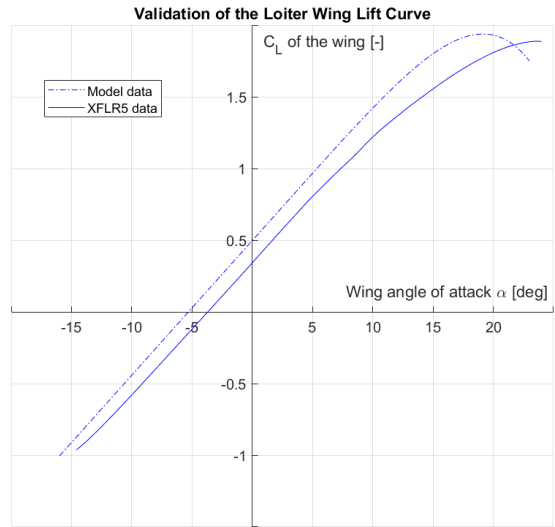
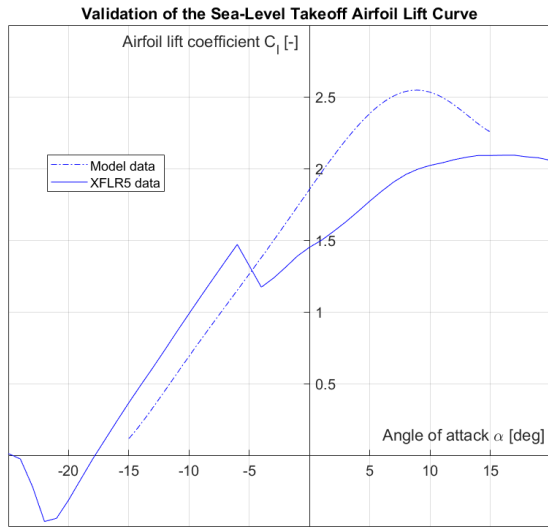
The drag of an aircraft is built up by the drag contribution of its individual cases. In this section the drag will be broken down for all its major components and each component will be analysed. In cruise and loiter conditions the drag is built up by the contributions from the wing, the fuselage, the empennage, the engine nacelles, the canopy, the armament, the canoe of the gun and miscellaneous components. In takeoff and landing configurations both the flaps and the landing gear have a major contribution to the drag and in combat the deployed gun causes an increment in drag. These situations will be analysed as well. Methods from Airplane Design Part IV [18] are used.

### Wing Drag

To begin with, the wing drag at subsonic speeds is given by the sum of the parasitic wing drag and the induced wing drag. The parasitic wing drag can be calculated using [Equation 10.20](#), where  $R_{wf}$  is the wing-fuselage interference factor, which is dependent on the Reynold's number over the fuselage,  $R_{LS}$  is the lifting surface correction factor and the airfoil thickness location parameter  $L'$ , which are both dependent on the location of the maximum airfoil thickness and the freestream Mach number and lastly the skin friction coefficient of the wing,  $C_{f_w}$ , which is dependent on the Reynold's number over the wing.  $S_{wet_w}$  is the area of the wing that is wetted by the flow around it.

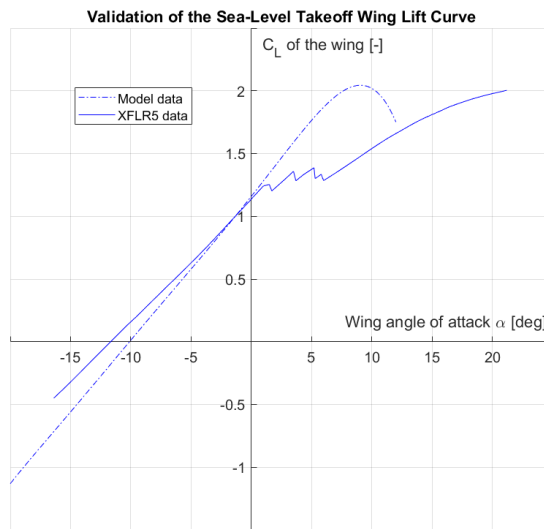
$$C_{D_{0w}} = R_{wf}R_{LS}C_{f_w}[1 + L'(t/c) + 100(t/c)^4] \frac{S_{wet_w}}{S} \quad (10.20)$$

The wing drag due to lift is related to the lift coefficient of the wing from [section 10.1](#) via [Equation 10.21](#).



(a) Flaps down sea-level takeoff lift curves for the airfoil. The model is compared to validation data.

(b) Flaps up loiter lift curves for the wing. The model is compared to validation data.



(c) Flaps down sea-level takeoff lift curves for the wing. The model is compared to validation data.

Figure 10.7: Theoretical wing lift curves vs. XFLR5 data.

Here  $v$  and  $w$  are both parameters that account for the additional drag due to the wing tip twist. The Oswald's efficiency factor in this relation can be approximated for each flight situation using Equation 10.22, where  $R$  is the leading edge suction parameter, which is dependent on the leading edge Reynold's number and the geometry of the wing.

$$C_{D_{L_w}} = \frac{C_{L_w}^2}{\pi A e} + 2\pi C_{L_w} \epsilon_t v + 4\pi^2 \epsilon_t^2 w \quad (10.21)$$

$$e = 1.1 \frac{(C_{L_{\alpha_w}}/A)}{R(C_{L_{\alpha_w}}/A) + (1-R)\pi} \quad (10.22)$$

### Fuselage Drag

Similarly to the wing drag, the fuselage drag has an induced drag component and a zero-lift drag component. The zero-lift drag of the fuselage is given by Equation 10.23. The new parameters introduced are the skin friction coefficient of the fuselage,  $C_{f_{fus}}$  and  $S_{wet_{fus}}$ , which are both defined in a similar manner as for those of the wing. Furthermore, the fuselage base drag coefficient,  $C_{D_{b_{fus}}}$ , contributes to  $C_{D_{0_{fus}}}$  as well. The fuselage base drag is dependent on the diameter of the fuselage base  $d_b$  and is calculable using Equation 10.24. The zero-lift coefficient of the fuselage without base contribution,  $C_{D_{0_{fus-base}}}$  can be calculated using Equation 10.23, with  $C_{D_{b_{fus}}}$  left out.

$$C_{D_{0_{fus}}} = R_{wf} C_{f_{fus}} \left[ 1 + \frac{60}{(l_f/d_f)^3} + 0.0025 \frac{l_f}{d_f} \right] \frac{S_{wet_{fus}}}{S} + C_{D_{b_{fus}}} \quad (10.23)$$

$$C_{D_{b_{fus}}} = \frac{0.029(d_b/d_f)^3}{\left[ C_{D_{0_{fus-base}}} (S/S_{fus}) \right]^{1/2}} \frac{S_{fus}}{S} \quad (10.24)$$

The induced drag of the fuselage can be approximated by Equation 10.25, in which  $\alpha$  is the aircraft angle of attack,  $S_{b_{fus}}$  is the fuselage base area and  $\eta$  is the ratio of drag of a finite cylinder over the drag of an infinite cylinder, which is dependent on the fineness ratio of the fuselage, defined as  $l_f/d_f$ . Moreover,  $C_{d_c}$  is the experimental steady state cross-flow drag coefficient for a circular cylinder and  $S_{plf_{fus}}$  is the area of the fuselage planform.

$$C_{D_{L_{fus}}} = 2\alpha^2 \frac{S_{b_{fus}}}{S} + \eta C_{d_c} \alpha^3 \frac{S_{plf_{fus}}}{S} \quad (10.25)$$

### Empennage Drag

Like the wing and fuselage drag components, the empennage drag can be split up in the parasitic drag and the induced drag. The parasitic drag can be calculated using Equation 10.20, which has been used for the wing as well. The right substitutions have to be made however for the Reynold's number range and geometry of the empennage.

The empennage drag due to the lift can be approximated using Equation 10.26. The Oswald's efficiency factor of the horizontal tail can be calculated with Equation 10.22 with the appropriate substitutions for the horizontal tail geometry.

$$C_{D_{L_{emp}}} = \frac{C_{L_h}^2}{\pi A_{he_h}} \frac{S_h}{S} \quad (10.26)$$

### Engine Nacelle Drag

The nacelle induced and zero-lift drag is estimated using the same equations as for the fuselage drag. This is because of the fact that nacelles are assumed to have the same shape as "small" fuselages.

As the engine nacelles are installed on top of the wings, the interference drag between the nacelles and the wings have to be accounted for. This can be done by applying Equation 10.27 for propeller aircraft. Here  $c_n$  is the chord length at the spanwise location at which the nacelle is installed,  $b_n$  is the diameter of the nacelle,  $\Delta C_{l_1}$  is equal to 0.2 for nacelles on top of the wing and  $\Delta C_{l_2}$  is a function of the nacelle incidence angle.

$$C_{D_{n_{int}}} = 0.036 \frac{c_n b_n}{S} (\Delta C_{l_1} + \Delta C_{l_2})^2 \quad (10.27)$$

### Flap Drag

Flaps do not only provide an increment of lift for the wing, they also increase drag. The flap drag can be divided into the profile drag increment, the induced drag increment and the interference drag increment.

Firstly, the profile drag increment can be calculated using Equation 10.28, in which  $\Delta C_{d_{p\Lambda_{c/4}=0}}$  is the airfoil drag increment for zero quarter-chord sweep, which has a magnitude that depends on the type of flaps, the flap-chord-over-total-chord ratio and the flap deflection angle.

$$\Delta C_{D_{\text{prof flap}}} = \Delta C_{d_{p\Lambda_{c/4}=0}} \cos \Lambda_{c/4} \frac{S_{wf}}{S} \quad (10.28)$$

The induced drag increment is dependent on the flap geometry and can be approximated with Equation 10.29, where  $K$  follows from the flap size.

$$\Delta C_{D_{i\text{ flap}}} = K^2 (\Delta C_{L\text{ flap}})^2 \cos c/4 \quad (10.29)$$

Lastly, the increment in interference drag coefficient is given by multiplying the increment in profile drag coefficient by a constant  $K_{\text{int}}$  which is different for each type of flap.

### Landing Gear Drag

In order to calculate the drag that is introduced by the the landing gear the contribution of both the nose gear and the main gear have to be summed. For each individual gear the drag coefficient has a zero-lift component and a component that varies with the lift coefficient. These two components are summed in Equation 10.30.  $C_{D_{\text{gear } C_L=0}}$  is the zero-lift gear drag coefficient, which can be taken from historical data,  $p$  is a factor that is dependent on the shape of the gear and accounts for the induced gear drag and  $S_{\text{gear}}$  is the reference gear area.

$$C_{D_{\text{gear}}} = \sum_i \left\{ \left[ \left( C_{D_{\text{gear } C_L=0}} \right)_i + p_i C_L \right] \frac{(S_{\text{gear}})_i}{S} \right\} \quad (10.30)$$

### Canopy Drag

The canopy drag coefficient can readily be calculated using Equation 10.31, where  $\Delta C_{D_{\text{can}}}$  can be calculated from the geometry. In this design the choice was made to minimise this drag by choosing the most aerodynamically beneficial shape. Furthermore  $S_{\text{can}}$  is defined to be the maximum frontal area of the canopy.

$$C_{D_{\text{can}}} = (\Delta C_{D_{\text{can}}}) \frac{S_{\text{can}}}{S} \quad (10.31)$$

### Stores Drag

As the aircraft carries external armament, the armament causes an increase in drag coefficient as well. The drag coefficient of each individual store can be approximated using the method described for the fuselage and the nacelles as the stores can be simplified to resemble "small" fuselages as well. In order to calculate the total drag due to the stores, the individual store drag coefficient have to be multiplied by the store interference factor,  $K_{\text{store}}$ , which is equal to 1.3 for external stores.

For this design analyses it is assumed that the aircraft is carrying a total of six AGM-65 Maverick missiles on the wings and three Mk83 bombs on the bottom of the fuselage.

The stores are assumed to be close to the wings and fuselage and it is therefore assumed that the drag due to the pylons is negligible.

### Canoe Drag

In order to approximate the drag coefficient of the canoe, it is assumed that it can be simplified to have the same shape as the canopy. The canoe drag will thus be calculated using the same methods as for the canopy.

### Gun Drag

The drag of the gun during the combat phase, is approximated using the same methods as for the landing gear. It is assumed it behaves as a nose gear shaped as a long solid rod.

## Results

The results of the drag build-up can be seen in Figure 10.8. Figure 10.8a shows that the parasitic drag of the combat phase is higher than those of the loiter and cruise phases. This is due to the gun that is deployed for the combat phase only. Compared to the loiter phase, the cruise phase has a bigger zero-lift drag coefficient. This is due to the fact that the cruise phase is performed at a considerably higher Reynold's number, therefore increasing the skin friction and in turn increasing the drag.

The drag polars for sea-level and 10.000 ft takeoff are drawn in Figure 10.8b. It can be seen that the contribution of the landing gear and the deployed flaps causes an increase of 250 % in  $C_{D_0}$  when compared to the loiter drag polar. When comparing the sea-level and the 10,000 ft takeoff, it can be seen that both drag polars are alike. This can be contributed to the fact that both situations have similar Reynold's numbers.

Lastly, the drag polars for the landing are portrayed in Figure 10.8c. Again, an increase in parasitic drag can be seen due to the flaps. The landing flap deflection angle causes an increase in  $C_{D_0}$  for both sea-level and 10,000 ft landing.

## Desired Lift Coefficient

Using the drag polars and the lift curves established above,  $C_L/C_D$  and  $C_L^{3/2}/C_D$  curves can be drawn. For the cruise phase it is desired to fly at the maximum lift-over-drag ratio and for the loiter phase  $C_L^{3/2}/C_D$  should be maximised. The resulting  $C_L/C_D$  for cruise and  $C_L^{3/2}/C_D$  curves are plotted in Figure 10.9. The maximum  $C_L/C_D$  is equal to 15.68, which occurs at a  $C_L$  of 0.83, which is therefore the desired lift coefficient during cruise. The maximum  $C_L^{3/2}/C_D$  is equal to 16.38, which occurs at a  $C_L$  of 2.03. Theoretically, this would be the desired  $C_L$  for the loiter phase. When doing a sanity check, however, this lift coefficient is deemed unfeasible for the entire loiter phase. In order to properly size the design lift coefficient, further investigation has to be done.

## Verification & Validation

Since the drag build-up method used is based on well-established formulas the only verification necessary according to section 4.5 is verification of the actual software written for calculations. Thus, the code was verified through performing consistency and continuity tests. During testing, the code performed as expected and is henceforth considered verified.

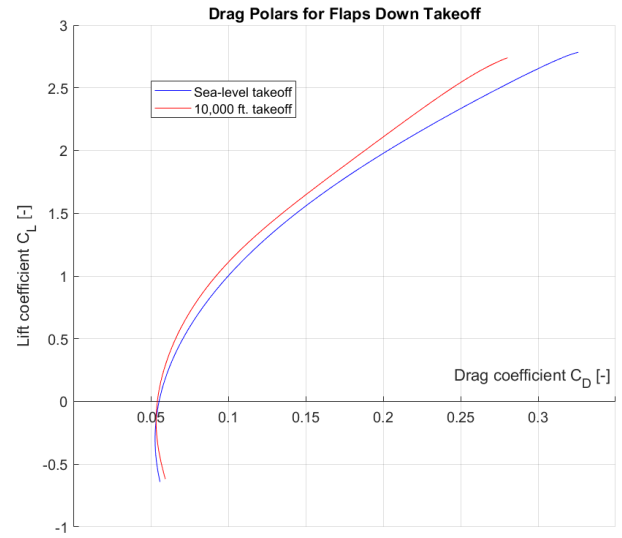
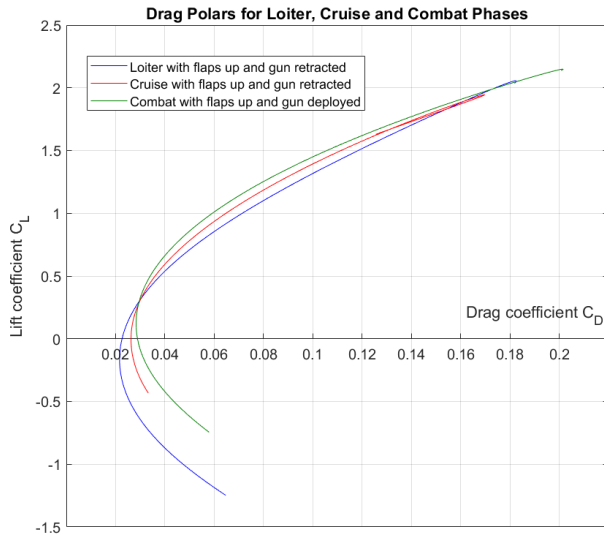
## 10.3. Moment characteristics

In this section an analysis will be done to estimate the pitching moment coefficients. This analysis will first be done for the airfoil, then the wing and finally the aircraft. The result of the analysis will be the relationship between the lift and moment coefficient, following the method of Roskam [18]. The  $C_L - C_m$  curve will only be determined for the linear region of the  $C_L - \alpha$  curve, because there is no method to accurately estimate the pitch break of the curve. The method of Roskam for constructing the curve will be the same for the airfoil, wing and aircraft and is shown below. The analysis will be done for loiter, cruise and landing and take-off at sea level and 10 000 ft with flaps retracted and for take-off and landing with flaps deployed.

1. Determine the zero-lift moment coefficient,  $C_{m_0}$ .
2. Determine the reference point  $\bar{x}_{ref}$  and the aerodynamic centre  $\bar{x}_{ac}$ . With this the slope  $\frac{dC_L}{dC_m}$  can be determined as well.
3. Determine the moment coefficient  $C_m^*$  at the last lift coefficient  $C_L^*$  of the linear range of the lift curve.
4. Determine the increment of the moment coefficient when deploying flaps,  $\Delta C_m$ .
5. Determine the flapped moment coefficient  $C_{m_{flapped}}^*$  at the last lift coefficient,  $C_{L_{flapped}}^*$  of the linear range of the lift curve.
6. Construct the curve.

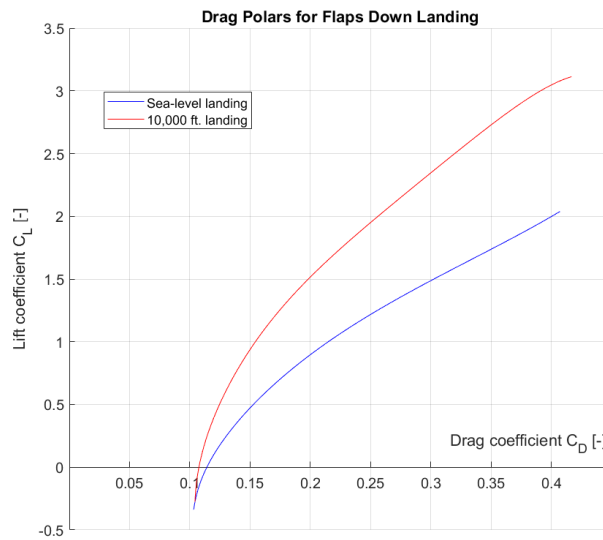
### Airfoil Pitching Moment Coefficient

To determine the variation of the airfoil pitching moment when varying the airfoil lift coefficient, a reference point should be determined first. For the airfoil analysis this will be done at the leading edge. Next is the



(a) The drag polars for the loiter, cruise and combat phases.

(b) Drag polars for sea-level and 10,000 ft takeoff.



(c)

Figure 10.8: Drag polars for sea-level and 10,000 ft landing.

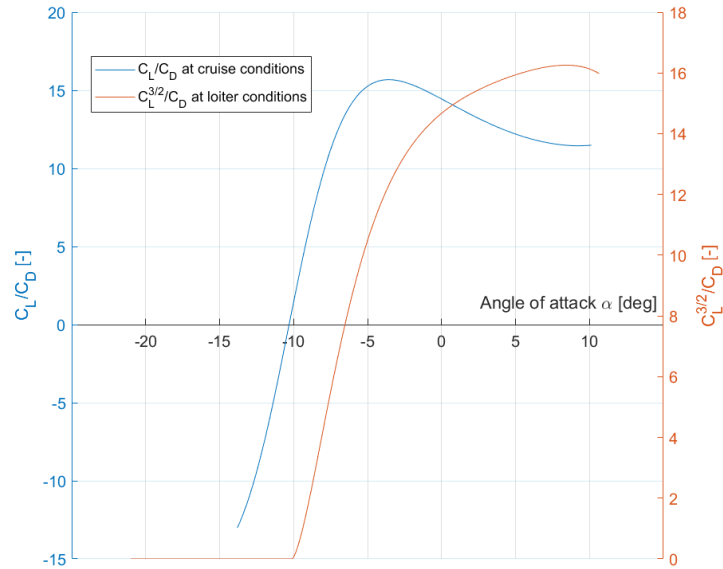


Figure 10.9:  $C_L/C_D - \alpha$  for the cruise phase and  $C_L^{3/2}/C_D - \alpha$  for the loiter phase.

location of the aerodynamic centre. This is assumed to be at 25% of the chord, which is a valid assumption.

With Equation 10.32 the airfoil pitching moment coefficient  $c_m$  can be determined.  $c_{m_0}$  is the moment coefficient at zero lift and is determined in the analysis of the airfoil in the lift characteristics section. Using this equation, the slope of the  $c_m$  vs.  $c_l$  can be determined as well, as shown in Equation 10.33, where  $\bar{x}_{\text{ref}}$  and  $\bar{x}_{ac}$  are the locations as fraction of the chord.

$$c_m = c_{m_0} + c_l \frac{x_{\text{ref}} - x_{ac}}{c} \quad (10.32)$$

$$\frac{dc_l}{dc_m} = \frac{1}{\bar{x}_{\text{ref}} - \bar{x}_{ac}} \quad (10.33)$$

Next step is to determine  $c_l^*$ , the lift coefficient at which the linear relation between  $c_l$  and  $\alpha$  ends. This is done with Equation 10.34, where  $\alpha^*$ ,  $\alpha_{0_l}$  and  $c_{l_\alpha}$  are taken from Table 10.1.

$$c_l^* = c_{l_\alpha} (\alpha^* - \alpha_{0_l}) \quad (10.34)$$

### Flaps deployed

With the equations above the curve can be made with flaps up. Now the effect of deploying the flaps will be considered. A change in the camber of the airfoil (so flaps deployed) does not influence the slope of the curve and therefore the slope will be the same. First the increment in  $c_m$  will be determined, using Equation 10.35, where  $\frac{x_{cp}}{c}$  is the location of the centre of pressure on the chord and  $\frac{c'}{c}$  is the increment of the chord length due to the flaps.

$$\Delta c_m = \Delta c_l \left( \frac{x_{\text{ref}}}{c} - \frac{x_{cp}}{c'} \frac{c'}{c} \right) \quad (10.35)$$

The flaps deployed curve will shift with the value of  $\Delta c_m$ . With the same equations as flaps down,  $c_l^*$  can again be determined to construct the curve. The curve is shown in Figure 10.10. As can be seen, the curves with flaps retracted are all almost the same, except for a slight shift for cruise conditions. This shift is caused by higher speed at which the aircraft flies. This means that  $c_{m_0}$  becomes more negative and  $c_{l_\alpha}$  increases, which in turn increases  $C_l^*$  as well. Also the curves with flaps deployed differ from each other, which is obvious, since during landing the flap deflection angles are higher compared to take-off flap deflection. Therefore, during landing a larger (more negative)  $\Delta c_m$  occurs and increases the pitching down moment.

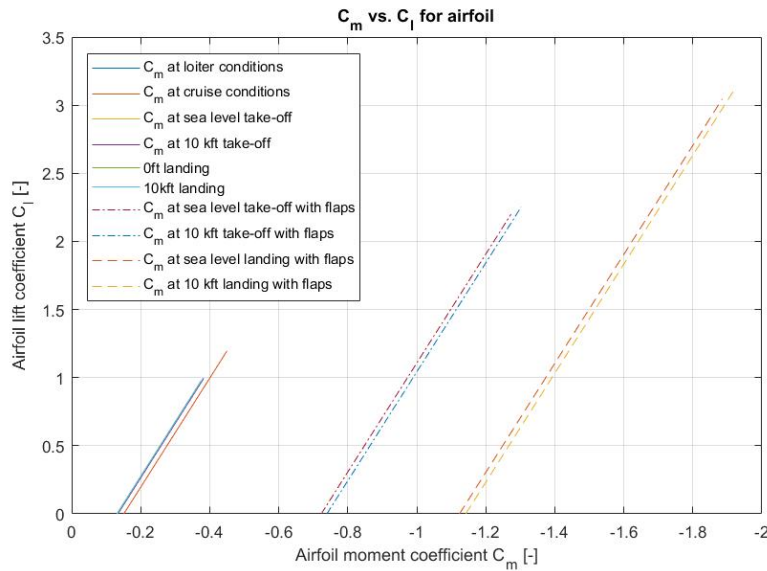


Figure 10.10: Wing moment coefficient vs. wing lift coefficient at the leading edge of the airfoil.

### Wing Pitching Moment Coefficient

In order to analyse the wing for the moment coefficient, the wing must be reduced to one chord, which is the mean aerodynamic chord (MAC). The reference point of the calculations will be the leading edge of the MAC. The next step is to calculate  $C_{m_{0w}}$  and is done with Equation 10.36.

$$C_{m_{0w}} = \frac{AR}{AR + 2} \frac{C_{m_{0root}} + C_{m_{0tip}}}{2} \quad (10.36)$$

The slope of the curve can again be calculated and is done using Equation 10.37.  $n_{ref}$  is the location of the moment reference centre relative to the wing apex and  $n_{ac}$  is the location of the wing aerodynamic centre relative to the wing apex.

$$\frac{dC_L}{dC_{m_w}} = \frac{1}{\frac{n_{ref} - n_{ac}}{c_{root}} \frac{c_{root}}{MAC}} \quad (10.37)$$

Using Equation 10.34 again, but then substituted for values of the wing,  $C_{L_w}^*$  can be calculated and finally  $C_{m_w}^*$  as well at that lift coefficient, which makes the  $C_{L_w} - C_{m_w}$  curve complete.

### Flaps deployed

With the wing lift coefficient with flaps deployed  $C_{L_w \text{flapped}}$  obtained from the lift analysis,  $\Delta C_{m_w}$  can be calculated using Equation 10.38.  $K_p$  is the flap span factor and  $\Delta C_{L_w}$  is the lift increment due to the flaps for a reference wing.

$$\Delta C_{m_w} = (\bar{x}_{ref} - 0.25) C_{L_w \text{flapped}} + K_p \left[ \frac{\Delta C'_m}{\Delta C_{L_{refw}}} C_{L_{refw}} \left( \frac{c'}{c} \right)^2 \right] - K_p \left[ 0.25 C_{L_w} \left( \left( \frac{c'}{c} \right)^2 - \frac{c'}{c} \right) \right] + K_p C_{m_w} \left[ \left( \frac{c'}{c} \right)^2 - 1 \right] \quad (10.38)$$

Again, using  $C_{L_w}^*$ , the last angle of the linear range of the lift curve can be used to determine the last point of the curve with the same method as in the airfoil moment coefficients. The final curve can be found in Figure 10.11. The same conclusion as the airfoil curve can be drawn.

### Aircraft Pitching Moment Coefficient

The analysis of the aircraft moment coefficient is a bit more elaborate than the previous ones. This is because fuselage and the tail has to be added. Therefore,  $C_{m_0}$  is as follows, where  $k$  is a factor to account for the Mach number at the specific condition.

$$C_{m_0} = C_{m_{0h}} + k(C_{m_{0w}} + C_{m_{0f}}) \quad (10.39)$$

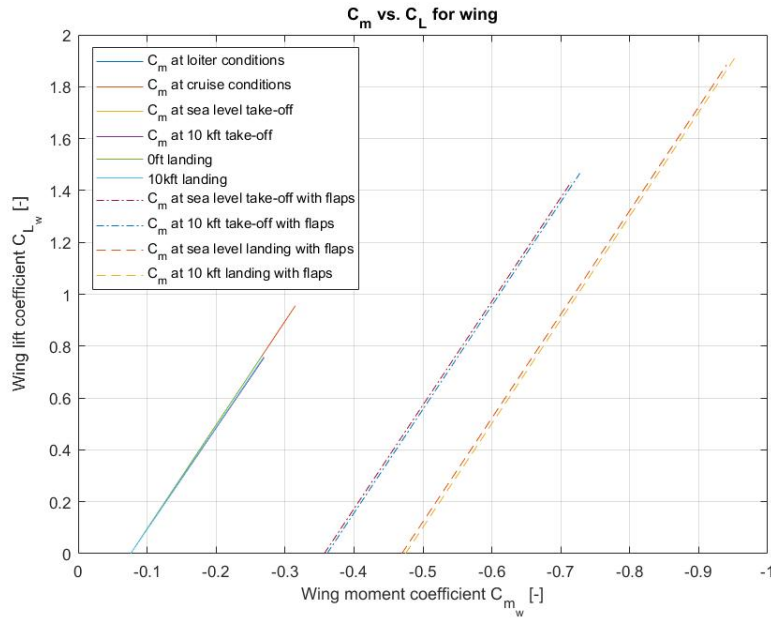


Figure 10.11: Wing moment coefficient vs. wing lift coefficient at the leading edge of the mean aerodynamic chord.

The zero-lift moment coefficient of the fuselage is calculated with Equation 10.40. The fuselage is divided into 13 segments from nose to tail, where  $w_{f_i}$  is the width of the segment,  $\Delta x_i$  is the length of the segment,  $i_{cl_f}$  is the incidence angle of the fuselage camber relative to the fuselage reference plane at the centre of each fuselage increment and  $k$  is a factor to account for fuselage fineness ratio.

$$C_{m_{0f}} = \frac{k}{36.5S\bar{c}} \sum_{i=1}^{i=13} \left( w_{f_i}^2 (i_w + \alpha_{0L_w} + i_{cl_f}) \Delta x_i \right) \quad (10.40)$$

Finally, the zero-lift pitching moment coefficient due to the horizontal tail can be computed using Equation 10.41. The point about which the moment coefficient of the aircraft is calculated is the average centre of gravity. In flight the moment acting around the c.g. determines the stability of the aircraft and therefore that is the reference point.

$$C_{m_{0h}} = (\bar{x}_{ref} - \bar{x}_{ac_h}) C_{L_{0h}} \quad (10.41)$$

The slope of the curve can be determined as follows:

$$\frac{dC_L}{dC_m} = \frac{1}{\bar{x}_{ref} - \bar{x}_{ac_A}} \quad (10.42)$$

Where the location of the aircraft aerodynamic centre as fraction of the MAC can be found with Equation 10.43.  $\bar{x}_{ac_{wf}}$ , the aerodynamic centre of the fuselage and wing combined can be calculated using Equation 10.44,  $\eta_h$  is a geometric parameter needed to calculate the horizontal tail curve slope and the downwash gradient  $\frac{d\epsilon}{d\alpha}$  is determined in lift characteristics section.

$$\bar{x}_{ac_A} = \frac{\bar{x}_{ac_{wf}} C_{L_{\alpha_{wf}}} + \left[ \eta_h C_{L_{\alpha_h}} \left( 1 - \frac{d\epsilon}{d\alpha} \right) \frac{S_h}{S} \bar{x}_{ac_h} \right]}{C_{L_{\alpha}}} \quad (10.43)$$

For the following equation, the shift in aerodynamic centre caused by adding the fuselage to the wing,  $\Delta x_{ac_f}$  is determined in Equation 10.45. The equation for  $\frac{dM}{d\alpha}$  is also shown below, where the fuselage is again divided into 13 segments and analysed for width, downwash gradient and length per segment.

$$\bar{x}_{ac_{wf}} = \bar{x}_{ac_w} + \Delta \bar{x}_{ac_f} \quad (10.44)$$

$$\Delta x_{ac_f} = - \frac{dM/d\alpha}{\bar{q} S \bar{c} C_{L_{\alpha_w}}} \quad (10.45)$$

$$\frac{dM}{d\alpha} = \frac{\bar{q}}{36.5} \frac{C_{L\alpha_w}}{0.08} \sum_{i=1}^{i=13} \left( w_{fi}^2 \frac{d\bar{\epsilon}}{d\alpha} \Delta x_i \right) \quad (10.46)$$

Now the aerodynamic centre of the aircraft is obtained, which is around 0.11 of the MAC for every condition, the slope of every condition is known. Using Equation 10.34, but substituted for aircraft values,  $C_L^*$  and  $C_m^*$  can be calculated and finally the curve with flaps retracted can be constructed. The last step is to determine the curve with flaps deployed.

### Flaps deployed

First the increment of aircraft pitching moment increment due to flaps has to be estimated. This is done using Equation 10.47, where  $\epsilon_f$  is the incremental downwash angle at the horizontal tail due to the flaps.  $\Delta C_m$  can be added to  $C_{m_0}$  to find  $C_{m_0}^*$ .

$$\Delta C_m = \Delta C_{m_w} + C_{L\alpha_h} \eta_h \frac{S_h}{S} (\bar{x}_{ac_h} - \bar{x}_{ref}) \Delta \epsilon_f \quad (10.47)$$

Since the slope will be the same as the flaps up curve, the final step is to determine  $C_{L_{flapped}}^*$ , which is the increment in lift coefficient due to flaps obtained in the lift characteristics. The curve is shown in Figure 10.12. It is obvious that for this curve the slope is positive, in stead of negative, which was the case for the airfoil and wing curves.  $C_{m_\alpha}$  is an important parameter for the stability and can be obtained by multiplying  $\frac{dC_m}{dC_L}$  with  $\frac{dC_L}{d\alpha}$ . This yields a value of  $0.8481 \text{ rad}^{-1}$  and is not what is desired. The reason why the slope is negative is because of the locations of centre of gravity and the aircraft aerodynamic centre. To be more precise, the a.c. is at in a range of 23.0% to 24.5 % of the MAC and c.g. is located at 36.5%. This means that with increasing  $C_L$ ,  $C_m$  becomes more positive. A more detailed analysis on the effect of having a positive  $C_{m_\alpha}$  will be discussed in section 12.7. In the recommendations section will be discussed how to obtain a negative  $C_{m_\alpha}$ .

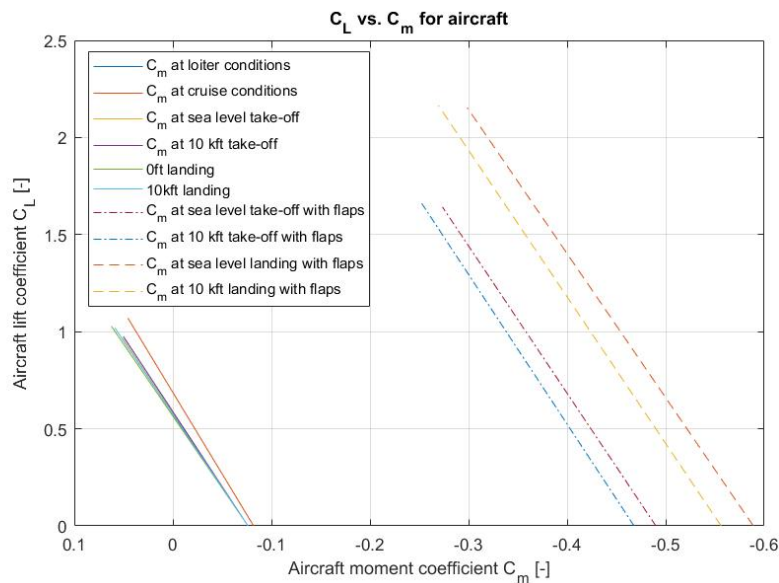


Figure 10.12: Aircraft moment coefficient vs. aircraft lift coefficient at the average centre of gravity of the aircraft.

### Verification & Validation

For the airfoil, wing and aircraft moment curves, the reference point is set at the aerodynamic centre to verify the code. Since at the aerodynamic centre the moment coefficient does not change with angle of attack and thus lift coefficient, this should result in vertical lines in the  $C_L - C_m$  curves, which is the case. Also the reference point is placed on the other side of the aerodynamic centre than the actual analysis, which gave results that the negative slopes became positive and the other way around, which was expected.

# 11

## Flight Performance

This chapter deals with the aircraft's flight performance calculations. The engine selection and general turboprop computations are discussed first, as the remainder of flight performance depends on it. Then, the take-off and landing performance is considered, followed by the method used to calculate fuel required. Then, the payload-range diagram of the aircraft is discussed, along with the new potentially feasible mission profiles that the aircraft can perform, followed by the refined turboprop performance computations from design phase 2 and the aircraft performance diagram. The verification and validation of the software used in the performance calculations are presented at the end of the chapter.

### 11.1. Engine Selection & Turboprop Characteristics

Since the concept that won the initial trade-off was a turboprop aircraft, a specific engine had to be selected in order to continue performance calculations for the aircraft. Furthermore, to estimate the performance of the turboprop engines properly, some important turboprop calculations were performed.

#### Engine Selection

For propeller engines, the specific fuel consumption is very low compared to turbofans. As such, it was clear that most turboprops would be able to meet range and endurance requirements with no issues. However, the thrust-to-weight ratio requirement of 0.26 was difficult to evaluate due to the thrust of turboprop engines varying with airspeed (and altitude). The T/W requirement was assumed to be most critical at ingress velocity, resulting in the entire propulsion system being designed around it. The thrust was then evaluated via Equation 11.1 at ingress velocity.

$$T \cdot V = P_a \quad (11.1)$$

This yielded a power requirement of around 6000 kW, meaning that only a few high-power engines were available for use. From these options a configuration with two Rolls Royce AE2100A engines, which mount Dowty Aerospace R381 six-blade propellers, was deemed most suitable due to their low specific fuel consumption and dry mass. The main characteristics of this engine can be found in Table 11.1<sup>1</sup>. The engine runs on standard JP-5 and JP-8 fuel [19].

Table 11.1: AE 2100A specifications.

Characteristic	Unit	AE 2100A
Power available	kW	3096
Specific fuel consumption	N/J	$6.8 \times 10^{-7}$
Dry Weight	kg	715.8

#### General Turboprop Performance Computation

For the calculation of turboprop flight performance, initially the calculation methods presented during the Introduction to Aerospace Engineering I course from the TU Delft were used [20]. This method uses the assumption that the shaft power of the engines remains constant, irrespective of altitude. In reality this is only true up to a certain altitude. The value obtained from Janes [21] is the "flat-rated" power output. This means that a contingency with respect to the maximum thermodynamic power is taken to account for sub-optimal conditions. This makes the assumption of constant shaft power with increasing altitude viable, but the available power will still be overestimated for high altitudes.

<sup>1</sup>Jane's Aero-Engines - <https://janes.ihs.com/AeroEngines/Reference> [Accessed 24-05-2018]

A second assumption states that the useful power, available for thrust generation, is constant with airspeed. In reality the useful power is lower at the extreme operating conditions. The variable pitch propellers can correct for this effect to a certain extent but, primarily in the lower speed regimes, the assumption does not hold and the available power will be overestimated. The benefit of the two aforementioned assumptions is that the available power,  $P_a$ , can be described with the use of just two other parameters: the propulsion efficiency  $\eta_p$ , and the shaft power  $P_{br}$ . In Equation 11.2 this relation is stated.

$$P_a = \eta_p P_{br} \quad (11.2)$$

By setting up the equations of motion in the horizontal direction using the free-body diagram from Figure 11.1, the left-hand side of Equation 11.3 can be obtained. Then, it is assumed that the thrust vector is aligned with the flight path thus  $\cos \alpha_T = 1$ . For thrust angles within  $8^\circ$ , this assumption causes an error of less than 1%. Thereby, Equation 11.3 can be rewritten to the relation on the right-hand side.

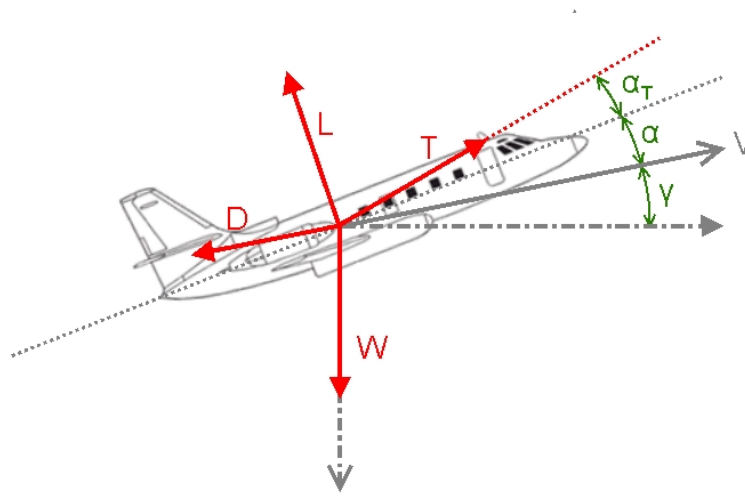


Figure 11.1: Free-body diagram of the aircraft during climb

$$T \cos(\alpha_T) - D - W \sin(\gamma) = T - D - W \sin(\gamma) \quad (11.3)$$

With the use of Equation 11.1 and Equation 11.4 and steady, horizontal flight conditions, Equation 11.5 is obtained. With this equation and the lift and drag polars from the aerodynamic analysis, the climbing performance and the maximum airspeeds at varying altitudes were computed.

$$DV = P_{req} \quad (11.4)$$

$$TV - DV - WV \sin(\gamma) = P_a - P_{req} - WRoC = 0 \quad (11.5)$$

## 11.2. Take-off & Landing Performance

The takeoff and landing distances were evaluated via total force during take-off and landing, for which the following equations were used [22]:

$$F_{TO} = T - D - D_g \quad (11.6)$$

$$F_{land} = T_{rev} + D + D_g \quad (11.7)$$

$$D_g = \mu(W - L) \quad (11.8)$$

In the above equations,  $D_g$  refers to friction drag caused by rolling/braking, and  $\mu$  refers to the braking/rolling friction coefficient, depending on whether it is used for landing or take-off respectively. For the take-off thrust,

the following relation was used [23]:

$$\bar{T} = 5.75P_{TO} \left( \frac{ND_p^2}{P_{TO}} \right)^{1/3} \quad (11.9)$$

Here,  $\bar{T}$  refers to the average take-off thrust in lbf,  $P_{TO}$  to the maximum take-off power in hp,  $N$  to the number of engines, and  $P_{TO}/D_p^2$  to the propeller disk loading, which was set at 17.5. This yielded an average take-off thrust of 103 066 N. For the reverse thrust used in the landing calculations, a thrust of 40% of the takeoff thrust was assumed [24].

The take-off calculation used maximum static thrust and take-off  $C_{L_{max}}$ . The acceleration force was used to numerically integrate the entirety of the distance travelled up until the velocity of the aircraft reached lift-off velocity, which was 110% of stall speed (as per USAF standards [23]). The rolling friction coefficients used ranged from 0.02 for asphalt to 0.10 for long grass. It's likely that the aircraft will only operate on short grass (rolling coefficient 0.05), but long grass was also accounted for.

The landing calculation assumed an approach speed equal to 120% of stall speed (as per USAF standards). One second after touchdown, full reverse thrust and brakes are initiated. At this moment, the  $C_L$  also decreases to  $C_{L_0}$ . The braking coefficients used range from 0.2 for wet grass [25] (to prevent skidding), to 0.5 for dry asphalt [23]. Both rolling and braking coefficients vary with velocity, but were assumed constant for this analysis.

The take-off and landing distances were calculated for altitudes of 0 and 10 000 ft for all types of runway surfaces, present in Table 11.2. Note that these are take-off and landing distances assuming maximum thrust during take-off run, and maximum reverse thrust and braking. The only values presented here are for dry asphalt and wet grass, as these are the two extremes in terms of take-off and landing performance. Surfaces that assumed a take-off rolling friction coefficient and landing braking coefficient between the values for wet grass and dry asphalt are loose worn gravel and hard turf. Landing distances were also calculated with extreme conditions, including engines inoperative and brakes inoperative. The most critical cases of these combinations are presented in Table 11.3, all of which were evaluated only for 10 000 ft altitude, as this was the most critical altitude. The combinations of all brakes and engines inoperative during landing, as well as one engine operative during take-off both did not meet the runway length requirements.

Table 11.2: Minimum take-off and landing distances for specified conditions

Condition	Altitude	Take-off Distance [m]	Landing Distance [m]
Dry Asphalt	Sea Level	599.4	325.7
Dry Asphalt	10 000 ft	811.8	433.4
Wet Grass	Sea Level	649.0	444.8
Wet Grass	10 000 ft	878.6	598.5

Table 11.3: Critical landing conditions and their respective landing distances.

Condition	Dry Asphalt, Only Brakes	Wet Grass, Only Brakes	Any Surface, Only $T_{rev}$
Landing Distance [m]	631.0	1120	908.8

This concludes that under any critical conditions, the aircraft will be able to take-off and land on any type of runway in less than the required distance of 6000 ft, with a decent margin for pilot error available.

### 11.3. Fuel Burn Estimation

In order to analyse the total amount of fuel required for the mission profile described in section 3.1, a separate iteration-integrated piece of software was developed. This code used aircraft properties imported from the main variable file, as well as the set mission profile as inputs. This included the loiter time, combat radius, and combat time. The program then used a numerical integration to simulate fuel burn during the various mission phases. This consisted of take-off and acceleration to climb velocity, climb, travel to combat area and descent, loiter, combat phase, climb, travel back to base, and landing and reserve fuel.

For take-off, the same equations used in section 11.2 were used, and maximum power use was assumed. The simulation for take-off stopped after reaching a velocity of 120 m/s, which is when climb started. The

climb phase also assumed maximum power, and analysed the aircraft's vertical velocity and air density over time, via Equation 11.5. Both the climb and take-off calculated time required for each phase, which was then multiplied by the maximum fuel consumption per unit time (associated with maximum power use). This resulted in an average rate of climb of around 20 m/s. Once the cruise altitude has been reached, the cruise phase starts. This was evaluated via Equation 11.10. The range equation directly outputs a weight fraction which is then used to calculate the fuel used for cruise phase 1. Note that this phase includes descent to loiter altitude, as this can be done via reduction of altitude and velocity during the cruise phase. The loiter phase used equation Equation 11.11, and resulted in an end weight after loiter, which in turn produced a fuel weight and weight fraction. Following the loiter phase, the combat phase was evaluated purely based on combat time, for which maximum power use was assumed. A final climb and cruise phase were then evaluated via aforementioned methods, after which the final descent, landing, and reserve fuel criteria were evaluated from MIL-C-5011 standards [26]. These assumed a total amount of fuel required for landing, descent and reserve to be equal to 20 minutes of endurance worth of fuel plus 5% of initial take-off fuel. This value was then taken to be the maximum fuel weight at take-off. For the maximum fuel weight required, the engine warm-up and taxi phases must also be accounted for, the two of which have been taken as 2% over the MTOW as per [4].

$$R = \frac{\eta}{C_p} \frac{C_L}{C_D} \ln \left( \frac{W_1}{W_2} \right) \quad (11.10)$$

$$E = \frac{\eta_{\text{prop}}}{c_p} \frac{C_L^{1.5}}{C_D} \sqrt{2\rho S} (W_2^{-0.5} - W_1^{-0.5}) \quad (11.11)$$

In order to minimise fuel burn for the given mission profile in the above equations,  $\frac{C_L}{C_D}$  and  $\frac{C_L^{1.5}}{C_D}$  must be maximised for range and endurance respectively. These relations were plotted for the selected airfoil and the optimal points selected to ensure maximum operating efficiency. This software yielded a total fuel required of 5200 kg, including all reserves and engine warmup and taxi. This concludes that the mission profile as described in section 3.1 is fully achievable with the current design.

## 11.4. Payload-Range & Mission Profile Analysis

As a final range estimation for the aircraft, a payload-range diagram has been made. The range has been calculated via aforementioned range equations for 5 separate cases. The nominal ferry range is 5244 km, exceeding the required range requirement by 1244 km. When an external 600 gallon fuel tank is attached<sup>2</sup>, the ferry range extends to 6798 km. The weights and ranges calculated at points 0-5 are present in Table 11.4.

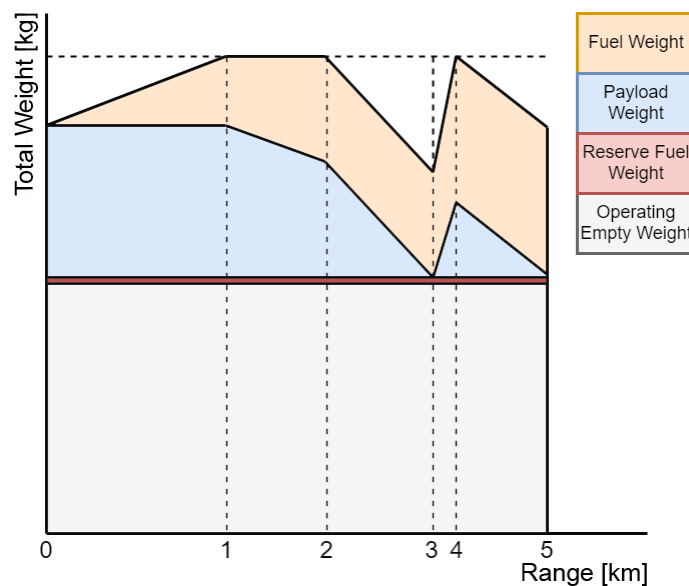


Figure 11.2: Aircraft payload-range diagram.

<sup>2</sup>IMI - 600 Gallon fuel tanks - <http://www.oocities.org/capecanaveral/5415/fuel.html> [Accessed 25-06-2018]

In the above table, points 1 and 4 are of special interest as they allow the aircraft to perform better in terms of payload and fuel capability respectively. These points have been put in the mission profile context. With regards to point 1, it was determined that the aircraft is capable of performing the same mission profile with a loitering time reduced to 2 hours. The extra payload capability could prove useful in certain situations. A second, 'bomber' type mission was also analysed, and included no loiter phase and a 20 minute combat phase during which at least 5 tons of payload are dropped. It was determined that the aircraft can travel 990 km from base, release payload, and return to base. With regards to point 4, it was determined that the loiter time can be increased up to 10 hours within the nominal mission profile. As there are regulations on time a pilot can spend flying, the combat radius was also increased further while keeping the original 6-hour time. A combat radius of 1350 km is achievable with the same mission profile, but lowered payload as per the above table. The resulting payload-range diagram can be found in [Figure 11.2](#). Note also that the nominal range is 3783 km, and the nominal ferry range is 5244 km. When an external fuel tank is added, the ferry range becomes 6798 km.

Table 11.4: Payload-range diagram point specifications.

Point	Range [km]	TOW [kg]	OEW [kg]	Reserve fuel [kg]	Fuel [kg]	Payload [kg]
0	0	17063	11447	255	0	7000
1	2433	21880	11447	255	3178	7000
2	3783	21880	11447	255	4817	5361
3	5244	16544	11447	255	4817	0
4	5556	21880	11447	255	6702	3446
5	6798	16716	11447	255	6702	172

## 11.5. Improved Aircraft Performance Computations

In this section, the aircraft performance will be analysed. The general equations and performance computations from [section 11.1](#) are used again as a basis. Since those methods use quite over-simplified assumptions, a more detailed performance analysis will be presented now by using the results from the detailed aerodynamic analysis in [section 10.2](#), and by improving on some assumptions and simplifications.

### Propeller Efficiency Computation

In order to obtain more accurate performance characteristics, the assumption of constant propulsive efficiency with varying airspeed was refined. Primarily the accurate propulsive efficiency at low airspeeds is of importance, since the aircraft will be using most of its fuel during loitering. Since propeller performance data is very difficult to acquire, efforts were focused on obtaining the most accurate estimations possible. To gain insight in the general behaviour of propeller efficiency, [Figure 11.3](#) was used. It was obtained from the Unified Propulsion Lecture of the MIT [27]. It is a plot of the typical propeller efficiency as a function of advance ratio. The advance ratio,  $J$ , is defined as the ratio between the airspeed of the aircraft and the rotational airspeed of the propellers:  $J = V_{TAS}/(nD_{prop})$ , where  $n$  represent the number of revolutions per second.

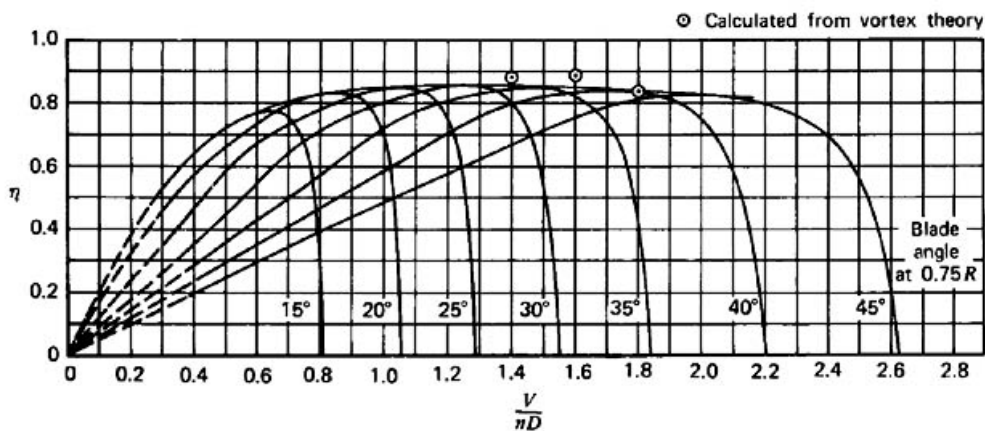


Figure 11.3: Typical propeller efficiency as a function of advance ratio

Subsequently, the most accurate specifications for the airfoils on the Dowty R381 propeller were obtained

from the manufacturers website<sup>3</sup>. There, it is stated that the very similar R408 propellers use the ARA-D/A airfoil sections. For these types of airfoils, a NASA research [28] was available that contained wind tunnel test data of propellers with these airfoils. Only a limited amount of data points were available, so these were interpolated such that the resulting maximum efficiency curve was similar in shape to the curve following all maximum values in Figure 11.3, resulting in Figure 11.4.

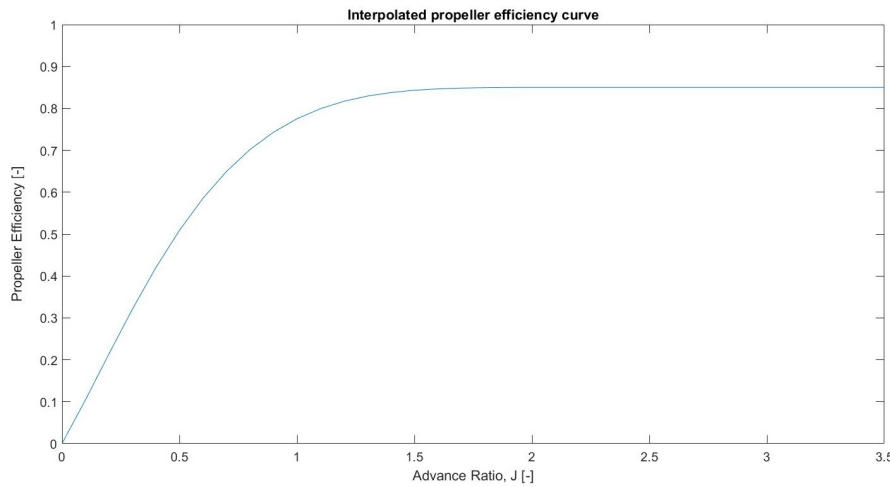


Figure 11.4: Interpolated maximum propeller efficiency as a function of advance ratio, for the Dowty R381 variable pitch propeller.

Unfortunately, the tested propeller was unswept, and three-bladed. This differs substantially from the six-bladed Dowty R381 model. Generally, adding more blades to a propeller mostly decreases the efficiency at lower airspeeds, since blades cause flow disturbance for each other. To correct for the over-estimation of the low speed efficiency, the effective increase of the advance ratio was scaled down for airspeeds lower than the loitering speed. The loitering speed was selected, based on typical turboprop thrust diagrams from [20]. The advance ratio scaling was performed by first calculating the maximum static thrust, using Equation 11.12. Then the thrust-induced airspeed was calculated using Equation 11.13. Both equations used  $\eta_{p,TO} = 0.53$ , obtained from NASA [28].

$$T_{TO} = (\eta_{p,TO} P_{br})^{(2/3)} (2\rho S_{prop})^{(1/3)} \quad (11.12)$$

$$V_i = \sqrt{\frac{\eta_{p,TO} T_{TO}}{2\rho S_{prop}}} \quad (11.13)$$

The normal definition of the advance ratio does not include the induced airspeed velocity. However, for the low-speed regimes, a linear interpolation was made to obtain "effective" values for the advance ratio. The advance ratio at static conditions was calculated by substituting  $V_i$  for  $V_{TAS}$ . At static conditions, this results in a value for  $J$  of roughly 0.5. When comparing the propeller efficiency obtained via  $J$  from Figure 11.4 to the initial reference value from NASA, the difference was found to be only 1.8%. This is a good indication for the validity of the created method. Unfortunately, no further quantification of the efficiency error can be made, due to the lack of available data. However, the initial assumption that over-estimated the propeller efficiency during low airspeeds has been removed, and the results were checked to be more conservative.

### Computation of Power and Thrust Coefficients

As with lift and drag computations, it is beneficial to work with the dimensionless equivalents of shaft power and thrust. The necessary conversions are defined in Equation 11.14 and Equation 11.15. With these relations, the advance ratio can be rewritten, as defined in Equation 11.16 obtained from the aforementioned MIT Propulsion lecture[27].

$$C_P = \frac{P_{br}}{\rho n^3 D_{prop}^5} \quad (11.14)$$

$$C_T = \frac{T}{\rho n^2 D_{prop}^4} \quad (11.15)$$

<sup>3</sup>Dowty Propellers - <http://dowty.com/products/regional-airliners/> [Accessed 25-05-2018]

$$J = \frac{V_{TAS}}{nD} = \frac{\eta_{prop} C_P}{C_T} \quad (11.16)$$

For the computation of the power coefficient, the initial assumption of constant shaft power was revised. From [21], it was found that the maximum thermodynamic power of the AE 2100 engine is in excess of 4474 kW. By using Equation 11.17, obtained from [5], and the flat-rated engine power specification, the altitude at which the engine shaft power started to decrease, was calculated and found to be 3690 m. Between sea level and this altitude, the flat-rated power value was used. At altitudes higher than 3690 m, the shaft power was calculated using Equation 11.17, with  $(P_{br,eq})_0 = 4474 \text{ kW}$ .

$$\frac{P_{br,eq}}{(P_{br,eq})_0} = \left( \frac{\rho}{\rho_0} \right)^{0.75} \quad (11.17)$$

## 11.6. Aircraft Performance Diagram

The aircraft performance diagram is a diagram in which all possible (static) flying conditions are shown. The boundaries on the performance diagram are created by a multitude of reasons, discussed one by one in this section. Finally, the diagram will be presented.

### Maximum Available Thrust Boundaries

By using all results obtained in the previous section, for any given flight condition the parameters in Equation 11.16 are known, except for the thrust coefficient. This one unknown can be calculated, and via Equation 11.15 it was converted into the actual thrust values. This result was combined with the lift and drag computations from the detailed aerodynamic analysis from chapter 10 to compute the set of conditions at which the available thrust was equal to the drag. Two sets of these specific conditions were calculated: one for the minimum, and one for maximum airspeeds at which it occurs. These generate the first two boundaries on the performance diagram.

### Propeller Tip-speed Boundaries

The next constraint to be computed, is caused by the maximum Mach number that the propeller tips may experience. If the propeller tips would exceed this speed, the airflow near the tips would become critical. This results in vibrations and high efficiency losses. The airspeed that a propeller tip experiences is described by Equation 11.18, which can easily be rewritten to use the Mach number instead of the true airspeed. The maximum Mach number that the propeller tips of the Saab 2000 experience was obtained via Janes [29] and was used as the tip Mach constraint. It was also found that this aircraft reduces the propeller RPM to 950 for cruise flight because of this phenomena. Therefore, the boundaries for both 950 and 1100 RPM were computed using Equation 11.18.

$$V_{tip} = \sqrt{V_{TAS}^2 + \left( \frac{1}{2} n D_{prop} \right)^2} \quad (11.18)$$

### Stall Speed Boundary

Another important boundary in the performance diagram is generated due to the stall speed. This boundary was created by simply evaluating the required airspeed at the maximum lift coefficient in clean configuration, obtained from the aerodynamic analysis. Finally, the airspeeds at which Mach drag divergence starts to occur were also used to generate a boundary on the performance diagram. With all the boundaries generated, the final performance diagram was created. It is presented in Figure 11.5.

### Final Results

The green region in Figure 11.5 represents the complete range of flight conditions in which the aircraft can be operated. The extra region of high altitude, high speed flight that is provided by the reduction in propeller RPM is represented by the light green area. In Table 11.5 the main performance characteristics are presented. The maximum rate of climb is calculated by using Equation 11.5 and maximising  $P_a - P_{req}$ .

## 11.7. Verification & Validation

As no complete mission profile and fuel data is available from any manufacturer, the complete fuel calculation code was not validated. It was however verified as a whole via methods described in section 4.5, and its

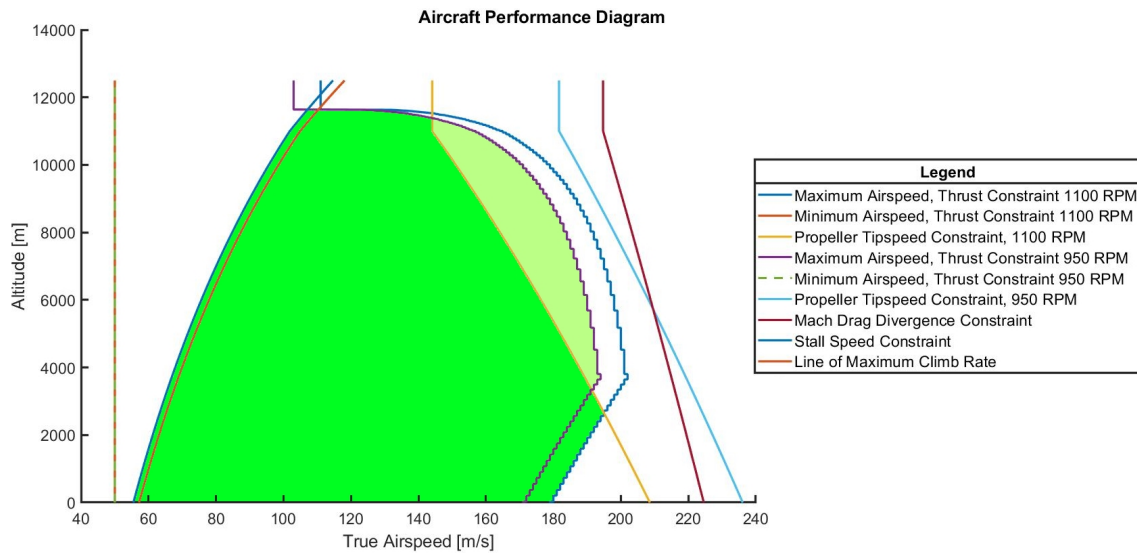


Figure 11.5: Aircraft performance diagram, the coloured regions indicate the range of operable flight conditions.

Table 11.5: Main Performance Characteristics

Characteristic	Value
Maximum true airspeed	195 m/s
Absolute Flight Ceiling	11630 m
Maximum rate of climb	15.6 m/s

individual contributions verified and validated. This was done with data on the Gulfstream IV, obtained from Globalair<sup>4</sup>, and Oswald efficiency and SFC of 0.67 and 0.69 N/N/h respectively as described in [22]. The maximum range was calculated to be 7734 km, whereas the designated maximum range is 7778 km. The maximum rate of climb was determined to be 21.4 m/s with software, whereas the manufacturer specified maximum is 21.43 m/s at sea level ( $C_L$  of 1.2 at climb). The difference in range is around 0.5%, while in rate of climb it is 0.1%. The endurance data for the aircraft was not available, and the software was validated via several different problems from [22], with the maximum error being around 9.3%. The code estimated higher endurance than the solution, but this is likely due to the simplified assumptions in calculations of  $C_L$  and  $C_D$  used in the problems, as opposed to the method described above.

<sup>4</sup>Globalair - Gulfstream IV <https://www.globalair.com/aircraft-for-sale/Specifications?specid=236> [Accessed 26-06-2018]

# 12

## Empennage Design and Stability Analysis

In this chapter the methods used for sizing the empennage are elaborated upon. In order to use the tail sizing methods detailed below, several parameters from prior design aspects of the iteration process have to be known. As the iteration progresses, certain input parameters will become more accurate, which means the methods give more accurate results. First, the adaptations to conventional tail sizing methods necessary in order to use them for our split-x tail design are explained. Next, the tail sizing methods are explained starting with horizontal tail sizing methods and then the vertical tail sizing methods. Finally, the design process for the tail planform is discussed.

### 12.1. Adaptations of Conventional Tail Sizing Methods

Because of the unconventional tail design chosen for the aircraft, several adaptations had to be made to conventional tail sizing methods in order to properly size the tail. In the upcoming sections, the horizontal part of the split-x tail will be referred to as the stabiliser, and the angled parts will be referred to as x-areas. From an initial sizing, it was found that the required horizontal and vertical tail surface areas were approximately equal. Thus, it was decided to put the x-areas at an angle of 60 deg. Conventional tail sizing methods generally offer sizing methods for the horizontal and vertical surfaces as a ratio of the main wing area, while the x-areas of the chosen tail design combine these functions. Thus, the outputs gained from the tail sizing methods are  $\frac{S_H}{S}$  and  $\frac{S_V}{S}$ , while  $S_S$  and  $S_X$  are the ones needed to establish the actual dimensions of the tail. To resolve this incongruity, without having to conjure up novel tail sizing methods for this tail design, the following methods were used to determine the x-areas and stabiliser area from the required horizontal and vertical tail surface areas. First, it was assumed that the x-areas provided equivalent functionality as their projections as vertical and horizontal surface areas [30]. Next, since the x-areas are solely responsible for the required vertical surface area, their area was determined from the required vertical surface area.

$$S_X = \frac{S_V}{4 \cdot \sin(60 \text{ deg})} \quad (12.1)$$

From this, the horizontal projection of the x-areas was calculated and the stabiliser area determined as follows:

$$S_S = S_H - 4 \cdot \cos(60 \text{ deg}) \cdot S_X \quad (12.2)$$

### 12.2. Preliminary Horizontal Tail Sizing

An initial estimation of the required horizontal tail surface area was performed according to the method described by Roskam [1]. Additionally, the required horizontal tail surface size was increased by 30% to increase its redundancy and thus survivability. The amended formula used for calculating the horizontal tail surface ratio is Equation 12.3.

$$\frac{S_H}{S} = (1 + \text{horizontal redundancy}) \cdot \bar{c} \cdot \frac{V_H}{l_H} \quad (12.3)$$

The mean aerodynamic chord was determined in chapter 10, while the tail volume  $V_H$  was taken as 0.41 from statistical data on reference aircraft [1]. Lastly, the longitudinal wing position had to be initially determined in order to calculate the tail arm  $l_H$ .

#### Preliminary Longitudinal Wing Positioning

Since the preliminary longitudinal wing positioning was done before the design and placement of many sub-systems of the aircraft in the fuselage, this estimation was done by using weight fractions from statistical data on reference aircraft [1]. At this stage of the design process, the wing was placed so that the most aft c.g. would be precisely at  $0.25\bar{c}$ . For the calculation of the c.g. limits, the placement of fuel and payload was

estimated. In this initial stage, it was assumed that the payload would hang under the wing, and thus act at  $0.25\bar{c}$ . Similarly, for the fuel was also assumed to be located primarily in the wing, acting at  $0.25\bar{c}$  as well. Thus, the payload and fuel weight could be disregarded from the preliminary longitudinal wing positioning. The statistical weight fractions from Roskam [1] can be seen in Table 12.1.

Table 12.1: Statistical weight fractions from Roskam [31].

Group	Weight Fraction
Wing group	0.1095
Empennage group	0.0243
Fuselage group	0.1190
Propulsion group	0.0028
Fixed equipment group	0.1412
Landing gear group	0.0438

Next, in order to be able to place the c.g. at the desired location by determining the longitudinal wing position, these groups had to be grouped in a more general wing and fuselage group. The meaning of these overarching groups is that the wing group's location is fixed with respect to the wing, whereas the fuselage group's locations are fixed with respect to the fuselage. The wing group was composed of the wing, propulsion, and landing gear groups. The fuselage group was composed of the fuselage, empennage, and fixed equipment groups. Next, the location of these group's individual c.g. had to be estimated. These were merely initial estimates, and would be further refined during the more accurate c.g. calculations as part of the class II weight estimations. The values chosen can be seen in Table 12.2.

Table 12.2: Chosen c.g. locations of individual groups.

Group	Relative c.g. location with respect to fuselage
Fuselage group	$0.5 \cdot l_{\text{fuselage}}$
Empennage group	$l_{\text{fuselage}}$
Fixed equipment group	$0.4 \cdot l_{\text{fuselage}}$
Group	Relative c.g. location with respect to the LEMAC
Wing group	$0.4 \cdot \bar{c}$
Propulsion group	0
Landing gear group	0

Next, the weight fractions of the overarching wing and fuselage groups were calculated by adding the weight fractions of their constituent groups. With this and the values from Table 12.2, the c.g.'s of the wing and fuselage groups were calculated using Equation 12.4.

$$\text{c.g.} = \frac{\sum Wf_i \cdot \text{c.g.}_i}{\sum Wf_i} \quad (12.4)$$

Finally, in order to determine  $x_{\text{LEMAC}}$  for the placement of the c.g. at  $0.25\bar{c}$ , Equation 12.5 was used.

$$x_{\text{LEMAC}} = \text{c.g.}_{\text{Fuselage group}} + \frac{Wf_{\text{Wing group}}}{Wf_{\text{Fuselage group}}} \cdot \text{c.g.}_{\text{Wing group}} - 0.25 \cdot \bar{c} \quad (12.5)$$

### 12.3. Vertical Tail Sizing

Similarly to the preliminary horizontal tail sizing, an estimation of the required vertical tail surface area was performed according to the method described by Roskam [1]. However, unlike the horizontal tail sizing, this method is the most detailed one used at this stage of the design. The formula used for calculating the horizontal tail surface ratio is Equation 12.6.

$$\frac{S_V}{S} = \bar{c} \cdot \frac{V_V}{l_V} \quad (12.6)$$

The tail volume  $V_V$  was taken as 0.0766 from statistical data on reference aircraft [1]. In the first stage of the design, the tail arm was calculated using the preliminary longitudinal wing positioning detailed in Equation 12.2. In the second stage of the iterative process, the tail arm was calculated using the more accurate longitudinal wing position, which is explained in section 12.4.

## 12.4. Detailed Horizontal Tail Sizing and Longitudinal Wing Positioning

To size the horizontal tail and determine the longitudinal wing positioning in more detail, equations for static stability, controllability, and longitudinal wing positioning in relation to the c.g. were combined to determine the horizontal tail size and longitudinal wing position. In order for an aircraft to remain statically stable, it needs to satisfy Equation 12.7.

$$\bar{x}_{c.g.} \leq \bar{x}_{a.c.} + \frac{C_{L\alpha h}}{C_{L\alpha A-h}} \left(1 - \frac{d\varepsilon}{d\alpha}\right) \frac{S_h l_h}{S \bar{c}} \left(\frac{V_h}{V}\right)^2 - \text{S.M.} \quad (12.7)$$

In order to keep the aircraft controllable, it needs to be able to be trimmed in different flight conditions. Thus, the aircraft needs to satisfy Equation 12.8.

$$\bar{x}_{c.g.} \geq \bar{x}_{a.c.} - \frac{C_{m a.c.}}{C_{L A-h}} + \frac{C_{L h}}{C_{L A-h}} \frac{S_h l_h}{S \bar{c}} \left(\frac{V_h}{V}\right)^2 \quad (12.8)$$

Next, based on the most aft and most forward mass and c.g. calculations of the fuselage and wing groups from section 8.3, the most aft and most forward c.g. locations of the aircraft can be determined for a given  $x_{\text{LEMAC}}$  using Equation 12.9. This formula is performed for all four possible combinations of most aft or forward wing and fuselage group c.g. locations, after which the minimum and maximum value are taken as most forward and most aft c.g. locations, respectively.

$$\bar{x}_{c.g.} = \frac{M_{\text{Wing group}} \cdot (\bar{x}_{c.g. \cdot \text{Wing group}} \cdot \bar{c} + x_{\text{LEMAC}}) + M_{\text{Fuselage group}} \cdot x_{c.g. \cdot \text{Fuselage group}}}{M_{\text{Wing group}} + M_{\text{Fuselage group}}} \quad (12.9)$$

Equation 12.7 and Equation 12.8 combined determine the most extreme c.g. limits the aircraft can have in order to ensure the aircraft's static stability and controllability for a certain  $\frac{S_H}{S}$ . Equation 12.9 was used to calculate the c.g. range for a wide range of values of  $x_{\text{LEMAC}}$ . Next, for each of the c.g. ranges calculated, it was determined whether they met the static stability and controllability requirements using Equation 12.7 and Equation 12.8. Finally, of the values for  $x_{\text{LEMAC}}$  that produced acceptable c.g. ranges, it was determined which value would produce the minimal value for  $\frac{S_H}{S}$ . These values for  $\frac{S_H}{S}$  and  $x_{\text{LEMAC}}$  are the final outcomes of the detailed horizontal tail sizing and longitudinal wing positioning, although it should be noted that the horizontal tail surface area still must be increased by 30% for redundancy as determined in section 12.2.

Since the value for the tail arm in this section was based on the previous wing positioning, the tail arm based on the new wing position has to be calculated, after which the horizontal tail sizing and longitudinal wing positioning methods in this section should be performed again until its outcomes converge.

## 12.5. Empennage Planform Design

After determining the surface areas of the different tail sections, the planform dimensions had to be decided upon. Because of the coupling of certain planform parameters of the x-areas and stabiliser, this process had to be performed several times in succession in order to converge on a proper planform. However, initially the taper ratio and sweep angle had to be chosen.

It was first decided to use a constant taper ratio of 1 for the entirety of the empennage. Although a lower taper ratio could have led to relatively lower structural weight, it would also have caused the structural design and production of this already complex design to become even more complicated [32]. Next, a sweep angle had to be selected. At this stage of the design no sweep is selected for the empennage, and since there is a taper ratio of 1 that applies to any location on the chord. No sweep is an acceptable choice since the aircraft flight envelope never reaches transonic speeds. Meanwhile, the advantages of having no sweep are that the effectiveness of the empennage is higher than it would have been with sweep [32].

Next, the effective aspect ratio's of the effective horizontal and vertical tails were determined in conjunction with the chord and span of the individual parts of the empennage in an iterative process. For the aspect ratio's, it was determined that an acceptable value for the effective horizontal tail was between 3 and 5, while for the effective vertical tails an acceptable value would be around 1 [32]. These values represent a trade-off between extra weight and increased effectiveness, based on commonly used industry values [32]. For the determination

of the aspect ratio used for aerodynamic calculations, several additional assumptions and alterations had to be made. First, the aspect ratio of the effective horizontal tail was found using Equation 12.10.

$$AR_{H_{eff}} = \frac{S_H}{\bar{c}^2} \cdot \frac{AR_{H_{eff}}}{AR_H} \quad (12.10)$$

Due to the fact that the vertical tail is effectively split between the left and right side of the tail, its aspect ratio will be proportionally lower. Equation 12.11 was used to calculate the aspect ratio.

$$AR_{V_{eff}} = \frac{1}{2} \cdot \frac{S_V}{\bar{c}^2} \quad (12.11)$$

For the actual calculations of the planform dimensions, Equation 12.12, Equation 12.13 and Equation 12.14 were performed in that order by first making a guess for the  $AR_{H_{eff}}$ . Afterwards,  $AR_{V_{eff}}$  is checked to ensure it is within the acceptable range of values. If it is found that a value is not yet acceptable, a different initial value for  $AR_{H_{eff}}$  is chosen and the calculations run again.

$$\bar{c}_x = \bar{c}_s = \sqrt{\frac{S_H}{AR_{H_{eff}}}} \quad (12.12)$$

$$b_s = \frac{S_S}{\bar{c}_h} \quad (12.13)$$

$$b_x = \frac{S_X}{\bar{c}_x} \quad (12.14)$$

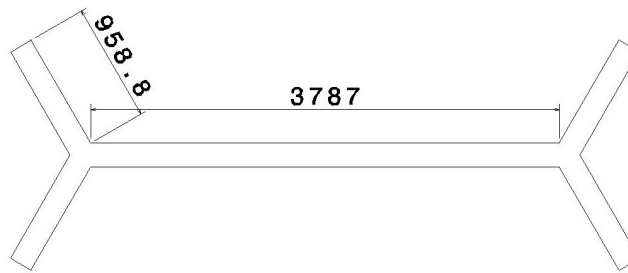


Figure 12.1: Split-x tail front view, all values given in mm.

## 12.6. Conclusion of the Empennage Design

After all tail sizing methods were performed and iterated according to the methods described in the previous sections, the results of said methods can be considered an accurate prediction for the ultimate actual characteristics of the aircraft. The most important parameters ultimately produced by the methods described, as implemented in the iterative process, are documented in Table 12.3

## 12.7. Static Stability Analysis

The first type of stability analysis that is done to ensure smooth flight operations, is a static stability analysis. Although the original requirements call for stick-fixed and stick-free static stability, however, the use of the actuators chosen in Figure 14.3 results in only stick-fixed stability being relevant for the aircraft. In chapter 10, the parameter  $C_{M_\alpha}$  was found to be  $0.8481 \text{ rad}^{-1}$ . This is not a desirable result, since any disturbance in the pitch of the aircraft will be exacerbated. In order to have static stability, the parameter  $C_{M_\alpha}$  should be negative instead. Static stability is one of the driving requirements of the horizontal tail sizing, however it was performed before the final aerodynamic analyses. Thus, the detailed tail sizing and wing positioning should be reiterated with the newly obtained values from the aerodynamic analyses in chapter 10.

## 12.8. Dynamic Stability Analysis

The sizing of the empennage focuses primarily on the static stability of the aircraft. However, achieving static stability is only part of the equation. To make the aircraft flyable without artificial stability measures, dynamic stability should also be achieved. The dynamic stability is analysed by looking at five different eigenmotions

Table 12.3: End results of the tail sizing and longitudinal wing positioning

Parameter	Value
$S_H$	10.85 m <sup>2</sup>
$S_V$	6.32 m <sup>2</sup>
$S_S$	7.20 m <sup>2</sup>
$S_X$	1.82 m <sup>2</sup>
$l_h$	7.38 m
$x_{LEMAC}$	6.12 m
$AR_{H_{eff}}$	4.5
$AR_H$	3
$AR_{V_{eff}}$	0.87
$\bar{c}_s$	1.90 m
$\bar{c}_x$	1.90 m
$b_x$	0.96 m
$b_s$	3.79 m
$\lambda_{tail}$	1

of the aircraft. These are the: dutch roll, short period, phugoid, spiral and damped roll. The first two should definitely be stable to make the aircraft flyable. The phugoid is generally a very slow oscillatory motion, which is why it does not necessarily have to be stable. However, the pilot would have to be focused continuously on the airspeed and altitude, which is obviously not preferred at all. In this section, the dynamic stability of the aircraft is analysed at combat conditions. This means an airspeed of 180 kts at an altitude of 100 m.

### Equations of Motion and Simplifications

To derive the different eigenmotions of the aircraft, the equations of motion should be analysed. The equations of motion are found by equating the forces and moments over all three axes to zero. Also, the kinematic equations are used. If this is done properly, two four by four state space matrices are obtained. The full derivation of these matrices can be found in the flight dynamics lectures notes [16].

The obtained state-state matrices contain a lot of control derivatives. Although almost all of them can be approximated using various methods, the matrices are simplified in order to reduce the workload. Also, because the approximation methods for the control derivatives are often not very accurate, it would be a waste of precision to consider the full state-space matrices. However, for all eigenmotions the most extensive simplified equations are used, to avoid losing too much precision. Below, the simplified equations of motion are presented that were used for the analysis. The equations for the short period, phugoid, spiral, dutch roll and aperiodic roll are presented in Equation 12.15, Equation 12.16, Equation 12.17, Equation 12.18 and Equation 12.19, respectively.

$$\det \begin{vmatrix} C_{Z\alpha} + (C_{Z\alpha} - 2\mu_c)\lambda_c & C_{Zq} + 2\mu_c \\ C_{m\alpha} + C_{m\dot{\alpha}} & C_{mq} - 2\mu_c K_Y^2 \lambda_c \end{vmatrix} = 0 \quad (12.15)$$

$$\det \begin{vmatrix} C_{Xu} - 2\mu_c \lambda_c & C_{Z_0} & 0 \\ C_{Zu} & 0 & 2\mu_c \\ 0 & -\lambda_c & 1 \end{vmatrix} = 0 \quad (12.16)$$

$$\lambda_c = \frac{2C_L (C_{l\beta} C_{nr} - C_{n\beta} C_{lr})}{C_{lp} (C_{Y\beta} C_{nr} + 4\mu_b C_{n\beta}) - C_{np} (C_{Y\beta} C_{lr} + 4\mu_b C_{l\beta})} \quad (12.17)$$

$$\det \begin{vmatrix} C_{Y\beta} & -4\mu_b \\ C_{n\beta} & C_{nr} - 4\mu_b K_X^2 \lambda_c \end{vmatrix} = 0 \quad (12.18)$$

$$(C_{lp} - 4\mu_b K_X^2 \lambda_c) \frac{pb}{2V} = 0 \quad (12.19)$$

Note that the different solutions of  $\lambda$  represent the eigenvalues for the particular eigenmotions. These eigenvalues indicate the behaviour of the eigenmotions. This is discussed in Equation 12.8.

### Derivation of Stability Derivatives

For this first analysis of the dynamic stability, stability derivatives of the aircraft need to be estimated before the eigenvalues of the state-space system can be calculated. Since approximate calculations were used to compute the eigenvalues, not all stability derivatives had to be known. The methods used to calculate the stability derivatives are taken directly from Roskam's Airplane Design Part VI [18], while the input values used, resulted from the aerodynamic analysis in chapter 10. It should at this point be noted that the calculated stability parameters are estimations, and not exact values. Ultimately, the stability derivatives can only really be known by performing flight and wind tunnel tests.

### Analysing Obtained Eigenvalues

If Equation 12.15 to Equation 12.19 are solved, the eigenvalues for every specific eigenmotion are found. These either real or complex eigenvalues are often referred to as 'poles'. Every pole or complex conjugate set, represents one particular eigenmotion. To see what the coordinates of the poles say about the characteristics of the eigenmotions, it is convenient to list for every pole (or complex conjugate set) its corresponding damping ratio ( $\zeta$ ), damped natural frequency ( $\omega_n$ ) and half amplitude period ( $T_{1/2}$ ). This is done in Table 12.4.

Table 12.4: Damping ratios and damped natural frequencies.

Eigenmotion	Eigenvalue	$\zeta$ [-]	$\omega_n$ [Hz]	$T_{1/2}$ [s]
Short period	$-0.0213 \pm 0.0560i$	0.256	1.63	0.9587
Phugoid	-0.00211	1.00	0	9.68
Spiral	0.00134	1.00	0	-15.2
Dutch roll	$0.00752 \pm 0.213i$	0.0353	7.36	2.72
Aperiodic roll	-1.18	1.00	0	0.0174

Note that a damping ratio equal to one and damped natural frequency equal to zero indicates that the motion has no oscillatory behaviour, and is thus purely exponential in nature. Let's discuss the behaviour of all the eigenmotions separately. Note that for many eigenmotions, values are compared to the values of the Cessna Citation II, which can be found in the lecture notes of the flight dynamics course [16].

First of all, for the short period the damping looks rather low. However, considering the half amplitude period of almost one second, this looks quite acceptable. The damped natural frequency is also good, since it does not deviate much from reference aircraft such as the Cessna Citation II.

The phugoid motion has a calculated natural frequency of zero, which means it is not oscillatory in nature, but purely exponential. However, since the eigenvalue is negative, it is in fact stable. If such a non oscillatory behaviour can be considered valid is highly doubtful. This is confirmed by the fact that the way  $C_{Z_u}$  is obtained is not reliable. This is mentioned in Roskam's Airplane Design Part VI [18], where the equation for the approximation of  $C_{Z_u}$  is listed. When the value is raised to a value similar to the Cessna Citation II, the phugoid does in fact show oscillatory behaviour.

The aircraft seems to be spirally unstable. This is not necessarily a problem, since apparently it takes approximately fifteen seconds to double the roll angle. This is thus very manageable.

As can be seen from the real part of the eigenvalues, the dutch roll seems to be unstable. As mentioned before, this is unacceptable if no artificial stabilisation system is applied. It is noticeable that the aircraft is unstable spirally and also unstable for the dutch roll. When looking at the values of  $C_{n_\beta}$  and  $C_{l_\beta}$ , which are the primary coefficients that determine the behaviour of the spiral and dutch roll, it can be noticed that  $C_{n_\beta}$  almost a factor ten lower than the Cessna Citation II, and  $C_{l_\beta}$  is positive instead of negative. This last coefficient would typically be the behaviour of an aircraft with negative dihedral. Recommendations concerning this part are given in section 12.9.

The aperiodic roll is the most simplistic of all motions, and the half amplitude period looks realistic and acceptable. As long as the motion is highly damped, it is not a problem.

### Verification & Validation

First off, the unit continuity and consistency tests, as detailed in section 4.5, were performed on the software implementation of the eigenvalue calculations. In addition, to verify the eigenvalue calculations and assumptions, a separate model was made through the use of a numerical model of the symmetric and asymmetric

equations of motion in a state-space model. However, since not all necessary stability and control derivatives for this state-space model could be estimated with sufficient accuracy at this point, known stability and control derivatives for a specific flight condition of a Cessna Citation were used to verify the eigenvalue calculations instead. The results of the verification calculations can be seen in [Table 12.5](#)

Table 12.5: Comparison of dimensional eigenvalues from the verification model and the model used for dynamic stability analysis.

Eigenmotion	Eigenvalue(s) from verification model	Eigenvalue(s) used
Short period	$-3.22 \pm 4.54i$	$-3.23 \pm 4.56i$
Phugoid	$-0.0148 \pm 0.140i$	$-0.00755 \pm 0.0995i$
Spiral	0.00515	0.00510
Dutch roll	$-0.774 \pm 4.78i$	$-0.866 \pm 4.65i$
Aperiodic roll	-10.2	-10.1

## 12.9. Recommendations

Once the more detailed aerodynamic analysis is completed, the tail sizing can be done in more detail again. With the input values for [Equation 12.7](#), [Equation 12.8](#) and [Equation 12.9](#) the exact required horizontal tail size and longitudinal wing position should be reiterated.

Furthermore, once the moments of inertia are initially estimated, the dynamic stability of the aircraft should be analysed again. Based on the outcomes of this more accurate analysis, it could be determined that a change in certain design parameters is desired. It also became clear that some of the eigenmotions showed strange, and sometimes unacceptable behaviour. For the phugoid motion, the reason assumed for showing no oscillatory behaviour is the unreliable approximation of the stability control derivatives. This can be solved by performing wind tunnel tests or CFD analyses. For the spiral and dutch roll instability, looking at the obtained values for  $C_{n\beta}$  and  $C_{l\beta}$ , the stability derivatives are likely to be non reliable as well. Also this should be further investigated using wind tunnel data or CFD analyses.

# 13

## Structural Analysis

The purpose of this chapter is to obtain a preliminary structural design for the wing, tail and fuselage sections of the aircraft. At this stage of the design only the wing box is engineered in detail. The fuselage and tail are subject to analysis in the future design phases. More information on this can be found in [chapter 20](#).

Firstly, in [section 13.2](#) the maximum load cases are identified. In [section 13.3](#) the wing design is performed, in which the failure modes were analysed extensively. The tail is discussed in [section 13.4](#), and in [section 13.5](#) the fuselage is discussed. Lastly, [section 13.6](#) discusses the materials which were chosen to implement into the design.

Please note that all unreferenced equations were obtained from *Aircraft Structures - for Engineering Students, Fifth Edition* by T.H.G. Megson. More information on this piece of literature can be found in the bibliography under number [33].

### 13.1. Coordinate System

Before any analyses may be performed, a coordinate system must be set up which is used throughout all calculations. The main coordinate system used throughout the structural analysis calculations can be seen in [Figure 13.1](#)<sup>1</sup>.

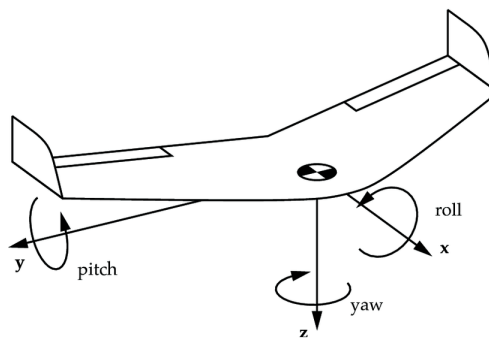


Figure 13.1: Coordinate system used throughout [chapter 13](#).

### 13.2. Maximum Load Cases

In this section the maximum load cases are identified and discussed. Firstly, the loading diagram is observed and explained. Secondly, the extreme load cases due to the nature of the missions are investigated.

#### Loading Diagram

In this subsection the load factor envelope is discussed. This envelope is used to identify the maximum load cases of the aircraft. These load cases then can be used to determine the maximum loads for the structural designing.

The loading diagram is presented in [Figure 13.2](#). On the vertical axis the loading  $n$  is shown, and on the horizontal axis the velocity in m/s is located. In red the load factors due to manoeuvres are displayed, and in

<sup>1</sup>Coordinate system of the body attached reference frame - [https://www.researchgate.net/figure/Coordinate-system-of-the-body-attached-reference-frame-The-common-names-for-the\\_fig2\\_40754972](https://www.researchgate.net/figure/Coordinate-system-of-the-body-attached-reference-frame-The-common-names-for-the_fig2_40754972)  
[Accessed 25-06-2018]

blue the load factors due to gusts are shown. The line from 0-A represents the load factor at  $C_{L_{max}}$ . Line A-D shows the max load factor line, and line D-E the line of maximum velocity. Furthermore, line 0-H shows the negative load factors due to the lowest  $C_L$  the wing is capable of. To conclude line H-F is the minimum load factor line as set by the requirements.

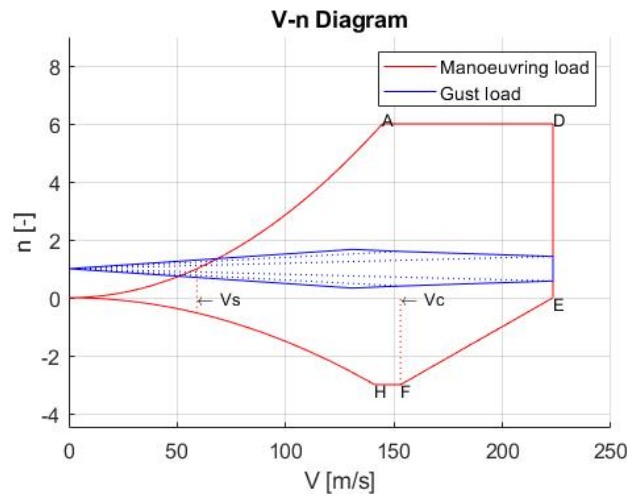


Figure 13.2: V-n Diagram.

For the gust loading diagram (blue) gust speeds of respectively 66 ft/s, 50 ft/s, and 25 ft/s were taken into account, which are FAR 25 regulations [1]. Since the designed aircraft requires military manoeuvring, the gust loadings are not dominant for the design. This is mainly due to the high load factor requirements (+6, -3) set by the customer.

From the analysis of the loading diagram, it can be concluded that the maximum load factors encountered by the aircraft during flight operations will be +6 and -3. However, to these values a safety factor of 1.5 has been applied. Hence the design load factors become +9 and -4.5.

### Landing On Austere Airfields

One mission specific load case will be the landing on austere airfields. During this type of landing, the shear forces introduced into the wing will be extensive. The magnitude of this shear force is calculated in this section.

During landing on austere airfields the aircraft main landing gear will encounter the biggest force during normal operations. It is important that the wing is able to cope with the shear forces this introduces into the airframe. During touchdown a maximum vertical speed of 10 ft/s is designed for [34]. However, a safety factor of 1.5 is applied which makes the maximum vertical speed equal to 15 ft/s. Using Equation 13.1, the kinetic energy of the aircraft is calculated at zero time before touchdown. Where  $W_{L_{max}}$  is the maximum landing weight, and  $V_{vertical_{max}}$  is the maximum vertical speed accounted for during landing.

$$E = \frac{1}{2} W_{L_{max}} V_{vertical_{max}}^2 \quad (13.1)$$

The work done during impact can be calculated using Equation 13.2. Where  $F_{landing}$  is the force introduced into the airframe during a landing at max vertical speed, and  $s$  is the deflection of the shock absorbers.

$$W = \frac{1}{2} F_{landing} s \quad (13.2)$$

By setting the kinetic energy equal to the work done during landing,  $F_{landing}$  can be calculated according to equation Equation 13.3. In this equation  $W_{L_{max}}$  is equal to 182 390 N according to the phase I iteration results (section 4.4), and  $s$  is set equal to 0.33 m

$$F_{landing} = \frac{W_{L_{max}} V_{vertical_{max}}^2}{s} \quad (13.3)$$

$F_{landing}$  is the dynamic load the aircraft observes during landing. So to calculate the total shear force per main gear strut Equation 13.4 is used.

$$V_{gear} = \frac{F_{landing} + W_{L_{max}}}{2} \quad (13.4)$$

From this analysis the result is a shear force per main landing gear strut  $V_{\text{gear}}$  equal to to 96 909 N.

### 13.3. Wing Structural Design

Identifying the forces acting on the wing is the first step in analysing the wing. The forces acting on the wing are as follows:

- Lift (distributed load).
- Weight of the wing (distributed load).
- Three hardpoints (point forces).
- Fuel weight (distributed load).
- Main landing gear (point force).
- Engine and propeller (point force).
- Drag (distributed load).

Assumptions that were made are as follows:

- The lift acts at 51% of the chord as this is the chordwise location of the aerodynamic centre, as shown in [Figure 13.3](#).
- The weights of the different components act at 50% of the chord.

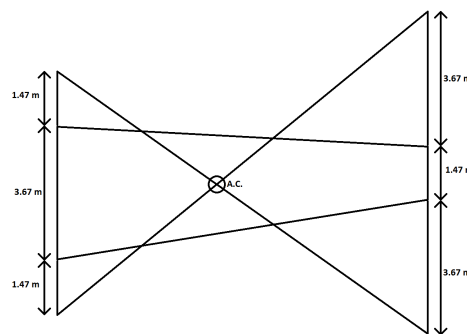


Figure 13.3: Method for finding the aerodynamic centre of the wing

To start the analysis, the forces and moments acting on the wing were evaluated during cruise and the internal reactions were found by analytic methods. Following this, the internal reactions were graphed to show the magnitude and direction of the internal reactions along the wing. [Figure 13.4a](#) shows the free body diagram front view of the right wing with the root on the right side of the aircraft in the y-z plane. [Figure 13.4b](#) shows the free body diagram looking top down in the x-y plane, again showing the forces acting on the wing.

Once these reactions were found in equation form, graphs were created showing how they vary along the span of the wing. These are shown in [Figure 13.5a](#) through [Figure 13.7b](#). Both wings are depicted in these graphs. Visible is a gap in the middle of each graph as the position along the wing takes into account the width of the fuselage which is 1.3 m.

The graphs below show the resultant forces and moments on both wings with the right wing being on the positive x-axis and the left wing on the negative x-axis. Starting with the resultant forces acting on the wing, [Figure 13.5a](#), [Figure 13.5b](#) and [Figure 13.6a](#) show the forces in the x, y and z-directions respectively. In the x-direction there is only drag of the wing and thrust of the engine acting. The drag is seen to be a trapezoidal distributed load over the length of the wing, explaining the quadratic decrease, and the thrust of the engine is assumed to be a point force which causes the step in the value around the 2.5 m mark, explaining the sudden step in force. The drag force is negative as the positive x-direction is towards the front of the aircraft which is also the direction the thrust is acting in. For the y-direction, there are no forces acting along the wing and so the graph is seen as a constant value of zero along both the left and right wing. Moving onto the forces in

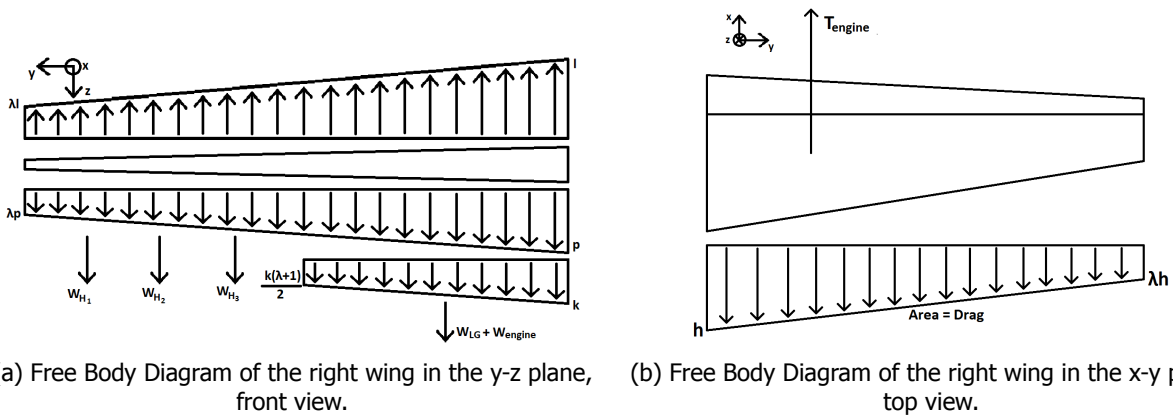
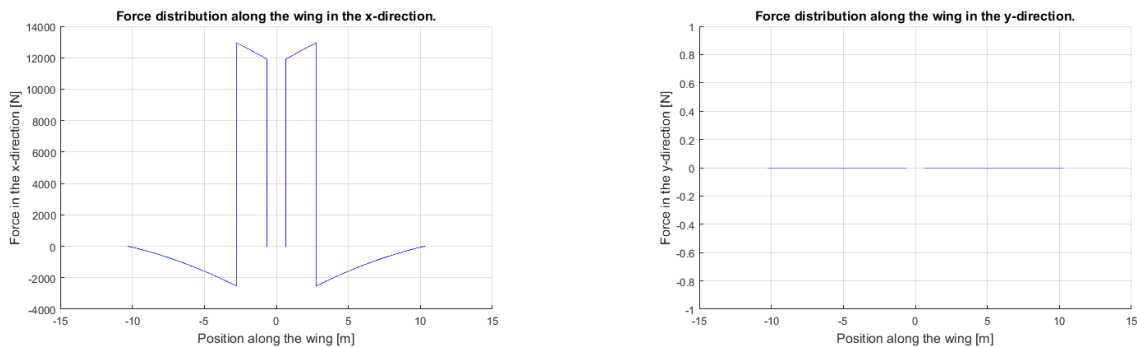


Figure 13.4: Free Body Diagrams of the right wing, front and top views in the y-z and x-y plane respectively.

the z-direction, in [Figure 13.6a](#) there is the lift acting along with the weight of the wing, the weight attached to the hardpoints, the weight of the fuel located in the wing, the engine and the landing gear. In order from right to left the components affecting the graph are the lift and wing weight, the three hardpoints which have each been assumed to carry the same amount of weight, the weight of the fuel which as a distributed load affects the gradient of the graph and finally a step caused by the engine and the landing gear. The resultant force is negative as the positive z-direction is downwards and the lift is greater than the weight of the different components.

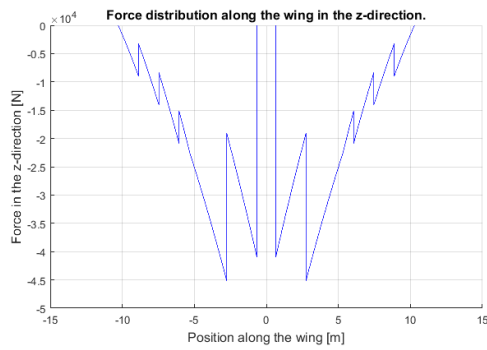
Looking at the moment graphs, [Figure 13.6b](#) shows the moments acting on the wing around the x-axis. All the forces that have been seen before cause moments around the x-axis however there are no pure moments meaning that there are no steps in the graph. The maximum moment is at the root as the lift generated by the wing is the dominant force over the wing. For the moments about the y-axis, these were taken about the quarter chord point on the wing as this is the line on the wing that is perpendicular to the fuselage. As said before, the weights of each wing component act at 50% of the chord and the lift is taken to act at 51% of the chord. The forces cause constant moments around the y-axis which are seen as steps in [Figure 13.7a](#) where the three hardpoints, the engine and the landing gear are. The lift, wing weight and fuel weight are all distributed loads causing a gradual increase in the moment rather than a step increase. The drag is the only contribution in [Figure 13.7b](#) from the tip of the wings until the position of the engine when the thrust causes a moment. As the thrust is much bigger than the drag, a bigger moment is caused meaning a sign change in the gradient of the graph and there being a net positive moment around the z-axis.



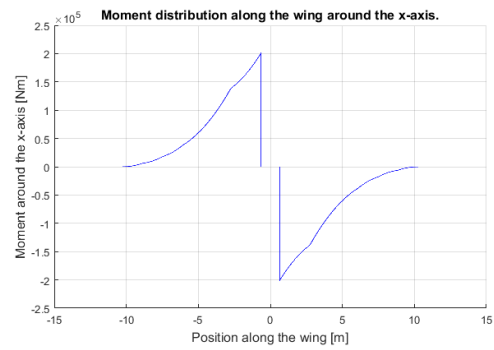
(a) Distribution of the resultant shear force in the x-direction along the wing during cruise. (b) Distribution of the resultant normal force in the y-direction along the wing during cruise.

Figure 13.5: Distribution of the forces in the x and y direction shown across the wing span during cruise.

Having the found the resultant forces and moments in the wing, these can then be used to find the forces and moments acting throughout the fuselage which is described in [section 13.5](#) but also the more extreme load cases can be analysed. The same equations that were used to find the resultant forces and moments in cruise can be used to analyse the forces and moments acting on the wing during the +9g load case.

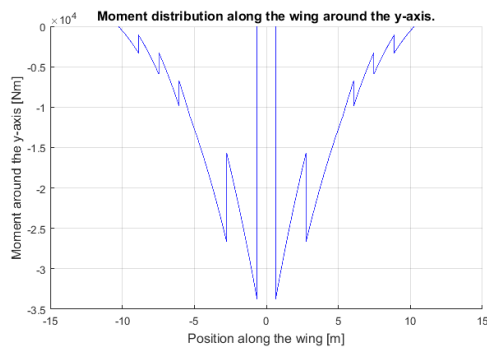


(a) Distribution of the resultant shear force in the z-direction along the wing during cruise.

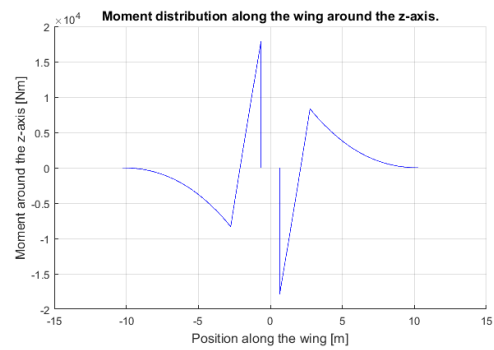


(b) Distribution of the resultant moment around the x-axis along the wing during cruise.

Figure 13.6: Distribution of the force in the z-direction and the moment around the x-axis shown across the wing span during cruise.



(a) Distribution of the resultant moment around the y-axis along the wing during cruise.



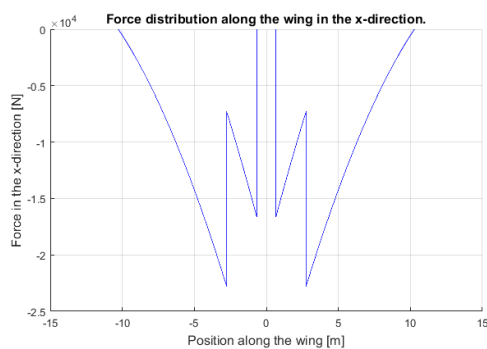
(b) Distribution of the resultant moment around the z-axis along the wing during cruise.

Figure 13.7: Distribution of the moments around the y and z axes shown across the wing span during cruise.

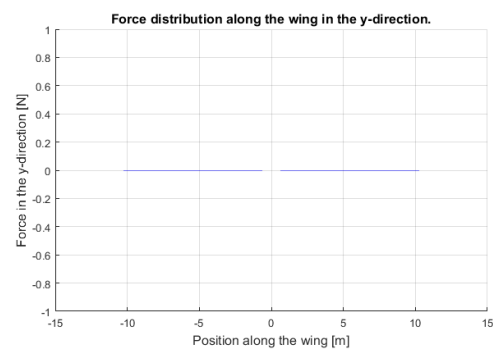
### Loading case +9g

During the case where the load factor becomes nine the lift is nine times greater than in the load case described above during cruise causing the drag to increase as well even though the weight components have the same weight. The increase of the lift and drag forces can be seen in [Figure 13.8a](#) through [Figure 13.10b](#). [Figure 13.8a](#) shows the thrust and the drag acting on the wing with the drag being much larger than in the corresponding figure above, [Figure 13.5a](#), whereas the force distribution in the y-direction has not changed as the lift and drag do not affect it. [Figure 13.9a](#) shows the forces in the z-direction which due to the lift increasing by a factor of nine has a higher gradient when compared to [Figure 13.9a](#). The point forces acting on the wing have the same values but are almost not visible due to this increased lift.

The gradient of [Figure 13.9b](#) is also greater than its corresponding graph in the cruise load case, [Figure 13.6b](#), and the maximum moment at the root is also greater due to the increased lift. As was seen with [Figure 13.8b](#), the increased lift is the biggest contribution to [Figure 13.10a](#) causing a much higher gradient and also making the moments caused by the weights of the different components on the wing hardly visible. The moments around the z-axis are seen in [Figure 13.10b](#) and due to the increase in drag, the thrust of the engine only lessens the gradient of the graph and does not change it as much as in [Figure 13.7b](#) meaning that the drag is still the dominant contribution to the graph.

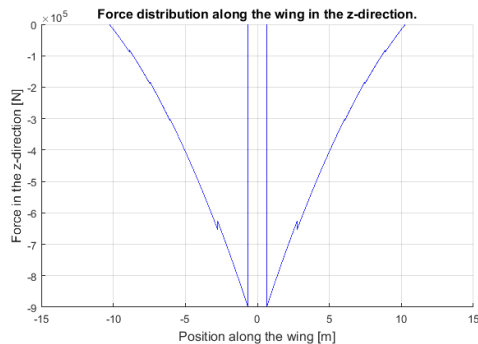


(a) Distribution of the resultant shear force in the x-direction along the wing during +9g loading.

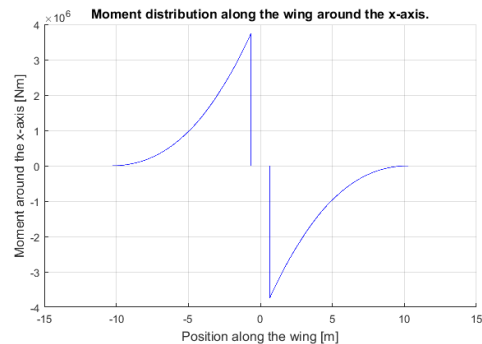


(b) Distribution of the resultant shear force in the y-direction along the wing during +9g loading.

Figure 13.8: Distribution of the forces in the x and y direction shown across the wing span during +9g loading.

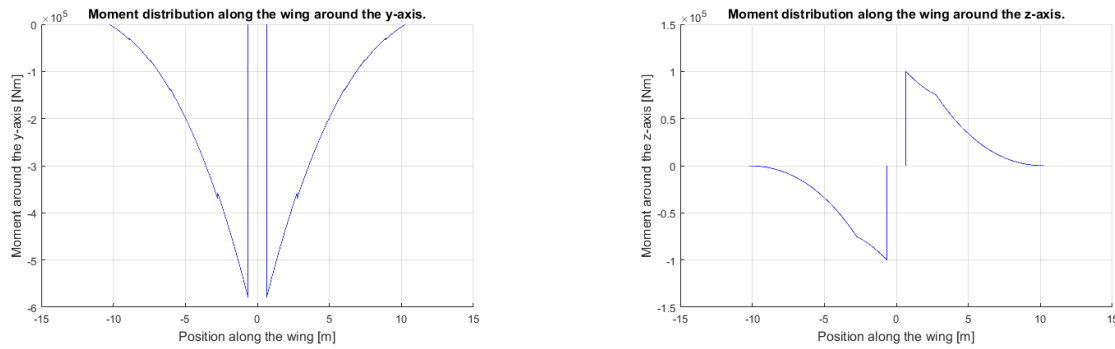


(a) Distribution of the resultant shear force in the z-direction along the wing during +9g loading.



(b) Distribution of the resultant moment around the x-axis along the wing during +9g loading.

Figure 13.9: Distribution of the forces in the x and y direction shown across the wing span during +9g loading.



(a) Distribution of the resultant moment around the y-axis along the wing during +9g loading. (b) Distribution of the resultant moment around the z-axis along the wing during +9g loading.

Figure 13.10: Distribution of the moments around the y and z axes shown across the wing span during +9g loading.

### Wing Box Designing Method

A wing box must be designed to withstand an array of failure types. However, designing a wing box has no standard recipe for which steps should be taken at what point. Alterations to any element affects all other elements in different failure modes. Due to this iterative nature of structural design, no intermediate results are shown, as they will be incoherent until all modes of failure are accounted for. The method will be described and the final results will be presented in the conclusion.

#### Wing box design assumptions

In the design process of the wing box, a few assumptions were made. The assumptions which were made decreased complexity of the process and time required to obtain a design of adequate accuracy. The assumptions are listed as follows. In the analyses, relevant effects of the assumptions will be discussed when apparent.

1. The wing box will possess a rectangular shape.
2. The wing box will be symmetric about z axis.
3. The wing box coordinate system will be aligned parallel to the body coordinate system of the aircraft.
4. The wing box will not twist along the wingspan.
5. No cutouts are designed at this design stage.
6. The wing box is the only carrier of loads exerted on the wing.
7. The wing box will taper in width and height along the span.
8. The amount of booms remains constant along the wingspan.
9. The front and aft spar locations remain at a constant percentage of to local chord.

#### Wing box shape

The general shape of the wing box is primarily dependent on the wing planform, fuel capacity and landing gear placement. Following from the planform requirements generated by aerodynamic analysis, the characteristics of the wing box can be calculated as follows. Firstly, the width scales with the chord length. The ratio between the root chord and tip chord been determined by the aerodynamic analysis to be equal to  $\lambda_{\text{chord}} = 0.4$ . The width taper ratio will therefore be equal to  $\lambda_{\text{chord}}$ . The aerodynamic analysis also determined the thickness over chord ratio, which was determined to be  $(t/c)_{\text{root}} = 0.18$  at the root and  $(t/c)_{\text{tip}} = 0.12$ . The shape following from the previous rules results in a rectangular-based frustum. The thickness taper ratio can be calculated to be 0.2667.

$$\lambda_{\text{thickness}} = \frac{(t/c)_{\text{tip}} C_{t,w}}{(t/c)_{\text{root}} C_{r,w}} \quad (13.5)$$

The wing box front and aft spar are located at a constant percentage of the chord. The front spar is located at 15% chord, while the aft spar is located at 60%. These locations have been determined to yield an optimal combination of effects. Firstly, a large wingbox height is desired since the skin and stringers located on the

top and bottom will possess a high Steiner term. This increases the moment of inertia while adding no weight. Secondly, the area enclosed by the wing box cross-section is desired to be large. This area is required for torsional resistance and available fuel tank volume. Thirdly, high lift devices must have sufficient room for proper operations and to house the actuator systems. Lastly, the landing gear placement plays a role. The forces generated by landing are considerable, and must be properly introduced into the structure. To ensure this, the landing gear will therefore be mounted at the aft spar. Due to the payload which is carried underneath the wings, the landing gear must retract forward into its nacelle. It is not desirable that the landing gear sticks out far towards the front. The aft spar position and landing gear size are designed such that the above aspects are taken into account, while ensuring the aircraft is stable on the ground.

Aerodynamic analysis has determined that the quarter chord sweep is zero. Since the quarter chord is therefore parallel to the body coordinate system, this is taken as a reference point for all forces exerted on the wing. However, as stated above, the wing box follows the spars which possess sweep. The wing box geometrical centre is used as reference point for all stress analysis. Transporting the forces in  $z$  from the quarter chord line to the wing box introduces a correction moment. The sum of the forces multiplied by the shift yields this moment. The shift described with respect to the quarter chord position is done using the root and tip chords. The torque about the wing box centroid along any position in  $y$  can be found in Equation 13.6.

$$\sum_{r=1}^n M_{y,wb} = \sum_{r=1}^n M_{y,qc} - \sum_{r=1}^n F_z \left[ ((S_a - S_f)C_{rw}/2) - \frac{((S_a - S_f)C_{rw}/2) - (S_a - S_f)C_{tw}/2}{\frac{b}{2}} y \right] \quad (13.6)$$

### Boom Method

The bending, shear and torsional loads were evaluated using a structural idealisation strategy known as the boom method. This simplifies multiple calculations greatly, such as the moment of inertia and shear flow determination. The effects the boom method has on the respective components of the design process will be indicated when applicable. Booms are theoretical lumps of effective area placed along the rectangular cross-section of the wing box. The boom areas correspond to the area which the actual longitudinal structural elements would possess located at the boom. These are the spars, skin and stringers. The vertical wing box elements represent the spars, while the horizontal elements represent the wing skin and stringers. The boom positions depend on the amount of booms which are placed on the respective side, as well as the height and width of the local cross-section. The amount of booms is constant over the length of the wingbox. The dimensions of the wing box cross-section can be determined with  $\lambda_{\text{chord}}$  and  $\lambda_{\text{thickness}}$ .

### Designing for Shear and Torsion

The forces in  $x$  and  $z$  and moments about  $y$  introduce shear stresses into the wingbox. These shear and torsion loads are mostly neutralised by the spars and skins, while the stringers add little resistance to shear. Therefore, only the spars and skins will be sized to resist these loads. Calculating the shear stresses in a cross-section is done by calculating the shear flow  $q_s$  throughout the fuselage. The shear flow can be interpreted as equal to the local shear stress multiplied by the local thickness. In open cross-sections, the shear flow is zero at any end of the cross-section. This is the case since there can be no stress at a free end. This is taken as a starting point, and Equation 13.7 is used to determine the shear flow throughout the rest of the cross-section.

$$q_s = -\frac{I_{xx}S_x - I_{xz}S_z}{I_{xx}I_{zz} - I_{xz}^2} \int_0^s txd s - \frac{I_{zz}S_z - I_{xz}S_x}{I_{zz}I_{xx} - I_{xz}^2} \int_0^s tzs ds \quad (13.7)$$

To evaluate this in a closed cell cross-section however, is more complicated. Firstly, there is no clear position where there is zero shear flow. This is the case since a closed cell has no free end. Therefore the cell must be cut to open the cell and start the determination of shear flow. The position where the cross-section is cut at may be assumed to have zero shear flow. Due to the boom representation, the continuous integral is replaced by a sum. A simplification may be made due to the following assumption made. The symmetry of the cross-section anywhere along the span causes the asymmetric moment of inertia  $I_{xz}$  to equal zero. The shear flow at any point is now approximated by Equation 13.8.

$$q_{s_{\text{open},i}} = -\frac{S_x}{I_{zz}} \left[ \sum_{r=1}^i B_r x_r \right] - \frac{S_z}{I_{xx}} \left[ \sum_{r=1}^n B_r z_r \right] \quad (13.8)$$

The shear flows along the cross-section have been determined. The cut made at the arbitrary point along the cell must be fixed. The cutting action will be amended by adding a constant correction shear flow to the cell,

$q_{s0}$ . The magnitude of the correction shear flow will be determined by taking moment equilibrium about any point. Since there naturally is no angular acceleration of the wing box during flight, the internal stresses must cause the same torque as the outside loads. The moments caused by internal stresses can be determined by multiplying the local shear flow by the local distance between booms and consequentially multiplying this with the respective moment arm. The moments were taken about the local centroid, since the boom positions depend on that location and can therefore be computed with Equation 13.9.

$$\sum_{i=1}^n p_i q_{s_{open},i} \sqrt{(x_{i+1} - x_i)^2 + (z_{i+1} - z_i)^2} + 2Aq_{s0} = V_x z_{V_x} + V_z x_{V_z} + M_y \quad (13.9)$$

Here  $A$  is the area enclosed by the local cross-section.  $p_i$  is the moment arm of the shear flow. Due to the rectangular shape of the cross-section, this is strictly a single distance in  $x$  or  $z$ , defined in the coordinates of the booms. Now that  $q_{s0}$  is known, the cell is closed and all shear flows along the cross-section can be described by Equation 13.10.

$$q_{s_{closed},i} = q_{s_{open},i} + q_{s0} \quad (13.10)$$

Performing the computations for a large number of steps along the span visualises the shear flow of the wing box along the span. The appropriate local thicknesses can be determined by dividing the shear flow by the shear yield strength, as shown in Equation 13.11. For a wing box with assumed boom areas of equal size, the shear flows at a local cross-section are visualised in Figure 13.11a. The shear flow behaviour along the span is visualised in Figure 13.11b. The introduction of shear force due to ordnance, engine and landing gear weight can be seen in the figure.

$$t_{design, shear, i} = \frac{q_{s_{closed}, i}}{\tau_{yield}} \quad (13.11)$$

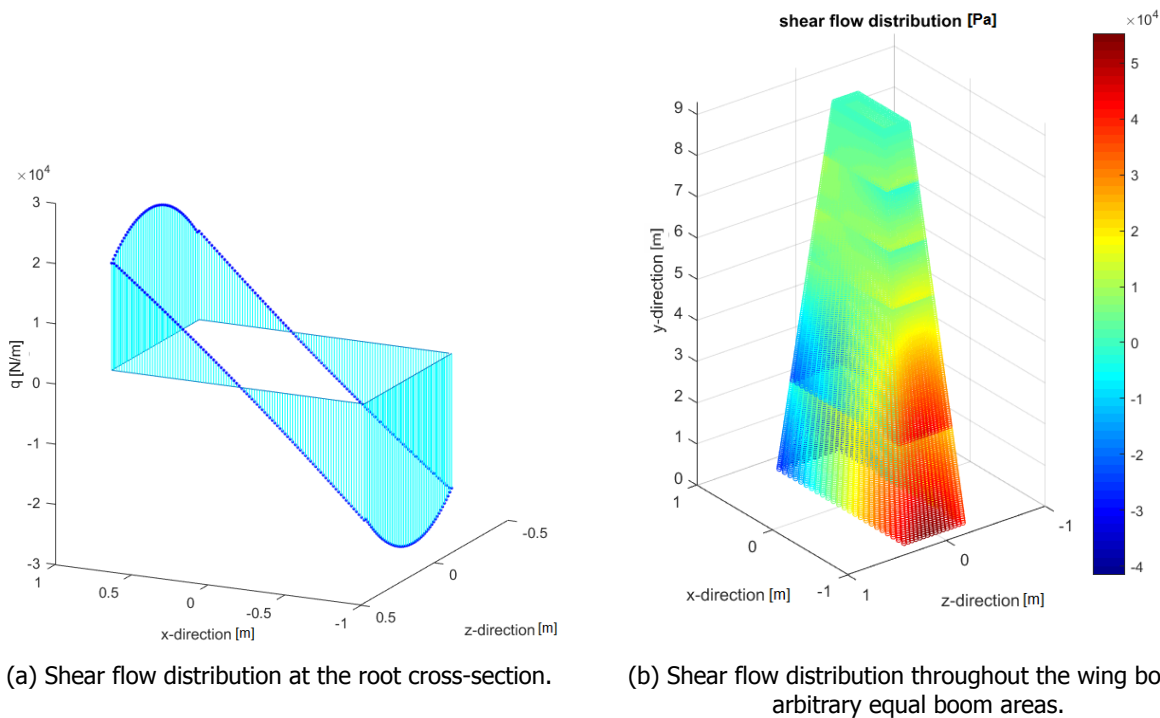


Figure 13.11: Shear flow distribution in the wing box and local cross-section.

The minimum required thicknesses of the skin and spars are evaluated on the whole cross-section along the span. To uphold the symmetry assumption, the skin thickness is designed to be mirrored at the top and bottom of the cross-section. The skin thickness is determined to be constant along a cross-section, as well as along the span. One reason is producibility. A skin of varying thickness is complicated to produce and expensive as well. Secondly, allowing skin panels to be larger, without discontinuities, reduces complexity and stress concentrations. Thirdly, since stringers still have to be added to resist bending and buckling, these can be reduced along the span due to the thicker skin being able to cope with a larger fraction of the loads. Lastly, since the structure needs to be designed in more detail in the future, this is deemed an appropriate method.

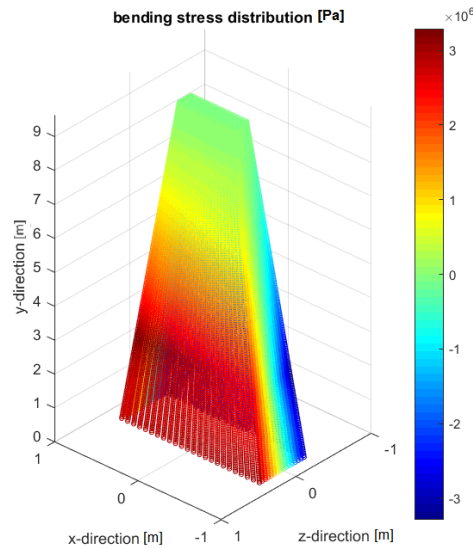


Figure 13.12: Bending induced normal stress distribution throughout the wingbox for equal boom areas

### Designing for Bending

The forces in  $x$  and  $z$  introduce moments into the wing box, which have to be resisted. The induced normal stresses due to bending can be evaluated with the local internal moment and moment of inertia. Due to symmetry, the determination of these stresses is done with Equation 13.12. The change in sign is due to the downwards defined  $z$ -axis.

$$\sigma_y = \frac{-M_x z}{I_{xx}} + \frac{M_z x}{I_{zz}} \quad (13.12)$$

The induced normal stress was visualised for booms of equal area to obtain insight in the 3-dimensional stress distribution. This is visualised in Figure 13.12.

The normal stresses are taken up by the skins, spars and stringers. While the spars simply require a certain thickness to be able to cope with the induced normal loads as well, there is a choice on the top and bottom of the wing box. Since the skin and stringers are located at a comparable vertical distance away from centroid, the necessary area to counteract the bending could be invested into a thicker skin or more stringers. Since compression buckling relies heavily on the local moment of inertia caused primarily by the stringers, as well as the distance between the stringers, the focus will go to the stringers. The skin should naturally have a sufficient thickness to cope with the combined loads of shear and normal stress. Having increased the skin thickness, the amount of stringers which are required along the span are calculated.

### Designing for Compressive Buckling

In areas of the wing where compressive stresses are present, buckling is another mode of failure which has to be considered. Especially during high manoeuvring loads, buckling is a design driver. During a +9g manoeuvre, the top will be in heavy compression, as will the bottom during -4.5. The buckling of the top and bottom of the wing box is analysed, where the skin plus stringers are analysed to fail as a whole.

#### Skin buckling

Staying true to the symmetry assumption, the amount of stringers placed on the top skin will equal the amount of stringers on the bottom skin. Comparing the +9g to the -4.5g, it is easily reasoned that the bottom skin requires less stringers than the top. Even though this may yield a sub-optimal solution, there is good reason to assume this at the moment. Since the wings are unarmoured and made of relatively soft aluminium, upon receiving ground fire, secondary structural elements may fail. Being damage tolerant is a vital requirement for performing the CAS role. With the current engagement philosophy in mind, the bottom of the wings and fuselage have the largest chance to be hit by ground fire. Possessing redundant stringers may increase survivability significantly.

Next to stringers, another output will be the rib placement in the wing box. Buckling depends on the length of the structure in line with the load. The top and bottom are fastened to the ribs and therefore will not buckle

there, as it is not free to move up nor down. The distance between the two ribs, the rib pitch, is therefore used and is a design variable.

Another element which has to be taken into account is the buckling mode. This mode is a constant, also known as the buckling coefficient, which can be determined by the mode of support of the analysed section. While for 1-dimensional problems the buckling coefficient is easily derived, 2-dimensional values have been experimentally established. The coefficient value per case is visualised in Figure 13.13. For any case which is analysed in this section, the members are fully clamped on four sides (CCCC in the figure). However, this is not the only thing which influences the constant. As can be seen, the aspect ratio of the panel also plays a role. The curve could be approximated and imported into the program to approximate the coefficient more accurately. However, there is no data for an aspect ratio below 0.8, and the curve is not continuous. The asymptotic value of 6.98 is taken to remain conservative.

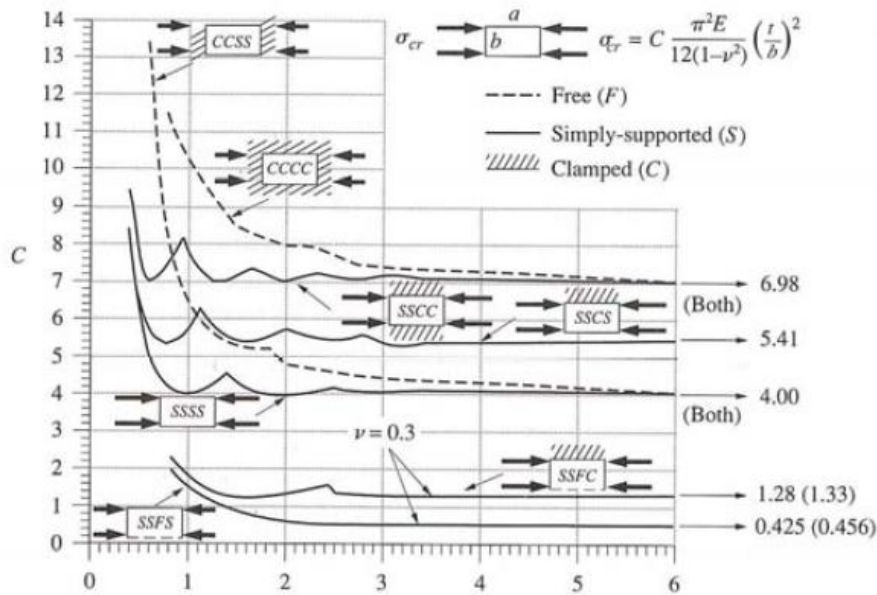


Figure 13.13: Buckling coefficient  $C$  [35].

The last input for the buckling equation depends is the Young's modulus of the material used. Aluminium needs a larger area to cope with the same stresses compared to high-strength steels or titanium. With this increased area comes the advantage of a much larger moment of inertia, at comparable weight. Aluminium is desired greatly in the buckling application due to this property. Now this has all been established, the critical buckling load  $P_{crit}$  can be described by Equation 13.13. In the equation  $C_{buckle}$  equals the buckling coefficient,  $E_{al}$  the Young's modulus of aluminium,  $I_{local}$  the moment of inertia of the local section and  $L$  is the rib pitch.

$$P_{crit} = \frac{C_{buckle} \pi^2 E_{al} I_{local}}{L^2} \quad (13.13)$$

Since the design outputs are the stringers and ribs,  $I_{local}$  and  $L$  must be found by iteration. This is not the only varying parameter however. The critical buckling load changes with the local stress and area. this is the case since the critical buckling load should be equal to the maximum compressive stress divided by the area. The maximum compressive stress can be determined by 13.12, where it can be seen that this again depends on the cross-sectional moments of inertia, which change due to stringer placement. The area also depends on stringer placement. Iterations must be performed to arrive at the optimal result.

The above method was applied for two cases:

1. +9g with no damage was evaluated to ascertain buckling resistance for this ultimate manoeuvring load.
2. 3g with damage was evaluated. Due to the high-risk functions the aircraft must perform, damage must be accounted for. The aircraft must be able to withstand buckling failure if a single stringer its connected rib fail, effectively doubling the stringer pitch and rib pitch. If damage is taken, it was deemed acceptable if manoeuvring loads are not above 3g, as the pilot should not push the damaged aircraft to clean maximum loads. It was found that this second case produced the most restrictive combination of stringer pitch and rib pitch.

### Spar buckling

The spar is not as straightforward to design for buckling as the skin mentioned above. During any flight condition, the normal stresses vary greatly over the spars. Generally it varies from compression on the top to tension at the bottom. Therefore, the highest moment about  $z$  was identified and isolated. Applying this moment on the wingbox yields a constant compression in one spar, and tension in the other. The stress present at the spar determined by Equation 13.12 was used in combination with Equation 13.13 is used to determine a minimum thickness for compression buckling.

### Designing for Shear Buckling

Another type of failure, especially occurring in thin-walled structural members, is shear buckling. The spars are analysed since these structural members are designed to carry most of the shear, and are not supported by stringers. The critical shear stress for shear buckling to occur can be found in Equation 13.14 [36]. Here  $C_{buckle}$  is the same buckling mode as found in 13.3, as the spar is held in place by the ribs and top skin.  $t$  is the local thickness, and  $L$  is the maximum length of the analysed rectangular spar section.

$$\tau_{crit} = \frac{C_{buckle}\pi^2 E_{al}}{12(1-\nu^2)} \left(\frac{t}{L}\right)^2 \quad (13.14)$$

### Structural Weight

The optimal result referred to in Figure 13.3 has not been established yet. Naturally, a structure should be able to cope with all design loads. Within that design space however, the optimal solution in aerospace would be the solution for the lowest weight. Naturally, the design should be safe and therefore proper safety margins are implemented, as well as conservative estimates for complex behaviour, such as buckling modes. For some design aspects, such as the stringer and rib placement to counteract buckling, there is no single solution. The lowest weight has been set as the goal, while ensuring safety and practical feasibility. Figure 13.3 elaborates on the section weights which were found. These weights were calculated with the density of the aluminium which is used in the wing box, which has a value of 2590 kg/m<sup>3</sup>. More information of this material can be found in section 13.6.

### Component Design

For the stringers and ribs, there are multiple designs possible while having comparable functionality. Some analysis has been done to assess their shape and general properties.

#### Stringers

The primary purpose of stringers is to increase local stiffness to avoid buckling failure, and ensuring the aerodynamic shape of the wing skin. There are multiple stringer designs used in the market, all of them fulfilling this purpose. A qualitative analysis has been done to select the optimal stringer for the wing box. The result of the qualitative analysis yielded a z-stringer design. Figure 13.14a presents the stringer cross-section and dimensions. Not presented is the thickness, which is 2.6 mm, which was chosen to be the same as the skin thickness for production reasons.

The Z-stringer was finally selected among many since it has the right combinations of properties. Firstly, due to its geometry, it can easily be attached with rivets. Due to the high likelihood of damage, fail-safe components must be easily replaceable. For stringers the preferred fastening method becomes rivets in combination with an adhesive bond. The z-stringer allows the placement of rivets on the bottom flange. Secondly, inspectibility plays a role. While hat stringers are very commonly used on surfaces with much compression, they enclose a space which cannot be inspected. This increases the chance of undetected cracks or corrosion. The z-stringer is fully inspectible and thus scores well in this category. Thirdly, stringer pitch comes to mind. A z-stringer is essentially half a hat stringer and therefore twice the number of z-stringers must be placed. The moment of inertia is essentially the same, but the stringer pitch is not. This lower stringer pitch decreases the free skin length which reduces critical buckling load of the skin. Lastly, if the aircraft wing is penetrated by a bullet, it can damage components. If a z-stringer is damaged, only half the cross-sectional area is lost compared to a hat stringer.

#### Spars

The spars were designed to resist most of the vertical shear loads. It has been designed to withstand shear buckling, as well as to introduce the loads into the skin by having a flange of sufficient size. The flange was sized with moment of inertia considerations, as well as remaining above 0.1 m to effectively transport loads from the spar to the skin and vice versa, taking into account stress concentrations. The flanges are a constant



Figure 13.14: Stiffener cross-sections. All dimensions are in m.

0.1082 m, while the spar height scales with the thickness taper ratio of the wing box. The root chord spar is visualised in [Figure 13.14b](#). The thickness of the is a constant 0.0055 m along the vertical element and horizontal elements.

### Ribs

While most ribs in the wing box carry light loads, there are a few ribs which are under heavy loads, which must be designed separately. These ribs are located either at hardpoints, the engine, and the main landing gear. The ribs were designed to assure proper wing box shape under their forces, as well as to effectively introduce loads into the local cross-section, mitigating stress concentrations. The aim of this subsection is to find the approximate thickness and stiffness to handle normal and buckling failure. It is a basic approximation, since rib loads are not easily determined. In this approximation, the weights will be used to obtain the final weight per section.

In the designing of the ribs, it is assumed that the ribs are of a rectangular shape. Also, the continuous spars were allowed to run through, reducing the effective width with an estimated factor 2. Furthermore it is assumed that the loads the ribs have to distribute are point forces introduced externally. The mentioned rib loads are:

- $F_{\text{hardpoint,max}} = 18\,093\text{ N}$ , derived from the maximum ordnance weight in [Table 6.3](#).
- $F_{\text{thrust,max}} = 34\,160\text{ N}$ , derived from engine thrust specifications in [chapter 11](#).
- $F_{\text{landing,max}} = 96\,909\text{ N}$ , derived from the hard landing loads, which can be found in [Figure 13.2](#).

The rib maximum normal stress is computed to find the required thickness for yielding. To counteract compression buckling, the ribs are stiffened with the same z-stringers as used on the skin. A hardpoint rib can be found in [Figure 13.15](#). As mentioned, this is a basic estimation of the weight and stiffening needed for the rib to function properly, and should be analysed in more detail in a later design stage. The rib which has to withstand the engine thrust should possess five stringers, in horizontal orientation. The rib which has to counteract the landing forces should possess 6 vertical stringers to avoid buckling. Since the engine and landing gear are attached to the wing box at the same position, these ribs must be combined. For now, this rib will possess six vertical stringers on one side, while having five horizontal stringers on the other. Further analysis is required on this particular rib, as high stress concentrations could be induced by poor rib design. The rib thickness was chosen to be same as the skin thickness required, 0.0026 m. This was done since the same plate material could be used for the skin as well for the ribs, decreasing production and logistical complexity, which translates into reduced costs.

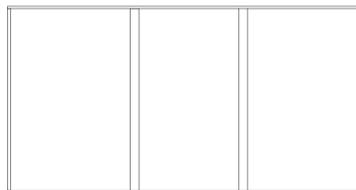


Figure 13.15: Front view of the hardpoint rib design.

### Mohr stress transformation

While all individual stress components are obtained in the methods described above, the final stress state of a particle is not yet known. The normal and shear stress on a particle are defined with the coordinate system which is chosen. To define the maximum stress from any direction on a particle, Mohr's stress transform is applied. Since thin-walled members and assumptions are being used, the transform will be in two dimensions. The stress transform can be visualised by Mohr's stress circle, which can be found in Figure 13.16<sup>2</sup>.

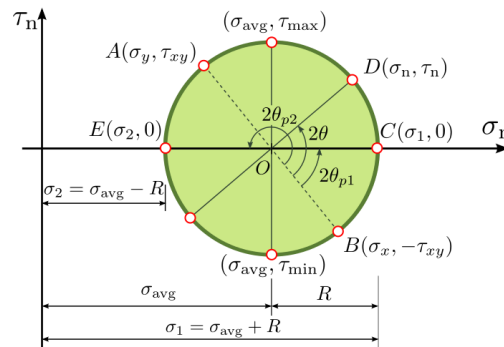


Figure 13.16: Mohr's stress circle.

If the normal and shear stresses are determined at a point, the transform can be performed. The stress state of the particle can be visualised by  $(\sigma_x, -\tau_{xy})$  (point B). Due to this particular structure and load cases, a particle can only possess a normal stress in the y-direction and a shear stress state. Therefore, point A is positioned on the  $\tau_n$  axis, while point B is the current stress state of the particle. The radius can be determined with trigonometric relations and consecutively, the maximum and minimum stress states are determined. The maximum normal stress state is equal to the average stress state plus the radius, while the maximum shear stress is equal to the radius. The results of this transform along the span of the wing box is visualised in Figure 13.19, Figure 13.21 and Figure 13.23. The maximum transformed stress values can be found in the last three columns of Table 13.3.

### Wing Box Parameters

After an iterative design period, the wing box design was finalised. The thicknesses of the skin, spar and rib can be found in Table 13.1. The section stiffener and weight parameters can be found in Table 13.2.

Table 13.1: Wing box thickness parameters.

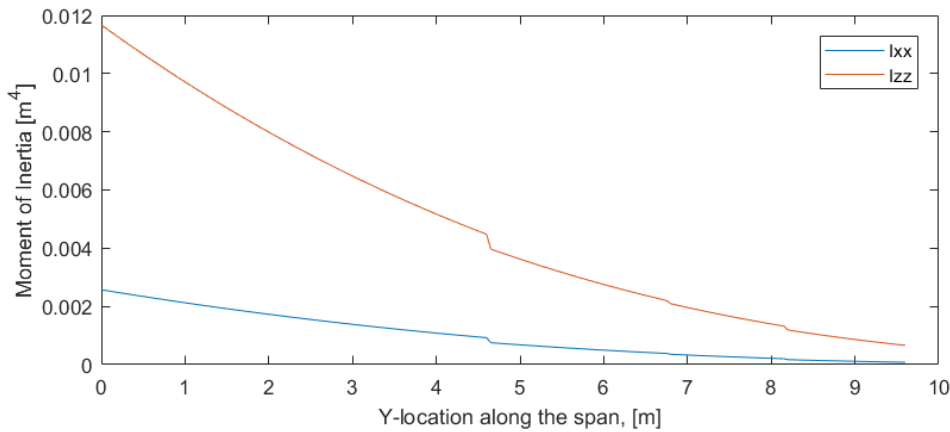
Skin thickness [m]	Spar Thickness [m]	Rib thickness [m]	Stringer thickness [m]
0.0026	0.0055	0.0026	0.0026

Table 13.2: Wing box section parameters.

Section [-]	Coordinates [m]	Stringers [-]	Stringer pitch [m]	Ribs [-]	Rib pitch [m]	Section Weight [kg]
1	$0.00 \leq y < 2.45$	28	0.0590	8	0.3063	280.81
2	$2.45 \leq y < 4.65$	28	0.0500	8	0.2750	229.92
3	$4.65 \leq y < 5.40$	20	0.0587	4	0.1875	67.44
4	$5.40 \leq y < 6.80$	20	0.0548	8	0.1750	119.07
5	$6.80 \leq y < 8.20$	18	0.0529	8	0.1750	104.04
6	$8.20 \leq y < 9.60$	14	0.0577	8	0.1750	86.00
<b>Total</b>	-	-	-	44	-	887.28

The amount of stringers per section was dominated by compression buckling with damage tolerance, at 3g. The stringers run until the last spar in the section, to ensure proper load introduction. This change in number of stringers from one section to the other leads to discontinuities in the moment of inertia. The moments of inertia about  $x$ ,  $I_{xx}$ , and  $z$ ,  $I_{zz}$ , are visualised in Figure 13.17.

<sup>2</sup>Mohr Circle plane stress - [\protect\unhbox\voidb@x\hbox{https://en.wikipedia.org/wiki/Mohr%27s\\_circle#/media/File:Mohr\\_Circle\\_plane\\_stress\\_\(angle\).svg}](https://en.wikipedia.org/wiki/Mohr%27s_circle#/media/File:Mohr_Circle_plane_stress_(angle).svg) [accessed 11-06-2018].

Figure 13.17: The moments of inertia about the  $x$  and  $z$  axis

The extreme stresses in the wing box are shown in [Table 13.3](#) per load case. This signifies the design-driving characteristics of the +9 g manoeuvre, while the -4.5 g manoeuvre and hard landing are less critical for wing box design. The fact that the -4.5 g load case is less relevant is due to the symmetrical approach used in the design process. For an asymmetric approach, the wing box could be tailored to be critical in both load cases. This would yield a lighter and thus more efficient design. The process however requires more time and for this stage of the design, would not yield much more accurate weights results specifically. This is the case since the design will need to be altered to account for stress concentrations. This will increase the weight again. A conservative approach which has been performed in this design process was deemed more suitable as an estimate of the weight. The Class II weight estimation yielded a structural wing weight of 993.95 kg. The total weight of the wing box is calculated to be 887.28 kg, as can be seen in the final row of [Table 13.2](#). The discrepancy in weight is most likely due to the exclusion of the aerodynamic skin which is not included in the wing box cross section.

An estimate of the extra weight can be made if the rest of the airfoil is added. If unstiffened skin will be added in the shape of the airfoil, the weight is estimated in [Equation 13.15](#). This leads to a weight of 1070.69 kg. This is not an accurate estimation. Firstly this is due to the crude method used for the skin weight estimation. Only using skin will in reality not happen, especially due to buckling effects. Secondly, as the moment of inertia and enclosed area will substantially increase, the required thicknesses of the established wing box will go down, and thus the weight will follow. Most likely the true value for the wing weight, were it fully developed, would lie between this 887.28 kg and 1070.69 kg. The class II estimate confirms this.

$$W_{\text{extra}} = 2 \frac{C_r + C_t}{2} (0.4 + 0.15) t_{\text{skin}} \frac{b}{2} \rho_{al} = 183.4 \text{ kg} \quad (13.15)$$

Table 13.3: Extreme stress values for extreme load cases

Case	Max. $\sigma$ [Pa]	Max. $\tau$ [Pa]	Min. $\tau$ [Pa]	Mohr $\sigma$ [Pa]	Mohr $\sigma$ [Pa]	Mohr $\tau_{\text{max}}$ [Pa]
+9g	$\pm 4.194 \times 10^8$	$2.385 \times 10^8$	$-2.034 \times 10^8$	$5.199 \times 10^8$	$-4.962 \times 10^8$	$\pm 3.111 \times 10^8$
-4.5g	$\pm 2.605 \times 10^8$	$1.271 \times 10^8$	$-1.542 \times 10^8$	$3.101 \times 10^8$	$-3.258 \times 10^8$	$\pm 1.961 \times 10^8$
HL (1g)	$\pm 1.867 \times 10^7$	$5.162 \times 10^7$	$-1.815 \times 10^7$	$6.161 \times 10^7$	$-5.841 \times 10^7$	$\pm 5.243 \times 10^7$

### Stress Distributions

The stress distributions for the final design are visualised below for different load cases. The spars and skins are shown with their respective local stress.

#### +9g

The +9g load case stress distributions can be found in [Figure 13.18](#). It shows the stress distribution of the bending induced normal stress distribution, as well as the shear distribution. These stresses were transformed as described in [Figure 13.3](#) to obtain the maximum stresses within the plane. For this specific load case, this was found to cause the largest stresses anywhere within the wing box. The value for this can be found in [Table 13.3](#), where it is shown in bold. The location of this maximum (tensile) stress is at the root chord vertex

at negative x, positive z. Since the yield stress of the material is  $5.2 \times 10^8$  Pa as described in section 13.6, this is designed to be just below it. The maximum shear is located at the root vertex, positive x, negative z. For the graphs showing the Mohr transformed normal stresses, a discontinuity can be seen. As can be seen in Figure 13.19a, the sign shifts at half the wing box height. This is the case since the transformed stresses of largest magnitude are plotted. The magnitude will be continuous, while the sign may not be.

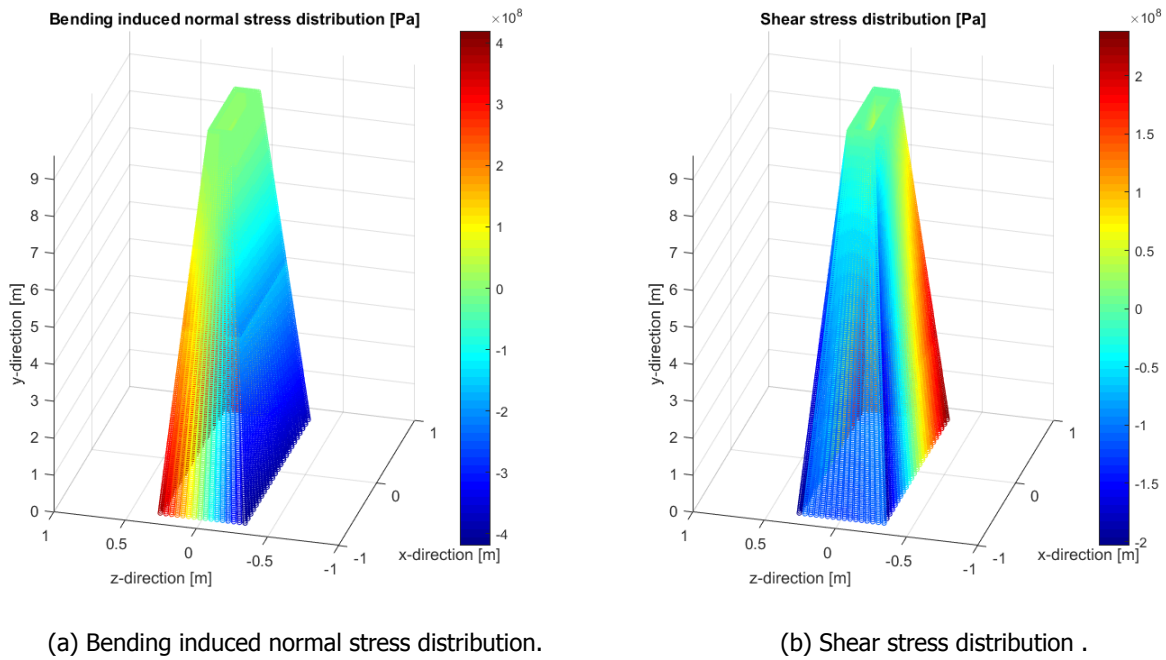


Figure 13.18: Stress distributions for the final spar and skin design for +9g.

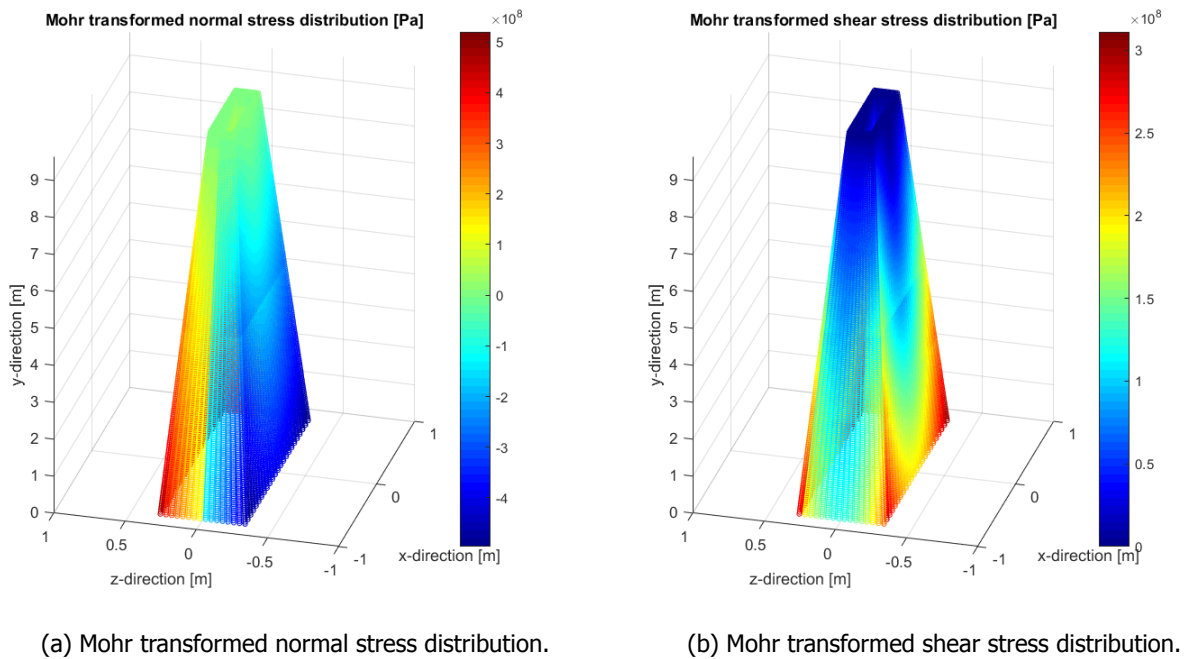
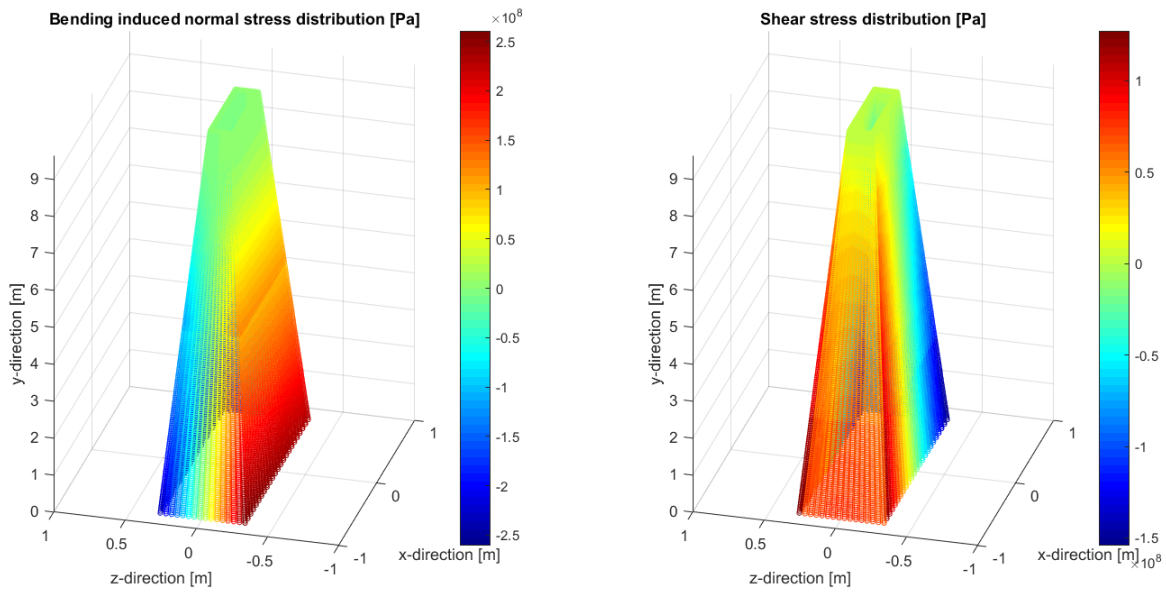


Figure 13.19: Stress distributions for the final spar and skin design for +9g.

**-4.5g**

The -4.5g load case stress distributions can be found in Figure 13.20. Similarly to the +9g case, the normal and shear stresses are visualised separately, before the transformed Mohr stress distribution is shown in Figure 13.21. The Mohr stress distribution discontinuity has the same reason as for the +9g load case. The

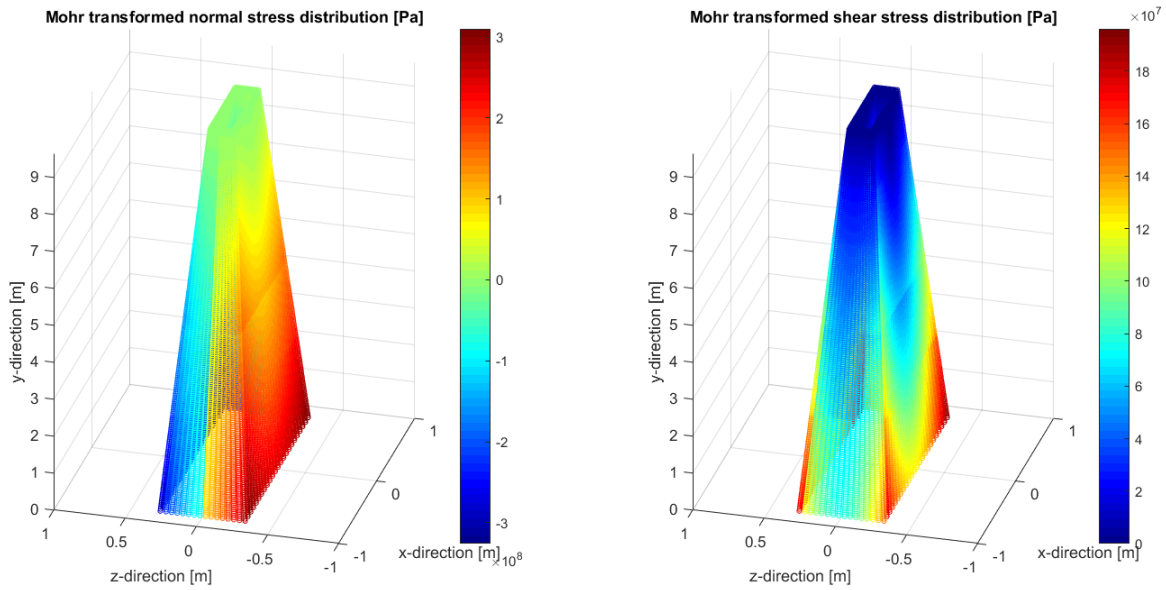
maximum normal stress is located at a root vertex, positive x, positive z. The maximum shear is located at the root vertex, at positive x, negative z.



(a) Bending induced normal stress distribution.

(b) Shear stress distribution.

Figure 13.20: Stress distributions for the final spar and skin design for -4.5g.



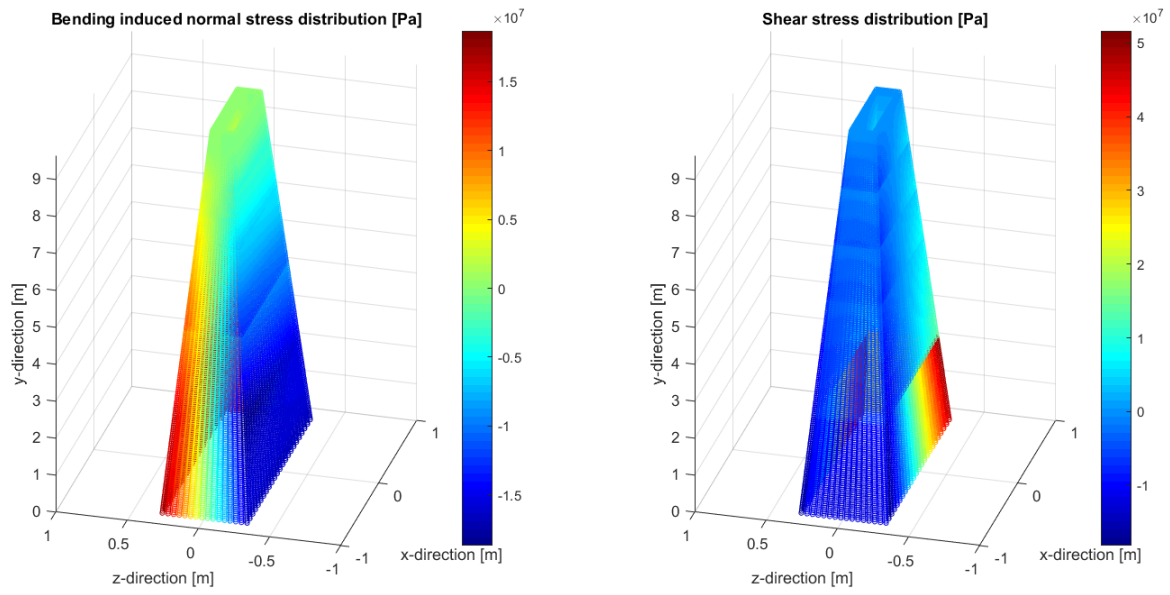
(a) Mohr transformed normal stress distribution.

(b) Mohr transformed shear stress distribution.

Figure 13.21: Mohr transformed stress distributions for the final spar and skin design for -4.5g.

**Hard landing at +1g**

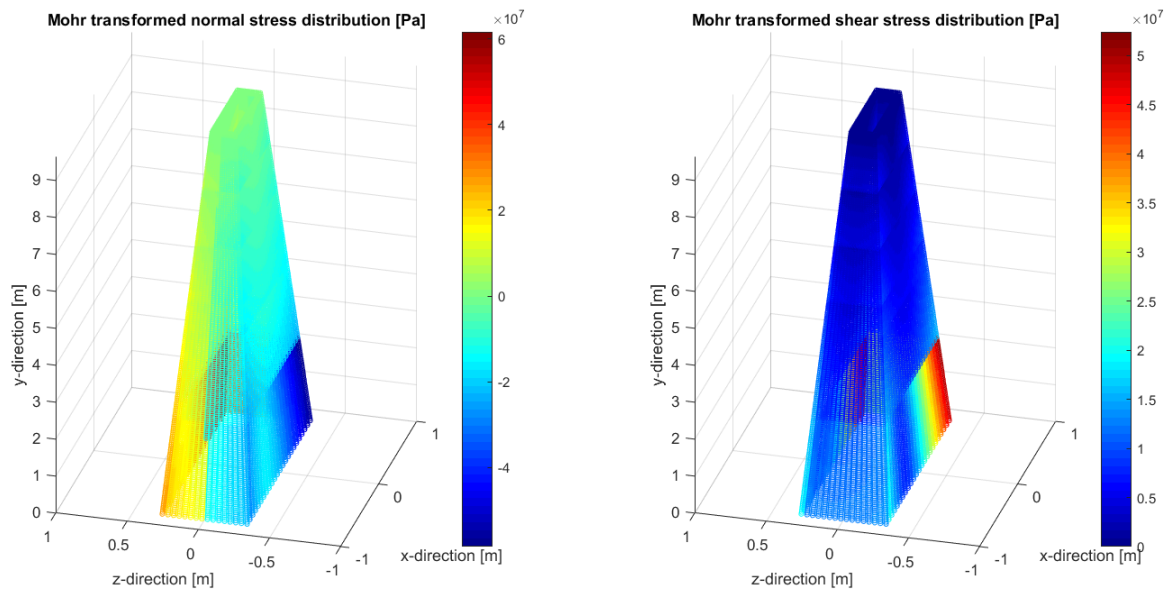
The hard landing load case stress distributions can be found in [Figure 13.22](#). Similarly to the other two cases, the normal and shear stresses are visualised separately, after which the transformed Mohr stress distribution is shown in [Figure 13.23](#). The Mohr stress distribution discontinuity has the same reason as for the +9g load case. the discontinuity in shear stress is logically due to the large induced shear load on the landing gear rib. The maximum shear stress location can be found at a root vertex, at positive x, positive z. The maximum normal stress can be found at the same position.



(a) Bending induced normal stress distribution.

(b) Shear stress distribution.

Figure 13.22: Stress distributions of the final spar and skin design for hard landing at +1g.



(a) Mohr transformed extreme normal stress distribution.

(b) Mohr transformed extreme shear stress distribution.

Figure 13.23: Mohr transformed Stress distributions of the final spar and skin design for hard landing at +1g.

## Wing Deflection

After analysing the forces on the wing, the deflection of the wing can be found. Due to the model of the forces that act on the wing standard solutions can be utilised to find the deflection distribution and the maximum deflection at the tip of the wing. The deflection distribution from each load was analysed separately and subsequently summed using the principle of superposition. The three standard solutions that were used were the solutions for a uniform distributed load, uniformly varying distributed load and a point force positioned at a point along the wing. For the deflection, the equations used for the three cases are Equation 13.16, Equation 13.17 and Equation 13.18 respectively.

$$v = \frac{\omega y^2}{24EI} (y^2 + 6l^2 - 4ly) \quad (13.16)$$

$$v = \frac{\omega_0 y^2}{120lEI} (10l^3 - 10l^2y + 5ly^2 - y^3) \quad (13.17)$$

$$v = \begin{cases} \frac{Py^2}{6EI} (3a - y), & \text{for } 0 < y < a \\ \frac{Pa^2}{6EI} (3y - a), & \text{for } a < y < l \end{cases} \quad (13.18)$$

$v$  is the deflection at a point  $y$  along the wing measured from the centre of the fuselage.  $E$  and  $I$  are the Young's Modulus and the Moment of Inertia of the designed wingbox structure.  $\omega$  and  $\omega_0$  are the maximum values of the uniform and uniformly varying distributed loads used for the lift and weights of the wing and fuel.  $P$  is the value of the point force that is looked at for example with the engine and landing gear.  $l$  is the semi span of the wing and  $a$  is the position from the centre of the fuselage to the point forces.

The deflection on the wing depends on the loads all along the wing as they all affect the value of the deflection at each spanwise point looked at. This means that it is not possible to "walk" along the wing and see how the deflection is distributed. This also means that, with these standard solutions a varying moment of inertia cannot be accounted for. The varying moment of inertia comes from the wing and wingbox being tapered in more than one direction, that is to say in chordwise length and thickness. This means that a constant moment of inertia should be used at this stage to find the deflection along the wing. The average value of the moment of inertia was calculated as the mean of the moments of inertia of each cross section that were spaced 0.0001 m apart. This gives an overestimation of the deflection that occurs at the sections of the wing that are closer to the root than the averaged and gives an underestimation of the deflection in sections that are further towards the tip than the average section. As can be seen in Figure 13.24 the wing curves slightly down and reaches a value of 0.0064 m downwards and then deflects upwards towards the tip reaching a final tip deflection of 0.4961 m upwards. The slight downward deflection in the graph could be explained by having the three hardpoints located on the wing.

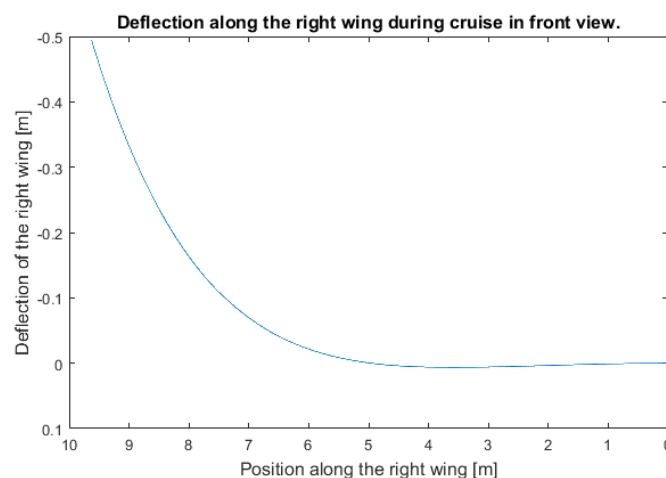


Figure 13.24: Deflection of the right wing during cruise condition looking at the front view.

## 13.4. Tail Design

The forces acting on the tail were identified as follows:

- Weight of the wing (distributed load).
- Drag (distributed load).

Considering the nature of the split X tail, the forces were looked at in terms of the  $x$ ,  $y$  and  $z$  directions as defined earlier in the chapter. This was done so that when the forces were calculated along the tail they could be easily translated into forces that can be used straight away with the fuselage force and moment equations. [Figure 13.25a](#) and [Figure 13.25b](#) show the free body diagrams of the right side of the split X tail in the  $y$ - $z$  plane and  $x$ - $y$  plane respectively and from these the cruise force and moment equations were found.

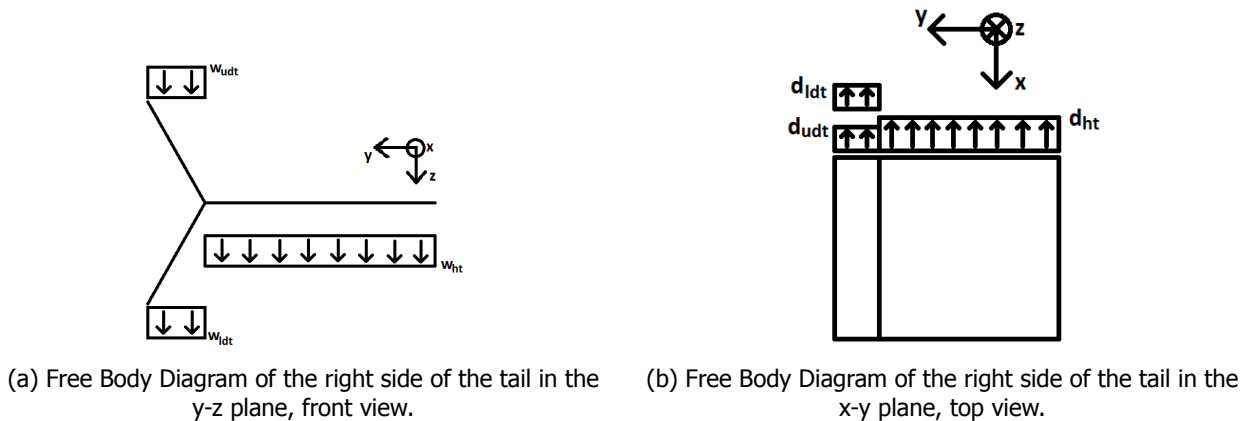


Figure 13.25: Free Body Diagrams of the right side of the tail looking at the front and top views in the  $y$ - $z$  and  $x$ - $y$  plane respectively.

The free-body diagrams result in [Figure 13.26a](#) through [Figure 13.28b](#). Then using these equations [Figure 13.26a](#) through [Figure 13.28b](#) are found showing the distribution of the resultant forces and moments throughout the tail.

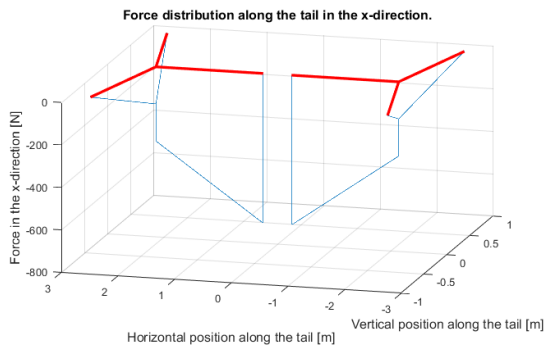
In [Figure 13.26a](#) through [Figure 13.28b](#) there are two sets of lines that have been plotted. The thicker red lines show the geometry of the split X tail and the thinner blue lines show the distribution of the relevant force or moment being looked at. [Figure 13.26a](#) contains only the drag acting on the tail which is assumed to be a distributed load with a constant magnitude due to the constant chord of the tail. This results in a constant gradient of the graph with a jump in the value of the resultant force at the junction between the upper and lower diagonal parts of the tail. This is because the drag acting on the diagonal parts of the tail combines at the junction with the horizontal tail giving a bigger magnitude in the drag force at that point. As with the wing there are no forces acting in the  $y$ -direction meaning that force distribution in [Figure 13.26b](#) is constant along the tail at a value of zero. In [Figure 13.27a](#) only the tail weight is present which is modelled as a constant magnitude distributed load. This causes a constant gradient with a jump at the junction between the diagonal and horizontal parts of the tail, again due to the combination of the forces acting on the tail.

The moments around the  $x$ -axis only concern the weight of the tail as there is no moment caused by the drag around the  $x$ -axis. [Figure 13.27b](#) shows the moment distribution caused by the weight along the tail which has a quadratic distribution as the weight is assumed to be a distributed load along the tail. [Figure 13.28a](#) is only affected by the weight along the horizontal tail as well, this is due to the drag of the horizontal tail assumed to be acting through the  $y$ -axis of the tail and therefore not causing a moment. However on the diagonal tail, the drag causes a positive moment around the  $y$ -axis along the upper diagonal tail and a negative moment along the lower diagonal tail which cancels out at the horizontal tail due to symmetric nature of the split X tail. The moment distribution around the  $z$ -axis, shown in [Figure 13.28b](#), is only affected by the drag on the tail and varies quadratically due to the drag being assumed to be a distributed load.

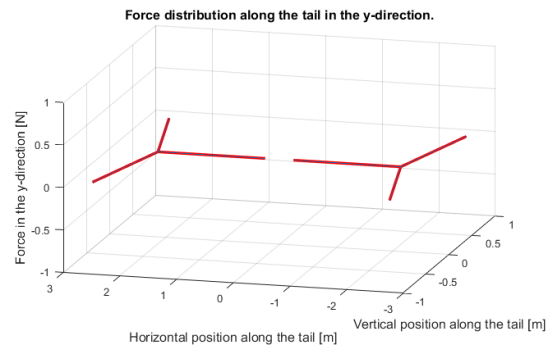
Lift was not taken into account during this analysis as the tail was considered to be in its equilibrium position. As the cross section is a symmetric airfoil, no lift is generated. However, if lift was considered, the graph concerning the  $z$ -direction, [Figure 13.27a](#), would have a smaller magnitude of force and the force may be in the negative  $z$ -direction. The moment distribution around the  $x$ -axis, [Figure 13.27b](#), would again have a smaller magnitude and maybe even reverse direction. For the moments around the  $y$ -axis shown in [Figure 13.28a](#), the

upper part of the split X tail would have a smaller magnitude, the lower part would have a larger magnitude and the horizontal part of the split X tail would have a smaller magnitude of moment due to the lift being added.

More extreme load cases can now be analysed using these equations and how the tail interacts on the fuselage can be looked into as well in the same way as with the wing.

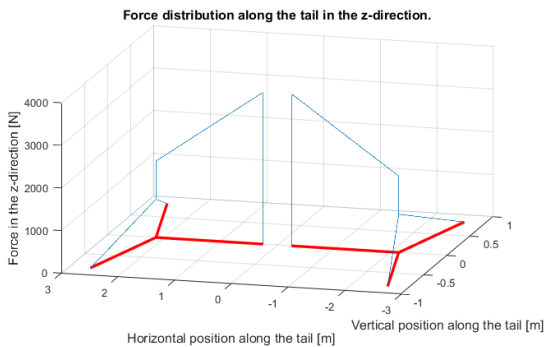


(a) Distribution of the resultant shear force in the x-direction along the tail during cruise.

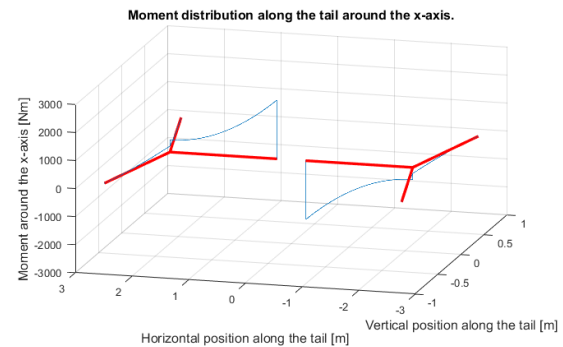


(b) Distribution of the resultant normal force in the y-direction along the tail during cruise.

Figure 13.26: Distribution of the forces in the x and y direction shown across the tail during cruise.

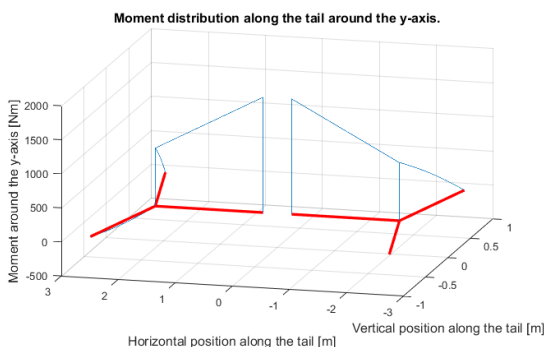


(a) Distribution of the resultant shear force in the z-direction along the tail during cruise.

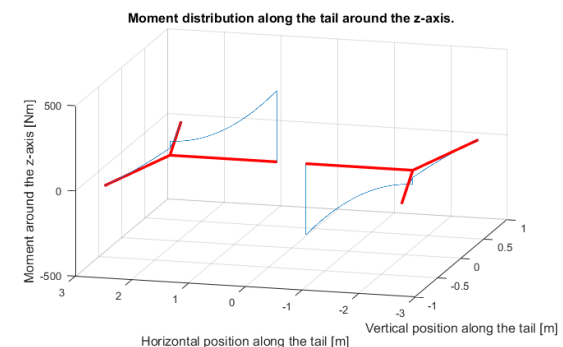


(b) Distribution of the resultant moment around the x-axis along the tail during cruise.

Figure 13.27: Distribution of the force in the z-direction and the moment around the x-axis shown across the tail during cruise.



(a) Distribution of the resultant moment around the y-axis along the tail during cruise.



(b) Distribution of the resultant moment around the z-axis along the tail during cruise.

Figure 13.28: Distribution of the moments around the y and z axes shown across the tail during cruise.

## 13.5. Fuselage Design

The first step in designing the fuselage is to identify and locate all forces which are acting on the fuselage. The forces acting on the fuselage are:

- Fuselage weight (Distributed load along the whole length of the fuselage).
- Nose landing gear force (Point force).
- Titanium bathtub weight (Distributed force along bathtub length).
- Gun force (Point force).
- Fuel weight (Distributed load along the length of the fuel tank).
- Forces and moments introduced by the wing (Point forces, moments).
- Forces and moments introduced by the tail (Point forces, moments).
- Forces introduced by the hardpoints (Point forces).

The assumptions used are:

- The bathtub width is equal to the width of the fuselage.
- The fuel tank width is equal to the width of the fuselage.
- The wing forces are acting at the middle of the wing root chord.
- The tail forces are acting at the middle of the tail root chord.
- The nose and tail cone are not analysed, they serve for aerodynamic purposes.
- The fuselage does not generate lift.

To start the fuselage analysis, the forces and moments acting on the fuselage were evaluated and the internal reaction forces were found by making cuts in the fuselage at an infinite number of points. Hereafter, the shear and moment diagrams were setup to identify the forces the fuselage has to withstand. From this analysis it became clear that the shear force introduced into the fuselage by the wing would become the dominant factor for the fuselage design. Hence, only the shear force in the xz-plane is analysed.

In support of this analysis, the free body diagram of the fuselage is displayed in [Figure 13.29](#), and an overview of the analysed forces in z-direction are given in [Table 13.4](#).

The shear force diagram according to the forces from [Table 13.4](#) can be seen in [Figure 13.30](#). In this diagram,

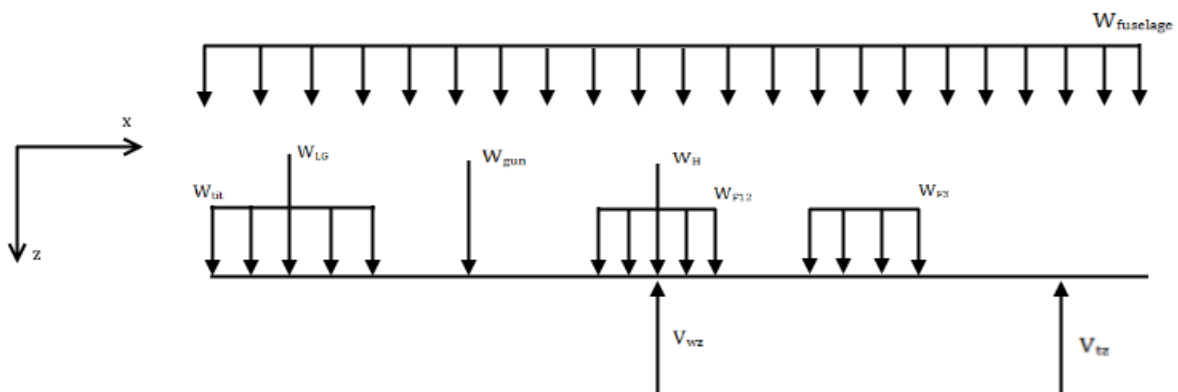


Figure 13.29: Fuselage Free Body Diagram.

it can be clearly seen that the wing shear force has the biggest impact on the shear forces in the diagram. Furthermore, the fuel loads and the tail shear force are the biggest contributors.

From this it can be concluded that in the fuselage analysis special attention should be paid to the location of the fuel tanks, wing attachment, and tail attachment. However, this will be done in later design phases.

## 13.6. Materials

Designing the structure of an aircraft includes the material choice for the respective components. The material choices to consider during the design are defined below. Their characteristics will be described, as well as listed in a table for comparison.

Table 13.4: Definition of forces in the fuselage during cruise flight.

Name	Magnitude	Description
$W_{\text{fuselage}}$	21 470 N	Weight of all the fuselage systems.
$W_{\text{tit}}$	5340 N	Weight of titanium bathtub.
$W_{\text{LG}}$	1438 N	Nose gear weight.
$W_{\text{gun}}$	8183 N	Gun weight.
$W_{\text{H}}$	16 875 N	Weight of 3 hardpoints at maximum load.
$W_{f_{1,2}}$	13 336 N	Fuel weight in fuel tanks 1 and 2.
$W_{f_3}$	13 336 N	Fuel weight in fuel tank 3.
$V_{wz}$	-88 024 N	Shear force introduced into the fuselage by 2 wings.
$V_{tz}$	8044 N	Shear force introduced into the fuselage by 2 horizontal tail surfaces.

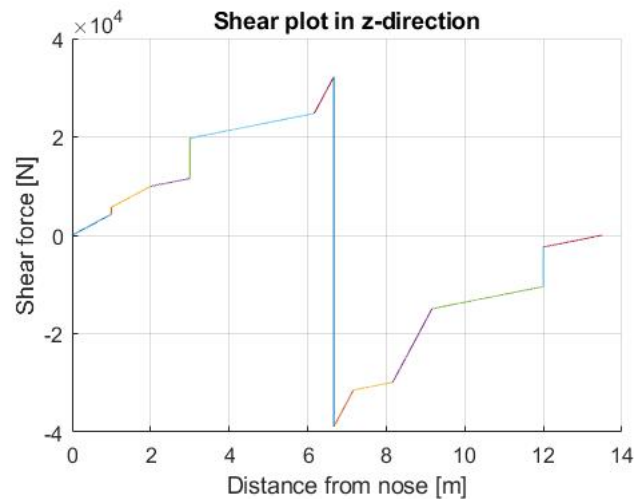


Figure 13.30: Fuselage shear force in z-direction.

## Aluminium

From the many different aluminium alloy options available in the market, the winner being the AL2090-T86 variant. Its main alloying element is lithium, whose alloying properties mainly provide an increase in Young's modulus as well as a lower density. Its properties have been ameliorated by specific heat treatments. It has seen wide implementation in the aerospace industry. Notable projects are SpaceX's Falcon 9<sup>3</sup>, the Airbus A380 and A350, the Boeing 787, Bombardier CSeries aircraft, Global 7000/8000 aircraft as well as the Gulfstream G650<sup>4</sup>. Next to favourable elastic and weight properties, it possesses exceptional damage tolerance characteristics, which is desirable in a CAS aircraft [37].

## Titanium

The titanium alloy considered for the aircraft structures is the Ti-10V-2Fe-3Al alloy. Its main alloying elements are vanadium, iron and aluminium. As the name suggests, these take up 15% of the weight of the alloy. It possesses high strength in tension and shear, as well as good ductility, fatigue life and toughness. It is widely used in the aerospace industry, mainly for safe-life components, such as the landing gear and airframe elements.

## Steel

The steel alloy which has been chosen to consider for structural application is the Fe-D6AC steel alloy. It contains a wide array of solutes, including chromium, molybdenum, manganese, silicon and vanadium. Its favourable combination of characteristics can be described by "medium carbon, low alloy, ultra high strength steel primarily designed for high strength structural applications ... [which] provides a high yield strength to [ultimate] tensile strength ratio, combined with good ductility. It has been selected for fracture toughness critical applications at a variety of strength levels." [38]. Especially this last characteristic is desirable for the CAS application.

<sup>3</sup>Falcon 9 structure <http://www.spacex.com/news/2013/03/26/falcon-9-structure> [Accessed 12-06-18]

<sup>4</sup>FAA Issues Special Conditions for Global 7000 Alloy <https://bit.ly/2JMEzRW> [Accessed 12-06-18]

Table 13.5: Metal alloys with its properties considered for structural design

Characteristic	Unit	AL2090-T86	Ti-10V-2Fe-3Al	Fe-D6AC
E-Modulus	[GPa]	76	107	210
Yield Strength	[MPa]	520	1170	1724
Ultimate Tensile Strength	[MPa]	550	1260	1930
Shear Modulus	[GPa]	28	42	84
Shear Yield Strength	[MPa]	320	669	862
Density	[kg/m <sup>3</sup> ]	2590	4650	7860

### Composite Considerations

The following paragraph is a direct quote from the chapter *"Fibre-Polymer Composites for Aerospace Structures and Engines"* from *"Introduction to Aerospace Materials"* by Adrian P. Mouritz [39]. The concise summation of arguments, as well as clear language usage by Mouritz was deemed best to directly quote.

"There are many advantages as well as several problems with using carbonfibre composites rather than aluminium in aircraft. The advantages include reduced weight, capability to manufacture integrated structures from fewer parts, higher structural efficiency (e.g. stiffness/weight and strength/weight), better resistance against fatigue and corrosion, radar absorption properties, good thermal insulation, and lower coefficient of thermal expansion. The disadvantages of composites include higher cost, slower manufacturing processes, anisotropic properties making design more difficult, low throughthickness mechanical properties and impact damage resistance, higher sensitivity to geometric stress raisers such as notches, lower temperature operating limit, and lower electrical conductivity. The carbon and glass fibres used in composite materials are brittle and fail at low strain. The fibre strength is determined by the largest flaw, which varies from fibre to fibre. As a result, the tensile strength of fibres varies over a wide range, and does not have a single strength value. Composites can absorb moisture and other fluids (e.g. fuel, hydraulic oil) which can adversely affect their physical and mechanical properties. The most common environmental durability issue for aerospace composites is moisture absorption from the atmosphere, particularly under hot/wet conditions."

A qualitative analysis resulted in the exclusion of composites. The major arguments derived from Mouritz's text are summarised here. Firstly, the anisotropic properties greatly complicate the design process of a complex structure such as a wing box. It may not even be possible to create a design which is much more efficient due to the combined loading in the wing box panels during the distinct manoeuvres. Secondly, the low impact damage resistance and brittleness is a key factor to marginalise composites. Due to the high-risk functions the aircraft must perform, it must be designed to take damage. Panels cannot be repaired as well as metals and the structural integrity after damage is difficult to evaluate. Thirdly, cost is an important factor in the design. The estimated costs do not outweigh the advantages presented. Combining these arguments caused the exclusion of composites in the wing box structural design process.

## 13.7. Verification & Validation

The verification and validation methods used during the structural design process are mentioned in this section. In general, verification procedures were followed as described in section 4.5. Firstly, all input variables were assigned a proper unit, to allow for unit testing. Secondly, continuity tests were performed to ensure dependency on the input and to discard outdated variables and code. Lastly, consistency tests were applied to ensure the behaviour of the code is as expected. Specific examples of verification are described below. Not many specific validation procedures have been followed due to the difficulty of obtaining reference data. However, a real-life inspection of aircraft structures was done, as described below.

### Fuel Volume Verification

The fuel volume available in the wing box was calculated using numerical methods. To verify the calculations performed, an analytic method for the volume of a frustrum was applied. The frustrum volume equation can be found in Equation 13.19.

$$V = \left[ (S_a - S_f) C_{r_{\text{main}}} \left( \frac{t}{c} \right)_{\text{root}} + (S_a - S_f) \left( \frac{C_{r_{\text{main}}} - C_{t_{\text{main}}}}{2} \right)^2 \left( \frac{\left( \frac{t}{c} \right)_{\text{root}} \left( \frac{t}{c} \right)_{\text{tip}}}{4} \right) \right] \frac{b}{4} \quad (13.19)$$

In Equation 13.19  $V$  is the volume of the frustrum,  $S_f$  and  $S_a$  are the locations of the front and aft spar respectively as a fraction of the chord.  $C_{r_{main}}$  and  $C_{t_{main}}$  are the root and tip chord lengths respectively while  $(t/c)_{root}$  and  $(t/c)_{tip}$  are the thickness over chord ratios of the the root and tip and  $b$  is the wingspan of the aircraft.

#### Weight Verification

As described in Figure 13.3, the aircraft weight was estimated to be 887.28 kg. Since this was established to be too light as described in the subsection, a range was set up between 887.28 kg and 1070.69 kg. Class II estimations were used to verify this estimate, which was positioned comfortably within the range, having a magnitude of 993.95 kg.

#### Component Thickness Comparison

To compare the cross-sectional thicknesses especially, real wing boxes were examined at the "Aerospace Hall" at Delft University of Technology. Especially the wing box of a Douglas DC-3 was examined. This was the case due to its comparable size and weight. Especially the component thicknesses were examined, which are not straightforwardly evaluated for stiffeners. The thicknesses were comparable, taking into account the different MTOWs and functionality, indicating producibility and a good indication of design feasibility. This comparison improved the confidence in the design.

This chapter deals with the detailed design of several subsystems, including landing gear, fuel, and electrical systems. The landing gear is sized and positioned first, followed by the fuel system. The electrical system follows and includes actuator design, power delivery, and the flight control system, among other things.

### 14.1. Landing Gear Design

In this chapter a detailed sizing of the landing gear will be established. This will include the landing gear location, number, type and size of the tires, length and diameter of the struts and finally the retraction feasibility and braking system selection. The landing gear design is divided into two design phases. The preliminary design is used for the position of the landing gear and is reiterated until the position meets the criteria. The detailed design phase is based on the position and weights from the iteration and is not iterated again.

In the conceptual design phase an initial design option tree was made, where several landing gear options were chosen. As the detail of the design is proceeding, it is determined that the only feasible landing gear configuration is the retractable tricycle. The retractable configuration was chosen due to loiter and performance considerations, while the tricycle offers good visibility and steering characteristics.

#### Preliminary Landing Gear Design

The landing gear location depends on the c.g. location. The most critical c.g. locations are the most forward and aft ones. These are used to determine if the aircraft meets the stability criteria, which consists of the lateral and longitudinal tip over criteria and the distribution of the loads on the nose and main landing gear.

First, the longitudinal tip over criterion is established. This criterion is met when the angle between the c.g. and the main landing gear is around 15 degrees. With the c.g. range of 6.118 m to 6.9844 m, this requirement is met with the longitudinal position of the nose and main landing gear at 1.50 and 7.57 m, respectively.

The lateral tip over criteria ensures that the aircraft cannot tip over over the axis between one side of the main landing gear and the nose gear. This mainly depends on the lateral position of the gears. As it is preferred to store the landing gear in a nacelle below the engine to reduce the landing gear length, it must be determined whether this provides enough lateral stability. The angle with this line and the c.g. should be smaller than 55 degrees. With the engine location set, this angle is for the most forward and aft c.g., around 45 deg, meaning the lateral stability criteria is met as well. The landing gear position is now fixed and the detailed landing gear design can be established. A visualisation of the longitudinal position of the landing gear can be found in [Figure 14.1](#).

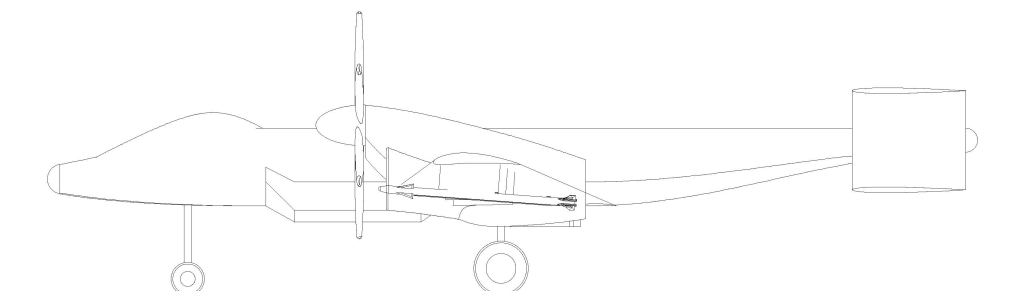


Figure 14.1: Drawing of the side view of the aircraft with the longitudinal position of the landing gear.

### Detailed Landing Gear Design

The entirety of this section deals with material obtained from [34], and as such all of the equations presented should be used with imperial units instead of SI. The aircraft must land on unpaved surfaces such as grass, gravel, and dirt. This was accounted for during the landing gear design via sizing of shock absorbers and tire pressure ranges. Tire pressure will not exceed 9.65 bar (140 psi) during takeoff and landing on austere airfields due to likelihood of larger loads caused by indentations on the airfield (as per austere airfield standards described in Roskam IV [34]).

The nose landing gear was sized based on the maximum dynamic load, obtained via equation Equation 14.1, which was divided by 1.5 to obtain the estimated maximum static load. A standard configuration of one wheel per main landing gear strut and one wheel per nose landing gear strut was considered, and the main gear was assumed to take 90% of the MTOW. From the Goodrich tire database, the most suitable tyres were selected based on maximum static load, maximum operating velocity, and inflation pressure. The maximum operating velocity was taken as the higher of either 120% of the landing stall speed, or 110% of the take-off stalls speed, in this case 88 m/s (197 mph) during landing. The selected main gear tires can take static loads up to 11800 kg at velocities up to 111 m/s, while the nose gear tyres can take static loads up to 4500 kg at the same velocity. Both selected tires are military-grade certified, and 36x11 and 22x8.5 inches in dimensions (diameter x width) respectively.

$$P_{ndyn_t} = W_{TO} \frac{l_m + (a_x/g)h_{cg}}{n_t(l_m + l_n)} \quad (14.1)$$

In the above equation,  $P_{ndyn_t}$  is the dynamic loading,  $W_{TO}$  the take-off weight,  $l_m$  the distance from the c.g. to the main gears,  $l_n$  the distance from the c.g. to the nose gears, and  $h_{cg}$  the height of the c.g..  $n_t$  is the number of wheels of the nose gear, and  $a_x/g$  was taken to be 0.45 as recommended.

Shock absorbers were sized next, via Equation 14.2 and Equation 14.3. These have been placed in the direction of the load (i.e. vertically) to ensure minimum deflection of aircraft during shock absorption in order to minimise the likelihood of the propeller striking the runway. The final shock absorber stroke (i.e. distance it deflects during hardest landing) is 0.333 m, and its diameter is 0.125 m.

$$s_s = \frac{0.5W_L w_t^2}{\eta_s n_s P_m N g} - \frac{\eta_t s_t}{\eta_s} + \frac{1}{12} \quad (14.2)$$

$$d_s = 0.041 + 0.0025\sqrt{P_m} \quad (14.3)$$

In the above equations,  $W_L$  refers to the landing weight,  $w_t$  to the sink (vertical landing) speed,  $\eta_s$  to the shock absorber efficiency,  $n_s$  to number of main gear struts,  $P_m$  to main gear static loading per strut,  $\eta_t$  to the tire absorption efficiency, and  $s_t$  to maximum allowable tire deflection, equal to half the tire diameter.  $\eta_s$  was taken to be 0.85 as liquid springs will be used in the shock absorbers (best performance relative to loads taken by aircraft), and  $\eta_t$  was taken at 0.47 as recommended.

Conventional steel brakes offer decent performance, but their lifespan varies greatly with duration and intensity of use. Carbon brakes offer much higher performance (average landing breaking coefficient up to 0.50) and a lifespan that varies with number of applications, which implies easier maintenance scheduling. Anti-skid carbon brakes have therefore been selected for use in the braking system.

A simple retraction system will be used for both the main and nose landing gears. The main landing gear will retract into a fairing located directly under the engine, whereas the nose gear will retract into the fuselage. The retraction system will consist of the main gear strut, as well as an actuator acting as a drag strut. This is shown in Figure 14.2.

### Ground Turn Performance

The user requirement regarding a ground turn with a radius of at most 120 ft has to be met with the chosen landing gear placement. The ground turn radius can be determined using Equation 14.4.

$$r_{ground} = \frac{l_{lg}}{\cos(90 - \alpha_{steer} + \alpha_{slip})} \quad (14.4)$$

Where  $r_{ground}$  is the ground turn radius,  $l_{lg}$  is the distance between the nose landing gear and the main landing gear,  $\alpha_{steer}$  is the steering angle and  $\alpha_{slip}$  is the slip angle. This equation was determined geometrically and

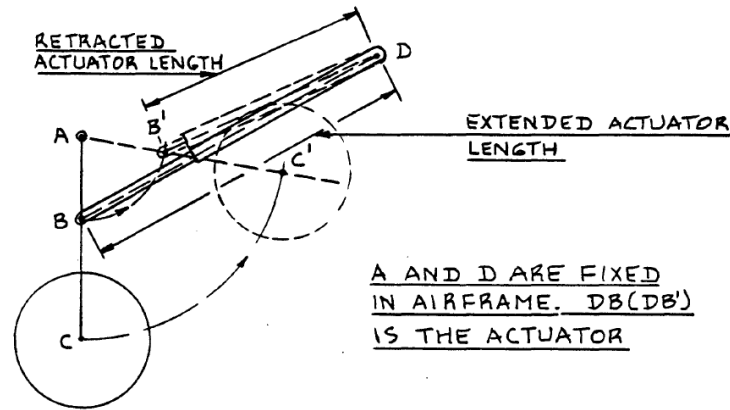


Figure 14.2: Proposed main and nose gear retraction mechanism [34].

verified using known numbers from Roskam Part IV [34]. When entering a value of 6.07 m for the landing gear distance and a value of  $5^\circ$  for the slip angle, the 120 ft radius is still achieved with very small steering angles. Since the steering angle of most aircraft is between  $50^\circ$  and  $80^\circ$  [34], this will not be a problem and the requirement regarding the ground turn radius is easily met.

## 14.2. Fuel System Description

In this chapter the entire fuel system of the aircraft is described. The aircraft can hold a maximum of around 5200 kg of fuel of which 2600 kg is located in the wings, and 2600 kg is located in the fuselage section (section 4.4 for further explanation). At first, the tank placement is elaborated on in Figure 14.2. Thereafter the specifics of the different tanks are discussed in Figure 14.2. Aerial refuelling is discussed in Figure 14.2, and lastly the recommendations for future design analyses are given in Figure 14.2.

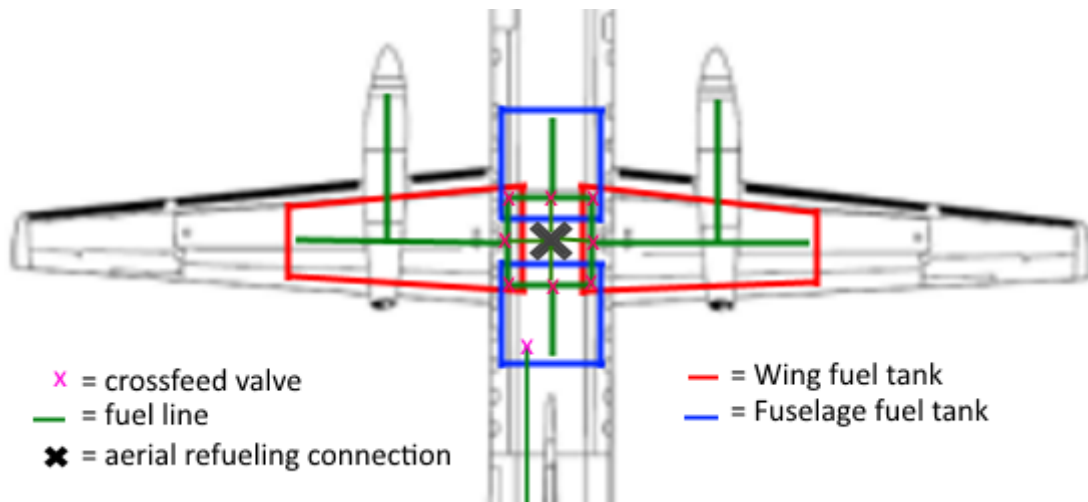


Figure 14.3: Fuel System Layout

### Tank Placement

The aircraft has four fuel tanks which are placed at thoughtful locations. There are two wing fuel tanks, which extend from half of the wing span and end in the fuselage. On top of that, there are 2 fuel tanks located completely in the fuselage. This is visually represented in Figure 14.3, where in red the wing fuel tanks are shown, and in blue the fuselage fuel tanks are shown.

### Fuel tank specifics

Half of the fuel is located in the wing tanks, since this relieves the bending moment of the wing and hence the wings will have a lower structural design weight.

However the downsides of this are, that the wings are exposed to damage due to enemy fire. Therefore the

wing tanks have to be self-sealing, such that they are able to cope with enemy rounds. In addition, ventilation and draining measures are taken to ensure no explosions due to gas build-ups occur after a bullet strike. Moreover, fire-suppressing open-cell foam fills empty spaces within the tanks.

The fuselage located fuel tanks are placed in the upper part of the fuselage. This is to protect them from damage due to bullet impact. Since these fuel tanks are in a relatively protected place, they are not self-sealing.

The fuselage fuel tanks are placed such that they can be used to shift the center of gravity of the aircraft by using crossfeed valves. The system is designed such that fuel can be transferred from and to each fuel tank. Using the crossfeeds the aircraft can be adjusted to a specific flight condition, by transferring fuel from one tank to another.

The fuel lines in each tank are all interconnected to each other via the main loop as indicated in [Figure 14.3](#). The fuel lines are located inside the tanks, such that they cannot get damaged by enemy rounds. Furthermore, there is one fuel line going to the back of the fuselage. This fuel line provides the auxiliary power unit of fuel, and will be empty during enemy engagement. Therefore, it can not endanger the aircraft when it is being penetrated by enemy rounds.

### Aerial Refuelling

The aircraft will be outfitted with the option to execute aerial refuelling missions. Initially the aircraft is designed to receive fuel from a tanker via a boom. In future design, the option of a probe refuelling mission can be researched, which is elaborated upon in [Figure 14.2](#).

The aerial refuelling connection is mounted in between the two fuselage mounted fuel tanks. This reduces the amount of fuel lines needed throughout the fuselage. The fuel can be distributed using the aforementioned crossfeed valves. However, the aerial refuelling manoeuvre will be a difficult one for the pilot flying the aircraft, since the aerial refuelling connection is behind the cockpit. Aerial refuelling can be used when the aircraft has to ferry from a operation base to the battlefield. The aircraft can extend its range by using aerial refuelling, and thus can be flown in a more efficient manner.

During enemy engagement, the wing fuel tanks are preferred to be empty. This can be made possible, by engaging the enemy at low fuel volume. And after enemy engagement the aircraft can setup a rendez-vous with a tanker aircraft to refuel. This increases pilot and aircraft safety, but makes the mission more complex and expensive to execute since a tanker operation should be executed simultaneously.

### Recommendations

In future design phases more in-depth analysis should be done on the fuel tank materials and internal layout. Since the aircraft can fly at high g levels, the tanks need to be able to deal with the fuel movement and weight during those manoeuvres.

Furthermore the fuel pumps should be designed. For the fuel pumps it is important that they are able to pump fuel to the engines during all manoeuvres within the flight envelope. This will require some special design features which need to be investigated in future design phases.

In addition, the option of a aerial refuelling probe should be researched. This aerial refuelling method has advantages over the boom method, since the pilot will be able to visually see the probe and can position the aircraft accordingly. However, it will increase the drag profile of the aircraft.

## 14.3. Electrical System

Recent years the aircraft industry is moving more and more to the MEA concept, which is the abbreviation of 'More Electric Aircraft'. This concept is very promising and will bring a lot of improvements to many aspects to the aircrafts operation. To name a few, significant payoffs will be found in reliability, maintainability, survivability, much lower operations and support costs, less impact on the environment (elimination of the hydraulic system) and improved performance [40]. To assure this aircraft will have a place in future military aviation, this aircraft will follow the MEA concept as much as possible. This also means that the aircraft will not have an hydraulic system to power for example various actuators. However, due to the strict financial budget, only proven technology will be considered for the design of this aircraft.

Especially when incorporating MEA concept, the electrical system is one of the most complicated systems carried by an aircraft. Therefore, this chapter will present a preliminary layout off the electrical system. The flight computer really is the heart of the electrical system. How the flight computer is build-up is discussed in [section 14.3](#). After this, the control system and electrical power system are discussed in [Figure 14.3](#) and [Figure 14.3](#), respectively.

### Onboard computer breakdown

To process the large amount of data produced by the sensors of the aircraft, an onboard computer is needed. The onboard computer has a large range of tasks, including presenting necessary information to the pilot, sending inputs to the control surfaces and managing various aircraft systems. Based on the different tasks, the onboard computer is separated into several divisions. This is schematically presented in [Figure 14.4](#).

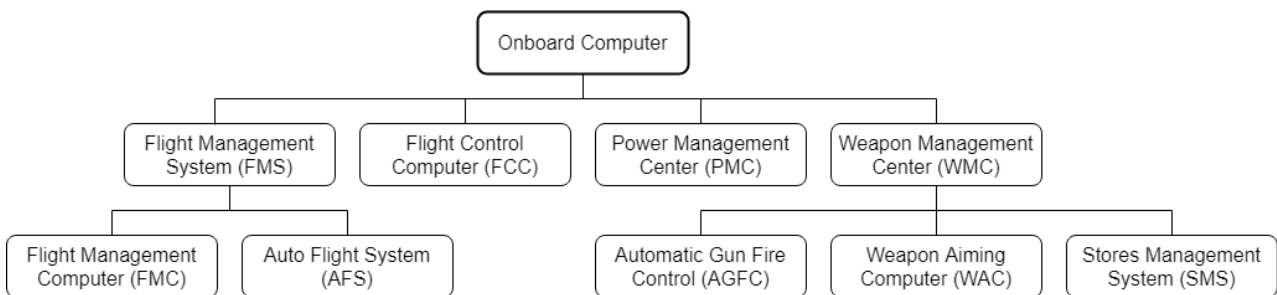


Figure 14.4: Onboard computer breakdown.

As can be seen, the onboard computer has four main divisions. The first one, the FMS, is in charge of inflight management of flight plans and navigation. It also includes the autopilot system. The second division is the FCC, which is, as will be clear in [Figure 14.3](#), a critical part of the aircrafts control system. Then there is PMC. As the name suggests, this part is in control of the complete power system. Because the aircraft will replace the hydraulic system by an electric system, the PMC will play a relatively large role compared to older aircraft. Lastly, the WMC is in control of all weapon systems onboard the aircraft. This includes managing weapons attached to the hard points on the wing, and assisting the pilot with aiming the gun [41]. Note that for the remaining of this chapter, the abbreviations shown in [Figure 14.3](#) will be used.

### Flight Control System

The flight control system is an essential system of almost all aircraft. Therefore, this section will give a very preliminary schematic layout of the FCS. As will become clear later, the aircraft will use a fully FBW control system instead of a more traditional mechanical control system. Why this choice is made is discussed in [Figure 14.3](#). The FCS can roughly be divided into three categories: the sensors, the FCC and the actuation systems. These categories will be discussed in [Figure 14.3](#), [Figure 14.3](#) and [Figure 14.3](#), respectively. [Figure 14.5](#) gives a schematic overview of the complete FCS.

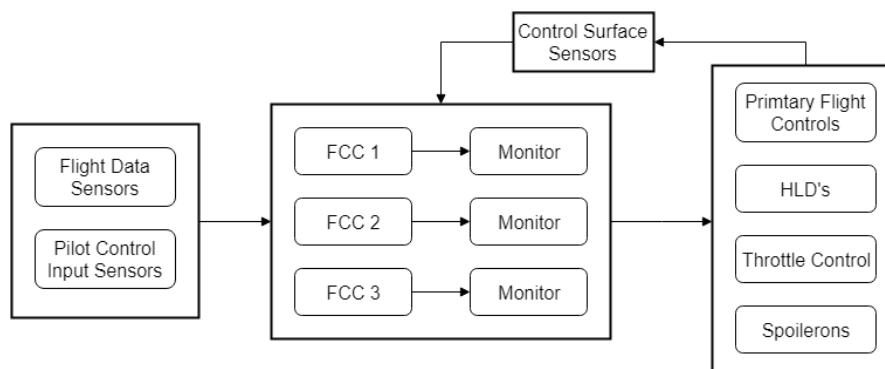


Figure 14.5: Flight control system layout.

### Fly By Wire system

Oftentimes the distinction is made between mechanical control systems and FBW (Fly By Wire) systems. Although this is a rather rough way to divide the different types of control systems in existence, below the main

reasons are listed for equipping this aircraft with a FBW control system.

First of all, compared to a mechanical system, FBW systems generally have a lower weight.[42] This is for the obvious reason that transferring forces between the control surfaces and the control column takes a lot more material than transferring an electrical information carrying signal. Especially because multiple parallel control systems are needed for the sake of redundancy, using FBW will save a significant amount of weight. How much weight this will save exactly is difficult to say at this stage of the design process.

Secondly, because the aircraft has a split-x tail instead of a conventional tail, the flight controls of pitch and yaw are highly coupled. A mechanical control system would in this case be incredibly complicated and heavy. Also, in case of malfunctioning control surfaces, intuitive control can not be guaranteed with a mechanical linkage. However, when using a FBW system, the conversion of control inputs to proper control surface deflections can simply be programmed into the FCC.

Lastly, FBW is way more versatile than a comparable mechanical control system. For example, flight envelope protection can be used to ensure safe operation of the aircraft. Dependent on the control authority or autonomy wanted by the pilot, different control laws can be selected during flight, dependent on the situation. Also, when the technology is mature enough, self learning control systems could potentially be implemented in the future [43].

### Sensors

The sensors of the aircraft provide information to the flight computer about the state of the aircraft and the intentions of the pilot. The sensors can be divided into three groups: flight data sensors, control surface sensors and pilot control input sensors. This can also be seen in [Figure 14.5](#).

The flight data sensors provide information to the FCC about the aircraft location, orientation and velocity. Because this information is critical for proper operation of the FCS, every primary flight data sensor is included at least three times. Primary flight data sensors measure critical parameters, such as airspeed and altitude. This way, in case one sensor malfunctions, the flight computer can decide which sensor is faulty using the voting principle. In rare situation that two primary sensors of the same kind fail simultaneously, other sensors can also be used to determine which one of the three is functioning properly. For example, the GPS can also give information about speed and altitude.

Control surface sensors give information about the position and status of the control surfaces, which can then be used by the FCC. This way, the control surfaces can easily be calibrated at any time, and the FCC can immediately notice when certain control surfaces malfunction.

Finally, pilot control input sensors measure the position of the flight controls, for example the side stick, throttle and rudder paddles. Buttons and switches in the cockpit also fall into this category. All these can be used by the pilot to communicate to the FCC where he or she wants to go.

### Flight Control Computer

The FCC is the central unit when it comes to controlling the flight path of the aircraft. Because it is such an important subsystem, reliability, and thus sufficient redundancy is of critical importance. To achieve the reliability comparable to mechanical control systems, the aircraft should be able to lose at least two flight computers at the same time.[44] In this case, using the voting principle, at least four parallel FCC's that perform the same tasks are necessary in order to be able to decide which FCC's malfunction. This is assuming the malfunctioning FCC's to not generate the same outputs, which would be a very unlikely scenario. Such a setup is called a 'quadruplex' FBW system.

An alternative to the quadruplex FBW system is the so called 'triplex monitored' FBW system. In this setup as the name suggests, only three parallel FCC's are used. In order to identify the malfunctioning FCC's, monitoring modules continuously check the outputs from the FCC's, as can be seen in [Figure 14.5](#). If one FCC gives unrealistic outputs, the monitoring module can exclude this malfunctioning FCC from the FCS. This triplex monitored FBW system is selected over the quadruplex FBW system because it is less expensive and requires less hardware while still providing enough reliability, especially for military applications [44].

To avoid common mode failure, dissimilar redundancy should be applied for both the software and hardware of the different FCC's. This means that the software running on the FCC's should be developed by different

companies or teams, who in turn use different algorithms. This way a bug in the software will only effect one FCC. Also, the FCC's should be composed of hardware that is developed by different manufacturers.

### Actuators

The actuators of the aircraft are responsible for controlling the orientation of most movable parts of the aircraft. For example, actuation is needed for primary and secondary flight controls, landing gear extension and retraction, braking and gun control. Commonly, a central hydraulic system is used for the actuation system. However, hydraulic systems have quite some drawbacks. Some of them are listed below [45].

- Low power density at the power distribution network level.
- Power management difficult at the power distribution network level, which impacts vulnerability.
- Need for fluid conditioning, which impacts serviceability.
- Fluids are bad for the environment, which impacts sustainability.
- Nonlinear behaviour, which increases control complexity.

Therefore, actuators are used that use electrical power instead. This is often referred to as Power By Wire. There are different types of actuators that are able to do this. The ones that will be installed on this aircraft are the so-called 'fixed displacement electro-hydrostatic actuators', or FD-EHA. These types of actuators have been proven in flight (e.g. on the F-35 Lightning II), and do not need a centralised hydraulic network [45].

To look at the control surfaces in particular, every control surface is equipped with two actuators, placed at some significant distance from each other. Because every rotation axis of the aircraft has at least two control services assigned to it (e.g. two ailerons for roll control), in the worst case scenario, more than three actuators need to fail in order to lose full control over one axis.

### Power System

The power system of an aircraft is responsible for, as the name suggest, transporting and delivering the right amount of power to all subsystems of the aircraft in a reliable and efficient way. Because it is such an important system, a power system layout is proposed in this section. Due to the general size and complexity of aircraft power systems, only a very preliminary design will be presented, just to give an overview of how all subsystems will connect to the power generating systems present in the aircraft.

The proposed power system can be divided into two parts. The first part consist of the power sources present in the aircraft. These sources either generate power or release stored power to the main power grid of the aircraft. This is discussed in Figure 14.3. The second part consists of the power grids and conversion circuits. This part is responsible for actually transporting the power through the aircraft and converting the power in such a way that it is usable for all electrical subsystems. This is because reality has shown that it is not feasible to force all electrical components to use for example the same voltage and frequency. This part is discussed in Figure 14.3.

### Power Sources

There are five subsystems that are able to deliver power to the main power grid: the engines, the APU, the ram air turbine, the battery and the ground power unit. Figure 14.6 shows how these subsystems are connected to the main power grid. Lets discuss the power sources one by one.

The main power sources when the aircraft is airborne are the engines. Each engine is linked mechanically to a 3 phase generator. These generators produce a 3 phase alternating current. Because the engine spins at very different angular velocities throughout the flight, the voltage and frequency produced by the generators will also vary significantly. To supply the main power grid with constant wave forms, commonly a CSD (Constant Speed Drive) is used [46]. However, due to it being a mechanical converter, this is a component that adds quite some weight to the engines. Because of the already present digital PMS, a VSCF (varying speed constant frequency) converter can be used. This is a relatively modern component that is able to convert, as the name suggest, a wild alternating power signal to constant wave forms. These VHCF's make use of a feedback system that can be controlled by the PMS, as can be seen in Figure 14.6. This constant 3-phase waveform is then fed to the main power grid.

The secondary power generating system is the APU (Auxillary Power Unit). The APU for this aircraft consist of a small turbine engine which is also mechanically linked to a 3-phase generator. Since this turbine has a

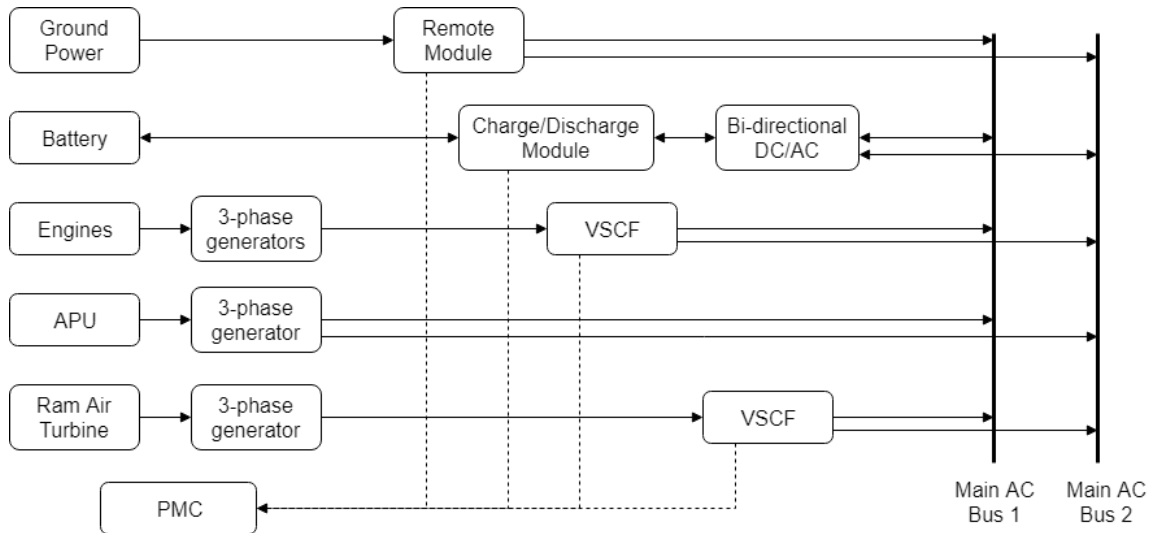


Figure 14.6: Power sources and their connection to the main AC grid.

constant angular velocity, the VSCF module does not have to be applied here to produce a constant waveform. In addition to the engines, the APU can convert chemical energy from the fuel to electrical energy. The aircraft can therefore generate its own electrical power, even when the engines are not running. Needless to say, this is an indispensable quality for ground operations, but also for example in case of a double engine failure during flight.

The last system that is able to generate electrical energy is the ram air turbine. This small turbine deploys from a convenient place on the fuselage to generate power in case of an emergency. This could be for example when the aircraft has ran out of fuel during flight and has used a large portion of the stored energy in the batteries. As with the engines, a 3 phase generator and VSCF module supply power to the main grid. Note that the ram air turbine only generates enough energy to power critical electrical aircraft systems, for example primary flight controls and avionics.

During operation, the amount of power that is fed into the grid is rarely equal to the power that is needed by all electrical systems present in the aircraft. Therefore, multiple batteries are installed to store excess energy or supply additional energy to the grid, depending on the situation. Besides providing the ability to operate low power systems for a limited amount of time without the engines or APU running, the battery is also necessary to start the APU, which uses an electrical starter motor. Since the batteries work on DC, a converter is necessary to connect the battery to the grid. Because the battery both delivers and consumes power, the converter should possess bi-directional characteristics.

The last system that can be used to provide energy to the power grid is the ground power unit. Although this system is not part of the aircraft itself, the aircraft should have the ability to connect to an external power source. This option can be used when electric systems have to be used for an extended period of time without having to start either the engines or APU, for example during maintenance.

#### Power Network and Conversion Circuits

As is clear now, the power sources are all connected to the main grid. There are two identical main grids to achieve redundancy, indicated with Main AC Bus 1 and Main AC Bus 2, as shown in Figure 14.6. Every bus consist of wires to propagate the 3 wave forms which differ in phase. Compared to a single phase systems, this three phase setup can transfer 2 times more power with the same amount of wires [47], which obviously saves weight or increases reliability. Also, when one of the wires of one bus gets damaged, that same bus is still able to transmit power using the remaining wires, although the electrical power converters should be designed to handle this change.

By far most systems in the aircraft need DC power, which is why most aircraft have a DC main grid. This allows having only one point of AC to DC conversion, namely after the generator. However, since the MEA concept is adopted for this aircraft, a large variation of electrical systems will be present in the aircraft. This also brings the need for a more versatile power network. Therefore, an AC main grid is used instead of a DC main grid. AC power is easier to convert to different voltage levels, and for example motor drives can simply

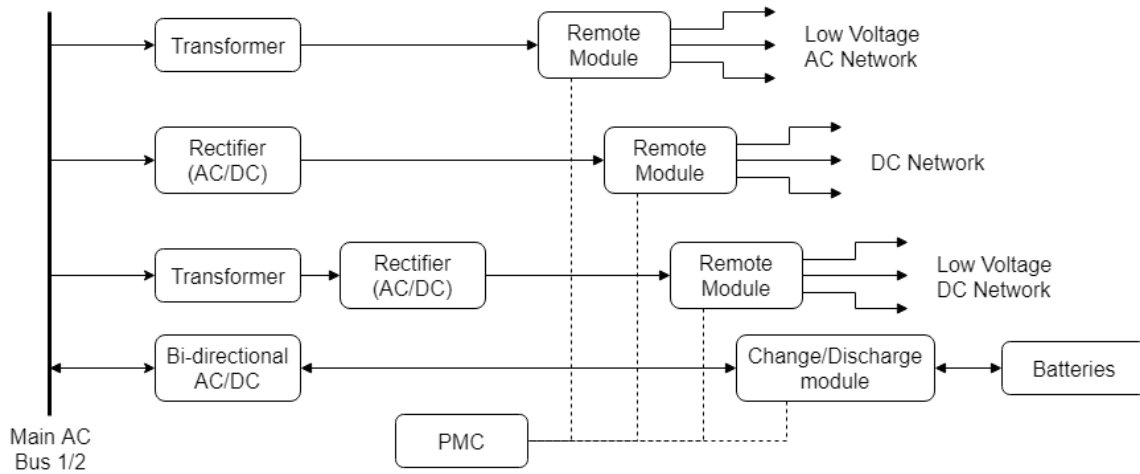


Figure 14.7: Power network and conversion modules.

be used. Also, with current technology and having an advanced power management system makes it possible to convert to DC in a later stage of the power transfer, without a significant increase in weight [46].

As can be seen in Figure 14.7, transformers and rectifiers are used to convert the AC power to different forms of power that are required by subsystems. After proper conversion, remote modules are used to distribute power over different subsystems. These remote modules are controlled by the PMC. Besides the gained versatility of using these remote modules, power peaks can be reduced which allows for a reduction in weight of wiring and electrical components. Note that in Figure 14.7, only one bus is presented for the sake of clarity. However, as mentioned before, the aircraft will carry to parallel and completely independent electrical systems for the sake of redundancy. This also means that both busses are connected to their own converters and remote modules.

# 15

## Market & Cost Analysis

To establish the competitive cost and volume of the market, a market analysis is performed. Building on the preliminary market analysis that was performed in the Baseline Report [3], this market analysis will be updated for the actual characteristics of the aircraft. Furthermore a cost analysis is performed such that it is possible to evaluate the expected return on investment. Firstly, the most important results of the analysis of the Baseline Report are discussed. Thereafter, market volume, possible market share and unit price are evaluated. Finally a cost analysis is performed, which includes the unit cost, operational cost, return on investment predictions and a cost breakdown structure.

### 15.1. Preliminary Market Analysis

In the market analysis performed in the baseline report, first multiple types of combat aircraft capable of performing CAS oriented missions were discussed. The following aircraft types were included: UCAV's, bombers, multi-role fighters, dedicated CAS aircraft, light attack counter insurgency aircraft and attack helicopters. These aircraft were analysed to potentially expose a niche on the market that the next-generation CAS could fill.

Building on the comparable aircraft investigation, a SWOT analysis was performed. The strengths and weaknesses were derived from a comparison of the user requirements with the comparable aircraft, while the opportunities and threats arose from the comparable aircraft and market situation alone. The SWOT diagram is shown in Figure 15.1 [3].

<b>Strengths</b> <ul style="list-style-type: none"><li>• Capable of withstanding most ground fire</li><li>• Substantial loitering time</li><li>• Use of relatively cheaper bullets</li></ul>	<b>Weaknesses</b> <ul style="list-style-type: none"><li>• Fixed-wing aircraft needs a runway</li><li>• Low flight exposes it to dangers from anti-aircraft artillery</li><li>• Manned flight puts a pilot at risk</li></ul>
<b>Opportunities</b> <ul style="list-style-type: none"><li>• Ageing fleet of dedicated CAS aircraft in need of replacement or upgrade</li><li>• No aircraft that can perform low and slow ground attacks, while also having high loiter capabilities</li><li>• No competitor aircraft capable of prolonged close air support due to limitations in armament</li></ul>	<b>Threats</b> <ul style="list-style-type: none"><li>• Market preference for multi-role aircraft</li><li>• High investments in existing projects such as F35 and MQ9</li><li>• Market push for unmanned platforms</li></ul>

Figure 15.1: SWOT diagram for market analysis.

Multiple conclusions arose from the SWOT analysis which were taken into consideration in the detailed design phase. Applying these conclusions will increase the potential market share the aircraft could capture [3]:

- Strong defensive systems will allow the aircraft to attack low and slow while remaining unaffected to possible attacks from the ground.
- Low-cost armaments will make the aircraft more cost-effective than competitors, which mostly use high-cost missiles.
- Corresponding to a low-cost method of striking, a method that would allow the aircraft to engage numerous times on a single sortie would make it more attractive than most currently available aircraft, which carry a limited number of armaments.

## 15.2. Market Volume and Available Share

To evaluate market volume, customers are approached from a general standpoint, i.e. only one customer will be considered: a single, general department of defence. To simplify this approach, only the biggest defence-spending countries around the world, namely the USA, China and Russia, which together are responsible for 53.1% of the world's military expenses [48], are considered. The dedicated CAS aircraft for the USA, China and Russia are the A-10, the Q5 and the Su-25 respectively. The amount of those aircraft which are in service as of 2018 are presented in Table 15.1 [49].

Table 15.1: Dedicated CAS aircraft in service.

Aircraft	Amount of aircraft in service (2018)
A-10	287
Q5	118
Su-25	197
Total	602

It should be noted that it would be more realistic to consider just the defence department of a single country, or an allegiance of countries, for instance NATO, as customer. However, for the purpose of this report, the market will be approached as it is now.

If the next-generation CAS aircraft is able to outperform all currently existing CAS aircraft and the customer is interested in replacing its entire CAS fleet, a maximum of 602 next-generation aircraft could be demanded. However, a 100% market share is extremely unrealistic and in reality, current CAS aircraft will gradually be taken out of service over the years, and not all of these aircraft will be replaced by dedicated CAS combat aircraft. As was discovered in the SWOT analysis of section 15.1, the market tends to push towards multi-role fighters like the F-35 and UAV's like the MQ-9 to fill the CAS role.

Multiple factors can however increase the market share of the new CAS aircraft and can make it a more favourable option for certain missions as compared to other aircraft types, thus taking a part of their market share. Firstly, the appliance of the conclusions which arose from the preliminary market analysis will increase the market share. Especially drones will give up part of their market share, since they have very few, expensive attacking options as opposed to the many and relatively cheap options the CAS aircraft has. Furthermore, a huge factor in aircraft demand is the unit price, which will be further elaborated upon in section 15.4.

Finally, at the introduction of a new aircraft, only a small market share will be captured, but this share could very well grow over time. Old aircraft types will gradually be replaced, which might take years. Furthermore, if the new design successfully shows its capabilities on the battlefield, it will increase the demand for the aircraft and thus also increase the market share. If the new aircraft proves to be very successful, the service life of the aircraft could even be expanded to multiple decennia. While an immediate capture of the entire CAS market with 602 aircraft is unrealistic, a total production of 600 or more aircraft is not, as can be seen in the 707 total A-10's<sup>1</sup> and 1320 total Su-25's<sup>2</sup> produced. Furthermore, the aircraft is likely to get damaged on the battlefield. This may increase the demand for a replacement aircraft or at least of replacement parts, which can be then be sold.

To conclude, the available market share will be small at first, but if the new CAS aircraft successfully proves its capabilities and reliability, its market share will significantly grow. The total amount of units that might be produced could very well be in the hundreds, but an exact number can not be estimated as of now. The aircraft's performance will establish that exact number.

<sup>1</sup>FAIRCHILD-REPUBLIC A-10 THUNDERBOLT II <http://www.uswarplanes.net/a10.html>[accessed 24-06-2018]

<sup>2</sup>Su-25 Frogfoot <https://www.globalsecurity.org/military/world/russia/su-25.htm>[accessed 24-06-2018]

### 15.3. Unit Price

Aside from establishing the proposed market share of the aircraft, a viable unit price also needs to be estimated in order to determine the financial feasibility of the aircraft. Since the price affects the number of aircraft sold and the unit cost, an optimum price point should be established. According to the principles of microeconomics, there is an inverse relationship between the unit price and units sold in competitive markets [50]. However, due to the low number of suppliers and customers in the CAS aircraft market, as well as the heterogeneity of aircraft available, this relationship does not accurately describe the market. Moreover, due to the fact that customers are governmental entities, their purchasing behaviour is beholden to public opinion and politics.

Establishing an actual optimum price point is outside of the scope of this report, not in the least because of its dependence on more accurate predictions of the unit cost and market share. However, an estimation of a viable unit price can be made based on the unit prices of other aircraft performing a similar role. In 2019, the U.S. Department of Defense budget request calls for a total of \$55.2 Billion on aircraft acquisition costs [51]. Of this, by far the largest category is combat aircraft of \$20.6 Billion. Included in this figure are several fixed-wing aircraft capable of performing a CAS role. The quantity and acquisition costs are expressed in Table 15.2.

Table 15.2: Acquisitions of fixed-wing aircraft supporting a CAS role by the U.S. Department of Defense for the U.S. Air Force.

Aircraft	Quantity	Total Price in \$M	Unit Price in \$M
F-35 Joint Strike Fighter	48	4,914.3	102.38
MQ-9 Reaper	8	392.2*	49.03*

\* This price includes one extra ground control station. The total price of 8 MQ-9's with 8 ground control stations is \$364.57 Million, and the unit price is \$45.57 Million.

For now, it is assumed that the unit price of the aircraft will be equal to the unit price of the cheapest currently available aircraft performing a CAS role, which is \$45.57 Million.

### 15.4. Unit Cost

To evaluate return on investment, the unit cost should also be estimated. This was done by using a DAPCA IV cost model modified by Raymer [24]. This model was made for conventional aircraft, but due to the unavailability of public military aviation data, it is regarded to be a sufficient rough estimate for the unit cost. The model takes the cost of the following parameters into account: development, materials, engineering, tooling, manufacturing, quality control, flight tests, engines and avionics. Furthermore, this model uses the empty weight, the maximum velocity and the amount of aircraft to be produced as main inputs. The method considers all costs, for instance salaries, to be in 1986 dollars. As a result, the model was adjusted for inflation, except for the costs of the engines and of the avionics systems, which were thereafter added.

The engine cost of the AE 2100 engine can be derived from the fact that in March 2004, eight AE 2100 engines were sold for a contract price of approximately 19 million USD<sup>3</sup>. Adjusting this amount for inflation, the unit cost of a single AE 2100 engine is estimated to be 3.1245 million USD. For the avionics system, the avionics cost of the Boeing F/A-18E/F Super Hornet was used as a reference value, since this is the only reference value on military avionics that could be obtained. The avionics system of the Super Hornet is 44% of the total unit cost [52]. A percentage of 44% is thus also used for this cost estimation.

The output of the modified DAPCA IV model is the unit cost of the aircraft as a function of the amount of aircraft produced. Unit cost decreases with an increasing amount of produced aircraft for two reasons. Firstly, the research and development cost is split over more aircraft and is thus smaller per aircraft. Secondly, during the production of an aircraft, the manufacturer learns from the production process and is able to produce the next aircraft cheaper. This is called the production learning curve and typically the labour cost per aircraft goes down with 20% for every doubling in the aircraft quantity [24]. Both these factors are taken into account in the modified DAPCA IV model.

The empty weight of the aircraft and the top velocity that followed from the iteration procedures were used as input of the model. The output can be seen in Figure 15.2.

<sup>3</sup>Engine data was obtained from Jane's All The World's Aircraft, online database: [https://janes.ihs.com/Janes/Display/jae\\_0754-jae\\_](https://janes.ihs.com/Janes/Display/jae_0754-jae_) [Accessed 19-06-2018]

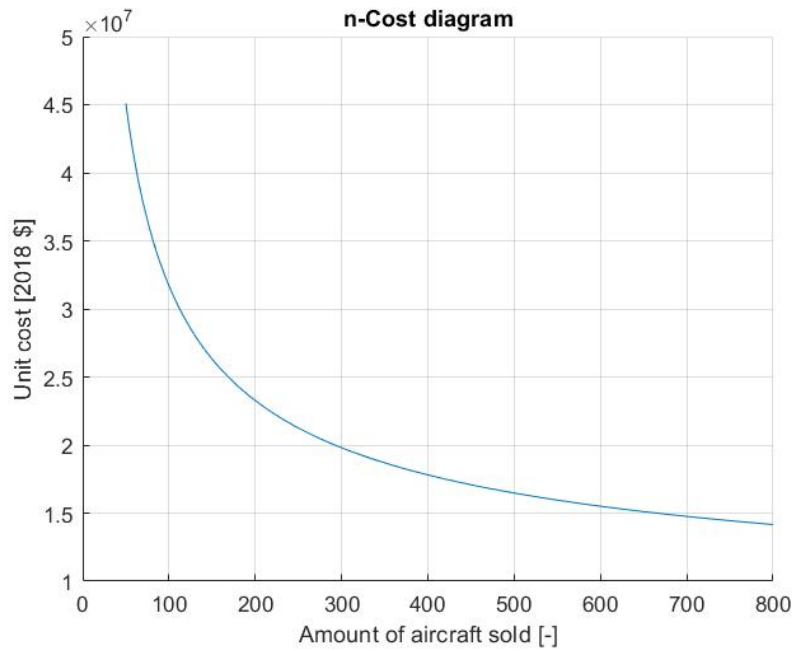


Figure 15.2: Cost per aircraft for total amount of aircraft sold.

As can be seen in the figure, the user requirement that demands a unit cost of under 15 million USD is once a total amount of approximately 650 units is produced and sold. According to the market volume analysis of [section 15.2](#), this value is possible to achieve if the design proves to be a large success. However, that is not guaranteed. For lower production quantities there will be a higher unit cost. The lowest production quantity that for now will be considered is 100 units sold, for a unit cost of 32 million \$. Although a production of 100 units is far from guaranteed, a maximum unit cost of 32 million \$ is a valid assumption, since the DAPCA IV model is unreliable for low production numbers due to its exponential nature. To check whether the design is still economically feasible to produce, the return on investment will be investigated in [section 15.6](#). But first, the operational cost will be determined.

## 15.5. Operational Cost

The hourly operational cost of the aircraft is estimated as the total cost of ownership of the aircraft divided by the flying hours. Thus, it stands to reason that higher availability, and thus flying hours, will lower this cost. Furthermore, good maintainability characteristics will lower the cost of maintenance, which is usually a significant part of the total cost of ownership. However, it should be noted that maintenance will still form a sizeable part of the total cost since the aircraft is likely to need unscheduled maintenance after operating over hostile territories. Since the design is currently in too early a stage to assess the actual operational costs in an accurate manner, the cost is instead estimated using the available operational costs of other aircraft flown by potential customers.

From the U.S. Department of Defense [\[53\]](#), the operational cost of several military aircraft was found. The first interesting thing to note from these figures, was the difference in operational cost between different aircraft based on the C130 platform and aircraft based on the updated C130J platform that perform a similar function. [Table 15.3](#) clearly shows that newer aircraft hold an operation cost that is about 2-3 times lower than similar, but older aircraft.

It is expected that the aircraft being designed will similarly enjoy the benefits of technological advances that made this decrease in operational cost possible. The second aspect noted from the figures from the U.S. Department of Defense, was that aircraft deployed in combat generally have a higher operating cost than aircraft not deployed in combat, such as, VIP transport aircraft and maritime patrol aircraft. Since the aircraft is designed for combat in a similar function as the A-10 Thunderbolt II, that aircraft's operational cost of \$6,273 is used for reference [\[53\]](#). Based on the above cited figures, it is estimated that the operational cost of the aircraft in this report will be about half of that, due to the updated characteristics of the new design. The operational cost is estimated the range of \$2,500 to \$3,500. It is important to note that this cost excludes fuel and ammunition cost.

Table 15.3: Difference in operational cost of C130 based aircraft vs. C130J based aircraft.

Aircraft	Operational Cost [\$]	% difference w.r.t. C-130J based similar aircraft
EC-130J	6,119	-
HC-130J	5,977	-
MC-130J	4,857	-
EC-130H	17,624	188%
HC-130N	11,854	98%
HC-130P	12,327	106%
MC-130H	14,466	198%
MC-130P	9,566	97%

To estimate the fuel cost, the resulting fuel weight of [section 4.3](#) of 5200 kg is used. For kerosene which has a density of 0.8 kg/m<sup>3</sup> and a price per gallon of 2.08 \$<sup>4</sup>, this comes down to a cost of 3691 \$ for full fuel tanks. Ammunition costs varies with the chosen missile load-out, but ammunition costs for the mounted gun are approximately 350 \$ per 100 rounds<sup>5</sup>.

## 15.6. Return on Investment

In order to determine if continuing with the design and production of the aircraft is financially feasible, the expected return on investment is calculated. The formula used for calculating the return on investment is shown in [Equation 15.1](#). Note that the development cost has been included in the unit cost estimations.

$$\text{Return on investment} = \frac{\text{Unit price} - \text{Unit cost}}{\text{Unit cost}} \quad (15.1)$$

The previously determined unit cost range of 32 million \$ to 15 million \$ and the unit price of 45.57 million \$ is used in this calculation. After performing [Equation 15.1](#), a range for the return on investment between 42.4% and 203.8 % is found. Thus, the project is profitable and should be continued.

## 15.7. Cost Breakdown Structure

The Cost Breakdown Structure for the aircraft is shown in [Figure 15.3](#). This figure is used as an overview to identify all the cost related activities of the post-DSE design phase. The total cost of a single aircraft during its lifetime is divided into design costs, production costs and operational costs. Design costs are a single large expenditure, divided by the total amount of aircraft produced, while production and operational costs are applied to all aircraft separately. The operating expenses cost of packages 1.1, 2.1, and 3.1 include travel, office and production space, legal advice and security among other things. Propulsion unit cost as well as avionics cost are discussed in [section 15.4](#), operational costs in [section 15.5](#) and all other costs in the figure are estimated by the cost model used in [section 15.4](#).

<sup>4</sup>Kerosene daily prices, <https://www.indexmundi.com/commodities/?commodity=jet-fuel>, [accessed 25-06-2018]

<sup>5</sup>Autocannon ammunition [http://www.pmulcahy.com/ammunition/autocannon\\_ammunition.html](http://www.pmulcahy.com/ammunition/autocannon_ammunition.html), [accessed 25-06-2018]

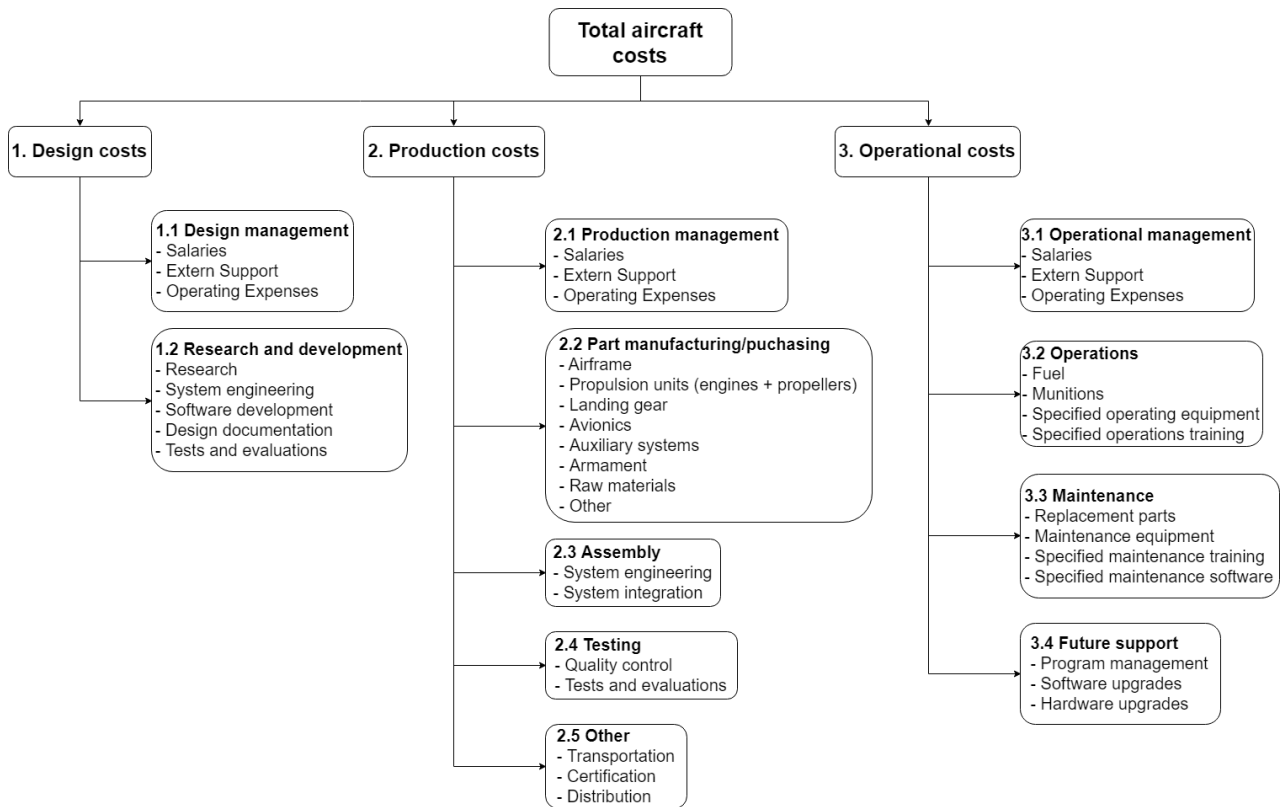


Figure 15.3: Cost breakdown structure.

## Sustainable Development Strategy

As a close air support combat aircraft's primary design driver is combat effectiveness, sustainability is not a driving requirement. Measures have, however, been implemented to ensure that sustainability has been considered at each design step throughout the project duration, including development, operation and end-of-life.

During engine selection, the specifications of each engine have been considered to ensure a sustainable option is picked. The jet-based TF34 was heavily favoured due to its ability to use biofuels. However, due to its inability to perform with respect to the loiter requirement, it has been discarded from further consideration. The T56 and AE2100 engines by Rolls Royce have been considered for the final stage. The T56 has the advantage of biofuel use [54], while the AE2100 has a significantly lower (around 15%) fuel consumption. These two engines of comparable performance were taken into context of the aircraft mission profile, as described in section 3.1, where their emissions have been analysed via total fuel consumption. It was determined that the T56, would require around 19% more fuel for the same mission, due to the lower fuel efficiency and higher engine and fuel weight. The main environmental impact of aircraft originates from  $CO_2$  emissions [55], for which the C-HEFA biofuels used on the T56 have emissions lower than that of regular jet fuel by only 1%, as the biofuel only reduces emissions significantly in terms of black carbon mass. The use of biofuels therefore implies a major sustainability impact mostly in terms of use of renewable resources. The AE2100 engine has been selected over the T56 as biofuel blends may not be available at all times in all operating conditions, and due to the fact that the lower fuel efficiency of the T56 will likely result in higher (non-bio)fuel use. The absolute  $CO_2$  emissions of the AE2100 are also lower than that of the T56, regardless of the fuel type used. The AE2100 also implies economic sustainability, as it is cheaper to operate and cheap to maintain due to sharing most of its parts with the T56, as it was developed as its successor<sup>1</sup>. Further research could prove that the use of biofuels is still feasible on an unmodified AE2100 engine based on its similarity with the T56.

In terms of operation, the armaments of the aircraft have also been checked for sustainability, where possible. Usually, fighter and attack aircraft such as the A-10 carry depleted uranium rounds due to the material's incendiary and explosive properties<sup>2</sup>. Depleted Uranium is a radioactive material consisting almost completely of the  $^{238}U$  isotope. Even though the radioactivity of depleted uranium is relatively limited, compared to natural Uranium, its long half-life causes it to accumulate over a longer period<sup>3</sup>. Soil gets contaminated when bullets penetrate the ground, and its radiation disturbs the human and animal growth process [56]. Ammunition with depleted Uranium has therefore been excluded as a design option, as the additional environmental damage outweighs the added explosive and incendiary properties which are achievable by other means. Additionally, the operational cost of the aircraft implies far greater economical sustainability compared to competitor aircraft, as discussed in Chapter 15.

With respect to the end-of-life, the reusability and/or recyclability of parts is taken into account. In terms of reusability, the aircraft system equipment, engines, landing gear, and avionics are some components which could be re-used as maintenance parts or in production of new units. Aluminium 2090 has been determined as the primary structural material, making up most of the aircraft's OEW. As production of aluminium by recycling only requires 5% of that of production from raw material while emitting only 4% of the  $CO_2$ , there is great incentive to apply recycling as both an environmentally and economically sustainable end-of-life strategy [57]. However, titanium and steel will also be used in the aircraft, adding to the complexity of aircraft aluminium recycling. This is often the case with aircraft, also due to the fact that aircraft aluminium alloys are very high in alloying elements. Recycled aluminium often displays inferior material properties in comparison to primary production. However, industries with less extreme performance requirements, particularly the commercial automotive industry, can benefit from the recycled aluminium and can ensure that there is a consistent demand for it. This requires well-established material extraction and separation technologies on the recycling

<sup>1</sup>GlobalSecurity - AE2100 <https://www.globalsecurity.org/military/systems/aircraft/systems/ae2100.htm> [Accessed 14-06-2018]

<sup>2</sup>FAS - PGU-14/B <https://fas.org/man/dod-101/sys/land/pgu-14.htm> [Accessed 25-05-2018]

<sup>3</sup>IAEA - Depleted Uranium <https://www.iaea.org/topics/spent-fuel-management/depleted-uranium> [Accessed 30-06-2018]

---

site/area. With that in mind, it is recommended that the following steps be taken to ensure that the (aluminium specific) recycling/scraping plan of the aircraft is optimised for sustainability, as per [57]:

- Each of the aircraft components is to be analysed for quantity of recyclable aluminium, and each of the used aluminium alloys identified.
- The economical benefits of aircraft relocation prior to scrapping should be evaluated. Component pre-sorting should also be evaluated, as opposed to automatic (machine) sorting of scrapped metal, or a combination of both.
- Studies on quality and properties of the recycled aluminium should be performed, and its potential applications identified.

Although aluminium is the easiest component to plan for recycling, other components of the aircraft also have potential to ensure a sustainable end-of-life. These are titanium and steel alloys used throughout the aircraft, as well as batteries, wires, avionics, tyres, and various thermoplastics. Most of these show considerable energy savings with respect to from-scratch production [58].

## Reliability, Availability, Maintainability and Safety

In this chapter the RAMS characteristics of the aircraft are discussed. The expected reliability and availability is predicted, and ways to improve both for the aircraft are presented. Furthermore measures to improve the maintainability of the aircraft are explained. Finally, the redundancy and safety approaches are elaborated, which are closely tied to the risk assessment that follows.

### 17.1. Reliability

Reliability is an important quality of any combat aircraft. Aircraft failure on a mission is devastating, as it risks the pilot ending up into enemy territory or worse. Increased reliability compared to similar aircraft would make the aircraft more desirable among potential buyers. The reliability of this specific design is analysed considering the engine reliability and the fly-by-wire control system reliability. Finally, some other measures that have been taken to increase the reliability of the aircraft will be discussed.

Firstly, the reliability of the Rolls-Royce AE 2100A engine is analysed. All data in this section regarding the engine is taken from Jane's Aero Engines database<sup>1</sup>. This engine has previously been used to power the Saab 2000 aircraft. In 1998, 143 of these engines were produced and by October 1999 flight-time in scheduled service was 750 000 hours. For the Saab 2000, dispatch reliability was 99.85% as of late 1999, which suggests that the same dispatch reliability, if not more, should be achieved for the aircraft, when considering the engine type only. In 1998, production of the Saab 2000 was stopped, so more recent data is unavailable, even though all the aircraft are still in service. Furthermore, the gearbox is known to have a design life of 30 000 hours.

Secondly, the fly-by-wire control system reliability is considered. Three separate fly-by-wire systems are installed on the aircraft to achieve a triply redundant system. Furthermore, three flight-control computers will be operating in parallel. This means that the aircraft will still be fully controllable if two of the fly-by-wire systems have failed or the software or hardware of the flight computers is in any way compromised. This in itself makes the control system configuration much more reliable. Moreover, Dolega states that fault detection methods should be introduced into the sensors and actuators of the system to further increase the reliability [59]. The most simple fault detection methods consist out of comparing the signals received with a computer model and could thus be easily achieved. More research into fly-by-wire reliability is recommended to investigate this further.

Numerous other measures have been taken to increase the reliability of the aircraft, these can be found in section 17.4 about safety and in section 17.5, the risk analysis, since they are so closely tied in to both. Other than what has been discussed, it was not possible to quantify any more regarding reliability, due to the lack of publicly available data. What has been discussed will be used to evaluate the availability of the aircraft in the next section.

### 17.2. Availability

The availability of an aircraft fleet refers to the percentage of aircraft ready for deployment/operation at any given moment. One way to ensure high availability is the use of established, simple and robust systems. The use of the established AE2100 engines, as well as the established XM301 weapons system increases availability. Operational limits and maintenance procedures have already been established, ensuring maximum availability without failure. These maintenance procedures are the second main factor contributing to aircraft availability [60]. Maintenance can be preventative or unscheduled, the latter of which is especially applicable for CAS aircraft. It is therefore logical that proper maintenance scheduling for preventative maintenance, as well as

<sup>1</sup>Jane's All The World's Aircraft, online database: [https://janes.ihs.com/Janes/Display/jae\\_0754-jae\\_](https://janes.ihs.com/Janes/Display/jae_0754-jae_) [Accessed 19-06-2018]

enabling speedy unscheduled maintenance will directly lead to greater fleet availability. Data on maintenance characteristics for military aircraft is hard to quantify, but known characteristics of the AE 2100 engine are shown in Table 17.1 [61].

Table 17.1: AE 2100 engine availability characteristics.

Property	Unit	AE 2100
Mean Time Between Repairs (MTBR)	hours	3500
Maintenance actions	Per hour of flight time × 100 (%)	50

Maintenance intervals differ from component to component depending on how often/when they are used in the aircraft lifecycle. There are four main maintenance intervals for aircraft components that should be accounted for when creating a preventative/regular maintenance plan<sup>2</sup>:

- **Flight Hours** - Used for items that are in operation throughout the aircraft runtime, such as fuel pumps and electrical generators. This is used as an interval for engine maintenance.
- **Flight Cycles** - Used for items that are operated a fixed number of times per flight, such as pressurisation and landing gear. This is used as an interval for fatigue testing.
- **Calendar Time** - Used for items that wear regardless of aircraft operation, such as e.g. fire extinguishers. This is used as an interval for corrosion testing.
- **Operating Hours** - Used for items whose wear is independent of the above, or items not operated every flight, such as the APU.

Due to the nature of CAS missions, unscheduled maintenance is to be expected in higher frequencies than with regular aircraft. It is therefore imperative that components with a high failure rate (caused by enemy fire) be identified and be easily accessible and interchangeable. All operating bases should also have the personnel and equipment to perform these repairs, such as e.g. spare propeller blades. This is further discussed in the following sections on maintainability and safety, both of which contribute to aircraft availability.

### 17.3. Maintainability

Maintenance scheduling and operations typically make up 10-25% of an aircraft's operating costs [62]. Designing for maintainability can reduce the aircraft's operational costs and reduce maintenance time, which in turn directly affect economic sustainability and operational availability. The main factors affecting maintainability of an aircraft are system accessibility, visibility, testability, complexity, interchangeability, and identification and labelling of parts [63]. Complexity refers to number of steps taken before the specific part/system is reached (i.e. removing certain systems to reach another), while interchangeability refers to the ease of replacing a component with an identical copy.

The engine has been placed on top of the wing for a variety of reasons, one of which is ease of maintenance. In order to ensure that engine change-out time is minimised, the engines have been placed directly on top of the wing. This means that only a single crane is necessary to remove the engine. Furthermore, as almost the entirety of the engine is exposed on top of the wing, repairs are facilitated by high accessibility and visibility. As there is little data for the engine-change out times of the AE2100A, the AE2100D3 engines of the C-130J have been taken as reference. These officially require around 4 hours for a full engine swap, including a crew of four men. This is effectively equal to the required man-hour time which assumes 8 hours of labour by 2 technicians. As the number of crew members is likely difficult to reduce due to the engine size, the requirement for engine change-out is only partially met.

Easy-access panels will be placed throughout the aircraft, including on the wing where the fuel tanks are, on the sides of the fuselage to access the fly-by-wire control paths. The XM301 gun is easily accessible for maintenance via the integrated deployment mechanism, and this is especially useful due to its complexity. Interchangeability of parts has also been considered during design. The ruddervators are interchangeable from side to side as they contain symmetrical airfoils, as well as the engines and main landing gears.

<sup>2</sup>Skybrary - Aircraft Maintenance [https://www.skybrary.aero/index.php/Aircraft\\_Maintenance](https://www.skybrary.aero/index.php/Aircraft_Maintenance)

## 17.4. Safety

Safety is the only true measure of airworthiness. The nature of CAS missions implies earlier failure rates for various aircraft components, particularly those that are within the enemy line of fire, such as the wing and fuel tanks, hydraulic systems, control surfaces, and engines. This poses high requirements with respect to aircraft survivability, or its ability to return to base and land with critical components damaged. With this in mind, measures were taken to reduce aircraft vulnerability in terms of component redundancy, component location, active and passive damage suppression, and component shielding with respect to most aircraft systems based on recommendations from [64]. These measures have directly tied into the risk assessment in the following section.

To address the fuel system vulnerabilities, two fuel tanks have been placed on the top part of the fuselage to minimise likelihood of tank puncture. The two fuel tanks placed in the wing will be self-sealing to minimise impact of enemy fire and will contain redundant fuel pumps. These will also be filled with open-cell foam to ensure that fire cannot occur inside the tanks. The tanks will be surrounded by closed-cell foam that ensures fire cannot spread within the empty wing cavities, as well as that no leaks to the outside can occur. For the propulsion system, the engine has been placed on top of the wing as the underlying wing structure and the fuel tanks within it are likely to take most of the damage. The attached propellers must also remain rigid after taking a round in order to prevent propeller parts from striking the fuselage/armaments. For the control system, redundancy of control system paths (one line of control paths running through left, and one through right side of fuselage), as well as splitting control surfaces into two different parts, the failure of either of which would imply negligible consequences for aircraft survivability. There is redundancy in vertical and horizontal (control) surfaces via the x-tail, redundancy in yaw stability due to potential differential thrust generation, redundancy in thrust generation via having two engines, and redundancy via the presence of two control systems and three flight computers. Should any of these components fail, the aircraft would be able to safely return to base.

Other than redundancy measures, safety measures that minimise likelihood of aircraft and pilot harm have been implemented. These are in the form of active and passive countermeasures. In terms of passive countermeasures, the entirety of the bottom of the cockpit is covered by a titanium bathtub, identical to that of the A-10, which protects the pilot from 23mm rounds, potentially up to 57mm<sup>3</sup>. The bathtub will also contain the aircraft's flight computers and avionics, shielding them from any potential enemy fire and thereby removing the need for their redundancy. The control system will be designed in such a way that the aircraft remains controllable with only one engine operative. Additionally, the aircraft will include a fake canopy positioned directly under the real canopy to ensure that the orientation of the aircraft is unclear to enemy ground forces. As the aircraft features a mobile turret, strafe runs will be less dangerous due to the aircraft's ability to engage enemies at higher altitudes.

Active countermeasures will include SUU-42A/A flare and chaff pods, as well as compatibility with the AN/ALQ-131 Airborne Self Protection Jammers. The first will ensure safety from heat-seeking missiles and short-term radar detection, while the second serves an active defensive role via denying targeting information to enemy electronic targeting systems. Another active 'countermeasure' will be the presence of AIM-9 Sidewinder air-to-air missiles which ensures the pilot is not defenceless in the air.

In case of a critical strike or catastrophic aircraft failure, the pilot may eject from the aircraft as a last resort. The ejection seat present is a zero-zero seat, meaning that it will ensure that the pilot lands safely even at zero altitude and velocity.

## 17.5. Risk Assessment

This section identifies risks related to CAS missions and discusses a corresponding mitigation strategy. The risks are presented in an enumerated way, and the corresponding mitigation strategy is written in italicised text. The main operational risks have been presented first, relating to risks exclusively associated with the day-to-day aircraft operation. Following those, system risks have been presented, which relate to (un)expected functioning of the most critical aircraft systems.

<sup>3</sup>Cradle Aviation Museum - The Titanium Bathtub - A-10 Survivability [http://www.cradleofaviation.org/history/history/aircraft/a-10\\_survivability.html](http://www.cradleofaviation.org/history/history/aircraft/a-10_survivability.html) [Accessed 19-06-2018]

### Operational risks

- 1. Propeller blade breaking off as a result of enemy fire** - While executing CAS missions there is a chance of the propellers being hit by enemy fire. In the worst case scenario a propeller is damaged and unable to continue its operations. It is also possible that the fragments from the damaged propeller will hit the fuselage, which can potentially rip the airframe apart. The probability of this issue occurring is low and the performance consequences are marginal, as the aircraft is able to fly with only one propeller active.  
*The propeller used will be designed to remain rigid when taking 7.62mm rounds [64]. Note that this does not mean that the propeller will be able to continue nominal operations. The engine which is attached to the propeller should be turned off to prevent the propeller from spinning out of control, and the aircraft has to return to base with one engine inoperative. To prevent the airframe from being penetrated by propeller fragment, the fuselage is reinforced with titanium strips along the line of action of the propeller.*
- 2. Armament hitting the propeller** - 3 hardpoints are located underneath each wing. When armaments are dropped from these hardpoints, there is a possibility of hitting the propeller, creating a dangerous situation for both the airframe and pilot. The probability of this event occurring is negligible, however when it happens the consequences are severe. At least the respective propeller will be damaged, and the aircraft will have to continue the flight on one engine. But the consequences can become severe if the armament detonates close to the aircraft. *To prevent armament from hitting the propeller, the engine is placed on top of the wing. Hence, the propeller area in reach of the hardpoints is minimised. Secondly, the armament placed within reach of the propeller area is non-propelled to prevent the armament from obtaining a forward motion when it is dropped and striking the propeller. All armaments are jettisoned via explosive charges that release the front part of the projectile slightly before the back to ensure a nose down pitch is created.*
- 3. Engine damage due to enemy fire** - Since the aircraft will perform its CAS mission on relatively low altitudes, there is a possibility of being hit by enemy forces. There is a realistic possibility of being hit by enemy fire, and an inoperative engine implies end of mission. *To prevent the engine from being hit by enemy fire, the engine is placed on top of the wing. As a consequence, the fuel tanks now have to deal with enemy fire from the ground. To prevent this from becoming a risk the fuel tanks will be self-sealing and are placed away from ignition sources. Furthermore, the fuel tanks in the wing will be depleted first and hence will carry minimum amounts of fuel during combat. If it is, due to the nature of a specific mission, necessary to engage the enemy with empty fuel tanks (e.g. higher payload capacity required), the aircraft is refuellable in air.*
- 4. Lift/control surface damage due to enemy fire** - During combat engagement, there is a chance of control surfaces being damaged by enemy fire. There is a possibility of the airframe being penetrated by bullets, or being under attack of missiles.  
The probability of occurrence of this event is low, and the performance impact is marginal. *To prevent damage from bullets, the entire airplane is either armoured or redundant at critical locations. The pilot and flight computers will be surrounded by a titanium bathtub, to ensure a safe cockpit environment. Furthermore, the fuel tanks are able to cope with enemy fire as explained before. With the control systems in mind, the tail has redundant control surfaces, as well as the wing.*
- 5. Bird strike** - A bird strike is a regular event during the day to day aircraft operations. This is especially true for CAS due to the fact that the aircraft spends a lot of time at relatively low altitudes during take-off, the engagement of enemy forces, and landing.  
The possibility of this event occurring is high, however the performance impact will be negligible. *A bird strike itself, can only be mitigated by a bird control unit on the ground. However, one cannot expect a bird control unit at the location of enemy forces. Since the aircraft has turboprop engines, the bird will already have been ingested by the propeller before being able to enter the engine air intake. Combined with the relatively low velocity during loiter, the propeller blades' composite construction ensures they are able to cope with the impact of birds.*
- 6. Critical Strike** - Due to the nature of CAS operations, it is possible that the aircraft will be a target of a surface-to-air missile or other anti-air measures. This could critically damage the aircraft and therefore lead to pilot fatality.  
This event has a low probability of occurring, but when it occurs the consequences will be severe. *The aircraft has been fitted with a wide array of active and passive countermeasures to minimise likelihood of enemy striking the plane. These have been detailed in [section 17.4](#), and include flares, chaff dispensers,*

*ECM jammers, air-to-air missiles, armour plating, and a fake canopy, among others. In case of the strike occurring, consequences can be minimised via deployment of the emergency ejection seat.*

### Systems failure

1. **Control system failure** - A control systems failure can cause the pilot to have a complete loss of control of the aircraft. This can lead to a fatal crash.  
The possibility of this event happening is negligible, however the consequences will be severe.  
*This risk is mitigated by designing a redundant control system. The fly-by-wire control system that is used in the aircraft has triple redundancy, since three systems are installed. Each of these systems' wires go through a different part of the aircraft. The APU, ram air turbine, and two engines produce electrical power for the entire system. There are three flight computers, all of which are located at different places within the titanium bathtub. Finally, all control surfaces are either split or are controlled by more than 1 actuator, ensuring sufficient control system redundancy.*
2. **Loss of cabin pressure** - Since only the cockpit area of the fuselage is pressurised, and the cockpit is surrounded by the titanium bathtub, only malfunctioning of the cockpit glass / seal can cause a loss of cabin pressure. The chance of the cockpit glass getting hit by enemy fire is minimal.  
Therefore, a loss of cabin pressure is unlikely to occur. The impact on performance is minimal.  
*To mitigate the risk of losing cabin pressure, the aircraft has a built-in oxygen tank which can provide the pilot with oxygen during a loss of cabin pressure. However, this tank will only be needed when cabin pressure is lost at high altitude. At low altitudes, a loss of cabin pressure does not have a big impact on the flight performance and pilot safety.*
3. **Fuel system failure** - For the fuel system, the main vulnerabilities are in the form of fuel supply contamination, fuel leakage, and fires or explosions.  
A fuel system failure, has a low probability of occurrence. However, if it occurs the performance consequences can be severe.  
*Two fuel tanks have been placed on the top part of the fuselage to minimise likelihood of tank puncture. The two fuel tanks placed in the wing will be self-sealing to minimise impact of enemy fire. Fuel contamination is mitigated for by using 4 fuel tanks with separate fuel lines to the engines. This will make sure that the fuel system is still usable when 1 up to 3 fuel tanks are contaminated. Furthermore, the fuel pumps are located within the fuel tanks or on the opposite side of expected enemy fire to ensure minimal likelihood of damage due to enemy fire. Ventilation and draining measures were taken to ensure no explosions due to gas build-up occur after a bullet strike, and fire-suppressing open-cell foam fills the spaces within the tanks.*
4. **Landing gear failure** - The landing gear system can fail to deploy. This is a huge problem, since the aircraft is equipped with large-diameter turboprops. The propellers from the turboprop will not survive a belly landing. In addition, the fuselage of the aircraft could be damaged beyond repair.  
A landing gear failure has a low probability of occurrence, but when it occurs the consequences will be severe.  
*The aircraft is designed to be able to land without the nose landing gear deployed. In that case, only the nose will skid on the ground and the propellers will stay unharmed. The same holds for the case in which the nose landing gear is deployed but the main landing gear is not. However, to be sure the main landing gears will always deploy, a second landing gear extension method is built in. This method involves the pilot to unlock the landing gear safety pins from within the cockpit, after which the landing gear will extend due to gravity. In case the landing gear does not deploy, the pilot could speed this process up by pulling +g manoeuvres.*
5. **Flaps failure** - The flaps can either fail to retract after takeoff, or deploy before landing. When they fail to retract, the aircraft experiences too much drag to be able to perform its nominal mission profile successfully. In case the flaps fail to deploy, the aircraft has to perform a landing at higher than normal speed.  
A flaps failure has a negligible likelihood of occurrence with marginal consequences.  
*To mitigate the risk of the flaps failing to retract, the aircraft has a fuel dumping system. So in case the aircraft needs to return to base immediately after takeoff, it can dump fuel to achieve the desired landing weight.  
When the flaps fail to deploy before landing, the fuel dump system can also be used to minimise the landing weight of the aircraft. However, when there is no airport close by with a sufficient runway to accommodate for a higher landing speed, the aircraft has the capability of being aerial refuelled. This will extend the range of the aircraft, and hence improves the chance of reaching a runway of sufficient length.*

6. **Accidental weapon discharge** - This condition can either be due to pilot error, or malfunctioning systems. A accidental weapon discharge can endanger both the ground troops and the pilot. The pilot will experience a unexpected load factor due to payload being dropped. If this occurs while flying over friendly troops, it can endanger them.

In case of the gun being discharged, the flying characteristics of the aircraft are changed. This is not a good thing, and hence there has to be a mitigation strategy for it.

The likelihood of a accidental weapon discharge is negligible, and the performance impact is marginal. *To make sure an accidental discharge due to pilot error cannot occur, the discharging system is designed such that it takes two pilot actions before payload is discharged.*

*If the gun is discharged accidentally, the system can be shutdown manually by the pilot. Furthermore, when the ammunition for the gun is emptied, the gun will stop firing. This can impact the flying characteristics for a maximum of 40 s. This will be further discussed in section 6.1.*

To summarize all risks and mitigation strategies mentioned above, a risk map is presented in Figure 17.1.

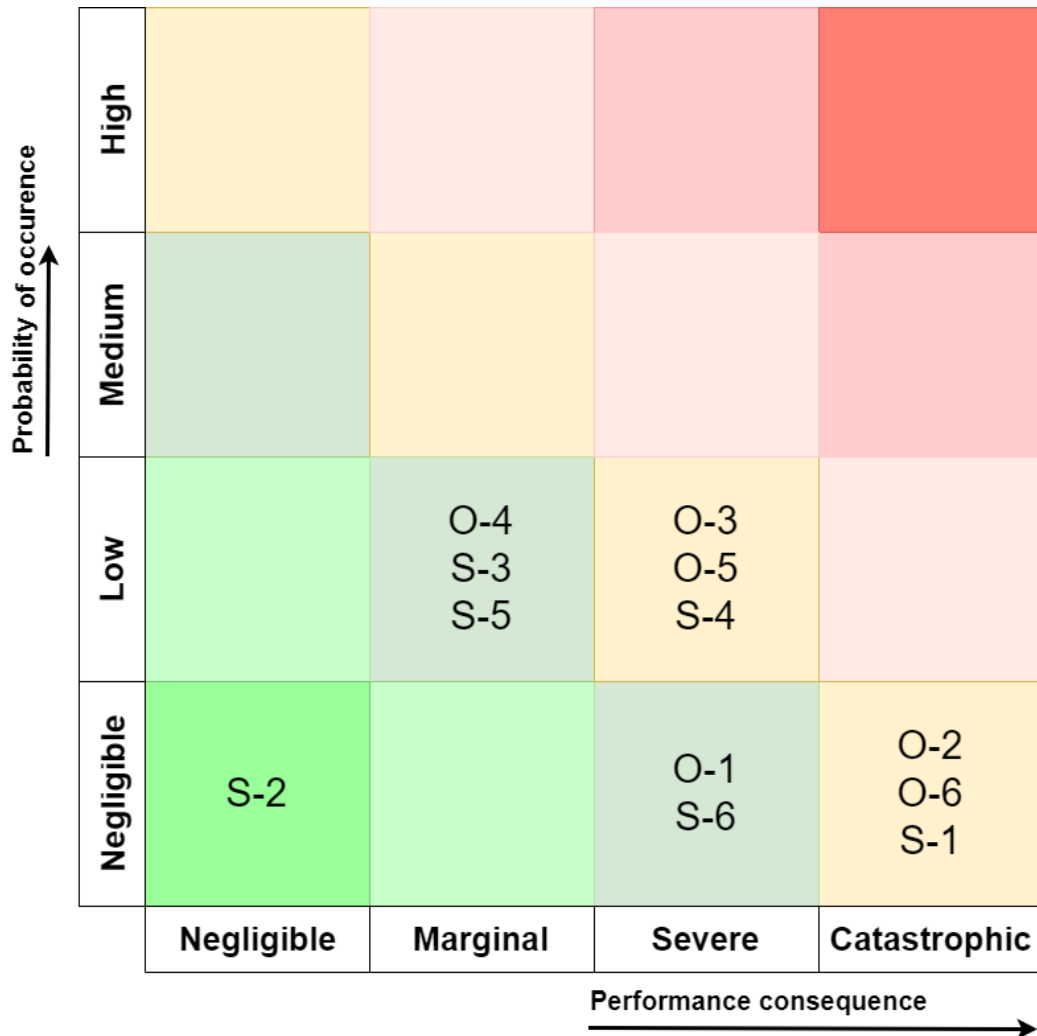


Figure 17.1: Final aircraft risk map incorporating aforementioned operational and system risks.

As can be seen from the above risk map, the only risks that are still relatively critical are those that cannot be accounted for further by any means. These have been put in the yellow boxes as further design should account for their minimisation. Catastrophic consequences imply loss of aircraft, as loss of pilot has been mitigated as much as possible via methods described in section 17.4.

# 18

## Operations and Logistics

In this chapter the operational procedures for the aircraft are discussed. First, JTAC communications and operational procedures for a combat mission are discussed. Thereafter, the operational procedures for the transporting of the aircraft and other logistics of aircraft operation are discussed.

### 18.1. JTAC

In order to perform the operations described in this chapter, Joint Terminal Attack Controller standards must be adhered to. These include the proper hardware and software installed in the cockpit for the pilot to use, as well as proper connectivity capabilities such as antennas and encryption tools. There is no indication any of the above mentioned elements depend on the design choices made at this stage of the design. Further research and design must be done in a later development stage of to ensure JTAC standards are implemented.

### 18.2. Combat Mission

It should be noted that during this analysis, it is assumed that the aircraft starts from a cold and dark (i.e. engines and power off) state. In preparation for a combat mission the aircraft should be loaded accordingly. Depending on the mission specific characteristics, the payload is placed on the hardpoints and the ammunition for the gun is loaded. Simultaneously, the aircraft can be refuelled. When all of this is going on, the pilot can enter the aircraft and start to configure all system for the flight. Meanwhile the ground engineers will do a quick checkup on the aircraft. In this quick checkup the tyres (incl. tyre pressure), the propeller blades, the turbine inlet clearance, and the moving control surfaces are visually inspected. If one of those checks fails, the aircraft is not allowed to proceed until the issue has been resolved. The engines can then be started and the aircraft can be configured for the taxi-out phase by the pilot. An operational flowchart for the combat mission is present in [Figure 18.1](#).

When the aircraft returns from its mission, the pilot sets the aircraft to a clean configuration and checks if all armaments are disarmed. When this is checked, the aircraft can safely taxi on to the ramp. At the moment the aircraft arrives on the ramp and the engines are shutdown, the ground crew can inspect the aircraft thoroughly for potential damage originating from the mission. At this stage the pilot, will shut all electrical systems of the aircraft down and reports to the ground crew about any discrepancies during the flight.

### 18.3. Gun Operation

As the aircraft contains a fully rotating turret, addressing its operation is a complex task. The simplest way for the pilot to operate the gun is with it pointing forward. This required no additional planning or training, as this is a well-established combat operation within most fighter/attack aircraft operations. Rotating the turret and firing, however, is more complex. As it is difficult to operate the gun while it is not facing the direction of the nose, one option is to have the pilot be able to rotate fire the gun while circling/flying above the enemy on autopilot. This would ensure that the aircraft is flying safely while the pilot is free to engage the enemy (visual provided via fuselage-mounted camera). This would likely require highly strenuous operational regulations due to safety concerns, leading to a second option. The gun operation could be done by a ground operator completely remotely, while the pilot controls the aircraft. This would be useful in situations where the full attention of the pilot is needed to avoid enemy fire, such as e.g. when the enemy is armed with surface-to-air missiles. A ground operator would also require high-speed and low-latency audio and visual transmission, which will likely be difficult to establish in some operational areas. As both options have their pros and cons, neither will be eliminated. Unless a more in-depth operational analysis is able to eliminate one of the options in favour of the other, both methods of gun operation will be used in different situations.

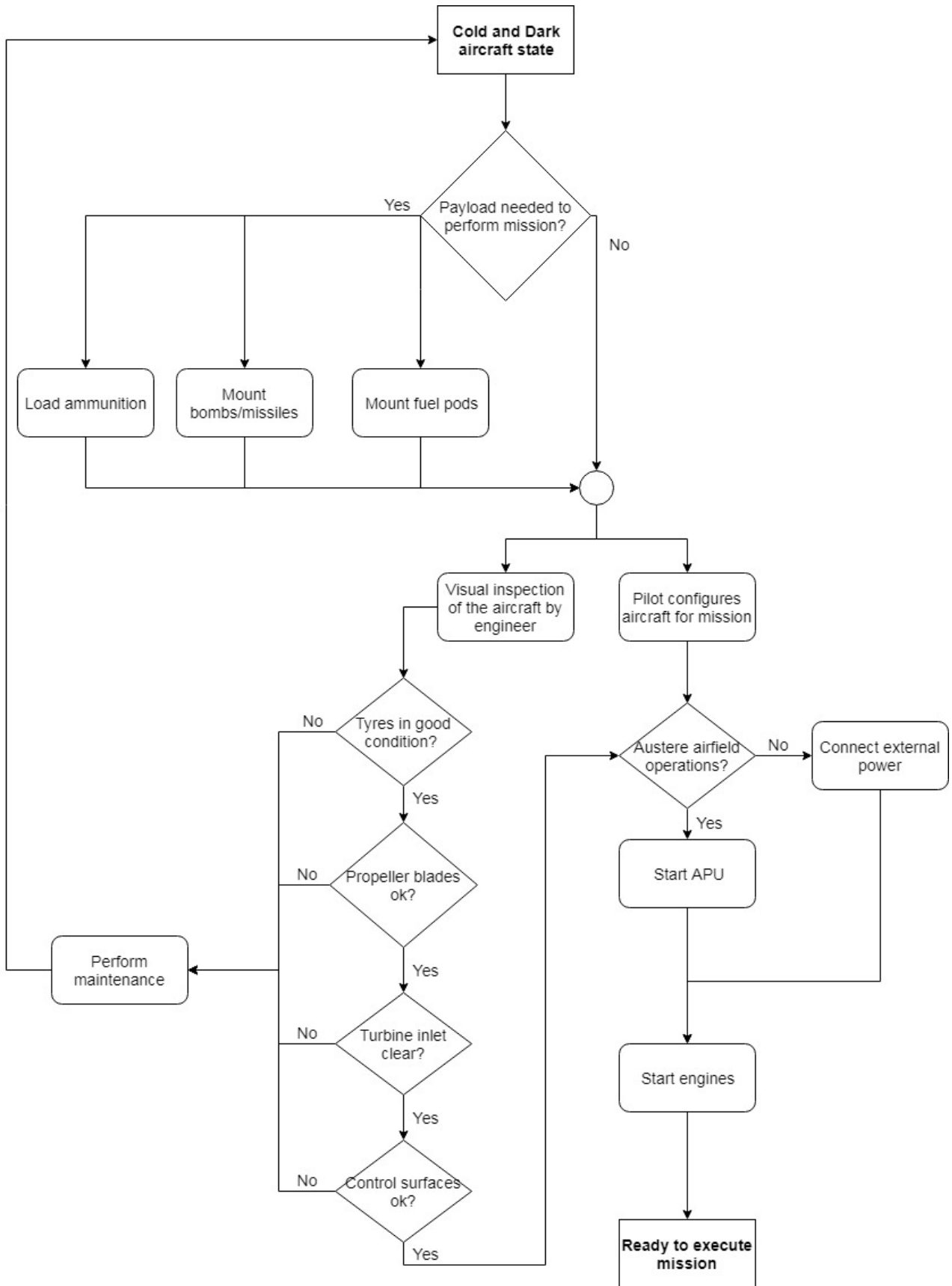


Figure 18.1: Operational flow - Cold and Dark state up to mission execution.

# 19

## Post-DSE Development

This chapter treats the post-DSE phases of the development and active life of the aircraft. The design and production phases will be treated in relative detail while the aircraft life will be evaluated at a lower resolution.

### 19.1. Further Technical Design

The level of detail that has been achieved at this design stage is equal to the preliminary design stage in the industry. However, more technical analysis is required in the detailed design phase before entering the pre-production stage. These phases, Class III and Class IV respectively, will treat these analyses. Class III continues with the recommendations of this report, while Class IV consists of detailed component analyses.

#### Class III

The project has entered the so-called Class III domain at the time this report was completed. Having performed relatively detailed analysis in aerodynamics, control & stability, performance, structural analysis and weight. The respective chapters have listed more required analyses in the recommendations section to be carried out in order to finish Class III. These recommendations are listed in the Gantt Chart, in addition to analyses performed in the industry. The chart can be found in [section 19.4](#).

#### Class IV

Class IV, also known in the industry as the detailed design stage, covers the most intricate design of the aircraft, at component level.

- FEM based methods should be performed at part level.
- detailed part CAD drawings should be created, at production quality level.
- Detailed component weight estimation and MOI estimation should be performed.
- An operations manual should be created.

This finalises the simulation phase of the aircraft design. After this stage, the physical aircraft must be tested and altered until the final product has been determined. Therefore, the production of the aircraft must be considered.

### 19.2. Production Plan

This section treats the identification, production and assembly of the aircraft, as well as the time which is needed to perform these tasks.

#### Aircraft Breakdown

In order to make a production plan, each of the separate aircraft components must be identified. These will then be assigned a manufacturer and location of production, as well as a relevant transport method to the sub-assembly location. Note that the following list has been simplified in the context of the DSE, as it is impossible to do a complete breakdown of the aircraft components at this stage. The following components have been identified:

- Ejection seat - Martin Baker, Uxbridge, UK
- Canopy - GKN Aerospace, UK (Amsterdam, Netherlands Branch)
- Bathtub - Timet, Salisbury, NC, USA

- Flight Computers & Avionics - UTC Aerospace Systems, Charlotte, NC, USA
- Electrical systems - UTC Aerospace Systems, Charlotte, NC, USA
- Actuator systems - UTC Aerospace Systems, Charlotte, NC, USA
- Wing & Tail section - FACC, Kammer, Austria - The company will supply flaps, ailerons, as well as the wing box and tail structure. They will also supply the main landing gear fairing. In case the workload is too high, they may be aided by Böhler Aerospace (Kapfenberg, Austria) in terms of structural component production.
- Fuselage section - GKN Aerostructures, Portsmouth, UK
- 20mm Gun - General Dynamics Ordnance & Tactical Systems, St. Petersburg, FL, USA
- Gun Turret - Nexter Systems, Versailles, France
- Landing Gear & Braking Systems - UTC Aerospace Systems, Everett, WA, USA
- Fuel system - Senior plc, Rickmansworth, UK
- Engines - Rolls Royce plc, UK (Singapore Manufacturing HQ)
- Propellers - GE Aviation, US (Dowty HQ Gloucester, UK)

Due to the United States International Traffic in Arms Regulations<sup>1</sup>, high-level defence technology cannot be exported. Many components are manufactured in the U.S, with no competitor of equal quality available outside of the United States. Since the U.S. market is also the largest, it is desirable that components are manufactured domestically to increase attractiveness regarding U.S. influence on the design and job creation. However, the amount of components manufactured in the EU is significant as well, having to ship many parts. Minimising transport due to costs and minimising risk, the most sensible location for shipping would therefore be close to the U.S. east coast. More specifically, Charlotte North Carolina appears suited for the needs. UTC Aerospace Systems is located in the same city, while Timet, which provides the titanium alloys, is located approximately 65km away. The size of Charlotte allows for the finding and housing of a major workforce, which might be required in the assembly process. As the largest components (fuselage, wing, tail) will be made in Europe, it seems to be logical to construct most sub-assemblies in Europe.

### Production Process

In order to ensure consistent delivery intervals, the production line should allow for continuous and orderly production. Each component supplied by the aforementioned suppliers must be uniquely identifiable and trackable to ensure missing components are accounted for and defective components are traceable. As each manufacturer likely has their own product labelling procedures, these must all be checked for coherence, and a component tracking system must be made. The production line must not stagnate when the supplies needed are not delivered on-time. Therefore, a warehouse (possibly more than one) will be located at the beginning of the assembly plant.

The environment in the warehouse must be controllable to ensure optimal storage conditions for all components. This way, the components can be assembled in their ideal environments. The warehouse must contain an additional batch of critical production components whenever possible. Additionally, contracts specifying consequences of supply/component delay will be made with each supplier to ensure fair compensation for bad on-time production performance. Each of the aforementioned aircraft elements will be part of a sub-assembly, after which it will be transported to the final assembly location for integration.

### Sub-assemblies

The assembly of the aircraft takes place in multiple phases. It is important to first assemble the main components before assembling the whole aircraft to keep the production process simple. The aircraft is divided in the following sub assemblies:

- Fuselage sub-assembly
- Wings sub-assembly

<sup>1</sup>What is ITAR? - <https://gov-relations.com/itar/> [accessed 02-07-2018]

- Landing gear sub-assembly
- Cockpit sub-assembly
- Tail sub-assembly
- Weapon system sub-assembly

**Final Assembly**

In the final assembly phase of the production process, all sub-assemblies are merged into the final aircraft. The order in which this is done can be seen in Figure 19.1.

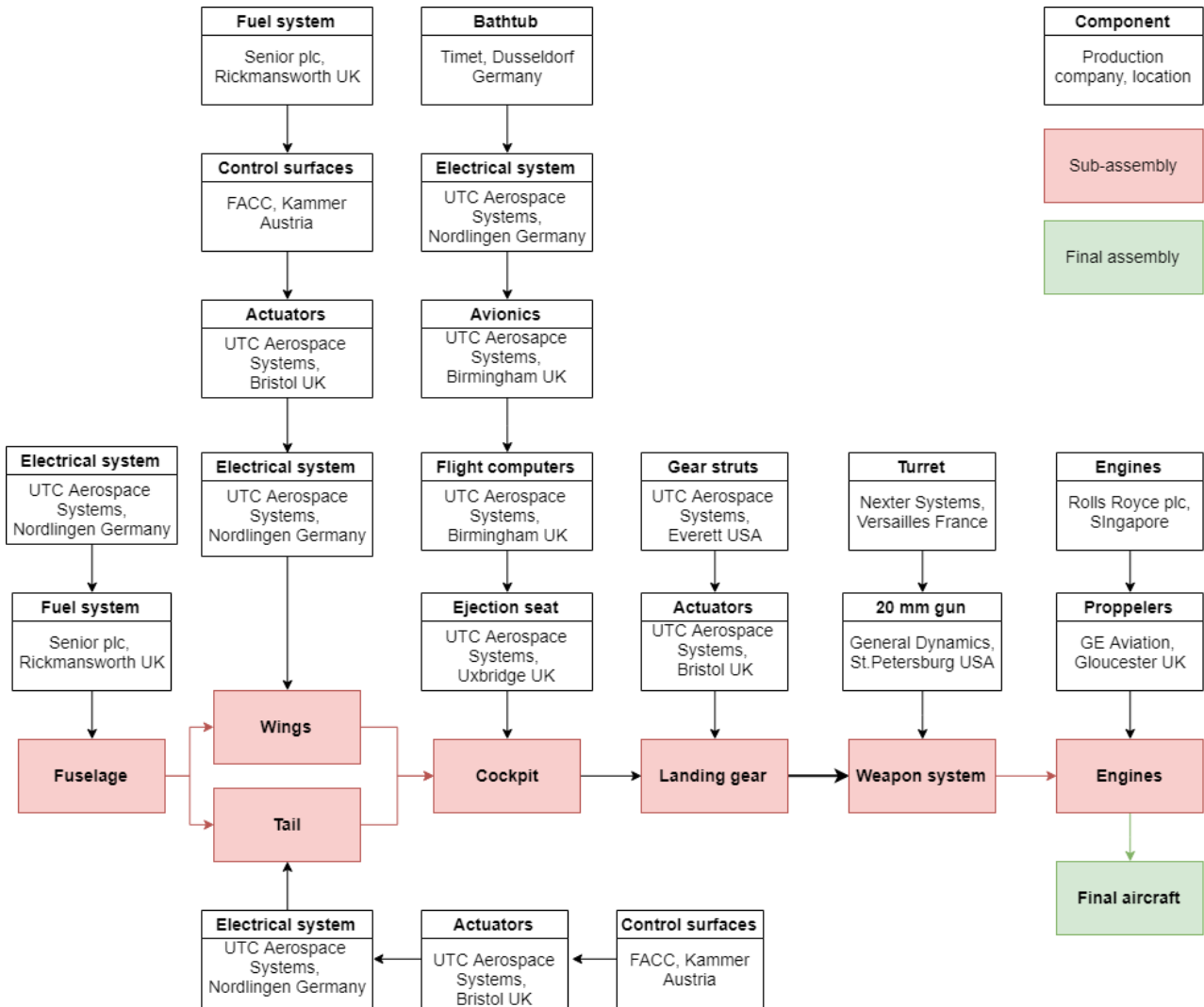


Figure 19.1: Flow chart of the production-plan.

The first step in the final assembling process is attaching the wings and the tail to the fuselage. These can be attached simultaneously since the fuselage is fixed by the jigs it is standing on, and the fuselage can not tip over due to a change in centre of gravity. Thereafter the cockpit is installed. This is done first thing after the wing and tail are attached, since the cockpit is the place where all flight computers and control systems are located. All components installed hereafter will have connections towards the cockpit, therefore it is installed at an early stage of the assembly. Next on the production line is the landing gear. When the landing gear is properly installed and tested, the jigs can be removed. Hereafter, the aircraft can be moved on its own landing gear to the next station where the complete weapon system is installed. Lastly, the engines will be installed. The engines are assembled at the end of the production line, since they will be the most expensive components of the aircraft.

As the aircraft's ferry range is 6800 km, it is possible that all aircraft are delivered by simply flying the aircraft to the destination. From the production location in Amsterdam, the aircraft could reach the United States, Canada, and Russia. Furthermore the aircraft's large ferry range would enable e.g. the USAF to easily reach any conflict area within less than a day.

### Production Timeline

As it is difficult to estimate the actual production process at this stage of design, historical data of aircraft that have been used for CAS missions will be used. These are the A-10, F-15, F-16, and F/A-18. A commonality between the development of all three aircraft is that a tender with a given set of performance requirements was initiated by the USAF. Then, several prototype aircraft are taken into the second phase, where real-world performance is tested and the winner selected. Only then does full-scale production actually start. In the context of the DSE, it is assumed that the aircraft design is (close to) final, and that full scale production can start as soon as the aircraft is certified for flight. The timelines of these three aircraft were compared in order to get an estimation of time required from start of production to delivery. These times include the entire process from prototype production, through certification, testing, full scale production, delivery, and up to operational introduction, and are summarised in [Table 19.1](#).

Table 19.1: Dates of first flights and operational introductions for various aircraft used in CAS operations.

Aircraft	First Flight	Operational Introduction
A-10	January 1973	October 1977
F-15	July 1972	January 1976
F-16	January 1974	August 1978
F/A-18	November 1978	November 1983

It can therefore reasonably be assumed that the a total of five years is sufficient to go from the first prototype to operational introduction. This would leave two years of further R&D before the first prototype is made. At peak production, 12 A-10 aircraft were being produced monthly<sup>2</sup>. The F-16 has delivered over 4500 units upto July 2016<sup>3</sup>, resulting in an average production rate of 10 aircraft per month for the entire project duration. It is therefore expected that a rate of 10 aircraft per month can be achieved, especially as the engines and gun are already tried-and-tested parts. With this rate of production, the final delivery for the current 600-aircraft market can be finalised in 2031, assuming deliveries start in 2025. Note that this does not include additional orders that may be placed due to loss of aircraft in operation.

### Test Aircraft Production

The production & testing phase commences with the production of multiple testing aircraft. More information on the production can be found in [section 19.2](#). The production process must be set up ad perfected which will take some substantial time. However, this should be done as much as possible in parallel with the design process and should therefore not cause major delays. According to the reference production data presented in the chapter, it is realistic to assume five years from first flight to operational introduction. The fully developed and proven engines will decrease this time significantly.

## 19.3. Operational life

The operational life of the aircraft depends on its effectiveness, upgradeability, functional need and operational costs. While the A-10 was designed especially suited to fight enemy armour, it has not been used for that purpose specifically in the last 40 years. Even though its core purpose might not be existent sometime in its operational life, modifications should extend its life time to a comparable lifetime as the A-10. These 40 years of operational lifetime are no exception. The Su-25, F-16, Harrier, and F/a-18 all possess operational lifetimes of at least 35 years, with a least several more years to come before end-of-life. A conservative operational lifetime of 30 years is therefore assumed, which has a reasonable probability of being exceeded. Upgrading the aircraft is essential to be able to reach this projected lifespan. Future technological advancements are sure to increase the effectiveness and efficiency of the aircraft, or to decrease cost while performing the same mission. In the past, most if not all military aircraft have undergone major upgrades, whose cost and time

<sup>2</sup>GlobalSecurity - A-10/OA-10 Thunderbolt II <https://www.globalsecurity.org/military/systems/aircraft/a-10-history.htm> [Accessed 25-06-2018]

<sup>3</sup>Defense News - Lockheed Martin Looks To Upgrade 500 In-Service F-16s <https://www.defensenews.com/digital-show-dailies/farnborough/2016/07/13/lockheed-martin-looks-to-upgrade-500-in-service-f-16s/> [Accessed 26-06-2018]

must be accounted for.

The end-of-life of the aircraft involves executing end-of-life procedures as described in [chapter 16](#). These involve analysis for reusable parts, and basic disassembly of aircraft components. The aircraft components are then shredded and the scrap analysed for recyclable parts. Depending on the political situation at the time of decommission, the aircraft may be immediately shredded to prevent hostile parties from obtaining any aircraft parts.

### 19.4. Post-DSE Gantt Chart

All of the aforementioned post-DSE activities are visualised in the post-DSE Gantt chart. It visualises the following design phases in high resolution, as the analyses which have to be performed are clear to the team. This graph can be found in [Figure 19.2](#). A second Gantt chart visualises the development process in low resolution until operational readiness, which is estimated to meet the requirement of 2025. This chart can be found in [Figure 19.3](#).

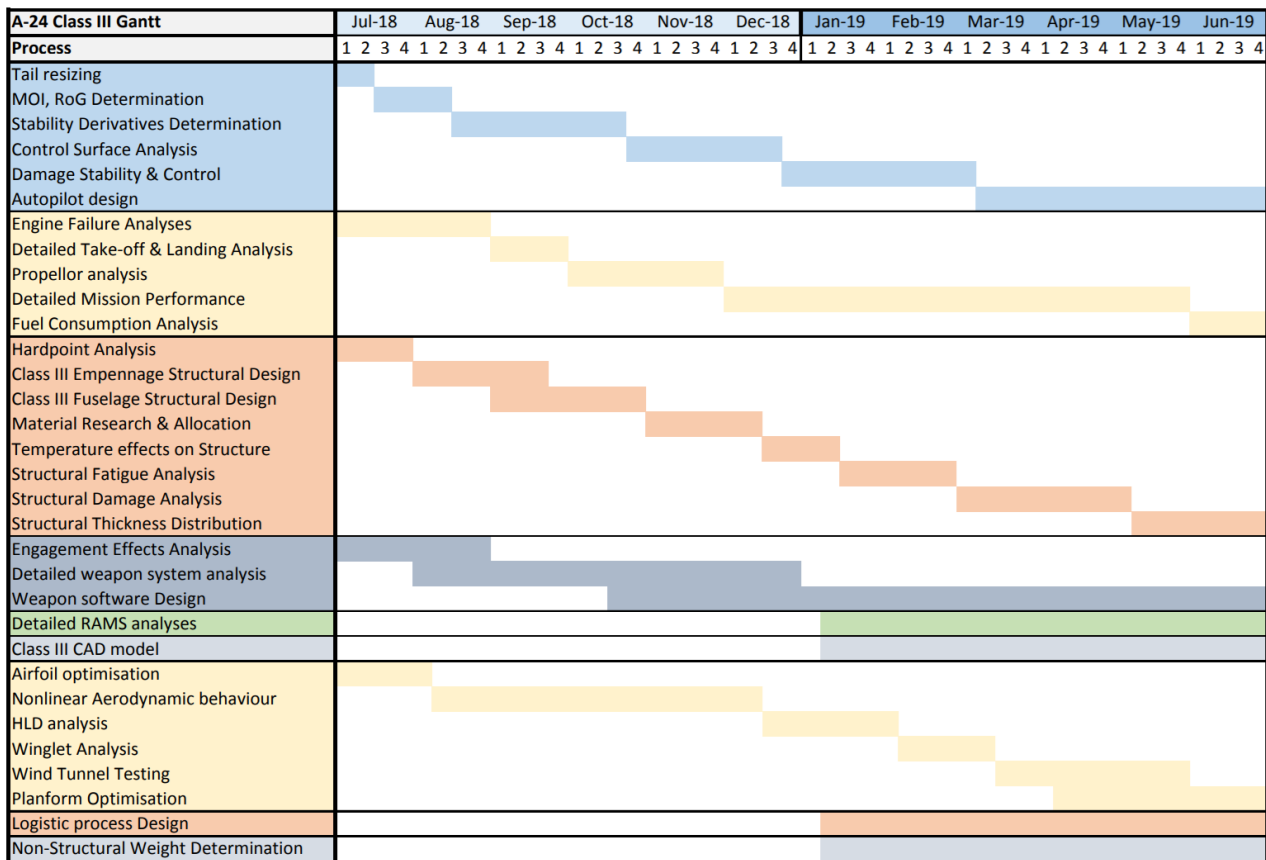


Figure 19.2: Detailed Gantt of the Class III Design stage.

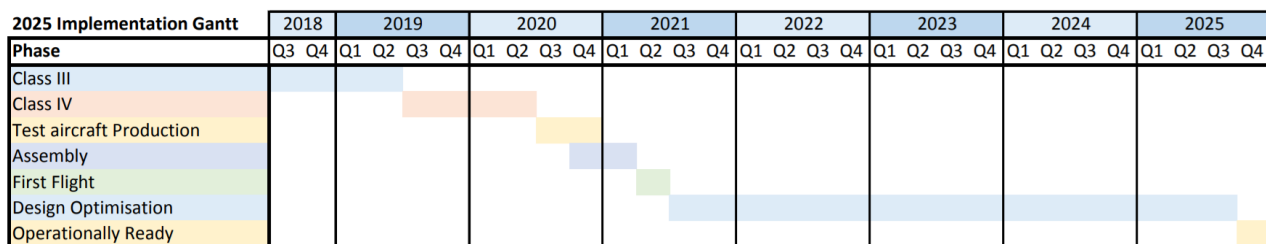


Figure 19.3: Development Gantt chart until implementation.

# 20

## Recommendations

The following recommendations were established by the design team, which will add a level of detail to the current design.

### Weapons

The XM301's characteristics, of which especially the accuracy, should be evaluated during flight in a multitude of orientations. The operation of the gun in combination with the camera should also be looked into, including a comparison/feasibility check of pilot/ground operator operation. The firing of the gun should be analysed structurally, especially considering impacts due to austere airfields and in-flight aerodynamic forces.

### Flight Performance

In terms of flight performance, a more detailed analysis of take-off and landing performance could also account for the nose-down moment caused by the brakes and nose up moment caused by the propellers' reverse thrust, as these are located at a certain vertical distance from the aircraft c.g. This would be done to ensure that the nose gear loads do not exceed the allowable loads.

During fuel burn calculations, conservative estimates were used to ensure that the probability of the final aircraft not meeting the mission profile is minimal. These include maximum power use in take-off, climb, and combat. The actual power settings for these phases should be computed to improve the accuracy of the required fuel, especially as this greatly influences the nominal payload weight. Moreover, the different mission capabilities analysed in [section 11.4](#) should further be explored to ensure that the full capabilities and potential applications of the aircraft are known. Finally, turning performance should be looked into more in-depth in the next design phase.

### Wing Design

During the airfoil selection the aforementioned database was used. At the stage and size of this design project, this resulted in a reasonable amount of airfoils suitable for the aircraft. However, there are a lot more airfoils and there is also a possibility to design own airfoils, optimised for the mission of the aircraft. Furthermore, in the airfoil selection it was assumed that all airfoils have the same  $C_m$  characteristics, which is obviously not the case.

For the wing design an interesting feature would be adding winglets. It is shown that winglets increase the wing aspect ratio and therefore efficiency. However, adding winglets, without doing extensive research about what the best design would be for this mission profile, would be too time consuming. Therefore, this is a point of attention for in future design.

During future design, other flaps and aileron configurations, for instance flaperons, should be considered to further improve the  $C_{l_{max}}$  and roll characteristics of the aircraft. Furthermore, differential ailerons should be analysed, to minimise the effect of yawing.

### Aerodynamics

In future research a closer look at the spanwise section lift distribution should be done, rather than taking the values at the MAC. Furthermore, off-nominal situations should be investigated as well, for example the increase in drag during engine shutoff and non-retracting gun. When better hardware is available, more extensive research can be done on the lift and drag characteristics of the wing and the aircraft. When the trim tab will be sized, the trim drag can be evaluated as well.

In later phases of the design more accurate CFD programs could be used to get more accurate results for the lift and drag characteristics for complex shapes like the split x-tail. Lastly, it should be noted that inputs for the lift and drag are taken from the performance department, while some of the outputs are inputs for performance. This means that in order to get more accurate values, future iterations should be performed. As already explained in the introduction of the moment characteristics section, the curves are only made for the linear region of the  $C_L - \alpha$  curve. When following the method of Roskam [18], the region from  $C_L^*$  to  $C_L^*$  in the  $C_L - C_m$  should be estimated by analysing the pitch break. However, this estimate does not give data to be able to plot the last part. Therefore, in next design phase, another method should be found to do this. This will give accurate results when the aircraft is flying at high angles of attack and thus, the stability of the aircraft at these angles can be predicted in a better way.

In order to obtain a negative  $C_{m\alpha}$ , a closer look has to be given at the equations for the aircraft pitching moment coefficient. As already mentioned, the c.g. is behind the a.c. There are two options to solve this problem: shift c.g. or shift a.c. The first option is to move mass forward of the aircraft. This is not possible, as already explained in section 7.3. This means that the aircraft a.c. has to be shifted. As can be seen in the Equation 10.43, the main parameters that influence the value are the tail and fuselage parameters. It is assumed that  $x_{ac,w}$  cannot be changed. To change the tail effect on the aircraft a.c., the size and arm should be changed, which means that new iterations has to be performed to obtain the optimal main wing and tail position. The a.c. of the wing fuselage combination cannot really be changed, as it mainly depends on  $C_{L\alpha_w}$ , which in this stage of the design cannot be changed. To conclude this, it is clear that the tail should be redesigned in such a way that  $C_{m\alpha}$  is negative and therefore the moment characteristic analysis should be included in the iteration process.

## Empennage design

Once the more detailed aerodynamic analysis is completed, the tail sizing can be done in more detail again. With the input values for Equation 12.7, Equation 12.8 and Equation 12.9 the exact required horizontal tail size and longitudinal wing position should be reiterated.

Furthermore, once the moments of inertia are initially estimated, the dynamic stability of the aircraft should be analysed again. Based on the outcomes of this more accurate analysis, it could be determined that a change in certain design parameters is desired. It also became clear that some of the eigenmotions showed strange, and sometimes unacceptable behaviour. For the phugoid motion, the reason assumed for showing no oscillatory behaviour is the unreliable approximation of the stability control derivatives. This can be solved by performing wind tunnel tests or CFD analyses. For the spiral and dutch roll instability, looking at the obtained values for  $C_{n\beta}$  and  $C_{l\beta}$ , the stability derivatives are likely to be non reliable as well. Also this should be further investigated using wind tunnel data or CFD analyses.

## Structures

The fuselage and tail cross-sections have not been designed yet. In the next design phase, one should start with calculating the loads in the fuselage and the tail respectively for the extreme load cases. Thereafter, the cross-sectional design of both parts can be started. The cross-sectional design should be started by using the discretisation techniques as used for the wing box design. Using these techniques a preliminary design for both the fuselage and tail cross-section can be set up. When the idealised cross-sections are finalised, they can be converted to more accurate cross-sections by selecting materials, stringers and skin thicknesses. When the more detailed cross-sections are setup, a more accurate cross-section can be designed. Eventually, the cross-sectional designs can be optimised in terms of weight and load carrying capabilities.

For all structural analyses performed, inertial forces are not analysed other than the hard landing load case. These loads should be identified and analysed in consecutive design stages.

When all cross-sections are designed, one should take a closer look at the structural connections of the wings to the fuselage, and the tail to the fuselage. These connections are of big importance, since it determines the structural integrity of the whole aircraft. If the design of those connections is insufficient, all previous results will not be usable.

More detailed analysis should also be performed on structural elements which introduce a large force into the structure in a small area. The rib located at the landing gear and hardpoints are an example of this. These hardpoints are currently modelled as point forces into the structure, while in reality more complex loading is

applied to the structure. These should be identified and analysed.

More advanced analyses should be performed to obtain a better structural design. Fatigue, corrosion and temperature analyses should be performed to design for the deterioration of the aircraft structure and consecutively the failure modes. To conclude the structural analysis, finite element analysis should be performed on the whole aircraft. Using finite element analysis the interaction, load paths and stress concentrations of all components can be analysed, to end up with the final structural design of the aircraft.

Finally, more detailed deflection analyses have to be performed. A deflection method must be found which incorporates the varying moment of inertia. Torsional deflection must be determined in a similar manner.

## Sustainability

With respect to sustainability, it is recommended that the biofuel feasibility with the AE2100A engine be tested. This would greatly improve the limited sustainability of the aircraft should it prove to be feasible. More detailed end-of-life procedures should also be developed to ensure all aircraft parts are accounted for at end-of-life, and that the aircraft's decommissioning does not harm the environment.

# 21

## Conclusion

A conclusion on the aircraft as a whole is best done by attempting to answer the project objective statement: "Deliver a successful and innovative close air support combat aircraft design which outperforms the A-10 in the current environment of asymmetric warfare."

Outperforming the A-10 in asymmetric warfare is most easily answered. The requirements were generated to address the present necessities in close air support. These requirements were met through the employment of systematic engineering design and advanced analysis methods. A comprehensive iteration setup as well as verification and validation methods were employed to ensure legitimate results. The integration of these processes resulted in a high-fidelity technical design, meeting all driving requirements. This comes at a cost, however, as the current aircraft design carries a minimum unit cost of \$ 15 million, while a fair market price for CAS aircraft is \$45 million. While this may be a limitation to potential customers, the unparalleled performance and low operational cost will likely make up for the steep sale price.

The loitering requirement was met by using highly efficient AE2100A turboprop engines, combined with an endurance-optimised wing, which also enabled the aircraft to exceed all range requirements. A multitude of airfield categories are available for use due to the engine placement, landing gear design, and high runway performance facilitated by the powerful engines. The nominal mission profile includes a 6-hour loiter time, including a nominal payload of 5361 kg. Integrated in the mission profile, this loiter time pushes the upper limits of pilot operation, resulting in a near-maximum duration flight cycle. The addition of an external fuel tank can further increase this to over 10 hours, making the aircraft very comparable to UAV loiter performance. The payload can be further increased to a maximum of 7000 kg.

The turret-mounted gun allows for an innovative CAS approach for an attack aircraft. Operated by either the pilot or a ground operator, it is able to engage mobile targets without the need for the pilot to steer in their direction. It is also able to shoot at targets behind and directly below the aircraft, allowing for longer engagement time per fly-by while removing the need for excessively long strafing runs. These capabilities allow the system to address the real-world need for a dedicated CAS aircraft with high battlefield availability and offensive capability, with a specification weight of 21 880 kg, which meets the maximum MTOW requirement of 23 000 kg. The favourable characteristics of the current design, in combination with the estimated development timeline, source prospects for a successful operational lifetime. It can therefore be concluded that the A-24 outperforms the A-10 in the contemporary CAS domain, and will successfully replace it.

## Bibliography

- [1] J. Roskam, *Airplane Design Part V - Determination of Stability, Control and Performance Characteristics: FAR and Military Requirements* (DARcorporation, 2003).
- [2] W.J.C. Verhagen, *Project Guide Design Synthesis Exercise - Next Generation Close Air Support Combat Aircraft*, Lucht- en Ruimtevaarttechniek, TU Delft, Kluyverweg 1, Delft (2018).
- [3] P. Bastiaanssen, C. Bogaerts, Y. Brouwer, J. Cogan, T. Dotman, A. Faddegon, D. Koch, J. Koopman, A. Nikolajevic, and T. P. de Boer, *Baseline report*, Tech. Rep. (TU Delft, 2018).
- [4] J. Roskam, *Airplane Design Part I - Preliminary Sizing of Airplanes* (DARcorporation, 1985).
- [5] G. Ruijgrok, *Elements of Airplane Performance*, 2nd ed. (VSSD, 2009).
- [6] G. L. Rocca, *AE3211-I - Slides 1 - Systems Engineering and Aerospace Design*, (2018).
- [7] E. M. W. Verhagen, *AE3200 - Workshop 3 - Project Management & Systems Engineering*, (2017).
- [8] W. van der Wal, *AE3212-II - Slides 1 - Simulation, Verification and Validation*, (2018).
- [9] General Dynamics: Ordnance and Tactical Systems, *Xm301 20mm lightweight gatling gun product brochure*, (2014).
- [10] General Dynamics: Ordnance and Tactical Systems, *F-22a 20mm gatling gun system product brochure*, (2014).
- [11] K. Huang, *Comanche RAH-66 Turreted Gun System (TGS)* (TACOM-ARDEC, 2008).
- [12] U.S. Government, *Code of Federal Regulations: Aeronautics and Space* (Government Printing Office, 2012).
- [13] M. H. Sadraey, *Aircraft Design: A Systems Engineering Approach* (John Wiley & Sons, 2013).
- [14] E. Torenbeek, *Advanced aircraft design: conceptual design, analysis, and optimization of subsonic civil airplanes* (John Wiley & Sons, 2013).
- [15] F. Oliviero, *AE2111-II - Aircraft aerodynamic analysis – Mobile surfaces of the wing*, (2018).
- [16] A. Mulder, W. van Staveren, J. van der Vaart, E. de Weerd, C. de Visser, A. in 't Veld, and E. Mooij, *Flight Dynamics Lecture Notes* (Faculty of Aerospace Engineering, Delft University of Technology, 2013).
- [17] F. Oliviero, *Aerospace Design and Systems Engineering Elements II - Slides 2 - Lift & Drag Estimation*, (2018).
- [18] J. Roskam, *Airplane Design Part VI - Preliminary Calculation of Aerodynamic, Thrust and Power Characteristics* (DARcorporation, 1987).
- [19] EASA, *Rolls Royce AE2100 Type Certificate Data Sheet*, (2008).
- [20] M. Voskuijl, *AE1110-I - Introduction to Aerospace Engineering I*, (2018).
- [21] B. Gunston, *Jane's Aero-Engines*, Tech. Rep. (IHS Markit, 2018).
- [22] M. Voskuijl, *AE2230-I Flight Mechanics*, (2013).
- [23] J. Roskam, *Airplane Design Part VII - Component weight estimation* (DARcorporation, 2003).
- [24] D. Raymer, *Aircraft Design: A Conceptual Approach* (American Institute of Aeronautics & Astronautics, 1995).
- [25] N. S. Currey, *Aircraft Landing Gear Design: Principles and Practices* (American Institute of Aeronautics & Astronautics, 1988).

- [26] USAF, *MIL-C-5011A Military Specifications - Charts, Aircraft Characteristics and Performance, Piloted Aircraft*, (1951).
- [27] Z. S. Spakovszky, *Unified: Thermodynamics and Propulsion* (MIT, 2012).
- [28] G. M. R.J. Jeracki, *Low and High Speed Propellers for General Aviation - Performance potential and Recent Wind Tunnel* (1981).
- [29] B. Gunston, *Jane's Aircraft Upgrades*, Tech. Rep. (IHS Markit, 2018).
- [30] D. Scholz, *Aircraft design - 9 empennage design*, (2017), open Educational Resource (OER) for Hamburg Open Online University (HOOU).
- [31] J. Roskam, *Airplane Design Part II - Preliminary Configuration Design and Integration of the Propulsion System* (DARcorporation, 1985).
- [32] R. Vos and J. Melkert, *Aerospace Design and Systems Engineering Elements I - Slides 7 - Landing Gear and Empennage* (2018).
- [33] T. Megson, *Aircraft Structures for Engineering Students*, 5th ed. (Elsevier, 2013).
- [34] J. Roskam, *Airplane Design Part IV - Layout of Landing Gear and Systems* (DARcorporation, 1988).
- [35] H. Curtis, *Fundamentals of Aircraft Structural Analysis*, (2018).
- [36] V. Piscopo, *Buckling Analysis of Rectangular Plates under the Combined Action of Shear and Uniaxial Stresses*, (2010).
- [37] D. G. R. William D. Callister, *Materials Science and Engineering: An Introduction*, 9th ed. (John Wiley & Sons, 2015).
- [38] Latrobe Specialty Steel Company, *Data sheet lescolloy d6ac vac-arc*, (2008).
- [39] A. P. Mouritz, *Introduction to Aerospace Materials* (Woodhead Publishing, 2012).
- [40] R. E. Quigley, *More Electric Aircraft*, Tech. Rep. (Wright-Patterson Air Force Base, 1993).
- [41] K. A. Rigby, *Aircraft Systems Integration of Air-Launched Weapons* (John Wiley & Sons, 2013).
- [42] J. E. Tomayko, *Computers take flight: A history of nasa's pioneering digital fly by wire project*, The NASA History Series (2000).
- [43] D. Nguyen and B. Widrow, *Neural networks for self-learning control systems*, IEEE Control Systems Magazine (1990).
- [44] A. J. Kornecki and K. Hall, *Approaches to assure safety in fly-by-wire systems: Airbus vs. Boeing*, Tech. Rep. (Embry Riddle Aeronautical University, xxxx).
- [45] J.-C. Mare and J. Fu, *Review on signal by wire and power by wire actuation for more electric aircraft*, Chinese Journal of Aeronautics (2017).
- [46] A. Emadi and M. Ehsani, *Aircraft power systems: Technology, state of the art, and future trends*, IEEE AES Systems Magazine (2000).
- [47] H. Cotton, *Electrical Technology* (Pitman, 1950).
- [48] N. Tian, *Trends in World Military Expenditure, 2016* (Stockholm International Peace Research Institute, 2017).
- [49] C. Hoyle, *World Air Forces 2018* (Flight International, 2018).
- [50] N. G. Mankiw, *Principles of Microeconomics*, 5th ed. (Cengage Learning, 2007).
- [51] Office of the Under Secretary of Defense (Comptroller), *Program acquisition cost by weapon system*, (2018).
- [52] U.S.A. Department of the Navy, *Department of the navy fiscal year (fy) 2012 budget estimates, Aircraft Procurement, NAVY Volume I: Budget Activities 1-4*, 32 (2011).

- [53] J. P. Roth, *Fiscal year (fy) 2016 department of defense (dod) fixed wing and helicopter reimbursement rates*, (2015), office of the Under Secretary of Defense (Comptroller).
- [54] T. W. Chan, *Immediate impacts on particulate and gaseous emissions from a t56 turbo-prop engine on a biofuel blend*, *Transportation Research Procedia* (2013).
- [55] A. Bows, K. Anderson, and P. Upham, *Aviation and Climate Change - Lessons for European Policy* (Taylor & Francis, 2008).
- [56] W. E. Briner, *The evolution of depleted uranium as an environmental risk factor: Lessons from other metals*, *International Journal of Environmental Research and Public Health* **3**, 129 (2006).
- [57] D. S.K., *Recycling aluminum aerospace alloys*, *Light Metals* (2007).
- [58] H. Lund, *McGraw-Hill Recycling Handbook* (McGraw-Hill Professional, 2001).
- [59] B. Dolega, *Active methods of increasing reliability of fbw control systems for small aircraft*, ISSN 1648-7788 AVIATION, Vol IX, No 1 (2005).
- [60] M. Verhoeff, W. Verhagen, and R. Curran, *Maximizing operational readiness in military aviation by optimizing flight and maintenance planning*, *Transportation Research Procedia* (2015).
- [61] National Research Council, *Improving the Efficiency of Engines for Large Nonfighter Aircraft* (National Academies Press, Washington DC, 2007).
- [62] C. H. Friend, *Aircraft Maintenance Management* (Pearson Longman, 1992).
- [63] U. D. Kumar, J. Crocker, J. Knezevic, and M. El-Haram, *Reliability, Maintenance and Logistic Support: - A Life Cycle Approach* (Springer, 2000).
- [64] R. E. Ball, *The Fundamentals of Aircraft Combat Survivability Analysis and Design* (American Institute of Aeronautics & Astronautics, 2003).

# A

## Class II Weight Estimation

The equations used for the Class II weight estimation are presented below having been split up into three sections. First the structural weight is presented, then the powerplant weight and finally the fixed equipment weight.

### A.1. Structural Weight

Here the wing,  $W_w$ , horizontal,  $W_h$ , and vertical tail,  $W_v$ , fuselage,  $W_f$ , and landing gear,  $W_g$ , weights are calculated with Equation A.1 through Equation A.5 respectively.

$$W_w = 3.08 \cdot \left[ \frac{K_w \cdot n_{ult} \cdot W_{TO}}{\frac{t}{c_m}} \left( \left( \tan(\Lambda_{LE}) - \frac{2 \cdot (1 - \lambda)}{A \cdot (1 + \lambda)} \right)^2 + 1 \right) \cdot 10^{-6} \right]^{0.593} \cdot (A \cdot (1 + \lambda))^{0.89} \cdot S^{0.741} = 1988.6 \text{ kg} \quad (\text{A.1})$$

$$W_h = 0.0034 \cdot \left[ (W_{TO} \cdot n_{ult})^{0.813} \cdot S_h^{0.584} \cdot \left( \frac{b_h}{t_{r_h}} \right)^{0.033} \cdot \left( \frac{\bar{c}}{l_h} \right)^{0.28} \right]^{0.915} = 536.0 \text{ kg} \quad (\text{A.2})$$

$$W_v = 0.19 \cdot \left[ \left( 1 + \frac{z_h}{b_v} \right)^{0.5} \cdot (W_{TO} \cdot n_{ult})^{0.363} \cdot S_v^{1.089} \cdot M_H^{0.601} \cdot l_v^{0.726} \cdot \left( 1 + \frac{S_r}{S_v} \right)^{0.217} \right]^{1.014} \cdot \left[ A_v^{0.337} \cdot (1 + \lambda_v)^{0.363} (\cos(\Lambda_{1/4_v}))^{-0.484} \right]^{1.014} = 191.4 \text{ kg} \quad (\text{A.3})$$

$$W_f = 2 \cdot 10.43 \cdot K_{inl}^{1.42} \cdot \left( \frac{\bar{q}_D}{100} \right)^{283} \cdot \left( \frac{W_{TO}}{1000} \right)^{0.95} \cdot \left( \frac{l_f}{h_f} \right)^{0.71} = 1673.3 \text{ kg} \quad (\text{A.4})$$

$$W_g = 62.61 \cdot \left( \frac{W_{TO}}{1000} \right)^{0.84} = 732.1 \text{ kg} \quad (\text{A.5})$$

### A.2. Powerplant Weight

The powerplant weight is made up of the engine,  $W_e$ , nacelle,  $W_n$ , air induction system,  $W_{ai}$ , propeller,  $W_p$ , fuel system,  $W_{fs}$ , in-flight refuelling,  $W_{inflight}$ , fuel dumping system,  $W_{fd}$ , engine control system,  $W_{ec}$ , engine starting system,  $W_{ess}$ , and the propeller control system,  $W_{pc}$ , weights. These weights are calculated in Equation A.6 through Equation A.15.

$$W_e = N_e \cdot W_{eng} = 1432.0 \text{ kg} \quad (\text{A.6})$$

$$W_n = 3.0 \cdot N_{inl} \cdot (A_{inl}^{0.5} \cdot l_n \cdot P_2)^{0.731} = 254.3 \text{ kg} \quad (\text{A.7})$$

$$W_{ai} = 0.32 \cdot N_{inl} \cdot L_d \cdot A_{inl}^{0.65} \cdot P_2^{0.6} + 1.735 \cdot [L_d \cdot N_{inl} \cdot A_{inl}^{0.5} \cdot P_2 \cdot K_d \cdot K_m]^{0.7331} = 83.8 \text{ kg} \quad (\text{A.8})$$

$$W_p = K_{prop1} \cdot N_p \cdot N_{bi}^{0.391} \cdot \left( \frac{D_p \cdot P_{TO}}{1000 \cdot N_e} \right)^{0.782} = 780.6 \text{ kg} \quad (\text{A.9})$$

$$W_{fs} = 80 \cdot (N_e + N_t - 1) + 15 \cdot N_t^{0.5} \cdot \left( \frac{W_F}{K_{sp}} \right)^{0.333} = 347.5 \text{ kg} \quad (\text{A.10})$$

$$W_{inflref} = 13.64 \cdot \left( \frac{W_F}{100 \cdot K_{sp}} \right)^{0.392} = 19.3 \text{ kg} \quad (\text{A.11})$$

$$W_{fd} = 7.38 \cdot \left( \frac{W_F}{100 \cdot K_{sp}} \right)^{0.458} = 12.7 \text{ kg} \quad (\text{A.12})$$

$$W_{ec} = 56.84 \cdot \left( \frac{N_e \cdot (l_f + b)}{100} \right)^{0.514} = 39.0 \text{ kg} \quad (\text{A.13})$$

$$W_{ess} = 12.05 \cdot \left( \frac{W_e}{1000} \right)^{1.458} = 29.2 \text{ kg} \quad (\text{A.14})$$

$$W_{pc} = 0.322 \cdot N_{bi}^{0.589} \cdot \left( \frac{N_p \cdot D_p \cdot P_{PO}}{1000 \cdot N_e} \right)^{1.178} = 72.6 \text{ kg} \quad (\text{A.15})$$

### A.3. Fixed Equipment Weight

The weights that make up the fixed equipment weight are the flight control system,  $W_{fc}$ , movable centre of gravity system,  $W_{fcg}$ , hydraulic and pneumatic system,  $W_{hps}$ , instrumentation, avionics and electronics,  $W_{iae}$ , electrical system,  $W_{els}$ , air-con, pressurisation, anti- and de-icing system,  $W_{api}$ , oxygen system,  $W_{ox}$ , auxiliary power unit,  $W_{apu}$ , furnishing,  $W_{fur}$ , paint,  $W_{pt}$ , armament,  $W_{arm}$ , and auxiliary gear,  $W_{aux}$ , weight. These are calculated in [Equation A.16](#) through [Equation A.27](#).

$$W_{fc} = K_{fcf} \left( \frac{W_{TO}}{1000} \right)^{0.581} = 595.1 \text{ kg} \quad (\text{A.16})$$

$$W_{fcg} = 23.38 \cdot \left( \frac{W_f}{100 \cdot K_{sp}} \right)^{0.442} = 38.3 \text{ kg} \quad (\text{A.17})$$

$$W_{hps} = 0.0098918 \cdot W_{TO} = 216.4 \text{ kg} \quad (\text{A.18})$$

$$W_{iae} = 0.040723 \cdot W_{TO} = 891.0 \text{ kg} \quad (\text{A.19})$$

$$W_{els} = 426 \cdot \left( \frac{W_{fs} + W_{iae}}{1000} \right)^{0.51} = 322.5 \text{ kg} \quad (\text{A.20})$$

$$W_{api} = 202 \cdot \left( \frac{W_{iae} + 200 \cdot N_{cr}}{1000} \right)^{0.735} = 161.6 \text{ kg} \quad (\text{A.21})$$

$$W_{ox} = 16.9 \cdot N_{cr}^1 \cdot 494 = 7.7 \text{ kg} \quad (\text{A.22})$$

$$W_{apu} = 0.0062185 \cdot W_{TO} = 136.1 \text{ kg} \quad (\text{A.23})$$

$$W_{fur} = 22.9 \cdot \left( \frac{N_{cr} \cdot \bar{q}_D}{100} \right)^{0.743} + 107 \cdot \left( \frac{N_{cr} \cdot W_{TO}}{100000} \right)^{0.585} = 72.8 \text{ kg} \quad (\text{A.24})$$

$$W_{pt} = 0.003 \cdot W_{TO} = 65.6 \text{ kg} \quad (\text{A.25})$$

$$W_{arm} = 0.01824863 \cdot W_{TO} = 399.2 \text{ kg} \quad (\text{A.26})$$

$$W_{aux} = 0.00250197 \cdot W_{TO} = 54.7 \text{ kg} \quad (\text{A.27})$$

A summary of these weights can be found in [section 8.2](#) which gives the value for the weights of each of the three categories and the final operating empty weight of the aircraft.

## Functional Breakdown Structure

The full FBS can be found in [Figure B.1](#) and [Figure B.2](#).

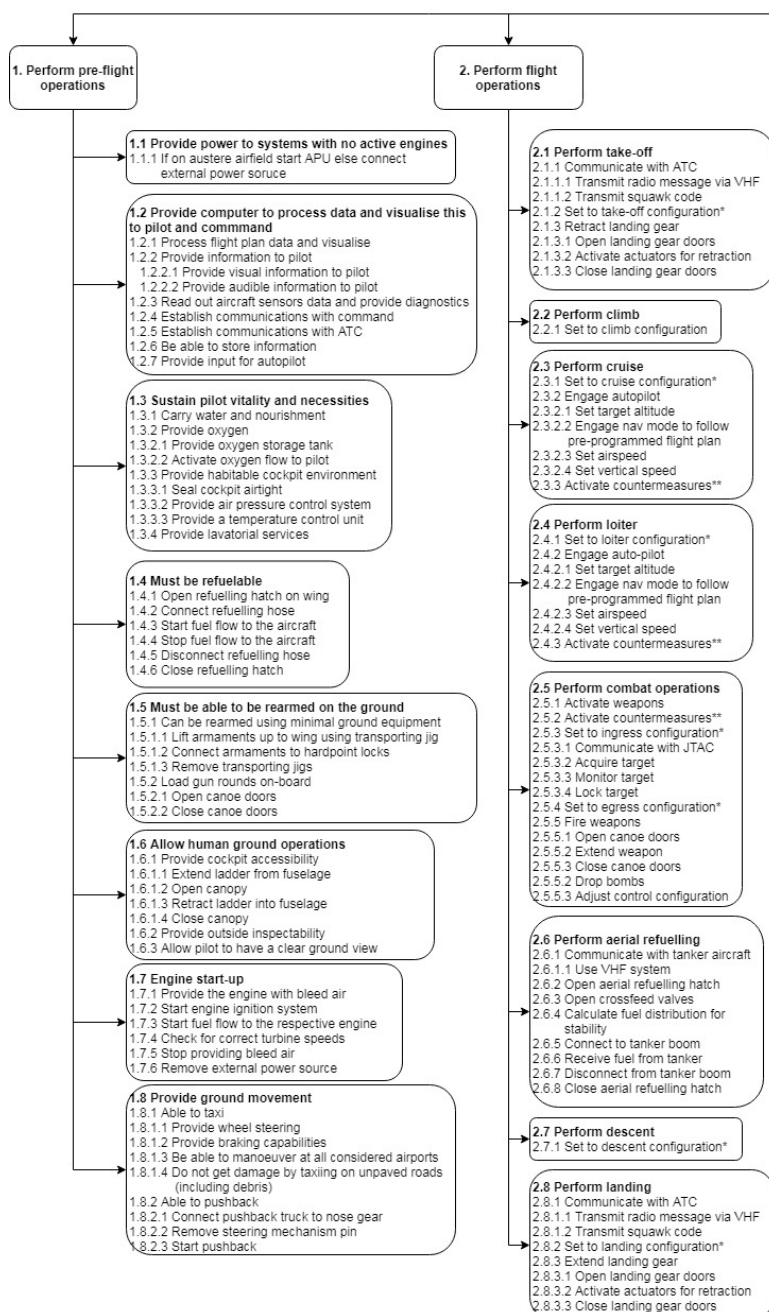


Figure B.1: Functional Breakdown Structure Part 1.

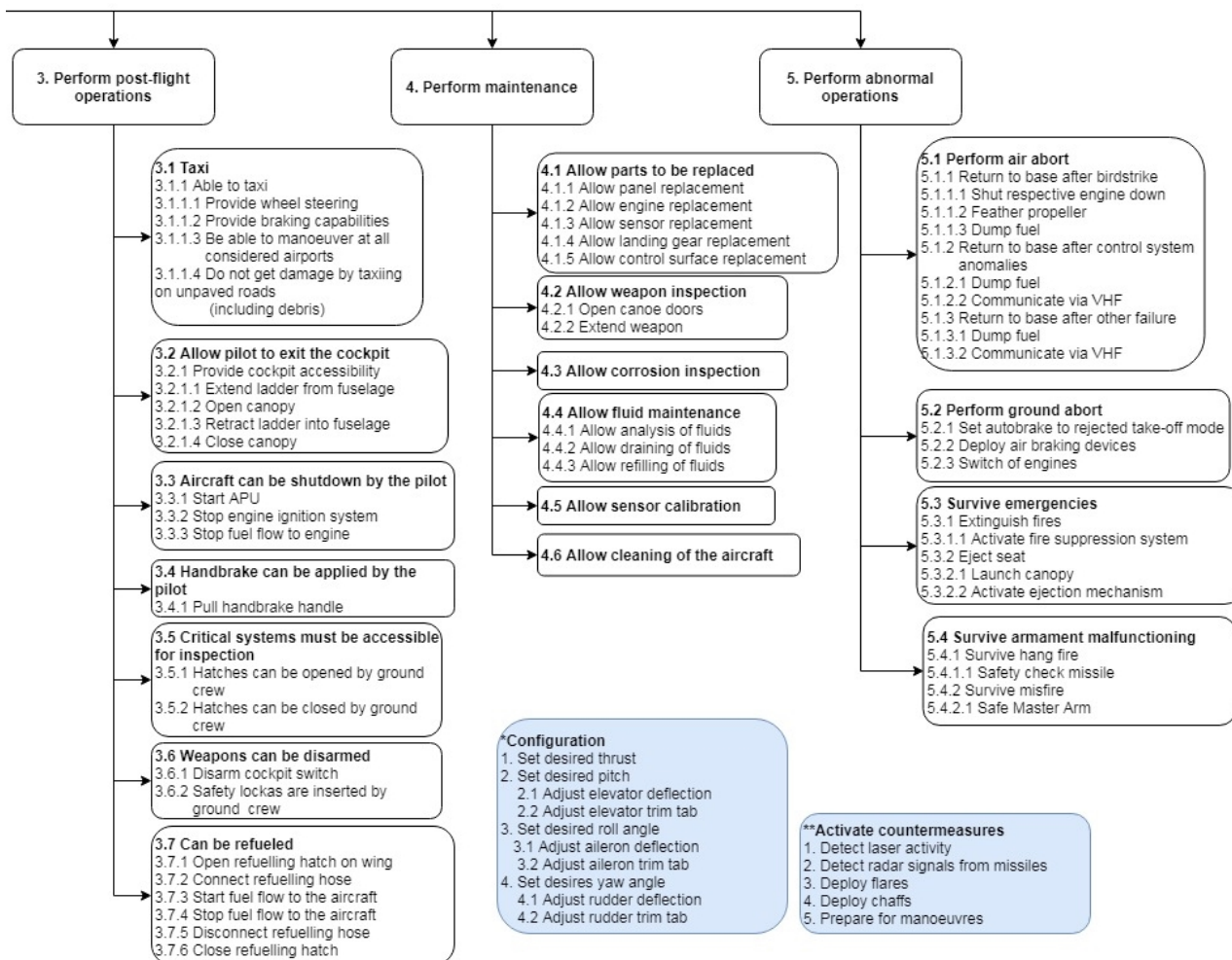


Figure B.2: Functional Breakdown Structure Part 2.

# C

## Requirements & Compliance Matrix

This chapter lists the most important system requirements that were used during the technical design stage of the project. Implicitly met requirements such as “being able to taxi” are not shown. The full list of requirements can be found in [3]. The final design values are examined to comply with the requirements. An indicator is present at every requirement that reveals how this particular requirement was obtained. The different indicators used are [U], [CS25], [RA], [DU], [F] and [L]. In the first section, the meaning of these indicators is explained. The second section contains the list of requirements. The final section contains some substantiation for the chosen values of the [L] category requirements.

### C.1. Requirement indicator definitions

**[U] (User requirements)** - These requirements are literally defined by the customer. Some user requirements are slightly adjusted to convert them to properly defined requirements. Note that, in consultation with the customer, some user requirements have been changed from the original user requirements for various reasons.

**[CS25] (Certification specifications)** - These requirements find their roots in the certification specifications for large aircraft, the CS-25 document. Large aircraft have to comply with these regulations with the goal of ensuring safety and performance. With the hope of adopting these features, some requirements are directly derived from the CS-25 document.

**[RA] (Reference aircraft)** - These requirements are derived from characteristics of reference aircraft. For a specific characteristic or value, the aircraft with the least constraining value is picked to generate a requirement. This is done to keep the design space as large as possible, without deviating significantly from existing aircraft.

**[DU] (Derived user requirements)** - These requirements are derived from a user requirement. In many cases this concerns sub-requirements that are derived from a more general user requirement.

**[F] (Rational functionality)** - These requirements follow from rational thoughts and are in all cases obviously needed to make the aircraft be able to perform its function.

**[R] (Remainder)** - These requirements follow from calculations, estimations and other methods.

### C.2. Requirement List

Code	The requirement description	✓ x~	Reference
<b>CASCA-PPFO</b>			
ASCA-PPFO-4)	The system shall allow aerial refuelling. [DU]	✓	<a href="#">Section 14.2</a>
ASCA-PPFO-4.1)	The system shall allow defuelling. [DU]	✓	<a href="#">Section 14.2</a>
ASCA-PPFO-5)	The system shall have a maximum ground turn radius of 120 feet (37 m). [U]	✓	<a href="#">Figure 14.1</a>

## CASCA-MAIN

CASCA-MAIN-3)	The system should be able to operate with minimal support infrastructure. [U]	✓	Chapter 11
CASCA-MAIN-3.1)	The system shall not use chilled fuels. [U]	✓	Section 14.2
CASCA-MAIN-4)	The system shall allow for complete engine replacement by 2 technicians within 8 hours. [U]	~	Section 17.3

## CASCA-COOP

CASCA-COOP-1)	The system shall have at least one weapon system with a lethal impact zone confined to a radius of 15 m. [L]	✓	Section 6.1
CASCA-COOP-2)	The system should have at least one weapon system with an 80 percent impact cone with an angle of 8 milliradians.[L]	✓	Section 6.1
CASCA-COOP-3)	The system shall have an ingress velocity of 180 KCAS at sea level (ISA). [U]	✓	Section 11.1
CASCA-COOP-4)	The system shall have a maximum manoeuvring load of +3g at ingress velocity at sea level (ISA). [U]	✓	Section 13.2
CASCA-COOP-5)	The system shall be compatible with JTAC standards. [U]	~	Section 18.1
CASCA-COOP-6)	The internal weapon system shall be able to disable ground targets at a range of at least 800 meters. [R]	✓	Section 6.1
CASCA-COOP-7)	The internal weapon system shall be able to penetrate Type IV armour plates within effective range. [F]	✓	Section 6.1

## CASCA-RALO

CASCA-RALO-1)	The system shall have a nominal range of 2000 km. [U]	✓	Section 11.3
CASCA-RALO-2)	The system shall have a loitering capability of 6 hours at 10000 feet in racetrack pattern at maximum endurance airspeed. [U]	✓	Section 11.3
CASCA-RALO-3)	The system shall have a ferry range of 4150 km. [U]	✓	Section 11.4

## CASCA-PERF

CASCA-PERF-1)	The system shall be able to achieve a rate of climb of 7.6 m/s at sea level (ISA). [RA]	✓	Section 11.3
CASCA-PERF-3)	The system shall be able to withstand g forces between -3g and +6g. [U]	✓	Section 13.2
CASCA-PERF-4)	The system shall be able to fly at an indicated airspeed of 129 m/s or more. [RA]	✓	Section 11.5
CASCA-PERF-5)	The system shall have a service ceiling of 7.0 km or higher. [RA]	✓	Section 11.5
CASCA-PERF-8)	The system shall have a thrust-to-weight ratio larger than 0.26. [RA][U]	✓	Section 11.1

## CASCA-STAB

CASCA-STAB-1)	The system shall be stick fixed statically stable. [F]	×	Section 12.7
CASCA-STAB-3)	The system shall be dynamically stable. [F]	×	Section 12.8

## CASCA-TAOF

CASCA-TAOF-1)	The system shall be able to take off at non-paved airfields. [U]	✓	Section 11.2
CASCA-TAOF-3)	The system shall have a take-off distance of less than 6000 feet at MTOW at 10 000 ft. [U]	✓	Section 11.2

**CASCA-LAND**

CASCA-LAND-1)	The system shall be able to land at non-paved airfields. [U]	✓	Section 11.2
CASCA-LAND-3)	The system shall have a minimum landing distance of less than 6000 m at MLW at 10 000 ft pressure altitude. [DU]	✓	Section 11.2

**CASCA-CONF**

CASCA-CONF-1)	The system shall be able to use conventional JP-X fuels. [DU]	✓	Section 11.1
---------------	---	---	--------------

**CASCA-MASS**

CASCA-MASS-1)	The MTOW shall be less than 23000 kg. [U]	✓	Section 4.3
CASCA-MASS-2)	The OEW shall include hardpoints, avionics, and electronics equipment. [U]	✓	Section 4.3
CASCA-MASS-3)	The Maximum Payload Weight of the system shall be at least 4000 kg including 1 crew member, armament and external fuel. [RA][U]	✓	Section 4.3

**CASCA-FINA**

CASCA-FINA-1)	The unit cost of the system shall be less than \$15 million. [U]	✓	Section 15.4
---------------	--	---	--------------

**CASCA-MASS**

CASCA-SUST-1)	The system shall be able to use biofuels. [U]	~	Chapter 16
CASCA-SUST-2)	The production processes shall release no harmful agents into the environment. [U]	✓	Section 19.2
CASCA-SUST-3)	The materials used shall release no harmful agents into the environment. [DU]	✓	Chapter 16

**CASCA-FLIS**

CASCA-FLIS-5)	The avionics of the system shall be able to be fully operational while the engines are not running. [F]	✓	Figure 14.3
---------------	---	---	-------------

**CASCA-DFNC**

CASCA-DFNC-1)	The system shall have active countermeasures. [U]	✓	Section 17.4
CASCA-DFNC-2)	The system shall have passive countermeasures. [U]	✓	Section 17.4
CASCA-DFNC-3)	The system shall be able to fly back to base after getting hit anywhere by a 7.62mm round. [U]	✓	Section 17.5

**CASCA-COSF**

CASCA-COSF-4)	The ordnance carried by the system shall be protected from touching the ground during take-off and landing. [F]	✓	Section 7.1
---------------	---	---	-------------